DROPS OF LIFE

Designing Membrane-bound and Membraneless Confinements

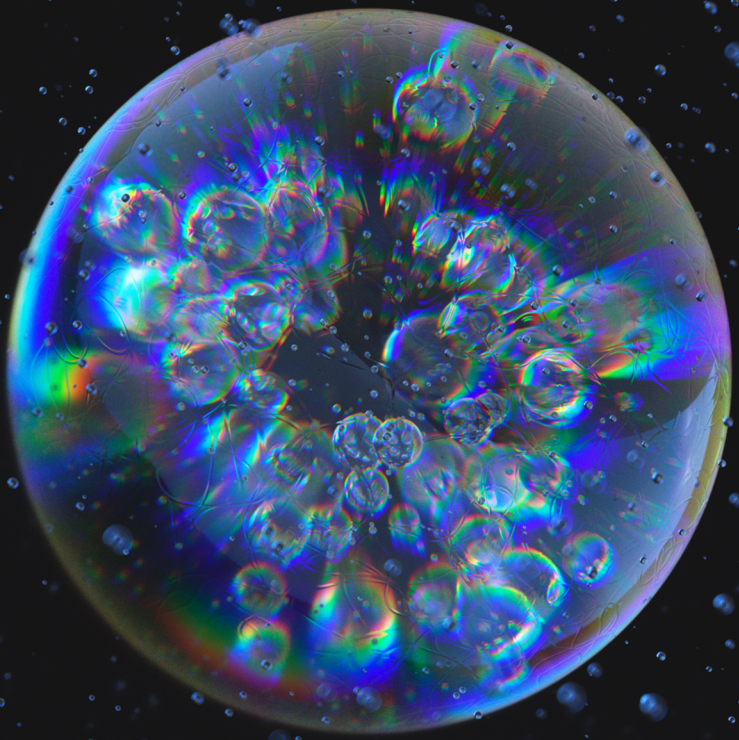

Ketan Ashok Ganar

Propositions

1. After all we know, disordered proteins are also ordered.
   (this thesis)

2. Bottom-up on-chip technology is the most efficient way to build a synthetic cell.
   (this thesis)

3. Confirmation bias hampers scientific output.

4. Traditional modes of scientific communication disregard general audience.

5. The COVID-19 pandemic taught us that human emotions are irreplaceable.

6. Poverty exists because it is non-contagious.

Propositions belonging to the thesis, entitled

Drops of Life: Designing Membrane-Bound and Membraneless Confinements

Ketan Ashok Ganar
Wageningen, 14 June 2024

Drops of Life

Designing Membrane-bound and Membraneless Confinements

Ketan Ashok Ganar

Thesis committee

Promotor
Prof. Dr J. van der Gucht
Professor of Physical Chemistry and Soft Matter
Wageningen University & Research

Co-promotors
Dr S.R. Deshpande
Assistant professor, Physical Chemistry and Soft Matter
Wageningen University & Research

Other members
Dr J. Hohlbein, Wageningen University & Research
Dr E. Spruijt, Radboud University Nijmegen
Dr E.B.A. Hinderink, Delft University of Technology
Dr D. Vorselen, Wageningen University & Research

This research was conducted under the auspices of Graduate School
auspices of VLAG Graduate School (Biobased, Biomolecular, Chemical, Food and Nutrition Sciences)

Drops of Life

Designing Membrane-bound and Membraneless Confinements

Ketan Ashok Ganar

Thesis

submitted in fulfilment of the requirements for the degree of doctor
at Wageningen University
by the authority of the Rector Magnificus,
Prof. Dr C. Kroeze,
in the presence of the
Thesis Committee appointed by the Academic Board
to be defended in public
on Friday 14 June 2024
at 4 p.m. in Omnia Auditorium

Ketan Ashok Ganar
Drops of Life: Designing Membrane-bound and Membraneless Confinements
209 pages

PhD thesis, Wageningen University, Wageningen, the Netherlands (2024)
With references, with summary in English

ISBN: 978-94-6469-921-0
DOI: https://doi.org/10.18174/657235

CONTENTS

Chapter 1

General Introduction

This chapter is based on the following articles

1. Ketan Ashok Ganar, Lawrence W. Honaker, and Siddharth Deshpande. "Shaping synthetic cell through cytoskeleton-condensate-membrane interactions." *Current Opinion in Colloid & Interface Science* 54 (2021):101459.

2. Bouzetos Evgenios, Ketan Ashok Ganar, Enrico Mastrobattista, Siddharth Deshpande, and John van der Oost. (*R)evolution-on-a-chip. Trends in Biotechnology 40. 1* (2022):101459. 60-76

1.1 BIOMOLECULAR ORGANIZATION OF CELLS

Living cells are extremely complex, which makes unravelling their emergent behavior indeed a difficult task. The plethora of molecular interactions that take place within the micron-sized cellular confinements is truly astonishing. Aside from studying cells as whole units, in what other ways can we decode their dynamic behavior at the molecular level? An effective alternative is to use purified cellular components and understand their behavior through using simplified *in vitro* setups. Such a strategy often also provides better control over the experimental parameters and easier manipulation of the system compared to *in vivo* studies. *In vitro* design of molecular reactions, particularly within cell-like enclosed confinements, has given rise to the idea of building synthetic cells.

Using the wealth of information on individual biomolecules, synthetic biologists are keen on designing and building artificial mimics of natural cells using minimal components[9, 10]. While *in vivo* genetic engineering and novel biomolecular pathways to reprogram organisms also fall under the broad umbrella of synthetic biology[16, 17], we specifically focus on the bottom-up creation of cell-like entities from purified as well as synthetic biomolecules. The idea underlying the construction of synthetic cells is crucial in obtaining the fundamental knowledge of biological systems with a lucrative application point-of-view, for example, in the field of molecular biosensing[20], metabolic engineering[22], and therapeutics, such as tumor suppression[23] and nanovesicles for drug delivery[17, 24, 25, 26]. The scope for synthetic biology remains wide open: it encompasses entities made from and incorporating naturally occurring biomolecules, bioinspired synthetic components, as well as entities without clear-cut biological analogs. From the many different modules some segments like growth, metabolism, transcription-translation, division, etc. are currently being investigated[27, 28, 29] with a key focus on how to control and regulate synthetic cell morphology[30]. We broadly divide the chapter in two domains. In the early sections (1.1 and 1.2), we discuss strategies aimed at inducing dynamic structural changes by using three distinct biological components—membranes, biomolecular condensates, and the cytoskeleton (**Figure 1.1**). The later sections (1.3 and 1.5) discuss different techniques to generate artificial compartments for building synthetic cells and its application in bioengineering (section 1.4).

Membranes are vital components of cells. In fact, every living cell has a ~5 nm thin membranous boundary composed of a lipid bilayer with proteins and other elements embedded in it. In addition, several membrane-bound compartments like nuclei, mitochondria, chloroplasts, etc. are crucial for intracellular biochemistry and organization. The amphiphilic nature of lipids, i.e., a hydrophilic headgroup linked

to hydrophobic tails, is responsible for their self-assembly, driven by hydrophobic interactions, into three- dimensional vesicular structures[31, 32]. The self-assembly of lipids and other natural, as well as synthetic amphiphiles, has been extensively utilized in bottom-up synthetic biology to form several different kinds of vesicles such as liposomes, polymersomes, and proteinosomes[33].

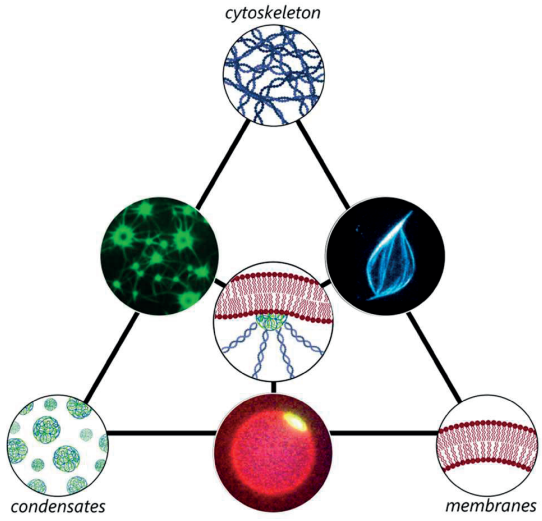

Figure I.1. Utilizing cytoskeleton-condensate-membrane interactions to shape synthetic cells.

A schematic expressing the interplay between active cytoskeleton, liquid condensates, and deformable membranes. Each side gives a representative example of an in vitro reconstitution of the pair in consideration, while the center presents achematic of an in vitro reconstitution of the three elements together. Appropriate dynamics between these three elements could help in structuring and functionalizing synthetic cells. Image adapted from the following references- cytoskeleton-condensate [1] , cytoskeleton-condensate [4] and condensate-membrane [2]

Micron-sized liposomes, also known as Giant Unilamellar Vesicles (GUVs), are particularly useful and popular scaffolds used for designing synthetic cells. This is mainly due to their suitable size (>1 μm) for visual inspection, standardized preparation methods, biocompatibility, ability to integrate transmembrane/membrane-interacting proteins, semi-permeable nature enabling transmembrane transport, and the low bending rigidity (~10 – 20 k^bT [34], where k^b is the Boltzmann constant and T is the temperature) making them suitable for shaping and structuring.

Along with membrane-bound organelles, another layer of sub-compartmentalization has become evident over the last decade: membraneless organelles[35, 36]. Also known

as biomolecular condensates (and simply referred to as condensates in this chapter), they are formed as a result of liquid-liquid phase separation (LLPS). LLPS is a consequence of the dissolved macromolecules having a higher affinity for each other than for solvent molecules. This results in free energy minimization manifested by the segregation of the involved macromolecules into two phases in equilibrium with each other: a condensed phase with a high concentration and a dilute phase with a much lower concentration[37]. Typically, condensates exhibit liquid-like properties: they form spherical droplets owing to their interfacial tension, they deform and flow under shear forces, and they undergo continuous internal diffusive rearrangement[37]. Numerous condensates have been found inside cells (nucleolus, Cajal bodies, stress granules, etc.) and have been identified to play diverse roles, ranging from selective enrichment of molecules and enhanced reaction kinetics to providing protective environments, acting as organizational hubs, concentration buffering, and more [38, 39]. The ability of condensates to physically manipulate their local environment primarily through interfacial tension forces (~0.1–100 pN μm^{-1}) and assist in mechanical work is only just beginning to be explored [40]. These unique properties of the phase-separated structures could play a particularly useful role in building synthetic cells.

The cytoskeleton, a highly dynamic proteinaceous scaffold, is responsible for cell mechanics, cellular motility, cell division, and intracellular transport. The cytoskeleton consists of three major proteins: actin microfilaments, microtubules, and intermediate filaments, with septins now being recognized as the fourth component[41]. The cytoskeletal elements, along with their numerous partner proteins, continuously (re) organize within the cytoplasm and provide a mechanical response against external forces. Actin and tubulin monomers polymerize at the expense of energy-rich nucleoside triphosphates to form polar filaments. Motor proteins (myosin in case of actin; kinesin and dynein in case of microtubules) migrate along these filaments and give rise to individual (e.g. cargo transport) or collective (e.g. contractile ring) motion and intracellular forces[42]. Septins are involved in a variety of membrane-remodeling processes, including cell division, cell motility, and cellular compartmentalization41. Encapsulation of purified cytoskeletal elements inside liposomes has shown substantial progress in recent years[43], and we will discuss them in the context of designing minimal, semi- or fully synthetic machineries capable of inducing dynamic morphologies.

1.2 TWO-WAY INTERACTION FOR DYNAMIC MORPHOLOGICAL CHANGES

While each of these three elements — cytoskeleton, condensates, and membranes — is important on its own, the interplay between them is even more vital to the

functioning of the cell. The interactions between the cytoskeleton and the cell membrane have already been extensively investigated, while the role of condensates in cytoskeletal and membrane dynamics is rapidly emerging. In the subsections below, we discuss recent advancements that have led to a better understanding of the dynamic interactions between these three biological components. First, we begin with a closer look at the specific pairs, cytoskeleton-condensate, cytoskeleton-membrane, and condensate-membrane, followed by discussing the three-way interactions involving all the components, as illustrated in **Figure 1.1**. The focus is particularly on the *in vitro* reconstitution approach, relevant to the bottom-up creation of synthetic cells. We will emphasize the impact condensates can have in shaping and structuring such synthetic cells.

1.2.1 Cytoskeleton–condensate interactions

Let us start with the behavior of cytoskeletal polymers in phase-separated environments, a newly discovered topic that is quickly gaining attention[44]. Like many other biomolecules, cytoskeletal proteins also have a tendency to be sequestered and concentrate inside condensates. What sets them apart, however, is their ability to undergo polymerization/depolymerization and form hierarchically assembled structures such as bundles and networks. This can exert internal/interfacial forces and deform the energetically favorable spherical shape of condensates. Furthermore, many cytoskeleton-associated regulatory proteins (plectin, tau, and epsin are just a few examples) contain intrinsically disordered regions[45] , increasing their propensity to undergo LLPS. Actin-binding proteins like N-WASP and cortactin (both act as nucleation promoting factors), for example, have been shown to become enriched within condensates[46, 47]. One of the first *in vitro* findings on actin-condensate dynamics demonstrated that actin filaments predominantly assembled at the surface of liquid droplets (**Figure 1.2a**)[3]. The condensates were made by the complex coacervation of polylysine (positively charged) and polyglutamic acid (negatively charged), two synthetic polypeptides. The spontaneous partitioning of actin at the interface substantially (approximately 50-fold) increased the rate of actin polymerization[3]. In another study, pre-formed actin filaments partitioned inside RNA/protein condensates that were initially isotropic in shape. However, owing to the anisotropic nature of the filaments, this led to the shape transformation of the condensates from spheres to tactoids (spindle-shaped droplets)[48]. This happened in a concentration- and size-dependent manner with deformations observed in droplets of a few hundred nanometers in diameter. In addition to its interactions with synthetic condensates, actin is also capable of forming liquid droplets together with naturally occurring actin-binding proteins, such as filamin, a bundling protein[49] . Similar to the previous example, the formed condensates displayed a tactoid shape as a result of the orientational ordering of actin filaments[7]. Moreover, the addition of myosin motors to the system resulted

in a surprising further observation: rod-like myosin clusters migrated to the midplane of the liquid droplet, leading to active deformation of the tactoids into two identical spindle-shaped actin liquid droplets joined by myosin puncta (**Figure 1.2b**). *In vitro* reconstitution of postsynaptic densities (protein-dense lamina located beneath the postsynaptic membrane) from neuronal cells was also shown to form condensates enriched in cortactin, an actin-binding protein and actin monomers[47]. This eventually promoted the formation of actin filaments and bundles, confirming that condensates can play a role in triggering actin assembly.

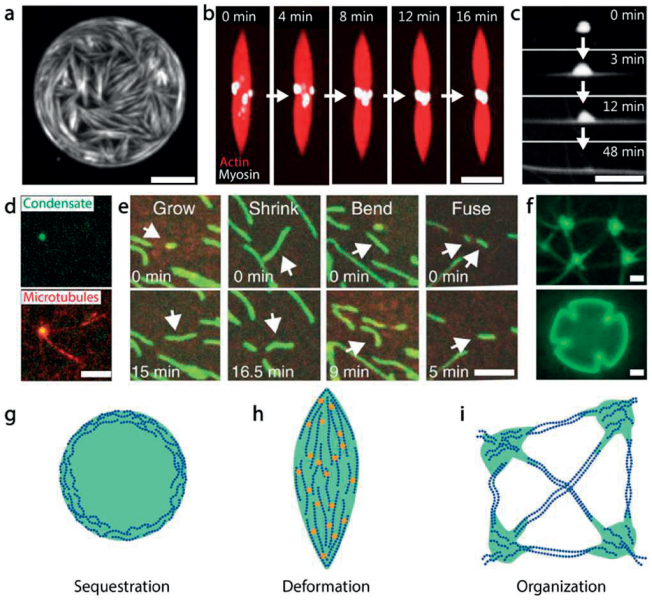

Figure 1.2: Cytoskeleton–condensate interactions.

(a) Actin partitions and polymerizes on the surface of polylysine/polyglutamic acid condensates with enhanced kinetics. (b) Actin filaments (red) and filamin form spindle-shaped condensates. Myosin motors (white)migrate toward the condensate midplane and promote droplet deformation, ultimately bisecting the liquid droplet into two equal halves. (c) Tubulin monomers partition inside tau condensates and polymerize in the presence of GTP. The growing microtubules dramatically alter the spherical shape of tau droplets through a wetting process. (d) Tubulin binding protein TPX2 co-condensates with tubulin and preferentially localizes on pre-existing microtubules, acting as a nucleating site for branching. (e) FtsZ monomers partition into polylysine/RNA liquid droplets (green). The rapid GTP-dependent filament turnover brings about a variety of condensate transformations such as growth, shrinkage, bending, fusion, and even division. (f) FtsZ monomers localize at the surface of polylysine/GTP coacervates and eventually form a network of FtsZ bundles interconnecting the individual condensates. The mechanical properties of the condensates are altered as seen through their fracture under mechanical stress. (g–i) Sketches depicting three key cytoskeleton (in blue)-condensate (in green) interactions: sequestration (g), deformations (h), and organization (i), in terms of providing nucleation or branching points, network formation, etc. All scale bars 5 μm. Images adapted from the following reference a[3], b[7], c[13]13, d [15], e [19] and f [1].

Similar to actin, tubulin has also been studied in phase-separated environments, with dramatic effects on the condensate morphology. One of the first studies of tubulin-condensate interactions was reported using an evolutionarily conserved BuGZ protein, which formed condensates *in vitro* and concentrated tubulin[50]. Subsequent *in vitro* studies revealed that tubulin monomers readily partitioned inside condensates formed by tau, a tubulin-binding protein found in neuronal cells. Interestingly, concomitant with the growth of microtubule bundles, tau droplets severely deformed, wetting the microtubule surface as the bundles grew in length (**Figure 1.2c**)[13]. Likewise, TPX2 protein, a spindle microtubule regulator, was observed to form liquid droplets together with tubulin. Notably, these TPX2-tubulin droplets preferentially localized on pre-existing microtubules, suggesting a mechanism for microtubule branching (**Figure 1.2d**)[15]. Parallel examples are also found in prokaryotes, especially in the case of FtsZ, a tubulin homolog involved in bacterial cell division[51] . FtsZ was shown to partition inside RNA/polylysine condensates. Analogous to the case of tau condensates, FtsZ polymerization actively deformed the liquid droplets. The rapid turnover of FtsZ filaments in the presence of a high concentration of GTP notably led to diverse morphological changes such as growth, shrinkage, bending, fusion, and division of these hybrid structures (**Figure 1.2e**) [19]. In another study, FtsZ was shown to partition on the surface of polylysine/GTP condensates. Since FtsZ polymerizes by hydrolyzing GTP, the condensates functioned as a fuel reservoir and dissolved over time. A network of FtsZ bundles emerged when GTP was present in a sufficient quantity, interconnecting the individual condensates. Furthermore, these FtsZ-coated condensates exhibited solid-like behavior, as they fractured under mechanical pressure, forming flower-like structures (**Figure 1.2f**)[1].

All these examples clearly indicate that cytoskeletal biochemistry is not only compatible with LLPS environments, but it further leads to enhanced cytoskeleton capabilities in terms of increased reaction rates and spatiotemporal regulation. Condensates can thus provide architectural scaffolds and serve as reaction hubs for organizing and orchestrating the cytoskeletal response, as sketched in (**Figure 1.2g-i**). Depending on the physical and chemical nature of the condensates, cytoskeletal partitioning and activity can be controlled, as evident from the given examples and sketches of surface localization (**Figure 1.2g**), shape deformation (**Figure 1.2h**), and provision of branching, as well as nucleation points (**Figure 1.2i**). Interestingly, once cytoskeletal elements self-assemble into dynamic, micro-sized, self-assembled structures, they can bring about diverse morphological changes to condensates, forcing them into non-spherical, stressed configurations. These out-of-equilibrium states could be potentially useful to form force-generating structures within synthetic cells.

1.2.2 Cytoskeleton–membrane interactions

Just as the scaffolding beams are necessary to support the tent, the cytoskeletal polymers can be roughly seen as the 'dynamic beams' that support the 'flexible walls' represented by the cell membrane. To unveil the role of the cytoskeleton in cellular morphogenesis, understanding the interaction of involved proteins with membranes is necessary. For this, purified protein systems have been extensively reconstituted both within and on the outer surface of GUVs, and this section reports the latest progress in this regard.

Caging multiple cytoskeletal proteins and further coupling them to the membrane in a natural/synthetic manner is a challenging task. Using natural linkers, i.e., membrane/membrane-interacting proteins, further adds to the complexity, and their use is not always feasible. Alternatively, synthetic linkers in the form of strong binding partners, such as streptavidin-biotin and histidine-nickel couplings, are easier tools to direct proteins onto a membrane. For instance, by doping liposomes with biotinylated lipids, streptavidin-tagged actin regulatory proteins could be readily recruited to the outer leaflet of the membrane[52] . These recruited complexes eventually led to actin localization at the membrane and subsequent polymerization induced tubes and spike-like inward protrusions in osmotically deflated 'floppy' liposomes[52]. It should be noted that the osmotic pressure difference across the liposomal membrane affects membrane tension: a liposome in a hypertonic environment will be deflated and will have a lower membrane tension compared to a liposome placed in a hypotonic environment. A recent investigation reinforced the role of membrane tension in supporting the deformations caused by a membrane-bound actin network. In non-deflated liposomes, capping protein- (regulator of actin filament elongation) bound actin filaments induced symmetric dumbbell-shaped deformations, whereas liposomes did not become deformed in the absence of capping protein[53]. However, in deflated liposomes, even in the absence of capping proteins, actin filaments alone induced symmetric dumbbell-shaped deformation to a similar extent as they did in the presence of capping protein, suggesting that the interplay between membrane tension and actin network dynamics governs cell shape. In addition to the membrane tension, the actin coat thickness also influences the extent and the way a vesicle will deform. In osmotically deflated actin-coated liposomes, the membrane underwent irreversible buckling or wrinkling, depending on the actin shell thickness (**Figure 1.3a**)[4]. For thinner actin shells, membrane buckling was predominant, whereas globular wrinkling was observed in the case of thicker actin shells. An alternate strategy to direct proteins to a membrane is by tagging them with a polyhistidine moiety and using nickel-containing lipids (e.g. nickel-nitrilotriacetic acid, Ni-NTA). A fine example is the recent use of histidine-tagged anilline proteins to reconstitute a minimal actomyosin cortex at the membrane, where sufficient membrane tethering and

motor activity resulted in bleb-like membrane deformations, reminiscent of the blebbing motility of cells (**Figure 1.3b**)[8]. Interestingly, blebbing could also be inhibited either by increasing the density of membrane/cytoskeleton linkers or by reducing the myosin concentration, highlighting the importance of membrane linkage, as well as motor activity for inducing membrane deformation. In another recent use of histidine-nickel coupling, encapsulation of capping proteins with other actin-binding proteins like profilin, Arp2/3, and the His-tagged VCA domain of NWASP-directed the protein complex to the lipid membrane. As a consequence of actin polymerization at the membrane, interesting topological deformations were observed in response to variations of capping protein concentration: lower concentrations of capping protein-induced star-like clusters on the membrane while higher concentrations promoted fission events[54] .

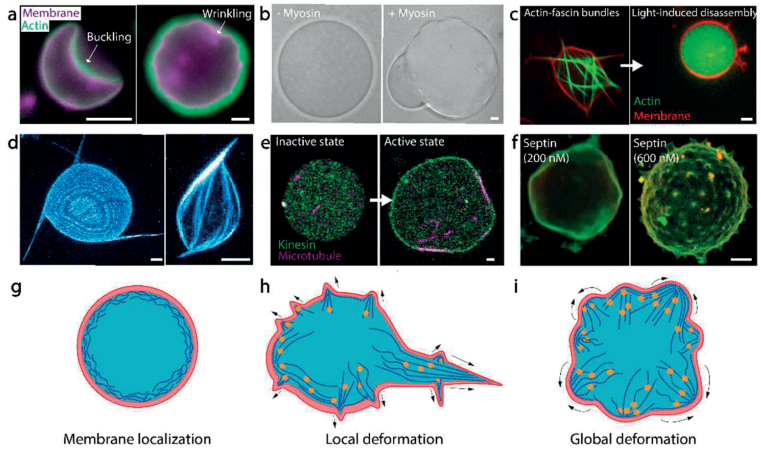

Figure 1.3:Cytoskeleton–membrane interactions.

(a) Actin (green) shell coated on the outer side induces either buckling or wrinkling of osmotically deflated liposomes (magenta), depending on the actin shell thickness. (b) Actomyosin cortex, anchored to the membrane by anillin through Ni-NTA-His bonding, induces bleb-like deformations only in the presence of myosin. (c) Liposome exhibiting prominent filopodia-like membrane protrusions, induced by actin-fascin bundles (left). The spherical shape of the liposome is restored upon actin disassembly induced by light (right). (d) Encapsulation of microtubule-kinesin system inside liposomes induces filopodia-like membrane deformations. The topological constraints and vesicle deformability lead to dynamic, shape-changing vesicles, with smaller vesicles (right) deforming more than bigger ones (left). (e) A microtubule-kinesin system caged inside liposomes (left) triggered local membrane deformations (right) in response to the kinesin motor activity coupled to the membrane via DNA-based linkers. (f) Septin filaments localize on liposomes consisting of phosphatidylinositol-4,5-bisphosphate lipids, flattening the membrane locally at low concentrations (left) and inducing spike-like membrane protrusions uniformly across the liposome surface at high concentrations (right). (g-i) Sketches showing showing the three prominent cytoskeletons (in blue)-membrane (in red) interactions: localization at the inner leaflet (g), local deformations (h), and global deformations (i). All scale bars 5 µm. Images adapted from following references a[4], b[8] ,c[12] ,d[5] ,e[18] and f[21]

Membrane deformations can also be induced by actin cross-linking and bundling proteins. As recently demonstrated, fascin-induced actin bundles formed prominent spiky filopodia-like protrusions in GUVs (**Figure 1.3c**, left panel)[12]. Upon light-induced disassembly of actin bundles, the spherical conformation of the liposome was restored within few minutes (**Figure 1.3c**, right panel). Microtubules have also been effectively explored in *in vitro* settings to deform vesicles. Similar to myosin motors sliding along actin filaments, kinesin motors glide over microtubules to generate active extensile stresses. Microtubules confined in GUVs, along with ATP-fueled kinesin motor clusters, demonstrated remarkable active topological dynamics[5]. The microtubules were adsorbed to the membrane through depletion interactions [55], and upon osmotic deflation, these vesicles showed periodic shape fluctuations characterized by a change in ellipticity and the formation of filipodia-like protrusions. The extent of topological deformations was found to be inversely proportional to the vesicle size, with smaller vesicles showing higher deviation from spherical shape and vice versa (**Figure 1.3d**)[5]. By deviating from the conventional usage of cellular machinery, an interesting study demonstrated the use of hydrostatic pressure to control the polymerization of tubulin encapsulated inside GUVs, leading to membrane deformations in the absence of motor proteins[56]. At lower pressure (0.1 MPa), tubulin polymerization induced prominent outward protrusions. These protrusions shrank rapidly at higher pressure (60 MPa), making it a reversible process. Lastly, using a totally synthetic route, DNA was used as an actuator to trigger microtubule-assisted shape changes. When engaged, the DNA linker transmitted the force generated by the motor to the membrane, resulting in a local flattening of the liposomal membrane (**Figure 1.3e**)[18]. Furthermore, this DNA 'clutch' could be rendered photosensitive in order to control the shape-changing behavior through exposure to light.

The fourth cytoskeletal element, septin, is also involved in membrane remodeling in cells and can bring about structural changes to vesicles through interactions with specific lipids [57], as demonstrated in a recent study. Similar to actin-binding proteins, the extent of deformation was concentration-dependent: at low concentrations, septin interactions led to the local flattening of the liposomal membrane indicating an alteration in the mechanical property of the septin-bound membrane (**Figure 1.3f**, right panel). At higher concentrations, septin developed evenly spaced, pronounced spikelike protrusions across the entire membrane (**Figure 1.3 f**, right panel)[21] .

Based on the above observations, it is evident that cytoskeleton-membrane interactions, as sketched in (**Figure 1.3g-i**), are very effective in bringing about active local (**Figure 1.3h**), as well as global (**Figure 1.3i**) membrane deformations. A key parameter that seems to play a crucial role in enhancing cytoskeleton-based morphological changes is the reduction of the membrane tension of vesicles, often achieved through osmosis.

Localization of the cytoskeletal filaments to the membrane is naturally facilitated by specific proteins acting as linkers. However, from the point-of-view of synthetic cells, a variety of synthetic membrane connectors can be used as replacements for natural proteins, partly simplifying the design process. Thus, condensates can be interesting choices to position the two elements in close proximity to each other. The next section discusses the interactions of condensates with membranes and how condensates can act as linkers between the cytoskeleton and the membrane.

1.2.3 Condensate–Membrane interactions

The previous two sections have looked at the roles the cytoskeleton can play in phase-separated and membranous environments to shape synthetic cells, but what about the interactions between condensates and membranes, where the cytoskeleton is less of a participant? While relatively less breadth of research has looked at this emerging field, we expect these interactions to play crucial roles in shaping synthetic cells. This section focuses on recent studies on condensates interacting with membranes. Moreover, we also describe relevant examples where the cytoskeleton is recruited to this hybrid interface, and the three elements coexist to form a basic structuring unit.

In principle, when a condensation trigger is met, condensates can be expected to be distributed randomly within confinement. However, many membraneless organelles within cells have designated locations[35, 36] , which has led to a body of recent work that looks into how this ordering and structure can be guided, and in this particular context, how condensates interact with membranous components of the cell[14, 58, 59, 60, 61] . This primarily uses *in vitro* reconstitution of analogs of cellular systems owing to the complexity of cellular machinery. A recent work explored using a liposomal membrane as support for condensation[2], as depicted in (**Figure 1.4a**) . To do so, liposomes were prepared using a mix of lipids involving a small amount of highly negatively charged lipids (phosphatidylinositol (3,4,5)-triphosphate). Strong electrostatic interactions between the overall negatively charged membrane and positively charged polylysine/ATP condensates promoted the adhesion of the formed condensates onto the liposome membrane, which could still migrate along the membrane. More notable, however, was that cholesterol-tagged RNA/spermine condensates wetted uncharged membranes[2] (**Figure 1.4a**, left panel), in opposition to the general tendency of the condensates to maintain their spherical shape; this wetting was due to the interaction of cholesterol with the membrane. Liposomes with sticky condensate patches were observed to adhere to each other at these patches (**Figure 1.4a**, right panel). This hints toward a possible role of the involved interactions to form multiparticle assemblies.

Such condensate-membrane interactions are certainly not only limited to liposomes, though: using proteinosomes as the containers, positively charged condensates were

similarly adsorbed to the negatively charged protein-based membrane[6] (**Figure 1.4b**). The study further showed that modulation of the salt content could additionally have strong effects on the eventual spatial arrangement of the condensates: added salt desorbed the condensates from the membrane owing to the screening of the electrostatic interactions, resulting in the desorbed condensates assuming a spherical shape, as confirmed by fluorescence imaging. An equally promising and interesting result in this study was that the condensates could be used as chemical reactors, enhancing the catalytic activity of enzymes once localized and sequestered at the protein-condensate membrane. The reversible switching of the condensation trigger proves promising here in that enzymatic or other reactive activity can thus become modulated via the adsorption and desorption process. Another study, illustrated in (**Figure 1.4c**), looked at the interaction between synthetic condensates and chloroplasts to create a photosynthetic protocell[11]. Again, using a charge-based attraction between positively charged condensates and the negatively charged chloroplast membrane, chloroplasts harvested from plants could be rapidly trapped within the phase separated liquid droplets. This endocytic step occurs within seconds and is reversible, with the release of the chloroplasts achievable simply by dissolving the condensate. The photosynthetic capabilities of the chloroplasts were preserved, thus confirming the biocompatible nature of these hybrid systems. While not a strictly condensate-membrane interaction akin to others, this fine example illustrates the use of charge-attraction principles to localize and trap organelles and other cellular components. A natural progression from solely looking at the interactions of condensates and membranes alone is the recruitment and local action of the cytoskeletal elements. One such example is found in cellular interstitial spaces in vertebrates, known as tight junctions. A recent study showed that these tight junctions are filled with a variety of proteins that phase separate and subsequently enrich as well as localize adhesion receptors, transcription factors, and cytoskeletal adaptors[62]. This further leads to the recruitment of actin, providing more rigidity and structure to the cells. This and a few other *in vivo* studies, along with *in vitro* reconstitutions of the involved set-ups, have looked at the interactions of the actin cytoskeleton with membrane-interacting condensates. One such example is where actin-binding protein complexes, such as N-WASP, NcK, and the transmembrane protein nephrin, were shown to form condensates at the membrane, and subsequently promoting the growth of actin at those sites[46] . The stoichiometric ratios of the condensate components had a direct effect on the membrane dwelling time of actin recruitment proteins: the lengthening of their dwelling time increased their overall activity in recruiting actin to the surface[46] . A similar study revealed that a phosphorylated state of the transmembrane LAT protein (linker for activation of T cells) promoted condensation with adaptor proteins Grb2 and Sos1 at the membrane[14]. As can be seen in (**Figure 1.4d**), these condensates recruited actin, leading to localized actin polymerization at these condensates and inducing shape

changes to them, similar to the examples in (**Figure 1.4c and e**). In the absence of actin, the shape assumed was more strongly interfacial tension-driven. In general, condensate-membrane interactions can be grouped under two categories: condensate attachment to a membrane, as depicted in (**Figure 1.4e**), and cytoskeletal recruitment to condensates in order to induce a regulated deformation, as shown in (**Figure 1.4f**). These previously illustrated examples, however, only begin to scratch the surface of the possible interactions between condensates and membranes. Another recent work has shown that condensate-membrane interactions can, by themselves, induce membrane deformations: a condensate attaching to the inside of a membrane can lead to invagination[63], which is striking considering that deformations in the membrane for locomotion and endocytosis, for example, are commonly assisted by the cytoskeleton. This condensation is driven by the LLPS of proteins at the membrane interface, reducing the interfacial tension and the associated energy cost of membrane deformation. This is an important finding, as it hints at the role of condensation in performing mechanical work at membranous interfaces and how the membrane itself is readily deformable through components apart from the cytoskeleton.

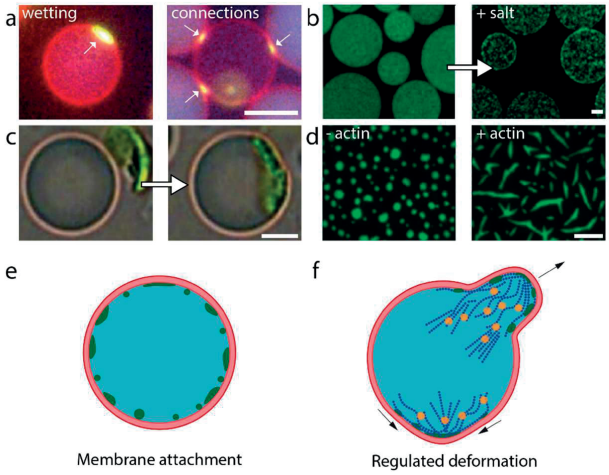

Figure I.4: Condensate–Membrane interactions.

(a) Cholesterol-RNA/spermine condensates wet at the liposome boundary due to cholesterol-mediated membrane anchoring, as indicated by the arrow (left panel). Multiple liposomes can be connected to each other through the condensate patches at the membrane, as indicated by arrows (right panel). (b) Reversible interaction of condensates with the membranous boundary of proteinosomes, modulated by tuning the ionic concentration. (c) Negatively charged membranous chloroplasts (green) can become rapidly engulfed by positively charged condensates (gray sphere), creating a kind of prototype photosynthetic cell. (d) The recruitment of actin to condensates localized at a membrane leads to anisotropic shape deformation of condensates, countering the interfacial tension that normally promotes their spherical shape. (e and f) The condensate (in green)-membrane (in red) interactions can be largely classified as membrane attachment interactions (e), where the condensates adsorb to the memb rane, and regulated deformations (f), which can involve cytoskeleton (in blue) recruitment to induce a shape deformation in the membrane. All scale bars 5 μm. Images adapted from following references a[2] , b[6] , c[11] , and d[14]

What applications could these condensate-membrane interactions, both with and without the involvement of the cytoskeleton, lead toward? We can, first of all, look at the membrane as a scaffold to build condensate sites, with a useful option of their reversible dispersal into the cytoplasm. The binary switch-like ability of condensation can further provide options for tuning and triggering catalytic and enzymatic activity: this can be incorporated into a feedback loop, much like in living cells, where the reactions become actuated based on the environment. These membrane-bound condensate sites can additionally act as docking stations to which the cytoskeleton attaches. By tuning the interfacial properties of the condensates, their eventual distribution on the membrane wall can additionally be directed, which, once the cytoskeleton is recruited, can further be tuned to achieve desired and specific shapes and cellular morphology. These local sites can also prove useful for incorporating membrane-bound organelles and other elements in desired positions.

1.3 ON-CHIP MICROFLUIDICS TECHNOLOGY FOR BIOENGINEERING.

Walking towards the goal of developing a sustainable synthetic cell, we used on-chip microfluidic platform as our working horse. Working with biological systems is often challenging particularly due to low sample quantity, hence reducing sample volumes is of key importance. The state-of-the-art microfluidics technology enables handling of small fluid volumes (in the range of microliter) and makes use of the predictable behavior of fluids at low-enough flow rates within microchannels of desired geometries. Microfluidic technology has revolutionized biological analysis tremendously by downscaling the laboratory-based systems popularly referred to as lab-on-a-chip devices. These miniaturized systems allow for a substantial reduction of required reagents as well as the analysis time. For example, a typical microtiter plate (96 wells) generally requires 50-100 μL of sample per well, whereas a typical water-in-oil droplet of 20 μm diameter produced using on-chip microfluidic setup corresponds to a volume of merely ~4 pL (i.e., more than seven orders of magnitude smaller). How do fluids flowing at smaller length scales and low-enough flow velocities differ from fluid flows that we experience in daily life, such as stirring black coffee? The main difference is a predictable laminar flow against an unpredictable turbulent flow, depending on whether the viscous forces or the inertial forces dominate the system. To determine which of these forces get an upper hand, one can calculate the Reynolds number (Re) for a system, which is defined as the ratio of inertial forces to viscous forces.

$$Re = \frac{\rho v L}{\eta} \qquad (1.1)$$

,

Here, ρ is the fluid density, υ is the velocity, L is the characteristic linear dimension of the system, and η is the dynamic viscosity. Typically, for Re <2000, viscous forces dominate, resulting in laminar flow[64]. Thus, while mixing of an ink drop in water is a turbulent phenomenon defined by the unpredictable nature of the motion of fluid as shown in (**Figure 1.5a**), on the contrary, two water streams meeting each other in a microfluidic device will simply flow parallel to each other (although they will mix in a diffusive manner further downstream) (**Figure 1.5b**). Calculating Re for a typical microfluidic system makes this clearer. For a water stream flowing through a microfluidic channel ($\eta \approx 10^{-3}$ Pa.s, $\rho \approx 10^{3}$ kg/m^3, $\upsilon \approx 1$ mm/s, L ≈ 100 μm),

Re ≈ 0.1 , confirming a laminar flow. The laminar nature of the fluid flow, combined with competing effects of the deformation of the interface by a local shear stress and the resistance to this deformation by interfacial forces, leads to production of micron-sized emulsion-based confinements of various nature[65].

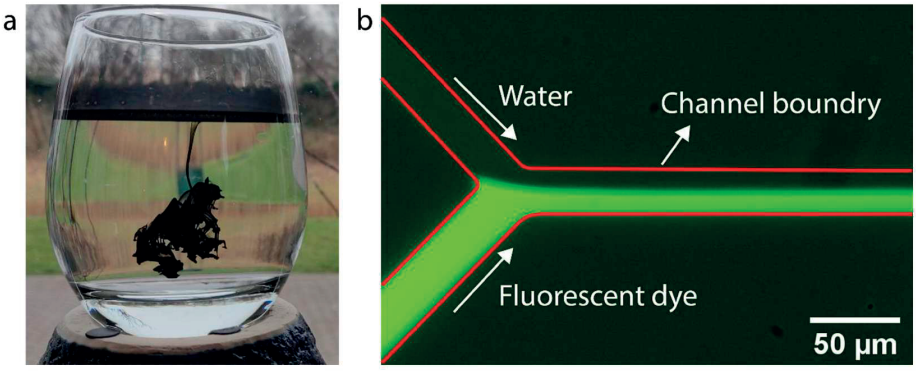

Figure 1.5: Turbulence and laminar flow.

(a) An ink drop mixing in water in a turbulent manner. (b) Demonstration of laminar flow in a lab-on-a-chip device by co-flowing two streams of water (with and without a fluorescent dye) parallel to each other without mixing.

1.4 CONFINEMENTS FOR APPLICATIONS IN SYNTHETIC CELL

Under the umbrella of building synthetic cells, various emulsion-based modules have been established from the standpoint of understanding the fundamentals of life together with a wide range of industrial applications. For instance, microemulsion-based confinements have been widely used for applications such as cargos for drug delivery[66], vaccine administration[67], tissue engineering[68], food industry[69, 70] as well as genetic engineering[71]. In this thesis, we also aimed to use emulsion-based confinements for protein engineering. The following section describes the principles of laboratory evolution of proteins along with the benefit of using emulsion as *in vitro* compartment for protein evolution.

1.4.1 Laboratory evolution of proteins

Darwin's theory of evolution states that species change over time and the evolved species inherit a set of genes from its ancestor[72]. However, this process of natural evolution is extremely slow and can take millions of years. Scientists have tried to accelerate this process using a laboratory-based adaptive evolution approach. To understand this,

let us assume a bacteria which ideally prefers 37°C as an ideal temperature to grow and divide. By slightly lowering the incubation temperature of the bacteria to 35°C, the bacteria is forced to respond and acclimatize to this new environment (**Figure 1.6** left panel). Although in principle all the bacteria (the beginning of experiment) are identical, some bacteria are better than others at coping with this stress of varied temperature resulting in a mixed population. Selecting for the better coping species, and repeating the cycle for multiple iterations ultimately leads to an evolved species of bacteria that has altered its metabolism and adapted to grow at lower temperature (**Figure 1.6**, right panel). Nonetheless, one of the drawbacks of this approach for bacterial evolution is the unpredictability in the nature of change that might occur during this process. For instance, in the above mentioned example the adaptation of bacteria to lower temperature could be due to either genetic modifications or metabolic changes or combination of both. Thus the lack of control over the system makes it difficult to associate the phenotypic behavior to precise changes in bacteria.

Secondly, highly characterized bacteria like *E.coli* are widely used as a confinement for evolving protein since they are easy to grow, have a well characterized genome, and give easy access to standardized protocol for genetic manipulations[73]. However, their use is limited and often fail due to cytotoxicity of protein, resistance to antibiotics, and the risk of bacteria rejecting the external gene in the process of multiple iterations[74]. Bypassing the use and only using cellular extract consisting transcription and translation machinery is beneficial for the purpose of cell free proteomics[75].

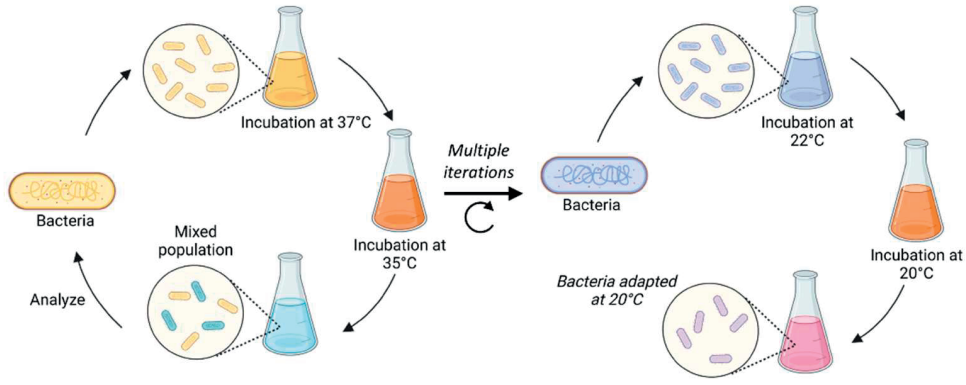

Figure 1.6: Adaptive laboratory evolution of bacteria.

Schematic depicting an example of adaptive laboratory evolution of bacteria by gradually reducing temperature. Multiple iterations of adapting the bacteria to lower temperature leads to an evolved species which grows at lower temperature

Cell-free *in vitro* directed evolution, is a prominent technique for the engineering of target proteins using similar principles of natural selection. The process involves three distinct steps: diversification of gene, selection of desired phenotype, and then subsequently screening of the positively evolved variant (**Figure 1.7**). For instance, when aiming to enhance the catalytic activity of an enzyme, the corresponding gene is subjected to diversification. This is easily done by introducing random mutations in the gene and thus generating a library of different genetic variants. Given the challenges of studying such a huge library as a whole, these gene variants are isolated individually by compartmentalizing, allowing to examine them individually. To link the genotype to its respective phenotype, a selection strategy is crucial to differentiate the better variants from a pool of bad ones. For examples a fluorescence-based strategy which links the enzymatic activity of protein to expression of fluorescence protein. The superior activity enzyme is fished out, and the respective genotype is recovered. Iterating this cycle several times yields a refined enzyme variant exhibiting enhanced activity compared to the wild-type variant.

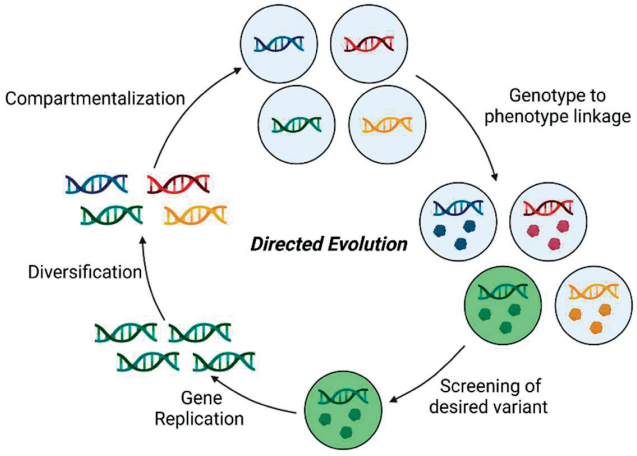

Figure 1.7:

Schematic depicting different steps like genetic diversification, compartmentalization, selection, and screening of desired variant to achieve protein evolution.

1.5 MICROFLUIDIC PRODUCTION OF EMULSIONS

The salient features of on-chip microfluidics as described in section 1.3 is highly favorable for controlled production of micro-sized emulsions in high throughput fashion. Additionally, emulsions generated using microfluidics are monodispersed, eliminating the size-based variation in experiment results. Additionally, emulsions can be designed to exhibit biocompatibility and their impermeable barrier assist to encapsulate and retain large molecules like DNA, RNA and proteins. This is an important feature essential to achieve genotype-to-phenotype linkage. In the following sections, we discuss plausible different types of emulsions that can be used, the state-of-the-art methodology to produce them, and finally comparing different types of emulsions highlighting its advantages and disadvantages.

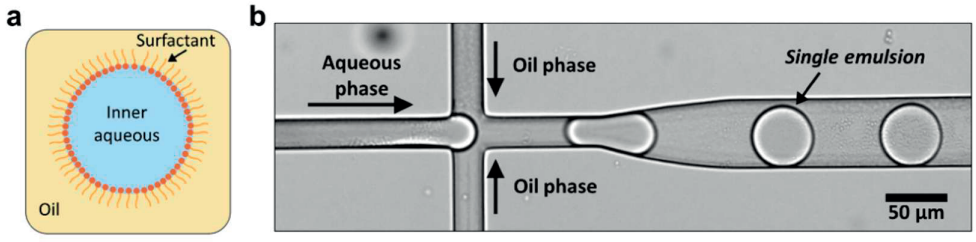

Figure 1.8: Anatomy of a single emulsion.

(a) Schematic representing surfactant stabilized water-in-oil single emulsion. (b) Production of micron-sized water-in-oil single emulsion using a microfluidic device with a flow- focusing junction

1.5.1 Single emulsion: water-in-oil confinements

Emulsion-based compartments can serve as an excellent model for cells, of which, single emulsions (hereby simply referred as emulsions) are most frequently used. Depending on the volume ratio of water to oil and the type of surfactant, either oil-in-water or water-in-oil emulsions are formed, with the droplet size ranging from a few nanometers to hundreds of micrometers[76]. Since oil-in-water emulsions are unsuitable to be used as compartments as most of the desired biochemical reactions require water-based aqueous environment, emulsions in this context refer to water-in-oil emulsions (**Figure 1.8a**). To prevent emulsion droplets from fusing, surfactants are routinely added to the oil and sometimes also to the aqueous phase[77]. Emulsions were initially generated in large numbers using straightforward bulk approaches, i.e., by mixing aqueous buffer with oil in presence of surfactants. However, this poorly controlled process generally resulted in highly polydisperse emulsion populations, seriously affecting the uniform encapsulation of reagents.

Despite the polydisperse nature of the emulsions, numerous studies have successfully demonstrated complex biochemical assays evolving proteins evolution[78, 79, 80, 81]. Nonetheless, polydispersity tends to hamper downstream screening, as small volumetric deviations can substantially affect the concentration of enzyme-derived products[82]. Incremental evolution campaigns will significantly benefit from uniform volumes as well as constant reagent concentrations and stoichiometry, highlighting the importance of monodisperse emulsions generated using microfluidics (**Figure 1.8b**). Highly monodisperse water-in-oil droplets are generated using on-chip microfluidics. For example, droplets of 45 μm in diameter, have been produced at a rate of 1–10 kHz [82]. Production rate can be substantially increased by operating multiple parallel production channels in a single microfluidic device, or by using a serial droplet-splitting technique, subsequently resulting in smaller droplets. Frequency up to 1.3 MHz was achieved by running multiple microfluidic devices in parallel[83]. Mechanical splitting of large droplets into smaller vesicles by introducing splitter array can also increase the throughput, preferably >1000 droplets/hour [84]. The high throughput nature, the excellent encapsulation, and the feasibility of subsequent gene expression within emulsions make this approach a highly suitable platform for laboratory evolution. Yet, one of the major limitations of these emulsions is their incompatibility for downstream screening using fluorescence-assisted cell sorting (FACS). This is due to the external oil phase, which is not suitable for commercial cell-sorting machines.

1.5.2 Double emulsion: water-in-oil-in-water confinement

This limitation of single emulsions can be resolved by using double emulsions. A typically used double emulsion for biological applications is a surfactant-stabilized water-in-oil-in-water emulsion, that is, an aqueous droplet containing the gene of interest along with the IVTT machinery, surrounded by an oil shell, and dispersed in the outer aqueous phase (**Figure 1.9a**).

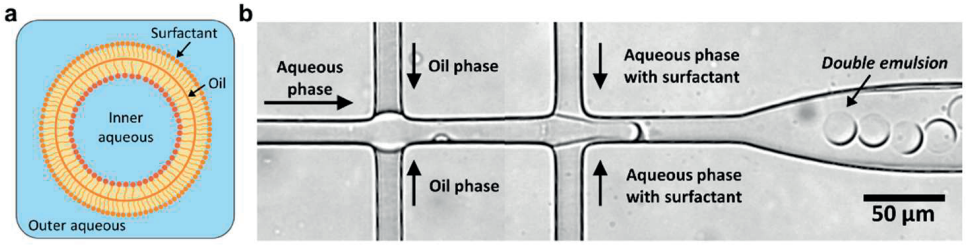

Figure 1.9:Anatomy of a double emulsion.

(a) Schematic representing surfactant stabilized water-in-oil-in-water double emulsion. (b) Production of micron-sized water-in-oil-in-water single emulsion using a microfluidic device with two flow- focusing junction connected via a bridge.

The presence of this external aqueous phase makes double emulsions compatible with commercially available droplet-sorting techniques like FACS. Double emulsions can be made in bulk by further emulsifying water-in-oil single emulsions, with the same key disadvantage of polydispersity. This limitation can be overcome using a microfluidic approach to obtain monodisperse double emulsions with efficient encapsulation (**Figure 1.9b**). While double emulsions have their own merit owing to the compatibility with downstream sorting processes, the on-chip production rate is relatively low but good enough to be used for laboratory evolution campaigns [85]. Indeed, double emulsions produced on-chip have has been successfully applied to screen and evolve soluble proteins [86, 87].

1.5.3 Liposome: semi-permeable membranous confinements

An alternative to emulsions is liposomes, whose boundary is composed of a continuous lipid bilayer. The lipid bilayer in turn is composed of phospholipids, which are surfactant-like amphiphilic molecules with a hydrophilic head and two hydrophobic chains, allowing them to self-assemble in aqueous environments to form such 3D containers (**Figure 1.10a**).

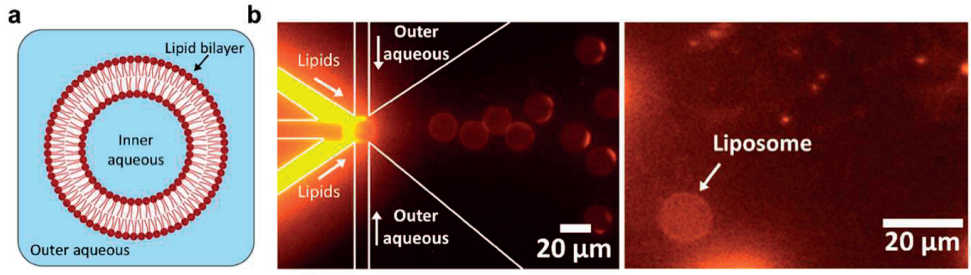

Figure 1.10: Anatomy of a liposome.

(a) Schematic of liposome depicting self-assembly of lipids to form lipid-bilayer. (b) On-chip generation of liposomes using octanol-assisted liposome assembly.

Liposomes have gained tremendous interest in the context of building synthetic cells[9, 33] and they are suitable compartment candidates, especially for membrane proteins. Their applicability has already been demonstrated by engineering an α-hemolysin variant, a membrane-bound toxin from Staphylococcus aureus, with enhanced pore-forming activity[88]. Liposomes can be produced in various sizes (tens of nm to hundreds of µm in diameter) and different lamellarities [unilamellar or multilamellar, having a single or multiple lipid bilayer(s), respectively]. For IVC applications, unilamellar liposomes of a few micrometers in diameter, also known as giant unilamellar vesicles (GUVs),

are preferred partly due to the detection limit of FACS measurements. GUVs can be generated via bulk techniques such as thin film hydration, rehydration of freeze-dried empty liposome (FDEL), and inverted emulsion transfer[89]. However, similar to emulsions, GUVs produced by bulk techniques suffer from polydispersity and an additional size-based sorting step in FACS is required. Two other drawbacks originating from bulk liposome production are the formation of multiple compartments (liposome(s) within a liposome) and multilamellarity.

Multicompartment liposomes tend to trap components between differsssent sub-compartments, causing inaccurate evaluation of enzymic activity. They also tend to yield low protein expression, which is undesirable for laboratory evolution[90]. Fortunately, several effective on-chip production techniques have been developed over the years, which could prove to be very suitable for evolution experiments. Octanol-assisted liposome assembly is a process akin to bubble-blowing (**Figure 1.10b**), where the initially produced double emulsions give rise to unilamellar liposomes within minutes[91, 92]. A similar technique was developed using a glass capillary-based approach and cell-free, GFP expression was carried out inside the liposomes[93]. Spatz and coworkers recently presented another approach, starting with copolymer-stabilized droplets to generate liposomes, termed droplet-stabilized GUVs[94]. When combined with a droplet splitting technique, an impressive production rate of $>10^6$ GUVs/min was reported[95]. Overall, on-chip GUV production is a promising approach, especially in terms of sample monodispersity and encapsulation efficiency.

1.6 OUTLINE OF THE THESIS

We are still at the initial stages of the monumental and exciting prospect of building autonomous, functional synthetic cells. Out of the numerous functional modules that synthetic biologists are seeking to build in a bottom-up manner, this thesis primarily aims on creating synthetic three-dimensional space to conduct complex biochemical reactions.

In **Chapter 2** we used bioinspired liquid droplets (biomolecular condensates) comprised of synthetic polypeptide (poly-L-lysine) and adenosine triphosphate. These liquid droplets served as template scaffolds for us to decorate cytoskeleton actin on the surface. Appropriate tweaking of physiological conditions led to the formation of actinosomes: three-dimensional, cell-sized confinements with a boundary made up of polylysine and actin filaments. We further characterized actinosomes and also demonstrated its biocompatibility by performing complex biochemical reaction like protein expression.

In **Chapter 3** we used on-chip microfluidic technology to generate micron-sized liposomes. We provide a detailed protocol highlighting the crucial steps to generate liposomes including photolithography, microfluidic assembly, and surface functionalization. The on-chip technology can efficiently encapsulate and retain phase separating biomolecules like polylysine and adenosine triphosphate, while small molecules like proton ions can migrate across the lipid bilayer. Externally changing the pH triggers homogenous solution of polylysine and adenosine triphosphate in the liposome to undergo phase transition to form biomolecular condensates.

With the growing interest in deciphering the role of liquid-liquid phase separation in biological systems, we explored a new direction: ticks. Current knowledge shows that ticks attach to their hosts for prolonged duration for blood feeding and this attachment of ticks is assisted via cement cone formation. In **Chapter 4** we shone light on how protein phase separation can potentially assist this process of tick adhesion. In the soup of complex tick saliva, we particularly focused on glycine-rich proteins since it is one of the most abundant protein families present in the tick saliva. We systematically characterized and determined both external physiological factors as well as intrinsic amino acid composition accountable for driving the phase separation.

In **Chapter 5** we upgraded our previously described on-chip microfluidic device for high-throughput generation of biocompatible confinements in the form of water-in-oil-in-water double emulsions. We used these synthetic confinements to evolve gene-editing enzyme (Cas9) using cell-free transcription and translation machinery. To achieve this, we developed multiple gene circuits linking enzyme activity to the expression of green fluorescence protein, enabling fluorescence-based fishing of positive variants of the enzyme.

Finally, in **Chapter 6** we provide a concluding general discussion summarizing the results of the chapters above. We further discuss the state-of-the-art in the field and put a perspective on the shaping synthetic cell using microfluidics.

REFERENCES

1. Fanalista F, Deshpande S, Lau A, Pawlik G, Dekker C. FtsZ-Induced Shape Transformation of Coacervates. *Advanced Biosystems* 2018, **2**(9)**:** 1800136.
2. Last MG, Deshpande S, Dekker C. pH-controlled coacervate–membrane interactions within liposomes. *ACS nano* 2020, **14**(4)**:** 4487-4498.
3. McCall PM, Srivastava S, Perry SL, Kovar DR, Gardel ML, Tirrell MV. Partitioning and enhanced self-assembly of actin in polypeptide coacervates. *Biophysical journal* 2018, **114**(7)**:** 1636-1645.
4. Kusters R, Simon C, Dos Santos RL, Caorsi V, Wu S, Joanny J-F*, et al.* Actin shells control buckling and wrinkling of biomembranes. *Soft Matter* 2019, **15**(47)**:** 9647-9653.
5. Keber FC, Loiseau E, Sanchez T, DeCamp SJ, Giomi L, Bowick MJ*, et al.* Topology and dynamics of active nematic vesicles. *Science* 2014, **345**(6201)**:** 1135-1139.
6. Booth R, Qiao Y, Li M, Mann S. Spatial positioning and chemical coupling in coacervate-in-proteinosome protocells. *Angewandte Chemie International Edition* 2019, **58**(27)**:** 9120-9124.
7. Weirich KL, Dasbiswas K, Witten TA, Vaikuntanathan S, Gardel ML. Self-organizing motors divide active liquid droplets. *Proceedings of the National Academy of Sciences* 2019, **116**(23)**:** 11125-11130.
8. Loiseau E, Schneider JA, Keber FC, Pelzl C, Massiera G, Salbreux G*, et al.* Shape remodeling and blebbing of active cytoskeletal vesicles. *Science Advances* 2016, **2**(4)**:** e1500465.
9. Rampioni G, D'Angelo F, Leoni L, Stano P. Gene-expressing liposomes as synthetic cells for molecular communication studies. *Frontiers in bioengineering and biotechnology* 2019, **7:** 1.
10. Göpfrich K, Platzman I, Spatz JP. Mastering complexity: towards bottom-up construction of multifunctional eukaryotic synthetic cells. *Trends in biotechnology* 2018, **36**(9)**:** 938-951.
11. Kumar BP, Fothergill J, Bretherton J, Tian L, Patil AJ, Davis SA*, et al.* Chloroplast-containing coacervate micro-droplets as a step towards photosynthetically active membrane-free protocells. *Chemical communications* 2018, **54**(29)**:** 3594-3597.
12. Bashirzadeh Y, Wubshet NH, Liu AP. Confinement geometry tunes fascin-actin bundle structures and consequently the shape of a lipid bilayer vesicle. *Frontiers in molecular biosciences* 2020, **7:** 610277.
13. Hernández-Vega A, Braun M, Scharrel L, Jahnel M, Wegmann S, Hyman BT*, et al.* Local nucleation of microtubule bundles through tubulin concentration into a condensed tau phase. *Cell reports* 2017, **20**(10)**:** 2304-2312.
14. Su X, Ditlev JA, Hui E, Xing W, Banjade S, Okrut J*, et al.* Phase separation of signaling molecules promotes T cell receptor signal transduction. *Science* 2016, **352**(6285)**:** 595-599.
15. King MR, Petry S. Phase separation of TPX2 enhances and spatially coordinates microtubule nucleation. *Nature communications* 2020, **11**(1)**:** 270.
16. Ausländer S, Ausländer D, Fussenegger M. Synthetic biology-the synthesis of biology. *Angewandte Chemie International Edition* 2017, **56**(23)**:** 6396-6419.
17. Smanski MJ, Zhou H, Claesen J, Shen B, Fischbach MA, Voigt CA. Synthetic biology to access and expand nature's chemical diversity. *Nature Reviews Microbiology* 2016, **14**(3)**:** 135-149.
18. Sato Y, Hiratsuka Y, Kawamata I, Murata S, Nomura S-iM. Micrometer-sized molecular robot changes its shape in response to signal molecules. *Science robotics* 2017, **2**(4)**:** eaal3735.
19. Te Brinke E, Groen J, Herrmann A, Heus HA, Rivas G, Spruijt E*, et al.* Dissipative adaptation in driven self-assembly leading to self-dividing fibrils. *Nature nanotechnology* 2018, **13**(9)**:** 849-855.
20. Trantidou T, Dekker L, Polizzi K, Ces O, Elani Y. Functionalizing cell-mimetic giant vesicles with encapsulated bacterial biosensors. *Interface Focus* 2018, **8**(5)**:** 20180024.

21. Beber A, Taveneau C, Nania M, Tsai F-C, Di Cicco A, Bassereau P*, et al.* Membrane reshaping by micrometric curvature sensitive septin filaments. *Nature communications* 2019, **10**(1)**:** 420.
22. Ullah MW, Khattak WA, Ul-Islam M, Khan S, Park JK. Metabolic engineering of synthetic cell-free systems: strategies and applications. *Biochemical Engineering Journal* 2016, **105:** 391-405.
23. Krinsky N, Kaduri M, Zinger A, Shainsky-Roitman J, Goldfeder M, Benhar I*, et al.* Synthetic cells synthesize therapeutic proteins inside tumors. *Advanced healthcare materials* 2018, **7**(9)**:** 1701163.
24. Parodi A, Molinaro R, Sushnitha M, Evangelopoulos M, Martinez JO, Arrighetti N*, et al.* Bio-inspired engineering of cell-and virus-like nanoparticles for drug delivery. *Biomaterials* 2017, **147:** 155-168.
25. Chen Z, Wang J, Sun W, Archibong E, Kahkoska AR, Zhang X*, et al.* Synthetic beta cells for fusion-mediated dynamic insulin secretion. *Nature chemical biology* 2018, **14**(1)**:** 86-93.
26. Xie M, Haellman V, Fussenegger M. Synthetic biology—application-oriented cell engineering. *Current opinion in biotechnology* 2016, **40:** 139-148.
27. Jia H, Schwille P. Bottom-up synthetic biology: reconstitution in space and time. *Current opinion in biotechnology* 2019, **60:** 179-187.
28. Deshpande S, Dekker C. Synthetic life on a chip. *Emerging Topics in Life Sciences* 2019, **3**(5)**:** 559-566.
29. Erb TJ, Jones PR, Bar-Even A. Synthetic metabolism: metabolic engineering meets enzyme design. *Current opinion in chemical biology* 2017, **37:** 56-62.
30. Mulla Y, Aufderhorst-Roberts A, Koenderink GH. Shaping up synthetic cells. *Physical biology* 2018, **15**(4)**:** 041001.
31. Tanford C. Interfacial free energy and the hydrophobic effect. *Proceedings of the National Academy of Sciences* 1979, **76**(9)**:** 4175-4176.
32. Israelachvili JN, Mitchell DJ, Ninham BW. Theory of self-assembly of hydrocarbon amphiphiles into micelles and bilayers. *Journal of the Chemical Society, Faraday Transactions 2: Molecular and Chemical Physics* 1976, **72:** 1525-1568.
33. Spoelstra WK, Deshpande S, Dekker C. Tailoring the appearance: what will synthetic cells look like? *Current opinion in biotechnology* 2018, **51:** 47-56.
34. Dimova R. Recent developments in the field of bending rigidity measurements on membranes. *Advances in colloid and interface science* 2014, **208:** 225-234.
35. Brangwynne CP, Eckmann CR, Courson DS, Rybarska A, Hoege C, Gharakhani J*, et al.* Germline P granules are liquid droplets that localize by controlled dissolution/condensation. *Science* 2009, **324**(5935)**:** 1729-1732.
36. Banani SF, Lee HO, Hyman AA, Rosen MK. Biomolecular condensates: organizers of cellular biochemistry. *Nature reviews Molecular cell biology* 2017, **18**(5)**:** 285-298.
37. Hyman AA, Weber CA, Jülicher F. Liquid-liquid phase separation in biology. *Annual review of cell and developmental biology* 2014, **30:** 39-58.
38. Shin Y, Brangwynne CP. Liquid phase condensation in cell physiology and disease. *Science* 2017, **357**(6357)**:** eaaf4382.
39. Holehouse AS, Pappu RV. Functional implications of intracellular phase transitions. *Biochemistry* 2018, **57**(17)**:** 2415-2423.
40. Bergeron-Sandoval L-P, Michnick SW. Mechanics, structure and function of biopolymer condensates. *Journal of molecular biology* 2018, **430**(23)**:** 4754-4761.
41. Mostowy S, Cossart P. Septins: the fourth component of the cytoskeleton. *Nature reviews Molecular cell biology* 2012, **13**(3)**:** 183-194.
42. Alberts B. *Molecular biology of the cell*. Garland science, 2017.

43. Bashirzadeh Y, Liu AP. Encapsulation of the cytoskeleton: towards mimicking the mechanics of a cell. *Soft Matter* 2019, **15**(42)**:** 8425-8436.
44. Wiegand T, Hyman AA. Drops and fibers—how biomolecular condensates and cytoskeletal filaments influence each other. *Emerging topics in life sciences* 2020, **4**(3)**:** 247.
45. Guharoy M, Szabo B, Martos SC, Kosol S, Tompa P. Intrinsic structural disorder in cytoskeletal proteins. *Cytoskeleton* 2013, **70**(10)**:** 550-571.
46. Case LB, Zhang X, Ditlev JA, Rosen MK. Stoichiometry controls activity of phase-separated clusters of actin signaling proteins. *Science* 2019, **363**(6431)**:** 1093-1097.
47. Zeng M, Chen X, Guan D, Xu J, Wu H, Tong P*, et al.* Reconstituted postsynaptic density as a molecular platform for understanding synapse formation and plasticity. *Cell* 2018, **174**(5)**:** 1172-1187. e1116.
48. Scheff DR, Weirich KL, Dasbiswas K, Patel A, Vaikuntanathan S, Gardel ML. Tuning shape and internal structure of protein droplets via biopolymer filaments. *Soft Matter* 2020, **16**(24)**:** 5659-5668.
49. Weirich KL, Banerjee S, Dasbiswas K, Witten TA, Vaikuntanathan S, Gardel ML. Liquid behavior of cross-linked actin bundles. *Proceedings of the National Academy of Sciences* 2017, **114**(9)**:** 2131-2136.
50. Jiang H, Wang S, Huang Y, He X, Cui H, Zhu X*, et al.* Phase transition of spindle-associated protein regulate spindle apparatus assembly. *Cell* 2015, **163**(1)**:** 108-122.
51. Erickson HP. FtsZ, a prokaryotic homolog of tubulin? *Cell* 1995, **80**(3)**:** 367-370.
52. Simon C, Kusters R, Caorsi V, Allard A, Abou-Ghali M, Manzi J*, et al.* Actin dynamics drive cell-like membrane deformation. *Nature Physics* 2019, **15**(6)**:** 602-609.
53. Simon C, Caorsi V, Campillo C, Sykes C. Interplay between membrane tension and the actin cytoskeleton determines shape changes. *Physical biology* 2018, **15**(6)**:** 065004.
54. Dürre K, Keber FC, Bleicher P, Brauns F, Cyron CJ, Faix J*, et al.* Capping protein-controlled actin polymerization shapes lipid membranes. *Nature communications* 2018, **9**(1)**:** 1630.
55. Asakura S, Oosawa F. On interaction between two bodies immersed in a solution of macromolecules. *The Journal of chemical physics* 1954, **22**(7)**:** 1255-1256.
56. Hayashi M, Nishiyama M, Kazayama Y, Toyota T, Harada Y, Takiguchi K. Reversible morphological control of tubulin-encapsulating giant liposomes by hydrostatic pressure. *Langmuir* 2016, **32**(15)**:** 3794-3802.
57. Bertin A, McMurray MA, Thai L, Garcia III G, Votin V, Grob P*, et al.* Phosphatidylinositol-4, 5-bisphosphate promotes budding yeast septin filament assembly and organization. *Journal of molecular biology* 2010, **404**(4)**:** 711-731.
58. Feng Z, Chen X, Wu X, Zhang M. Formation of biological condensates via phase separation: Characteristics, analytical methods, and physiological implications. *Journal of Biological Chemistry* 2019, **294**(40)**:** 14823-14835.
59. Söding J, Zwicker D, Sohrabi-Jahromi S, Boehning M, Kirschbaum J. Mechanisms for active regulation of biomolecular condensates. *Trends in Cell Biology* 2020, **30**(1)**:** 4-14.
60. Wu X, Cai Q, Shen Z, Chen X, Zeng M, Du S*, et al.* RIM and RIM-BP form presynaptic active-zone-like condensates via phase separation. *Molecular cell* 2019, **73**(5)**:** 971-984. e975.
61. Agudo-Canalejo J, Schultz SW, Chino H, Migliano SM, Saito C, Koyama-Honda I*, et al.* Wetting regulates autophagy of phase-separated compartments and the cytosol. *Nature* 2021, **591**(7848)**:** 142-146.
62. Beutel O, Maraspini R, Pombo-Garcia K, Martin-Lemaitre C, Honigmann A. Phase separation of zonula occludens proteins drives formation of tight junctions. *Cell* 2019, **179**(4)**:** 923-936. e911.

63. Bergeron-Sandoval L-P, Kumar S, Heris HK, Chang CL, Cornell CE, Keller SL*, et al.* Endocytic proteins with prion-like domains form viscoelastic condensates that enable membrane remodeling. *Proceedings of the National Academy of Sciences* 2021, **118**(50)**:** e2113789118.
64. Convery N, Gadegaard N. 30 years of microfluidics. *Micro and Nano Engineering* 2019, **2:** 76-91.
65. Shang L, Cheng Y, Zhao Y. Emerging droplet microfluidics. *Chemical reviews* 2017, **117**(12)**:** 7964-8040.
66. Bjerk TR, Severino P, Jain S, Marques C, Silva AM, Pashirova T*, et al.* Biosurfactants: properties and applications in drug delivery, biotechnology and ecotoxicology. *Bioengineering* 2021, **8**(8)**:** 115.
67. Brito LA, Malyala P, O'Hagan DT. Vaccine adjuvant formulations: A pharmaceutical perspective. Seminars in immunology; 2013: Elsevier; 2013. p. 130-145.
68. Aldemir Dikici B, Claeyssens F. Basic principles of emulsion templating and its use as an emerging manufacturing method of tissue engineering scaffolds. *Frontiers in Bioengineering and Biotechnology* 2020, **8:** 875.
69. Guzey D, McClements DJ. Formation, stability and properties of multilayer emulsions for application in the food industry. *Advances in colloid and interface science* 2006, **128:** 227-248.
70. Ozturk B, McClements DJ. Progress in natural emulsifiers for utilization in food emulsions. *Current Opinion in Food Science* 2016, **7:** 1-6.
71. Verissimo LM, Agnez Lima LF, Monte Egito LC, de Oliveira AG, do Egito EST. Pharmaceutical emulsions: a new approach for gene therapy. *Journal of drug targeting* 2010, **18**(5)**:** 333-342.
72. Ospovat D. The development of Darwin's theory: Natural history, natural theology, and natural selection, 1838-1859. Cambridge University Press, 1995.
73. Lee PS, Lee KH. Escherichia coli—a model system that benefits from and contributes to the evolution of proteomics. *Biotechnology and bioengineering* 2003, **84**(7)**:** 801-814.
74. Maddamsetti R. Universal constraints on protein evolution in the long-term evolution experiment with Escherichia coli. *Genome biology and evolution* 2021, **13**(6)**:** evab070.
75. Carlson ED, Gan R, Hodgman CE, Jewett MC. Cell-free protein synthesis: applications come of age. *Biotechnology advances* 2012, **30**(5)**:** 1185-1194.
76. Shi Z, Lai X, Sun C, Zhang X, Zhang L, Pu Z*, et al.* Step emulsification in microfluidic droplet generation: Mechanisms and structures. *Chemical Communications* 2020, **56**(64)**:** 9056-9066.
77. Autour A, Ryckelynck M. Ultrahighthroughput improvement and discovery of enzymes using droplet-based microfluidic screening. Micromachines 8 (4): 128. 2017.
78. Tay Y, Ho C, Drőge P, Ghadessy FJ. Selection of bacteriophage λ integrases with altered recombination specificity by in vitro compartmentalization. *Nucleic acids research* 2010, **38**(4)**:** e25-e25.
79. Takeuchi R, Choi M, Stoddard BL. Redesign of extensive protein–DNA interfaces of meganucleases using iterative cycles of in vitro compartmentalization. *Proceedings of the National Academy of Sciences* 2014, **111**(11)**:** 4061-4066.
80. Ellefson JW, Meyer AJ, Hughes RA, Cannon JR, Brodbelt JS, Ellington AD. Directed evolution of genetic parts and circuits by compartmentalized partnered replication. *Nature biotechnology* 2014, **32**(1)**:** 97-101.
81. Czapinska H, Siwek W, Szczepanowski RH, Bujnicki JM, Bochtler M, Skowronek KJ. Crystal structure and directed evolution of specificity of NlaIV restriction endonuclease. *Journal of molecular biology* 2019, **431**(11)**:** 2082-2094.
82. Chung CHY, Cui B, Song R, Liu X, Xu X, Yao S. Scalable production of monodisperse functional microspheres by multilayer parallelization of high aspect ratio microfluidic channels. *Micromachines* 2019, **10**(9)**:** 592.

83. Shim J-u, Ranasinghe RT, Smith CA, Ibrahim SM, Hollfelder F, Huck WT, *et al.* Ultrarapid generation of femtoliter microfluidic droplets for single-molecule-counting immunoassays. *ACS nano* 2013, **7**(7)**:** 5955-5964.
84. Abate AR, Weitz DA. Faster multiple emulsification with drop splitting. *Lab on a Chip* 2011, **11**(11)**:** 1911-1915.
85. Chong D, Liu X, Ma H, Huang G, Han YL, Cui X, *et al.* Advances in fabricating double-emulsion droplets and their biomedical applications. *Microfluidics and Nanofluidics* 2015, **19:** 1071-1090.
86. Zinchenko A, Devenish SR, Kintses B, Colin P-Y, Fischlechner M, Hollfelder F. One in a million: flow cytometric sorting of single cell-lysate assays in monodisperse picolitre double emulsion droplets for directed evolution. *Analytical chemistry* 2014, **86**(5)**:** 2526-2533.
87. Larsen AC, Dunn MR, Hatch A, Sau SP, Youngbull C, Chaput JC. A general strategy for expanding polymerase function by droplet microfluidics. *Nature Communications* 2016, **7**(1)**:** 11235.
88. Fujii S, Matsuura T, Sunami T, Kazuta Y, Yomo T. In vitro evolution of α-hemolysin using a liposome display. *Proceedings of the National Academy of Sciences* 2013, **110**(42)**:** 16796-16801.
89. Walde P, Cosentino K, Engel H, Stano P. Giant vesicles: preparations and applications. *ChemBioChem* 2010, **11**(7)**:** 848-865.
90. Sunami T, Sato K, Matsuura T, Tsukada K, Urabe I, Yomo T. Femtoliter compartment in liposomes for in vitro selection of proteins. *Analytical biochemistry* 2006, **357**(1)**:** 128-136.
91. Deshpande S, Caspi Y, Meijering AE, Dekker C. Octanol-assisted liposome assembly on chip. *Nature communications* 2016, **7**(1)**:** 10447.
92. Deshpande S, Dekker C. On-chip microfluidic production of cell-sized liposomes. *Nature protocols* 2018, **13**(5)**:** 856-874.
93. Deng N-N, Yelleswarapu M, Huck WT. Monodisperse uni-and multicompartment liposomes. *Journal of the American Chemical Society* 2016, **138**(24)**:** 7584-7591.
94. Weiss M, Frohnmayer JP, Benk LT, Haller B, Janiesch J-W, Heitkamp T, *et al.* Sequential bottom-up assembly of mechanically stabilized synthetic cells by microfluidics. *Nature materials* 2018, **17**(1)**:** 89-96.
95. Staufer O, Antona S, Zhang D, Csatári J, Schröter M, Janiesch J-W, *et al.* Microfluidic production and characterization of biofunctionalized giant unilamellar vesicles for targeted intracellular cargo delivery. *Biomaterials* 2021, **264:** 120203.

Chapter 2

Actinosomes: Condensate-Templated Containers for Engineering Synthetic Cells

This chapter is based on

Ganar, Ketan A., Liza Leijten, and Siddharth Deshpande. "Actinosomes: condensate-templated containers for engineering synthetic cells." *ACS synthetic biology* 11, no. 8 (2022): 2869-2879.

ABSTRACT

Engineering synthetic cells has a broad appeal, from understanding living cells to designing novel biomaterials for therapeutics, biosensing, and hybrid interfaces. A key prerequisite to creating synthetic cells is a three-dimensional container capable of orchestrating biochemical reactions. In this chapter, we present an easy and effective technique to make cell-sized porous containers, coined actinosomes, using the interactions between biomolecular condensates and the actin cytoskeleton. This approach uses polypeptide/nucleoside triphosphate condensates and localizes actin monomers on their surface. By triggering actin polymerization and using osmotic gradients, the condensates are transformed into containers, with the boundary made up of actin filaments and polylysine polymers. We show that the guanosine triphosphate (GTP)-to-adenosine triphosphate (ATP) ratio is a crucial parameter for forming actinosomes: insufficient ATP prevents condensate dissolution, while excess ATP leads to undesired crumpling. Permeability studies reveal the porous surface of actinosomes, allowing small molecules to pass through while restricting bigger macromolecules within the interior. We show the functionality of actinosomes as bioreactors by carrying out *in vitro* protein translation within them. Actinosomes are a handy addition to the synthetic cell platform, with appealing properties like ease of production, inherent encapsulation capacity, and a potentially active surface to trigger signaling cascades and form multicellular assemblies, conceivably useful for biotechnological applications

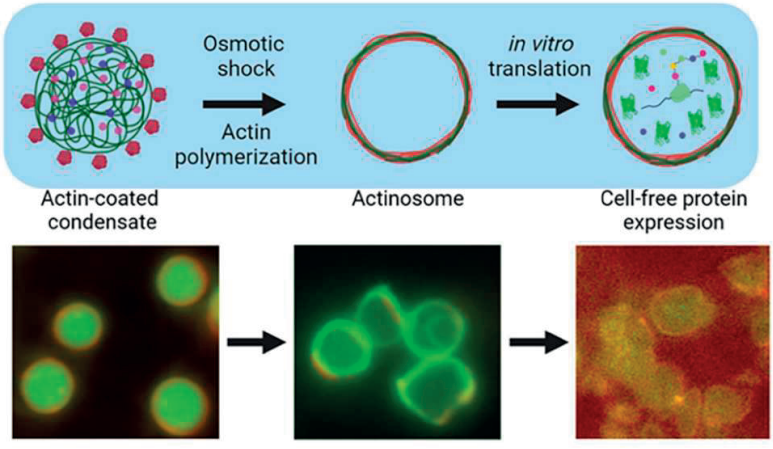

2.1 INTRODUCTION

Cells are highly complex systems consisting of a plethora of interconnected biomolecular networks, and this greatly limits our understanding of how they work. While deciphering molecular mechanisms in living systems is tedious, the *in vitro* reconstitution assay is an excellent complementary approach to studying specific cellular modules. In recent years, the bottom-up construction of synthetic cells has received tremendous attention, where compartmentalization is seen as an essential feature to mimic nature's way of organizing reactions and, at the same time, providing a superior control[1]. Synthetic cells typically refer to an enclosed three-dimensional structure capable of performing tasks similar to their biological counterparts. Different types of synthetic cells have been proposed, which can be broadly classified as membrane-bound and membraneless confinements[2, 3].

Membrane-bound compartments, built by the self-assembly of amphiphilic molecules, have been widely used as cell-mimicking prototypes[4]. This has led to the design of a wide variety of confinements such as surfactant-stabilized water-in-oil droplets, liposomes with a lipid bilayer as the boundary, and even completely synthetic containers such as polymersomes anddendrimersomes[5, 6]. These compartments are capable of reconstituting various biochemical processes within them and have been exploited to engineer a wide variety of cellular modules and to advance various applications like cell-free gene expression[7, 8] evolving proteins by directed evolution[9], cytoskeleton assembly [10, 11], growth and division[12, 13, 14], cargos for drug delivery[15], and printing artificial tissues[16, 17] In these confinements formed *via* the hydrophobic effect[18] the membrane usually acts as a physical barrier and restricts passive transport of molecules across them. This is commonly resolved by incorporating transmembrane proteins like α-hemolysin, making them selectively permeable[17, 19]. Additionally, newer strategies have been designed such as proteinosomes, which have a membrane comprising cross-linked, amphiphilic protein–polymer conjugates[20]. Unlike the relatively inert membranes of liposomes and polymersomes, the proteinaceous boundary of proteinosomes can perform enzymatic reactions[21]. Methods to produce the above-mentioned confinements suffer from various limitations: easy-to-use bulk methods have poor process control, high polydispersity (variation in the confinement size), and a low encapsulation efficiency. Employing microfluidic emulsion-based techniques effectively solve these issues, but at the cost of technologically advanced sophisticated and less-accessible setups[22, 23].

Biomolecular condensates, membraneless structures formed *via* the process of liquid–liquid separation (LLPS), have emerged as new types of synthetic bioreactors in recent years [24].After their discovery and realization of the prominent role they play in intra-

cellular biochemistry, they have been heavily exploited also in the realm of synthetic biology. Some salient features of condensates are their ability to sequester molecules and their assemblies[25], resistant to extreme conditions[26], performing biochemical reactions with increased reaction rates and enhanced enzyme kinetics[27, 28, 29], and exchange of molecules with their surroundings[24]. Interestingly, condensates have been explored as possible scaffolds to form synthetic containers[30]. For example, complex coacervates have been forged into multilayered compartments *via* a surface-templating procedure, albeit producing thick shells and the use of chemical treatments[31]. Another study demonstrated that the condensates formed by glutamic acid-rich leucine zipper and arginine-rich leucine zipper could be transitioned into hollow vesicles *via* temperature changes[32]. Alternatively, coacervate droplets can be coated with amphiphilic molecules; small unilamellar lipid vesicles were assembled at the interface of RNA/peptide droplets, transforming them into an RNA encapsulated membrane-bound confinement[33]. These studies highlight the potential of condensates as templates to form novel confinements but also present several limitations such as thick shells, low membrane permeability, and use of sophisticated protein engineering. If possible, one would desire a highly biocompatible proteinaceous confinement produced in a straightforward manner, without the use of complicated setups.

In this chapter, we present a straightforward bottom-up approach to make cell-sized (2–5 μm) confinements with proteins as the building blocks. We start with condensates made up of a polypeptide (polylysine, polyK) and nucleoside triphosphates (NTPs), a mixture of adenosine triphosphate (ATP) and guanosine triphosphate (GTP). We then use actin, the well-known cytoskeletal protein capable of forming filaments, to structurally modify the condensate droplets. Actin localizes at the condensate interface and rapidly polymerizes into filaments at the expense of a high concentration of ATP present in condensates. Under the right conditions, this leads to internal coacervate dissolution, followed by colocalization of polylysine with actin filaments at the surface, resulting in hollow containers, which we term actinosomes. We show that the ATP:GTP ratio is crucial in actinosome assembly, and permeability assays reveal actinosomes as stable, porous containers. Finally, we show the capability of actinosomes as bioreactors by carrying out *in vitro* translation of proteins. We believe the addition of actinosomes, which can be formed without any use of sophisticated setups and in a rapid manner, will be highly useful in the field of synthetic cells and to reconstitute reactions within cell-sized, biocompatible containers.

It is difficult to precisely define a synthetic cell in a single sentence, however, one can agree that a synthetic cell is a broad idea to create a man-made mimicry of a biological cell. The bottom-up on-chip approach can immensely help in addressing the complex biological phenomena, acknowledging the fact that the concept of synthetic cell in

itself is inherently subjective. For instance, a molecular biologist, who employs cells to produce proteins would view synthetic cells as protein-producing factories. A medical practitioner would interpret synthetic cell as an entity to deliver therapeutic molecules and possibly replace defective cells in humas body with better functional ones. A biophysicist, interested in understanding life, may envision synthetic cell to be a minimal entity that has the capability to self-replicate its components and eventually divide, thus completing the circle of life.

2.2 RESULTS AND DISCUSSION

2.2.1 Actin interaction with Multicomponent Condensates forms Actinosomes.

We started with the idea of using membraneless condensates as templates to coat a biomaterial and subsequently dissolve the inner condensate to form a stable container (**Figure 2.1a**) . We aimed to bring about the structural and chemical transformation of the condensate by coupling a biochemical reaction, ideally carried out by the coated biomaterial itself. Complex coacervates made up of positively charged polypeptides (polylysine, polyK; polyarginine, polyR) and negatively charged NTPs (adenosine triphosphate) are widely used model systems[34]. With NTPs (ATP and GTP in particular) also being the common energy currency for a wide variety of biochemical reactions, we hypothesized that polyK/NTP would be a good starting point for our experiments. For a fixed amount of polyK (5 mg/mL; molar charge concentration ~34 mM, assuming all lysine residues are charged and available; average molecular weight per residue 146.19 Da), we determined the optimal concentration of NTPs to attain maximum partitioning in the coacervate phase (**Figure S2.1**). For all of the experiments shown here, unless specified, polyK and total NTP concentrations were thus kept at 5 mg/mL and 5.4 mM, respectively. Using absorbance-based measurements, we estimated the amount of ATP inside the coacervates to be about 50 mM (in the absence of actin), i.e., about 250 times more concentrated than the dilute phase (**Figure S2.1**); the ATP concentration in the dilute phase was measured to be 0.19 ± 0.02 mM (see Materials and Methods). Our idea strengthened further when the addition of actin monomers to the system strongly partitioned them at the surface of these coacervates (**Figure 2.1b,c**), similar to the observations made with other coacervate systems[35]. Based on fluorescence measurements, we calculated the partition coefficient of actin at the interface to be significantly higher (5.3 ± 1.3, n = 61) compared to its partitioning inside the coacervate (3.2 ± 0.7, n = 66). In a similar manner, the partition coefficient for polyK inside the coacervate was determined to be (4.2 ± 0.8, n = 62). In addition, we used a salt-deficient buffer, keeping the interfacial

tension of the coacervate relatively high[36]. This also significantly prevented partitioning of actin inside the coacervate compared to the surface as we observed that actin relatively partitioned more inside the coacervates in the presence of salt compared to the coacervate–water interface (**Figure S2.2)**. Also, the actin present at the coacervate–water interface polymerized into filaments only in the presence of Mg^{2+} ions, as confirmed by the ATTO-594-phalloidin staining (**Figure S2.3**). We further measured the surface potential of the coacervates through ζ-potential measurements. We found the coacervates to be positively charged (16.9 ± 1.5mV; **Figure S2.4**), agreeing with previous observations[37]. Interestingly, we also noted that the surface charge always remained positive irrespective of whether the polyK or ATP was in excess, suggesting accumulation of polyK molecules at the surface. Actin being net negatively charged at neutral pH was thus thought to assemble on the surface through electrostatic interactions[38]. Indeed, surface charge measurements of actin-coated condensates showed significant reduction in the value of the ζ-potential to 7.8 ± 1.1 mV within minutes (**Figure S2.5**). Along with individual coated coacervates, we do observe connected structures of several condensates, which could be attributed to the lowering of the surface potential.

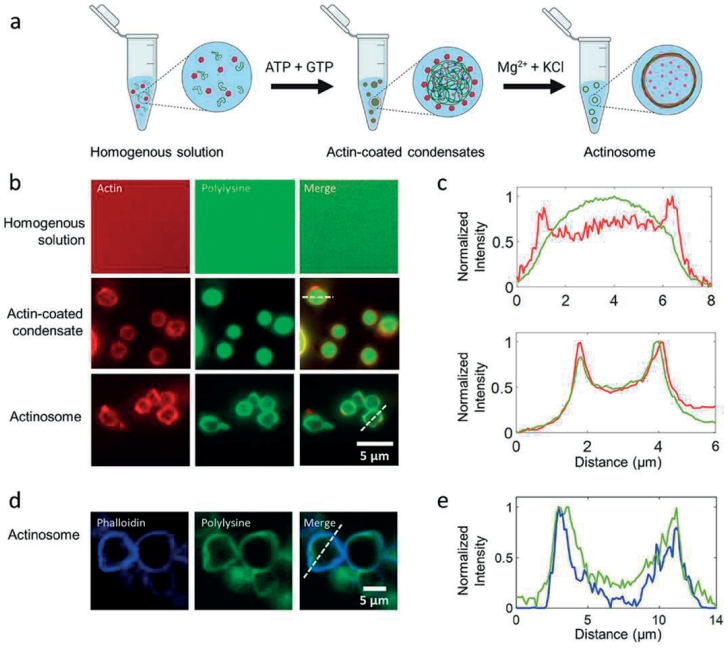

Figure 2.1: Condensate-templated actinosome formation.

(a) Schematic demonstrating stepwise addition of reagents to produce actinosomes. (b) Epifluorescence microscopy images at different stages of actinosome formation. Top: homogeneous mixture of ATTO-532-labeled actin monomers and FITC-labeled polylysine (labeled fraction 10% w/w). Middle: addition of the NTP mixture (GTP + ATP) triggers coacervation, resulting in polylysine/NTP coacervates with actin localized on the surface. Bottom: Mg2+ triggers actin polymerization at the expense of ATP hydrolysis, ultimately resulting in coacervate dissolution and formation of a shell made up of actin filaments and polylysine. (c) Line graphs corresponding to the dotted lines in panel (b) showing surface localization of actin on the condensates with polylysine concentrated in the interior (top) and localization of the actin and polylysine in actinosomes (bottom). (d) Confocal microscopy images of actinosomes stained with ATTO-594-labeled phalloidin (blue), which selectively binds to actin filaments; FITC-labeled polylysine (labeled fraction 10% w/w) is visualized in green. (e) Line graphs corresponding to the dotted lines in panel (d) showing surface localization of phalloidin-stained actin filaments (blue) along with polylysine (green).

We triggered actin polymerization by adding a hypertonic buffer containing divalent cations (Mg2+) and KCl. This initiated the ATPase activity of actin, leading to a rapid hydrolysis of ATP present in the coacervates and formation of actin filaments on the condensate surface. Phalloidin staining confirmed the formation of actin filaments at the condensate surface (***Figure 2.1d,e***). Additionally, the osmolarity shock induced via hypertonic buffer conditions initiated an outward flow of polyK from the coacervate toward the periphery where actin filaments are localized. To our pleasant surprise, when using an appropriate ratio of the ATP/GTP mixture, the condensates

were subsequently converted into micron-sized quasi-spherical confinements within a matter of minutes. As can be seen from the fluorescence images in ***Figure 2.1b***, actin and polyK signals completely colocalized at the boundary of the (previously present) condensates, while the polyK signal from the lumen was significantly reduced. We aptly termed these containers actinosomes, where the actin filaments together with polyK polymers formed the container boundary, confining a hollow lumen. We observed a higher partition of actin 8.1 ± 1.4 (n = 58) at the interface compared to 4.6 ± 0.7 (n = 61) inside the actinosome. The polyK localization also showed a similar trend of higher accumulation at the surface (2.9 ± 0.4; n = 59) compared to the interior of the actinosomes (2.0 ± 0.3; n = 61). Based on the small increase in the dilute phase intensity, a finite fraction of polyK was assumed to leave the condensates altogether. It is important to note that the combination of hyperosmotic shock and actin polymerization was necessary to form actinosomes. Only hyperosmotic shock or only actin polymerization resulted in actin-coated condensates but no actinosome formation (***Figure S2.6***). The hypertonic conditions likely decreased the interfacial tension and facilitated outward movement of polyK.

2.2.2 ATP:GTP Ratio is Crucial to Actinosome Formation.

Since ATP hydrolysis is crucial to coacervate dissolution and subsequent actinosome formation, we studied this further by tuning the ratio of NTPs. We maintained the total concentration of NTPs (GTP + ATP) constant at 5.4 mM and varied the amount of GTP from low to high, which we quantified as R = [GTP]/[NTPs]. At R = 0, i.e., when using only ATP, the coacervates immediately transitioned from a sphere to a collapsed state, resembling a crumpled structure, like a crumpled sheet of paper (upper panel in **Figure 2.2a**, **Supplementary movie 1**). This phenomenon can be explained as a combination of ATP hydrolysis and colocalization of polyK with actin together with the osmolarity-induced water efflux leading to the buckling of the formed structure. We observed this crumpling prominently for R values below 0.6 (**Figure 2.2b**). In contrast, actinosomes were efficiently formed for R values between 0.7 and 0.8 (**Figure S2.7**). As can be seen in the middle panel in (**Figure 2.2a**), the polylysine fluorescence rapidly decreased from the lumen and colocalized at the interface along with actin (**Supplementary movie 2**). Thus, sufficient ATP was present for actin polymerization at the surface, but at the same time, the inert GTP pool maintained enough osmolarity (~35 mOsm; hydrolyzed ATP possibly contributing further to the value), preventing complete crumpling and resulting in an actinosome with a wrinkled surface. The observed outward flow of polyK toward the periphery was likely promoted by the osmolarity shock induced via the hypertonic buffer. The lack of a coacervate interior, judged by the lack of polyK fluorescence in the lumen but rather its colocalization with actin, strongly suggests the presence of a non-phase-separated aqueous lumen. A z-stack of the actinosome makes this clearer, showing

colocalization of actin and polyK across the entire structure and showing actin- as well as polyK-depleted lumen (**Supplementary movie 3**). Owing to the slight crumpling of the shell due to osmotic effects, the formed actinosomes were not perfectly spherical but were quite irregular in shape. We calculated the average size of actinosomes, by approximating them as ellipses, to be 2.4±0.6 μm(major axis ± standard deviation; n = 107;**Figure 2.2c**). We measured the eccentricity (major axis/minor axis) to quantify their spherical nature. A value of 1.2 ± 0.1 shows that actinosomes remained reasonably spherical (**Figure 2.2d**).

We observed that not all of the actin-coated condensates converted into coacervates, possibly due to heterogeneity of the actin coating, subsequent inhomogeneous polymerization, and thus different degrees of osmotic shock between different condensates. The actinosome yield (number of actinosomes obtained/total number of actinosomes and actin-condensate structures) was determined to be ~0.7 (actinosomes, n = 198; actin-coated coacervates, n = 88). We also observed that the actinosomes tend to form clusters, i.e., two or more actinosomes sticking to each other (structures containing actin-coated condensates were excluded for analysis). Quantitative analysis showed that about 25% of the actinosomes remained in the individual isolated state, whereas the remaining 75% tended to form clusters of 2–5 actinosomes (**Figure S2.8**). At R values above 0.9, we observed a mixed population of both actinosomes and coacervates coated with actin (**Figure 2.2b**). At R = 1, we observed only actin-coated condensates (lower panel in **Figure 2.2a**; **Supplementary movie 4**). With not enough ATP to bring about actin polymerization and coacervate dissolution, these coacervates remained stable and did not show any morphological changes over time. Thus, the ratio of GTP to ATP is crucial to actinosome formation.

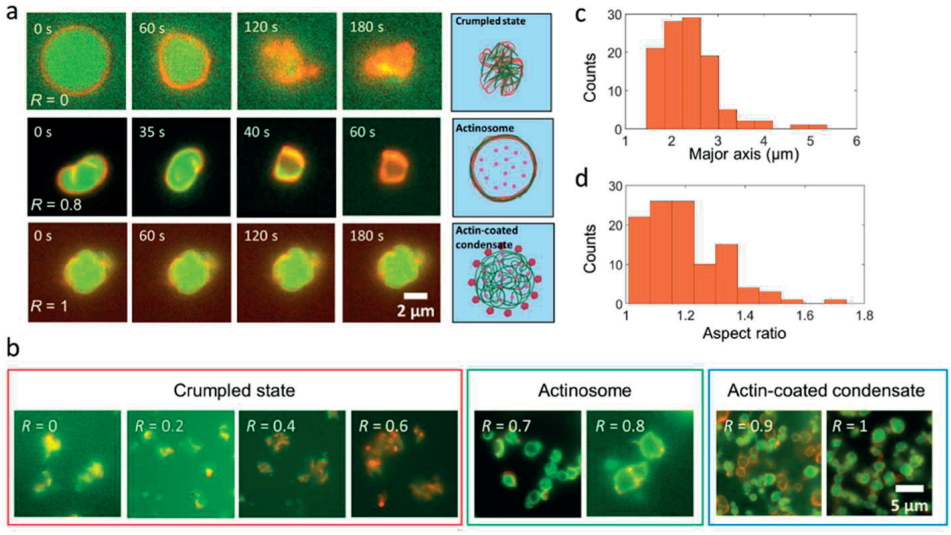

Figure 2.2: Actinosome formation depends on the ratio of NTPs present in thecondensates.

(a) Time-lapse images showing the actin-condensate dynamics at different R (=[GTP]/([GTP] + [ATP])) values. Low R values result in completely crumpled structures, intermediate values form cell-sized tinosomes, while higher R values result in stable actin-coated condensates. The inhomogeneous distribution of the actin signal on the actinosome surface is probably due to varying degrees of local actin polymerization. (b) Representative fluorescence images showing three key types of structures formed over the entire range of R. Actinosomes are obtained only within a narrow range ($0.7 \leq R \leq 0.8$). Lower values ($R \leq 0.6$) result in crumpled structures, while higher values ($R \geq 0.9$) lack enough ATP and form stable actin-coated condensates. (c) Frequency histogram showing the size distribution of actinosomes, with a mean size (major axis) of 2.4 ± 0.6 µm (n =107). (d) Frequency histogram showing the ratio of the major axis to the minor axis; the mean value of 1.2 ± 0.1 suggests that actinosomes tend to attain a roughly spherical morphology (n = 107). Images were acquired in epifluorescence microscopy.

We also checked the effect of the nature of the polypeptide on actinosome formation, where we used poly-L-arginine (polyR) to form the coacervates. While we obtained actin-coated condensates, we did not see complete crumpling when using only ATP or a container formation when using a mix of ATP and GTP; this trend continued even after doubling the salt concentrations (**Figure S2.9**). This is possibly due to the significantly higher (100-fold) viscosity and surface tension (5.8-fold) of the polyR-containing droplets as compared to polyK-containing ones[39], potentially preventing the rapid exchange of material across the interface and insufficient ATP diffusion to the surface.

2.2.3 Actinosomes Are Hollow and Porous Containers.

A mesh of polylysine and actin filaments comprises the actinosome surface. To characterize the surface permeability, we tested the diffusion-driven influx of dextran molecules of a variety of sizes into the actinosome lumen. We incubated premade actinosomes (R = 0.8) with FITC-labeled dextran solution (concentration kept constant at 4 μM for all of the experiments) of different molecular weights (M), viz., 3–5, 20, 70, and 150 kDa corresponding to the diameter of gyration (D_g) values of 3.81–4.52, 7.18, 10.90 and 14.05 nm, respectively[40] (**Figure 2.3a**). The low-molecular-weight dextran molecules (3–5 kDa) immediately t_0, corresponding to approximately within a minute after addition of dextran) permeated inside the actinosomes (**Figure 2.3b**). On the contrary, actinosomes were not permeable to any of the higher-molecular-weight dextran molecules (>20 kDa) for the entire duration of 60 min. **Figure 2.3b** shows the exclusion of 20 kDa dextran molecules from actinosomes, while (**Figure S2.10**)shows images corresponding to dextran assays corresponding to 70 and 150 kDa. To characterize the permeability, we measured the FITCdextran signal inside (I_{inside}) and outside ($I_{outside}$) actinosomes and calculated the normalized intensity as ($I_{inside} - I_{outside}$)/ $I_{outside}$. We analyzed this for images taken immediately (t_0 ,) as well as after one hour (t_{60}). The positive normalized intensity for 5 kDa (t_0 ,: 0.12 ± 0.07, n = 19; t_{60},: 0.23 ± 0.13, n = 20) dextran indicates influx of dextran inside actinosomes (**Figure 2.3c**). On the contrary, negative normalized intensity for 20 kDa (t_0,: −0.58 ± 0.11, n = 23; t_{60}: −0.58 ± 0.07, n = 24), 70 kDa (t_0,: −0.63 ± 0.07, n = 24; t_{60}: −0.57 ± 0.06, n = 30), and 150 kDa (t_0,: −0.67± 0.08, n = 25; t_{60} : −0.58 ±0.04, n = 35) clearly indicates exclusion of dextran inside the actinosomes. Based on the above analysis, we conclude that actinosomes are porous containers with a pore size of ∼5 nm and definitely below 7 nm (**Figure 2.3a,b**). After determining the pore size of actinosomes, we moved our attention to the topological characterization of actinosomes. For this, we performed scanning electron microscopy (SEM) on actinosomes to visualize the detailed surface morphology. We dried and sputtered samples of actinosomes (R = 0.74), crumpled condensates (R = 0.55), and actin-coated condensates (R = 0.92) for visualization (see Material and Method for details). The actinosome surface revealed a rough shell (**Figure 2.3d**) in which submicron-sized pores on the order of 0.02–0.05 μm in diameter were visible (**Figure 2.3e**), supporting the previously described permeable interface allowing migration of molecules across the rigid shell. In addition to this, visualizing a broken actinosome revealed a hollowness in the interior of the actinosome (**Figure S2.11a,b**). The shells appeared rigid, given that they survived the vacuum-drying process. On the other hand, the surface of polylysine/NTP coacervates (R = 0.92) with actin localized on the surface was relatively smooth and did not show any of the above-mentioned features (**Figure S2.11c**). At high ATP concentration (R = 0.55), crumpled structures were observed (**Figure S2.11d**), corroborating with the fluorescence images obtained before.

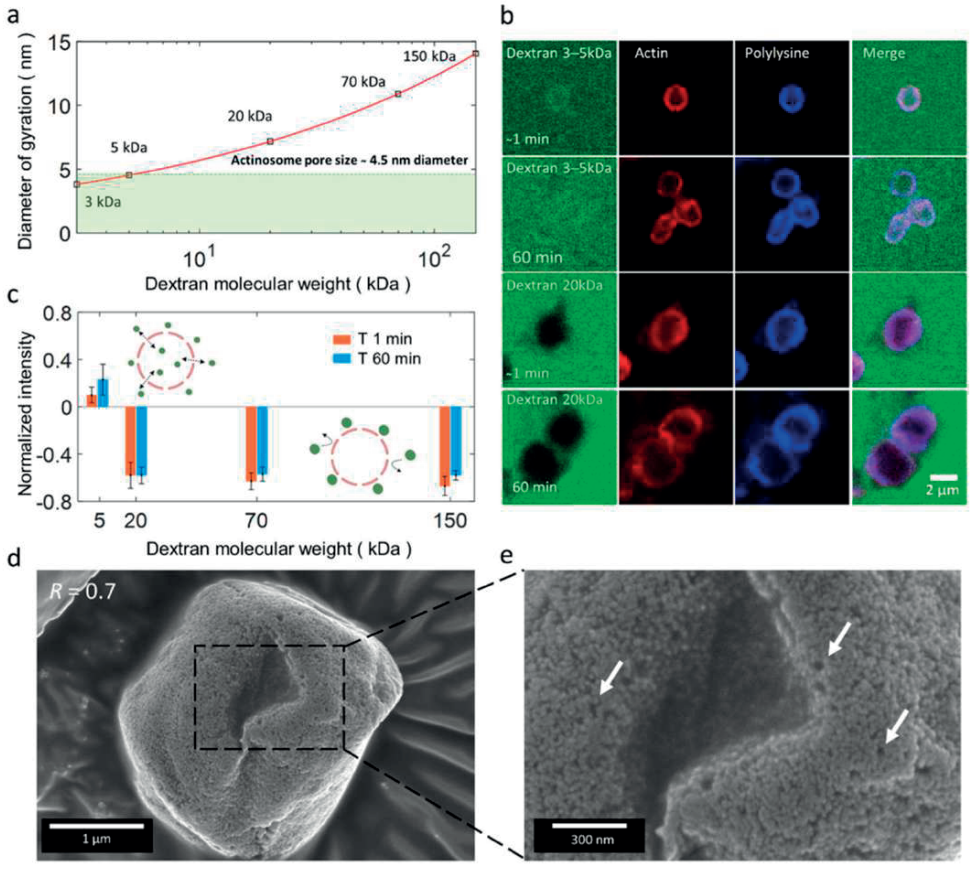

Figure 2.3: Actinosomes are porous and permeable to small molecules.

(a) Diameter of gyration (Dg) of dextran molecules as a function of their molecular weights (M). The red line follows the equation Dg = 2.64 ×$M^{0.33}$. (b) Confocal images showing the permeability of actinosomes (R = 0.7) to dextran molecules of different sizes, immediately (t^0) and 1 h (t^{60}) after incubation. Low-molecular-weight dextran (3–5 kDa) readily diffuses inside actinosomes, whereas high-molecular-weight dextran (20 kDa) is excluded from the actinosome. (c) Graph showing the normalized intensity (I_{inside}– $I_{outside}$)/ $I_{outside}$ of FITC-dextran at t^0 (red) and t^{60} (blue). Positive values indicate dextran diffusion into the actinosomes, while negative values indicate impermeability to dextran. Error bars indicate standard deviations. (d) Scanning electron microscopy images of actinosomes (R = 0.7) appear as slightly crumpled spheres, similar to fluorescence images. (e) A zoom-in reveals a rough, unstructured, porous surface. Several sub-µm-sized pores are clearly visible and indicated with arrows. Error bars indicate standard deviations.

2.2.4 Actinosomes Efficiently Encapsulate Biomolecules and Carry Out Complex Biochemical Reactions.

With the intention to confine molecules within the containers, we encapsulated RNA, given its central importance in the cellular metabolism, and added it to the starting mixture of polyK and actin. We found that fluorescently (Cy5) labeled RNA (a 20-mer polyU) could be efficiently encapsulated inside the actinosomes (**Figure 2.4a**). The partition coefficient of RNA was 4.0 ± 1.0 (n = 10) in the lumen of actinosomes and higher 7.0 ± 1.3 (n = 10) near the inner surface of actinosomes. This can be further seen by plotting a line profile of the fluorescent intensity across the actinosome showing colocalization of RNA and the polylysine signal (**Figure 2.4b**). This is likely due to the electrostatic interaction between negatively charged RNA and positively charged polyK polymers, leading to a nonhomogeneous RNA distribution. We did not see any appreciable leakage of RNA fluorescence outside the actinosomes over a course of more than an hour. One of the trademark properties of coacervates is their ability to selectively sequester biomolecules[41] within them, often up to orders of magnitude higher than the surroundings[42] Coacervates also provide a distinct microenvironment that can differ from the dilute phase like the concentration of metal ions (such as Mg^{2+})[25] Thus, condensate droplets acting as the initial scaffolds for actinosomes provide an excellent opportunity to preload the actinosomes with components of interest. We tested this strategy by sequestering a cell-free protein translation machinery (rabbit reticulocyte lysate) along with singlestranded, capped, and tailed mRNA encoding the enhanced green fluorescence protein (EGFP) inside the coacervate droplets (**Figure 2.4c**). This was done by adding the necessary components to the initial mixture prior to condensate formation. Upon subsequent actinosome formation, based on our pore size measurements, we expected the large biomolecules involved in the cell-free expression machinery to remain encapsulated within actinosomes. We then incubated the actinosomes at 29 °C and monitored the GFP expression in real time(**Figure 2.4d**, **Supplementary Movie 5**). As can be seen, fluorescence in the GFP channel steadily increased over the course of an hour, with the protein expression evident as early as in the first few attribute the quick maturation of GFP protein to the usage of an EGFP-mRNA construct and the cell-free translation machinery[43]. The protein expression taking place inside the actinosomes also suggests that the RNA is localized on the inner surface of the actinosomes (**Figure 2.4a**) and not on the outer one because otherwise the expressed proteins would have simply diffused away. Actinosomes encapsulating the *in vitro* translation machinery without the GFP-encoding mRNA showed no signal in the GFP channel over a similar time course (**Figure 2.4e**). The GFP expression was further analyzed by measuring the fluorescence signal intensity inside the actinosomes. A steady increase in intensity (n = 11) was observed for the first 20 min, which later plateaued (**Figure 2.4f**). Actinosomes without the GFP-encoding mRNA but still carrying the *in vitro*

translation machinery showed no increase in the signal intensity intensity (n = 6). The ease of encapsulating a complex machinery without needing any sophisticated setup and conducting biochemical reactions makes actinosomes suitable bioreactors.

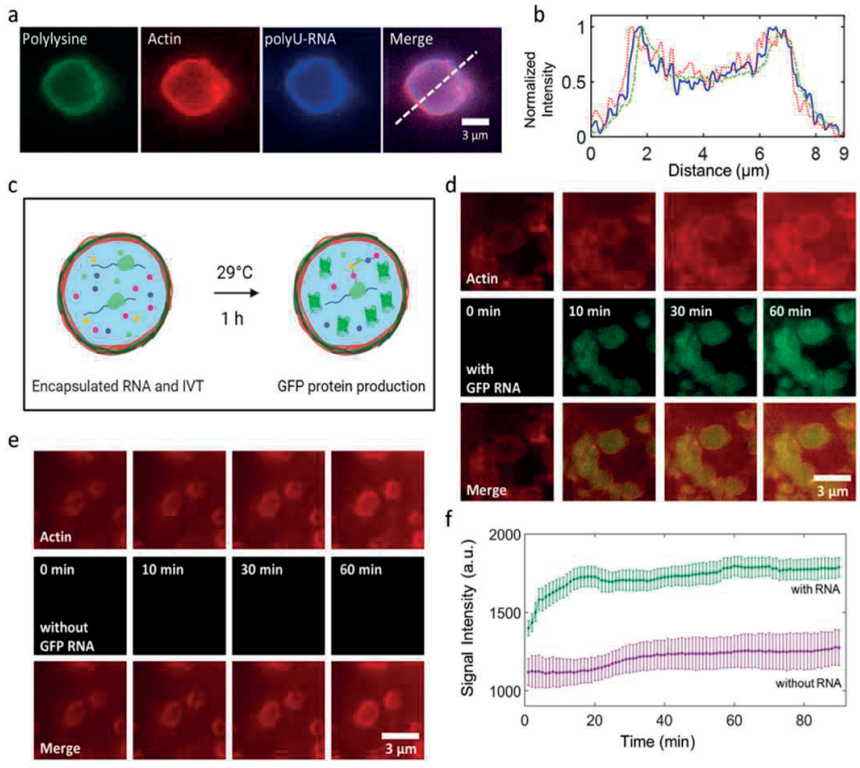

Figure 2.4: Actinosomes as protein-producing bioreactors.

(a) Encapsulation of Cy5-labeled RNA (1.25 mM, polyU 20-mer) encapsulated inside the actinosomes. (b) Line graph corresponding to the dotted line in panel (a) showing the localization of polyU-RNA (solid line, blue) near the actinosome border. Actin (dotted line, red) and polylysine (dashed line, green) profiles are also shown. (c) Schematic illustrating actinosomes encapsulating an in vitro translation machinery along with GFP-mRNA (left). Upon incubation, GFP-mRNA inside the actinosomes produces active GFP protein that remains encapsulated. (d) Expression of GFP inside actinosomes by encapsulation of GFP-encoding mRNA and a cell- free in vitro translation machinery (IVT). As can be seen, GFP fluorescence (green) increases over the course of an hour inside actinosomes, while the background remains dark, indicating the protein expression is carried out predominantly inside the containers. (e) Negative control (no GFP-mRNA but translation machinery is still present) showing no increase in fluorescence over the same duration. (f) Analysis of GFP expression inside actinosomes (n = 11) showed an initial steep increase before gradually reaching a plateau over the course of an hour. Analysis of actinosomes (n = 6) lacking GFP-encoding RNA but with encapsulated IVT had a significantly lower and a relatively constant signal intensity over the same period. We note that the t = 0 min corresponds to roughly 5 min after the reaction had started; the delay is caused due to technical limitations like adjusting the focus and selecting an optimal field-of-view. Error bars indicate standard deviations. Images were acquired in epifluorescence microscopy.

2.3 CONCLUSION

In this chapter, we have presented actinosomes: three-dimensional, cell-sized confinements with a boundary made up of polylysine polymers and actin filaments (**Figure 2.5**). The unstructured and porous proteinaceous shell provides a stable boundary, allowing biochemical reactions to take place inside the container. Actinosomes are quick and easy to make, especially compared to other containers such as liposomes and proteinosomes, which are currently used to form synthetic cells. Furthermore, the use of condensates as templates helps in encapsulation of a wide variety of biomolecules owing to their intrinsic ability to get sequestered in the condensate phase. The current extensive use of microfluidic techniques to generate highly monodispersed containers and achieve efficient encapsulation also adds a significant amount of complexity to the production techniques [44, 45]. An easy and robust process to produce microconfinements can thus be useful for specific purposes, especially in resource-limited conditions. We have shown that actinosomes are relatively straightforward to produce and can carry out complex biochemical reactions. While they might not be suitable for certain cellular features like growth and division, they are certainly appealing to be used as chemical nano-factories and for studying the effect of confinement on biochemical processes. With regard to monodispersed samples, actinosomes were found to be surprisingly uniform in size (average major axis: 2.4 ± 0.6 μm). We think this is due to nucleation, and subsequently coacervation, taking place homogenously throughout the solution and the droplets getting immediately stabilized by actin, further preventing their coalescence and leading to a fairly homogeneous size distribution. Changing the relative concentrations of principal components, especially actin, might allow further tuning of the size. With regard to its limitations, we do note that not all of the molecules can be naturally sequestered in condensates[46, 47]. Also, within actinosomes, small molecules are prone to diffusing across the boundary over time. Additionally, based on the coacervate species, the partition coefficient can vary ranging from ~1 to >100, suggesting not all biomolecules concentrate equally[48]. Finally, actinosomes have a tendency to form clusters and sometimes aggregate, which needs to be tackled to make them more suitable for systematic biological applications.

We propose the following mechanism for actinosome formation. We begin with an initial homogeneous solution of actin, polylysine, and other biomolecules that one wishes to sequester inside actinosomes. Upon addition of the NTP mixture (ATP + GTP) to the solution, complex coacervation is induced between polylysine and NTPs, forming coacervate droplets. Actin preferentially decorates the surface of the condensates, aided partially by the electrostatic interactions between the net negatively charged actin protein and positively charged condensates and the viscous nature of the coacervate due to the absence of salt. Other biomolecules present (ones that are

to be encapsulated inside) are likely to get partitioned inside, or alternatively at the surface of, the condensate. It is important to note that at this point, actin stays in the monomeric form as there are no Mg^{2+} ions present in the system, which are essential for polymerization. Addition of a salt-containing buffer (Mg^{2+} and KCl) triggers rapid actin polymerization at the expense of the ATP that is highly concentrated (~50 mM) in the condensates. Conversion of ATP into ADP and Pi (inorganic phosphate) leads to dynamic changes in the coacervate composition. However, polylysine polymers cannot readily diffuse outside and remain entangled within actin filaments to form an unstructured shell at the interface. This process continues until a majority of the polylysine is colocalized with the actin at the surface. This eventually leads to dissolution of the original condensate droplet to ultimately form a microcontainer, comprising an aqueous lumen surrounded by a proteinaceous shell.

We observe that the addition of a monovalent salt (KCl) plays an important role in actinosome formation. It weakens the electrostatic attractions between the coacervate components and possibly facilitates ATP consumption by actin. Furthermore, addition of KCl presents a hyperosmotic shock that seems to result in a water flux out of the forming actinosomes and induces an outward movement of polylysine molecules, allowing them to get entangled with actin filaments. This logic is consistent with the different scenarios we observe as we change R. In the case of a low-enough GTP content ($R \leq 0.6$), the hyperosmotic shock (Δc ~200 mosm;$\Delta P = \Delta cRT$ = 0.5 MPa) is too strong, resulting in significant loss of the water content from the condensate, eventually resulting in a crumpled state lacking structural integrity. At intermediate GTP contents (R = 0.7–0.8), while there is efflux of water, the NTP concentration (~50 mM) is enough to sustain the osmotic pressure difference until the salt equilibrates. At high GTP contents ($R \geq 0.9$), there are no significant morphological changes as the actin does not polymerize readily due to lack of enough ATP and thus condensate components do not really change. Thus, actin polymerization at the expense of ATP inside the condensates in combination with salt flux together drives actinosome formation.

In conclusion, actinosomes are a novel addition as synthetic cell containers with useful properties. They are easy to produce and require only basic lab equipment and commercially available proteins (**Figure 2.5a**). They have a porous membrane, with a pore size of ~5 nm, allowing easy transport of small biomolecules but retaining larger biomolecules (**Figure 2.5b**). As a result, they can efficiently encapsulate macromolecules, especially negatively charged polymers like RNA (**Figure 2.5c**). They can further carry out biochemical reactions by simply adding all of the required components in the initial mixture. We demonstrated this by encapsulating the entire translation machinery, which consists of complex biomolecules including enzymes

and tRNA molecules (**Figure 2.5d**). Lastly, actin-based membranes present interesting opportunities to functionalize these containers (**Figure 2.5e**). For example, actin can interact with numerous actin-binding proteins to initiate specific reactions at the interface. This can be used in forming communicative networks within a population or even physically connect the containers to form multicomponent, tissue-like structures. Such functionalities together with their highly biocompatible nature may allow actinosomes to interact with living cells and form hybrid interfaces. Further systematic research in these directions will reveal the true potential of these proteinaceous confinements and their use as scaffolds for synthetic cells.

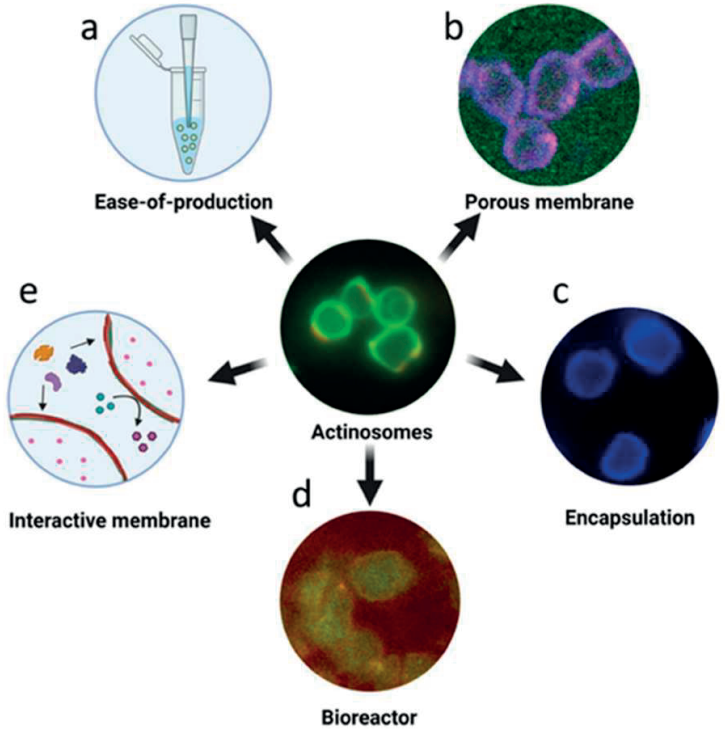

Figure 2.5: Salient feature of actinosomes.

Actinosomes are synthetic confinements with a boundary made of polyK and actin filaments. Several properties make them potentially useful containers for synthetic cell research. (a) They are easy to produce without the need for any sophisticated setups. (b) They have a permeable surface allowing small biomolecules to pass through. (c) They can efficiently encapsulate biomolecules owing to the inherent sequestration capacity of condensates. (d) They have the capacity to act as bioreactors to conduct complex reactions like protein translation. (e) The actin-based boundary opens up the possibility of having an interactive membrane for recruiting other proteins, designing signaling cascades, and forming multicellular assemblies.

2.4 MATERIALS AND METHODS

2.4.1 Chemicals and Proteins.

Unlabeled poly-L-lysine (molecular weight (*M*W) 15–30 kDa) and fluorescently labeled FITCpoly-L-lysine (*M*W 15–30 kDa) were purchased from Sigma-Aldrich. Individual nucleotides (ATP and GTP) were purchased from Thermo Scientific. Cy5-labeled polylysine (*M*W 25 kDa) was purchased from Nanocs Inc. Actin (rabbit skeletal muscle α actin), fluorescently labeled ATT0 532-actin (rabbit skeletal muscle α actin), and ATT0 594-actin were purchased from HYPERMOL in the form of lyophilized powders. The composition of the reconstitution buffer to dissolve actin monomers was 2 mM Tris (pH 8.0), 0.4 mM ATP, 0.1 mM $CaCl^2$, and 0.01mMdithiothereitol. The end composition of the actin polymerization buffer was 0.01Mimidazole pH 7.4, 0.1M KCl, and 2 mM $MgCl^2$. Fluorescently labeled ATTO-594-phalloidin was purchased from HYPERMOL (Cat. No. C8815-01). For permeability experiments, we used various FITC-labeled dextran solutions: *M*W 3–5 kDa (Sigma, Cat. No. FD4; mol FITC/mol glucose = 0.001–0.02), FITC-labeled dextran MW 20 kDa (Sigma, Cat. No. FD20S; mol FITC/mol glucose = 0.003-0.02), FITC-labeled dextran*M*W 70 kDa (Sigma, Cat. No. 46945; mol FITC/mol glucose = 0.004), and FITC-labeled dextran *M*W 150 kDa (Sigma, Cat. No. 46946; mol FITC/mol glucose = 0.004) to actinosome. Polyvinyl alcohol (PVA), molecular weight 30,000–70,000, 87–90% hydrolyzed, was purchased from Sigma-Aldrich.

2.4.2 Actinosome synthesis.

The process of making actinosomes can be summed up in three distinct steps: (1) preparing the actin–polylysine mixture; (2) forming coacervates with coated actin; (3) and actin polymerization and coacervate dissolution. Step 1: Monomeric actin and polylysine were reconstituted in the actin reconstitution buffer, with final concentrations of 3 μMand 5.05 mg/mL, respectively. The pH 8 of the buffer is crucial for monomeric actin stability. Additionally, it keeps the polylysine polymers positively charged. For microscopic visualization, the sample was doped with 10% fluorescently labeled actin (0.3 μM) and 1% FITC-poly-L-lysine (0.05 mg/mL). Step 2: To trigger coacervation, 5 mM NTP mixture (e.g., 1.25 mM GTP and 3.75 mM ATP) was added to the solution and gently pipetted to mix thoroughly. Step 3: To make actinosomes, actin polymerization buffer was added to the actin-coated coacervate solution. The sample was vortexed briefly to ensure sufficient mixing, followed by a short spin (1000 rpm for 5–10 s) to remove any large aggregates. The last step significantly increased the yield of separated (not connected in clusters) actinosomes.

2.4.3 ζ-Potential Measurements.

The net surface charge of the coacervate was determined by measuring the ζ-potential at 25 °C using the Malvern Zetasizer Nano instrument. The sample was diluted 1:20 and gently mixed prior to measurements. The ζ-potential for each sample was determined by taking the average measurement of three independent samples, where each measurement is the average of five readings from the same sample.

2.4.4 ATP Concentration Measurements.

To determine the NTP concentration required to obtain the maximum amount of the condensate phase for a given polylysine concentration, we prepared buffered solutions (2mMTris (pH 7.4), 100mMKCl, and 2 mM MgCl2) containing different concentrations of ATP (from 1.25 to 25 mM) while keeping the polylysine concentration constant at 5 mg/mL. The solution was incubated at room temperature for 15 min to equilibrate. The condensed phase was separated from the dilute phase by centrifugation at 10,000 rpm for 5 min. The concentration of the free ATP in the dilute phase was evaluated by measuring its absorbance at 259 nm using the molar extinction coefficient of ATP (15,400 $M^{-1}cm^{-1}$) using UV–vis absorption spectroscopy (NanoDrop2000/2000c spectrophotometer, Thermo Scientific). The concentration of ATP inside the coacervates was calculated as equation 2.1, where c_{dense} and c_{dilute} are the ATP concentration in dense and dilute phases, respectively, and f is the volume fraction of the dilute phase. Concentration in the dilute phase, c_{dilute}, was measured by absorbance as stated above. The fraction of the dilute phase, f, was estimated to be 0.9 by carefully removing the supernatant after centrifugation without disturbing the dense phase. For example, from a 40 µL sample, we estimated 36 µL to be the dilute phase.

$$c_{dense} = {c - c_{diliute} f}/{1 - f'} \quad (2.1)$$

2.4.5 Fluorescence Microscopy.

The samples were imaged on a Nikon-Ti2-Eclipse inverted fluorescence microscope, equipped with a pE-300ultra illumination system, using a Nikon Plan Apo 100*x*/1.45 NA oil objective. FITC-polyK and GFP expressions were detected using a 482/35 nm excitation filter and a 536/40nm emission filter (Semrock). Actin-ATTO-532 was detected using a 543/22 nm excitation filter and a 593/40 nm emission filter (Semrock). Actin-ATTO-594 was detected using a 628/40-25 nm excitation filter and a 692/40-25 nm emission filter (Semrock). The samples were illuminated at 2–5% laser intensity, and time-lapse images were acquired using a Prime BSI Express

sCMOS camera. Exposure time was usually 10–20 ms except for GFP visualization, when it was increased to 50–100 ms. The dextran influx assay was visualized using a confocal microscopy setup using laser of wavelengths 488, 561, and 640 nm for FITC-dextran, ATTO-594-labeled actin, and Cy5- labeled polylysine, respectively. For the phalloidin assay, actinosome (R = 0.8) was incubated for 1 h with 5 μL of phalloidin (stock prepared using manufacturer's protocol) and was visualized using a confocal microscopy setup 488 and 561 nm for FITC-labeled polylysine and ATTO-594-labeled phalloidin, respectively.

2.4.6 Microscopy Setup.

Samples were visualized in small chambers made of poly(dimethylsiloxane) (PDMS) and glass slides (**Figure S2.13**). The device was fabricated as follows. PDMS and the curing agent were mixed at a mass ratio of 10:1, and the air bubbles trapped during mixing were removed by desiccating in a vacuum desiccator. The mixture was poured on a silicon wafer (75 mm in diameter) and cured by baking at 80 °C for 4 h. Holes of 5 mm diameter were punched in the PDMS block using a biopsy punch. The PDMS and a clean glass slide (#1.5, VWR International) were plasma-treated and bonded together using a plasma cleaner (Harrick Plasma PDC-32G). To minimize coacervates wetting the surface, the glass slide was coated with 5% w/v poly(vinyl alcohol) immediately after plasma bonding. The PVA solution was incubated for 10 min in the wells and discarded. The wells were rinsed with Milli-Q water to remove uncoated PVA. The devices were baked at incubated 120 °C for 10 min to heat-immobilize the PVA polymers on the surface. The device was ready to use for microscopic visualization once cooled down.

2.4.7 SEM Microscopy.

The surface of actinosomes was analyzed by scanning electron microscopy. Actinosomes were prepared and vacuum-dried at room temperature on electrically conductive carbon adhesive discs mounted on a metal stub. The dried samples were sputter-coated with Tungsten (to obtain a thin film of ~12 nm). The acquired images were taken at approximately 65,000x–85,000x magnification at 2–3 kV accelerating voltage and 13 pA current.

2.4.8 RNA Expression in Actinosomes.

A capped and tailed messenger RNA (mRNA) template, encoding an enhanced green fluorescent protein, was synthesized from a linearized double-stranded DNA (**Figure S2.13**) using the HiScribe T7 ARCA mRNA kit (New England Biolabs, Ipswich, MA). The synthesized mRNA was purified using the Monarch RNA cleanup kit (New England Biolabs, Ipswich, MA), thereby removing the template DNA. GFP-encoding mRNA (final concentration 50 ng/μL) along with the 37.5% v/v *in vitro* translation

machinery Flexi Rabbit Reticulocyte Lysate System (Promega) was added along with actin and polylysine in step 1, prior to the addition of NTPs. This strategy allows efficient encapsulation of GFP-mRNA and translation machinery inside the actinosomes. Real-time expression of GFP was monitored by incubating actinosomes at 29 °C using the Okolab heating stage.

2.4.9 Image Analysis.

Since the morphology of actinosomes is close to that of a sphere, the size of the actinosomes was determined by fitting an ellipse using the Fitting Elipse function in Fiji. The obtained major and minor axes were used to determine the aspect ratio. For calculating the partition coefficient, the mean fluorescent intensity of actin, polylysine, or RNA inside or at the surface of the coacervates (I_{dense}) was measured for several coacervates, along with the mean fluorescent intensity outside the coacervates (I_{dilute}). The background intensity, I_{bg}, was measured outside the sample. The corresponding partition coefficient was then calculated as equation 2.2

$$P_{coacervate} = {I_{dense} - I_{bg}} \Big/ {I_{dilute} - I_{bg'}} \quad (2.2)$$

2.5 AUTHOR CONTRIBUTION

Ketan Ashok Ganar and Siddharth Deshpande conceived the idea. Ketan Ashok Ganar and Liza Leijten performed the experiments and analyzed the data. Ketan Ashok Ganar and Siddharth Deshpande wrote and edited the chapter.

2.6 ACKNOWLEDGEMENTS

The authors thank Jasper van der Gucht for fruitful discussions. The author acknowledge the help of Riccardo Antonelli and Tomas Kodger with scanning electron microscopy. The GFP-DNA template was a kind gift from Maria Forlenza and Mark Goldman (Aquaculture, Fisheries , and Immunology lab at Wageningen University). S.D. acknowledge financial support by the Innovation Program Microbiology grant (IPM-3), and by ENW-KLEIN grant (OCENW.KLEIN.465) from the Dutch Research Council (NWO). Schematics were created with Biorender.com

2.7 SUPPLEMENTARY FIGURES

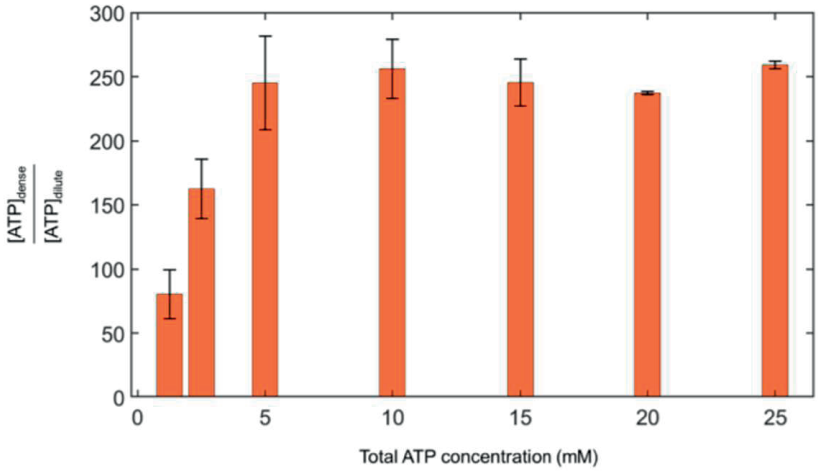

Figure S2.1: Determining the NTP concentration that leads to optimal coacervation with polyK.

Amount of ATP partitioned inside the dense phase at constant polylysine concentration of 5 mg/ml. The maximum partitioning (around 250-fold) was observed for a total ATP concentration above 5.0 mM (n = 3 experimental repeats; error bars indicate standard deviations; see Methods for details).

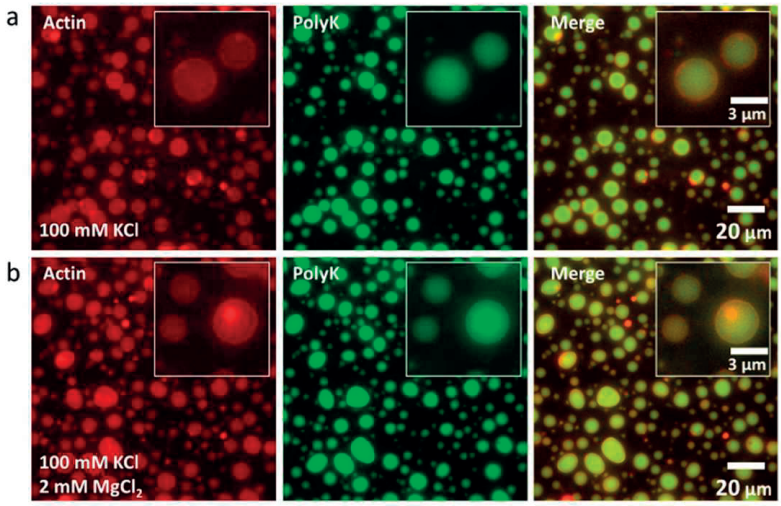

Figure S2.2: Presence of KCl in the initial reaction mixture leads to homogenous partitioning of actin in the coacervates and further inhibits actinosome formation. (a) Coacervate droplets composed of polyK/NTP (R = 0.7) made in presence of KCl sequester the actin within the coacervates, as opposed to its localization at the interface in absence of KCl (Fig. 1). (b) Triggering actin polymerization by adding MgCl2 does not result in actinosome formation. Images acquired in epifluorescence microscopy.

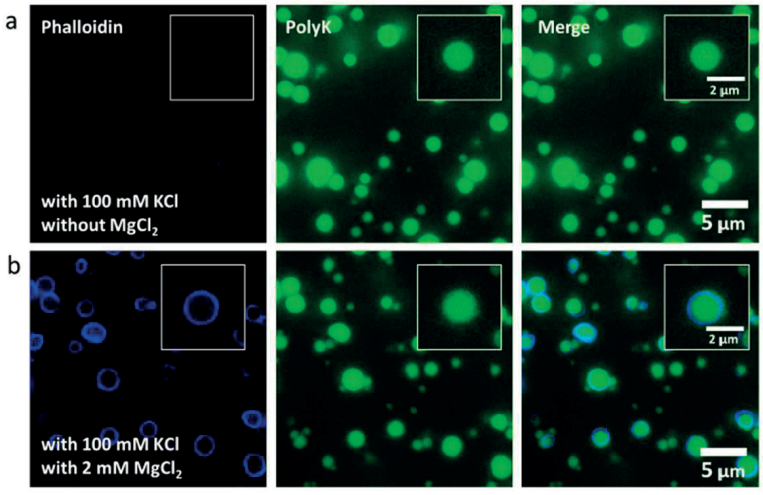

Figure S2.3: Phalloidin staining of actin-coated condensates reveals actin polymerization on the coacervate surface in presence of Mg2+. (a) Actin-coated coacervate droplets composed of polyK/NTP (R = 0.7) made in presence of KCl but witout Mg2+ ions show absence of actin filaments. (b) In presence of both KCl and Mg2+ ions phalloidin stains the actin filaments polymerized on the surface of coacervates. Image contrast settings are the same for individual channels. Images acquired in epifluorescence microscopy

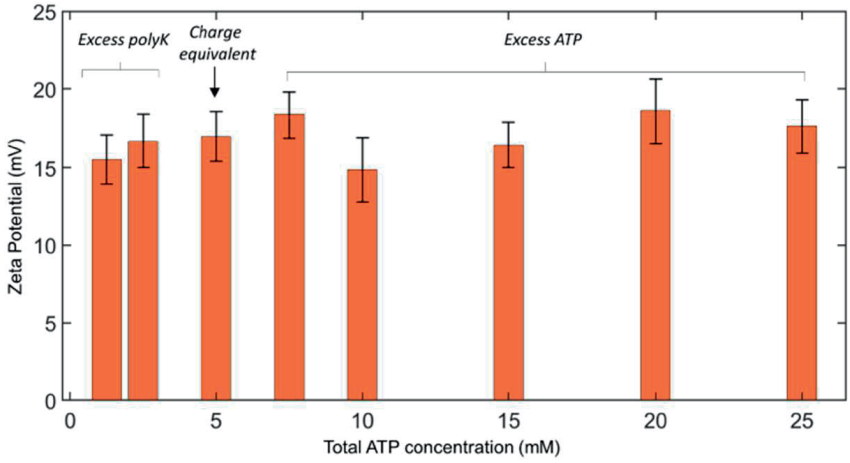

Figure S2.4: Surface charge of polyK/ATP coacervates stays constant over different ATP: polyK ratios. Zeta potential of the polyK/ATP coacervate droplets was measured over a concentration range of 1.25 – 25 mM, with polyK concentration kept constant at 5 mg/mL. The measurements covered three regimes: excess polyK (positively charged polymer), charge equivalent state (net neutral), and excess ATP (negatively charged multivalent molecule). The values stayed relatively constant (16.9 ± 1.7 mV) over the entire ATP concentration range, suggesting a net positive surface charge on the coacervate droplets irrespective of limiting or excess ATP concentrations (n = 3 experimental repeats, with each measurement being an average of 5 individual runs; error bars indicate standard deviations).

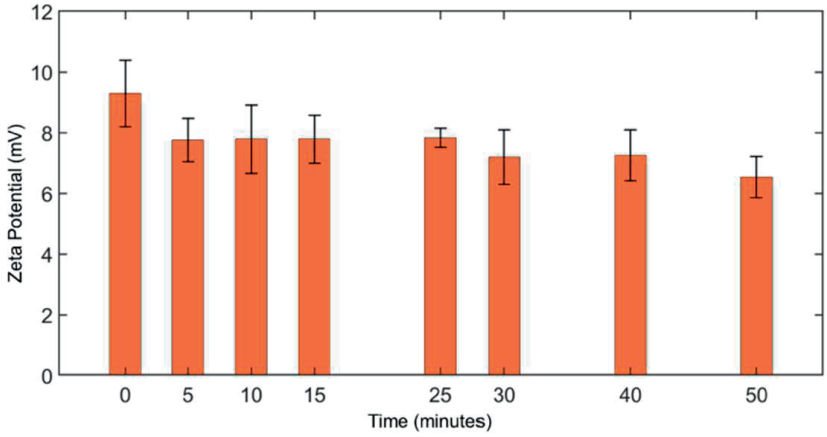

Figure S2.5: Surface charge of polyK/ATP coacervates in presence of actin monomers over time.

Zeta potential of polyK/ATP coacervate droplets was measured at different time points after the addition of actin. PolyK, ATP, and actin concentrations were respectively kept at 5 mg/mL, 5.4 mM, and 3 μM respectively; polymerization conditions were used. Immediately after the addition of actin, the surface charge was clearly lowered (< 10 mV) compared to when actin was absent (16.9 ± 1.7 mV; Supplementary Figure 3). This indicates efficient accumulation of actin at the surface. The surface charge was further decreased to 7.8 ± 0.7 mV after 5 minutes and then remained fairly constant over the entire time duration. (n = 3 experimental repeats, with each measurement being an average of 5 individual runs; error bars indicate standard deviations).

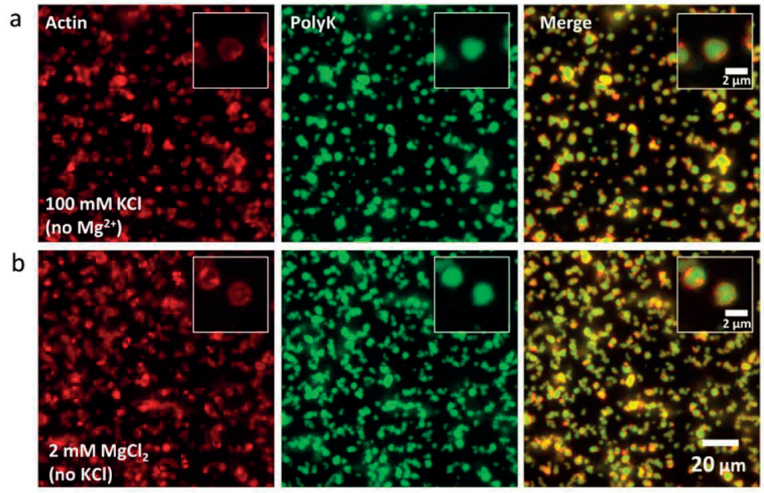

Figure S2.6: Only a hyperosmotic shock (without actin polymerization) or only actin polymerization (without hyperosmotic shock) do not form actinosomes. (a) Coacervate droplets composed of polyK/NTP (R = 0.7) made in presence actin monomers lead to actin-coated condensates but resist coacervate dissolution and actinosome formation despite KCl-induced hyperosmotic shock. (b) Coacervate droplets composed of polyK/NTP (R = 0.7) form actin-coated condensates but do not lead to actinosomes after the addition of Mg^{2+} but without any hyperosmotic shock, despite triggering actin polymerization. Images acquired in epifluorescence microscopy.

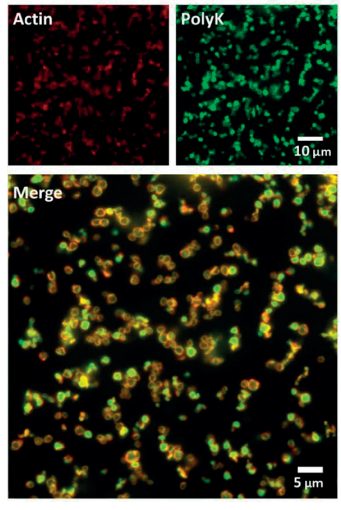

Figure S2.7: Efficient actinosome formation.

Full field-of-view of actinosomes synthesized using actin- coated polylysine/NTP condensates (R = 0.7). Images acquired in epifluorescence microscopy.

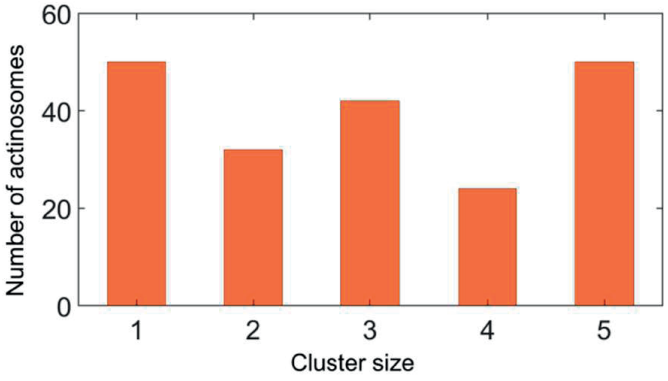

Figure S2.8: Actinosomes show tendency to cluster together.

Quantitative analysis of actinosomes (n = 198) show the tendency of actinosomes to form clusters of 2–5 units. Approximately 75% of actinosomes are in clustered state.

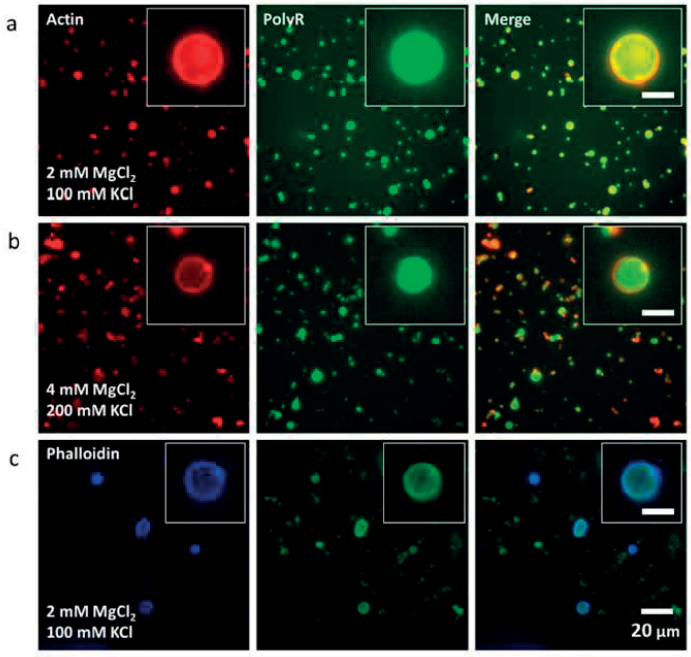

Figure S2.9: PolyR/NTP coacervates do not form actinosomes.

Coacervate droplets composed of polyR/NTP (R = 0.7) do not form actinosomes at similar buffer conditions (a) and even after doubling the concentrations of Mg2+ and KCl (b). Phalloidin staining confirms actin filament formation on the surface of the coacervates (c). Images acquired in epifluorescence microscopy.

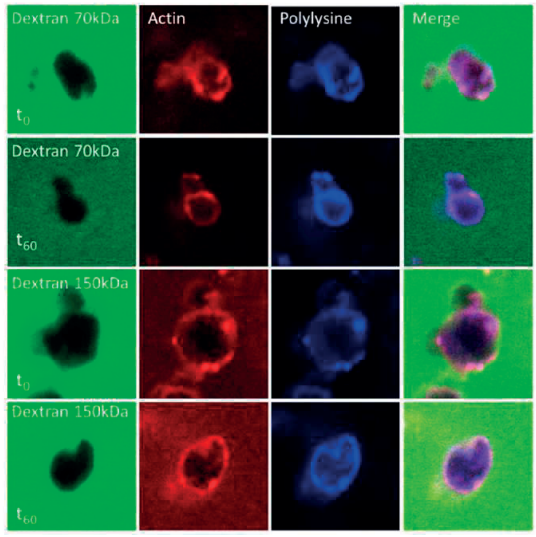

Figure S2.10: Actinosomes are impermeable to high molecular weight dextran.

Confocal images of pre-made actinosomes incubated with high molecular dextran, 70 kDa and 150 kDa corresponding to the diameter of gyration (Dg) of 5.45 and 7.02 nm respectively, showing the exclusion of dextran molecules within the actinosome interior. Two time slots are shown: right after the incubation (t0) and after 60 minutes (t60). Images acquired in confocal microscopy.

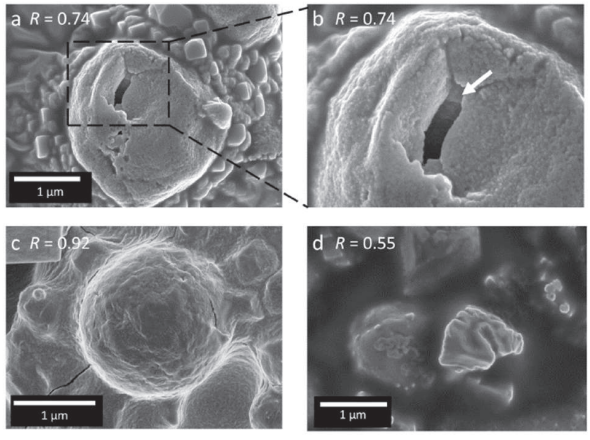

Figure S2.11: Scanning electron microscopy of actinosome at varying NTP ratio.

(a) Actinosome (R= 0.74) revealed a broken surface during the process of vacuum drying. (b) Zoom in showing a hollowness in actinosome interior. (c) Actin-coated condensates (R =0.92) showing a spherical morphology and a smooth surface without any pores or structuration. (d) Crumpled actin-polylysine structure (R= 0.55) because of high ATP concentration present in the condensates. The obtained structure is comparatively smaller and shows several folded surfaces.

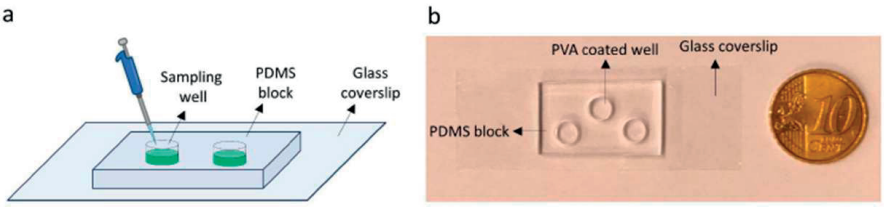

Figure S2.12: Experimental setup for the visualization of actinosomes.

PDMS block with wells (5 mm diameter) was bonded on a glass coverslip and the resulting well was coated with polyvinyl alcohol (PVA). (a) A schematic; (b) An actual device with three wells.

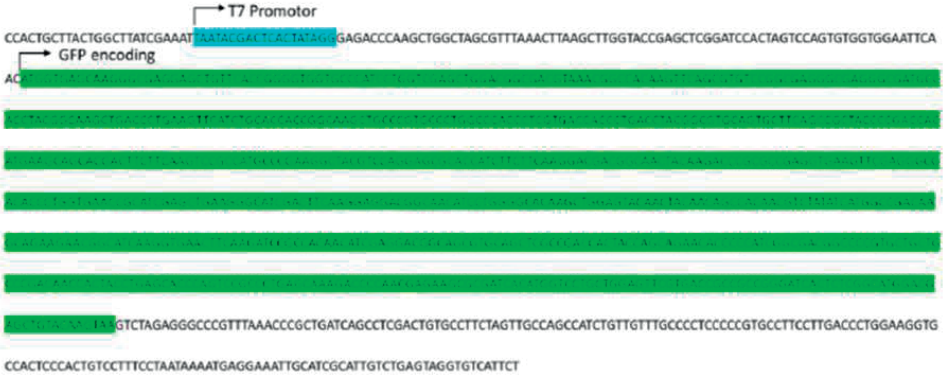

Figure S2.13: DNA template used for GFP production.

Template DNA encoding green fluorescent protein (highlighted in green) under the bacterial T7 promotor (highlighted cyan) that was used for cell-free in vitro synthesis of mRNA.

2.8 SUPPLEMENTARY MOVIE LEGENDS

The five supplementary movies belonging to this chapter could be found online at (https://pubs.acs.org/doi/10.1021/acssynbio.2c00290).

Supplementary Movie 1

Time-lapse showing the crumpling of polylysine/ATP condensate (green; $R = 0$) caused by a combination of hyperosmotic shock and ATP depletion via actin polymerization on the surface (red).

Supplementary Movie 2

Time-lapse showing the process of polylysine (green) getting expelled from actin-coated polylysine/ATP/GTP condensate ($R = 0.7$) due to hyperosmotic shock (100 mM KCl) to form an actinosome.

Supplementary Movie 3

Z-stack of an actinosome ($R = 0.7$). The two main components of actinosome, polylysine and actin are colored in green and red respectively.

Supplementary Movie 4

Time lapse showing polylysine/GTP condensate (green; $R = 1$) coated with actin (red) remaining stable over time.

Supplementary Movie 5.

Time-lapse showing the expression of GFP protein (green) by encapsulating GFP-encoding mRNA and *in vitro* translation machinery inside actinosomes (red; $R = 0.7$). GFP expression was imaged in real time by incubating the sample at 29°C using a heating stage mounted on the microscope.

REFERENCES

1. Jia H, Schwille P. Bottom-up synthetic biology: reconstitution in space and time. *Current opinion in biotechnology* 2019, **60:** 179-187.
2. Szostak JW, Bartel DP, Luisi PL. Synthesizing life. *Nature* 2001, **409**(6818)**:** 387-390.
3. Li M, Huang X, Tang TD, Mann S. Synthetic cellularity based on non-lipid micro-compartments and protocell models. *Current opinion in chemical biology* 2014, **22:** 1-11.
4. Robinson AO, Venero OM, Adamala KP. Toward synthetic life: Biomimetic synthetic cell communication. *Current opinion in chemical biology* 2021, **64:** 165-173.
5. Antonietti M, Förster S. Vesicles and liposomes: a self-assembly principle beyond lipids. *Advanced Materials* 2003, **15**(16)**:** 1323-1333.
6. Sherman SE, Xiao Q, Percec V. Mimicking complex biological membranes and their programmable glycan ligands with dendrimersomes and glycodendrimersomes. *Chemical reviews* 2017, **117**(9)**:** 6538-6631.
7. Soga N, Ota A, Nakajima K, Watanabe R, Ueno H, Noji H. Monodisperse liposomes with femtoliter volume enable quantitative digital bioassays of membrane transporters and cell-free gene expression. *ACS nano* 2020, **14**(9)**:** 11700-11711.
8. Godino E, López JN, Zarguit I, Doerr A, Jimenez M, Rivas G*, et al.* Cell-free biogenesis of bacterial division proto-rings that can constrict liposomes. *Communications biology* 2020, **3**(1)**:** 539.
9. Bouzetos E, Ganar KA, Mastrobattista E, Deshpande S, van der Oost J. (R) evolution-on-a-chip. *Trends in Biotechnology* 2022, **40**(1)**:** 60-76.
10. Ganar KA, Honaker LW, Deshpande S. Shaping synthetic cells through cytoskeleton-condensate-membrane interactions. *Current Opinion in Colloid & Interface Science* 2021, **54:** 101459.
11. Bashirzadeh Y, Liu AP. Encapsulation of the cytoskeleton: towards mimicking the mechanics of a cell. *Soft Matter* 2019, **15**(42)**:** 8425-8436.
12. Ivanov I, Lira RB, Tang TYD, Franzmann T, Klosin A, da Silva LC*, et al.* Directed growth of biomimetic microcompartments. *Advanced Biosystems* 2019, **3**(6)**:** 1800314.
13. Kretschmer S, Ganzinger KA, Franquelim HG, Schwille P. Synthetic cell division via membrane-transforming molecular assemblies. *Bmc Biology* 2019, **17:** 1-10.
14. Dreher Y, Jahnke K, Bobkova E, Spatz JP, Göpfrich K. Division and regrowth of phase-separated giant unilamellar vesicles. *Angewandte Chemie International Edition* 2021, **60**(19)**:** 10661-10669.
15. Lussier F, Staufer O, Platzman I, Spatz JP. Can bottom-up synthetic biology generate advanced drug-delivery systems? *Trends in Biotechnology* 2021, **39**(5)**:** 445-459.
16. Villar G, Graham AD, Bayley H. A tissue-like printed material. *Science* 2013, **340**(6128)**:** 48-52.
17. Booth MJ, Schild VR, Graham AD, Olof SN, Bayley H. Light-activated communication in synthetic tissues. *Science Advances* 2016, **2**(4)**:** e1600056.
18. Tanford C. The hydrophobic effect and the organization of living matter. *Science* 1978, **200**(4345)**:** 1012-1018.
19. Deng N-N, Yelleswarapu M, Huck WT. Monodisperse uni-and multicompartment liposomes. *Journal of the American Chemical Society* 2016, **138**(24)**:** 7584-7591.
20. Huang X, Li M, Green DC, Williams DS, Patil AJ, Mann S. Interfacial assembly of protein–polymer nano-conjugates into stimulus-responsive biomimetic protocells. *Nature communications* 2013, **4**(1)**:** 2239.
21. Huang X, Li M, Mann S. Membrane-mediated cascade reactions by enzyme–polymer proteinosomes. *Chemical Communications* 2014, **50**(47)**:** 6278-6280.

22. Weiss M, Frohnmayer JP, Benk LT, Haller B, Janiesch J-W, Heitkamp T*, et al.* Sequential bottom-up assembly of mechanically stabilized synthetic cells by microfluidics. *Nature materials* 2018, **17**(1)**:** 89-96.
23. Deshpande S, Caspi Y, Meijering AE, Dekker C. Octanol-assisted liposome assembly on chip. *Nature communications* 2016, **7**(1)**:** 10447.
24. Hyman AA, Weber CA, Jülicher F. Liquid-liquid phase separation in biology. *Annual review of cell and developmental biology* 2014, **30:** 39-58.
25. Frankel EA, Bevilacqua PC, Keating CD. Polyamine/nucleotide coacervates provide strong compartmentalization of Mg^{2+}, nucleotides, and RNA. *Langmuir* 2016, **32**(8)**:** 2041-2049.
26. Fetahaj Z, Ostermeier L, Cinar H, Oliva R, Winter R. Biomolecular condensates under extreme martian salt conditions. *Journal of the American Chemical Society* 2021, **143**(13)**:** 5247-5259.
27. Poudyal RR, Keating CD, Bevilacqua PC. Polyanion-assisted ribozyme catalysis inside complex coacervates. *ACS chemical biology* 2019, **14**(6)**:** 1243-1248.
28. Beneyton T, Love C, Girault M, Tang TYD, Baret JC. High-throughput synthesis and screening of functional coacervates using microfluidics. *ChemSystemsChem* 2020, **2**(6)**:** e2000022.
29. Sokolova E, Spruijt E, Hansen MM, Dubuc E, Groen J, Chokkalingam V*, et al.* Enhanced transcription rates in membrane-free protocells formed by coacervation of cell lysate. *Proceedings of the National Academy of Sciences* 2013, **110**(29)**:** 11692-11697.
30. Deshpande S, Dekker C. Studying phase separation in confinement. *Current Opinion in Colloid & Interface Science* 2021, **52:** 101419.
31. Williams DS, Patil AJ, Mann S. Spontaneous structuration in coacervate-based protocells by polyoxometalate-mediated membrane assembly. *Small* 2014, **10**(9)**:** 1830-1840.
32. Jang Y, Hsieh M-C, Dautel D, Guo S, Grover MA, Champion JA. Understanding the coacervate-to-vesicle transition of globular fusion proteins to engineer protein vesicle size and membrane heterogeneity. *Biomacromolecules* 2019, **20**(9)**:** 3494-3503.
33. Aumiller Jr WM, Pir Cakmak F, Davis BW, Keating CD. RNA-based coacervates as a model for membraneless organelles: formation, properties, and interfacial liposome assembly. *Langmuir* 2016, **32**(39)**:** 10042-10053.
34. Koga S, Williams DS, Perriman AW, Mann S. Peptide–nucleotide microdroplets as a step towards a membrane-free protocell model. *Nature chemistry* 2011, **3**(9)**:** 720-724.
35. McCall PM, Srivastava S, Perry SL, Kovar DR, Gardel ML, Tirrell MV. Partitioning and enhanced self-assembly of actin in polypeptide coacervates. *Biophysical journal* 2018, **114**(7)**:** 1636-1645.
36. Spruijt E, Sprakel J, Stuart MAC, van der Gucht J. Interfacial tension between a complex coacervate phase and its coexisting aqueous phase. *Soft Matter* 2010, **6**(1)**:** 172-178.
37. Last MG, Deshpande S, Dekker C. pH-controlled coacervate–membrane interactions within liposomes. *ACS nano* 2020, **14**(4)**:** 4487-4498.
38. Scipion CP, Ghoshdastider U, Ferrer FJ, Yuen T-Y, Wongsantichon J, Robinson RC. Structural evidence for the roles of divalent cations in actin polymerization and activation of ATP hydrolysis. *Proceedings of the National Academy of Sciences* 2018, **115**(41)**:** 10345-10350.
39. Fisher RS, Elbaum-Garfinkle S. Tunable multiphase dynamics of arginine and lysine liquid condensates. *Nature communications* 2020, **11**(1)**:** 4628.
40. Erickson HP. Size and shape of protein molecules at the nanometer level determined by sedimentation, gel filtration, and electron microscopy. *Biological procedures online* 2009, **11:** 32-51.
41. Reinkemeier CD, Girona GE, Lemke EA. Designer membraneless organelles enable codon reassignment of selected mRNAs in eukaryotes. *Science* 2019, **363**(6434)**:** eaaw2644.

42. Poudyal RR, Pir Cakmak F, Keating CD, Bevilacqua PC. Physical principles and extant biology reveal roles for RNA-containing membraneless compartments in origins of life chemistry. *Biochemistry* 2018, **57**(17)**:** 2509-2519.
43. Macdonald PJ, Chen Y, Mueller JD. Chromophore maturation and fluorescence fluctuation spectroscopy of fluorescent proteins in a cell-free expression system. *Analytical biochemistry* 2012, **421**(1)**:** 291-298.
44. Martino C, deMello AJ. Droplet-based microfluidics for artificial cell generation: a brief review. *Interface focus* 2016, **6**(4)**:** 20160011.
45. Göpfrich K, Platzman I, Spatz JP. Mastering complexity: towards bottom-up construction of multifunctional eukaryotic synthetic cells. *Trends in biotechnology* 2018, **36**(9)**:** 938-951.
46. Schmidt HB, Görlich D. Transport selectivity of nuclear pores, phase separation, and membraneless organelles. *Trends in biochemical sciences* 2016, **41**(1)**:** 46-61.
47. Al-Husini N, Tomares DT, Pfaffenberger ZJ, Muthunayake NS, Samad MA, Zuo T*, et al.* BR-bodies provide selectively permeable condensates that stimulate mRNA decay and prevent release of decay intermediates. *Molecular cell* 2020, **78**(4)**:** 670-682. e678.
48. Lyon AS, Peeples WB, Rosen MK. A framework for understanding the functions of biomolecular condensates across scales. *Nature Reviews Molecular Cell Biology* 2021, **22**(3)**:** 215-235.

Chapter 3

On-Chip Octanol-Assisted Liposome Assembly for Bioengineering

This chapter is based on

Chen, Chang[1*], Ketan A. Ganar[1*], and Siddharth Deshpande[1]. "On-Chip Octanol-Assisted Liposome Assembly for Bioengineering."*JoVE (Journal of Visualized Experiments) 193 (2023): e65032.*

ABSTRACT

Microfluidics is a widely used tool to generate droplets and vesicles of various kinds in a controlled and high-throughput manner. Liposomes are simplistic cellular mimics composed of an aqueous interior surrounded by a lipid bilayer; they are valuable in designing synthetic cells and understanding the fundamentals of biological cells in an *in vitro* fashion and are important for applied sciences, such as cargo delivery for therapeutic applications. This chapter describes a detailed working protocol for an on-chip microfluidic technique, octanol-assisted liposome assembly (OLA), to produce monodispersed, micron-sized, biocompatible liposomes. OLA functions similarly to bubble blowing, where an inner aqueous (IA) phase and a surrounding lipid carrying 1-octanol phase are pinched off by surfactant-containing outer fluid streams. This readily generates double-emulsion droplets with protruding octanol pockets. As the lipid bilayer assembles at the droplet interface, the pocket spontaneously detaches to give rise to a unilamellar liposome that is ready for further manipulation and experimentation. OLA provides several advantages, such as steady liposome generation (>10 Hz), efficient encapsulation of biomaterials, and monodispersed liposome populations, and requires very small sample volumes (~50 μL), which can be crucial when working with precious biologicals. The study includes details on microfabrication, soft-lithography, and surface passivation, which are needed to establish OLA technology in the lab. A proof-of-principle synthetic biology application is also shown by inducing the formation of biomolecular condensates inside the liposomes *via* transmembrane proton flux. It is anticipated that this accompanying video protocol will facilitate the readers to establish and troubleshoot OLA in their labs.

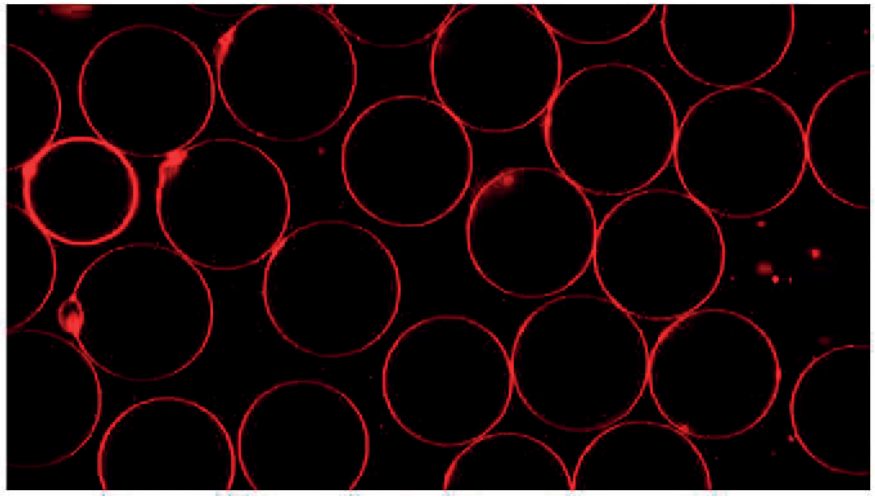

3.1 INTRODUCTION

All cells have a plasma membrane as their physical boundary, and this membrane is essentially a scaffold in the form of a lipid bilayer formed by the self-assembly of amphiphilic lipid molecules. Liposomes are the minimal synthetic counterparts of biological cells; they have an aqueous lumen surrounded by phospholipids, which form a lipid bilayer with the hydrophilic head groups facing the aqueous phase and the hydrophobic tails buried inward. The stability of liposomes is governed by the hydrophobic effect, as well as the hydrophilicity between the polar groups, van der Waals forces between the hydrophobic carbon tails, and the hydrogen bonding between water molecules and the hydrophilic heads[1, 2]. Depending on the number of lipid bilayers, liposomes can be classified into two main categories, namely, unilamellar vesicles comprising a single bilayer and multilamellar vesicles constructed from multiple bilayers. Unilamellar vesicles are further classified based on their sizes. Typically spherical in shape, they can be produced in a variety of sizes, including small unilamellar vesicles (SUV, 30-100 nm diameter), large unilamellar vesicles (LUV, 100-1,000 nm diameter), and finally, giant unilamellar vesicles (GUV, >1,000 nm diameter)[3, 4]. Various techniques have been developed to produce liposomes, and these can be categorized broadly into bulk techniques[5] and microfluidic techniques[6]. Commonly practiced bulk techniques include lipid film rehydration, electroformation, inverted emulsion transfer, and extrusion[7, 8, 9, 10]. These techniques are relatively simple and effective, and these are the prime reasons for their widespread usage in the synthetic biology community. However, at the same time, they suffer from major drawbacks with regard to the polydispersity in size, the lack of control over the lamellarity, and low encapsulation efficiency[7, 11]. Techniques like continuous droplet interface crossing encapsulation (cDICE)[12] and droplet shooting and size filtration (DSSF)[13] overcome these limitations to some extent.

Microfluidic approaches have been rising to prominence over the last decade. Microfluidic technology provides a controllable environment for manipulating fluid flows within user-defined microchannels owing to the characteristic laminar flow and diffusion-dominated mass transfer. The resulting lab-on-a-chip devices offer unique possibilities for the spatiotemporal control of molecules, with significantly reduced sample volumes and multiplexing capabilities[14]. Numerous microfluidic methods to make liposomes have been developed, including pulsed jetting[15], double emulsion templating[16], transient membrane ejection[17], droplet emulsion transfer[18], and hydrodynamic focusing[19]. These techniques produce monodispersed, unilamellar, cell-sized liposomes with high encapsulation efficiency and high-throughput.

This chapter details the procedure for octanol-assisted liposome assembly (OLA), an on-chip microfluidic method based on the hydrodynamic pinch-off and subsequent solvent dewetting mechanism[20] (**Figure 3.1**). One can relate the working of OLA to a bubble-blowing process. A sixway junction focuses the inner aqueous (IA) phase, two lipid-carrying organic (LO) streams, and two surfactant containing outer aqueous (OA) streams at a single spot. This results in water-in-(lipids + octanol)-in-water double emulsion droplets. As these droplets flow downstream, interfacial energy minimization, external shear flow, and interaction with the channel walls lead to the formation of a lipid bilayer at the interface as the solvent pocket becomes detached, thus forming unilamellar liposomes. Depending on the size of the octanol pocket, the dewetting process can take tens of seconds to a couple of minutes. At the end of the exit channel, the less dense octanol droplets float to the surface, whereas the heavier liposomes (due to a denser encapsulated solution) sink to the bottom of the visualization chamber ready for experimentation. As a representative experiment, the

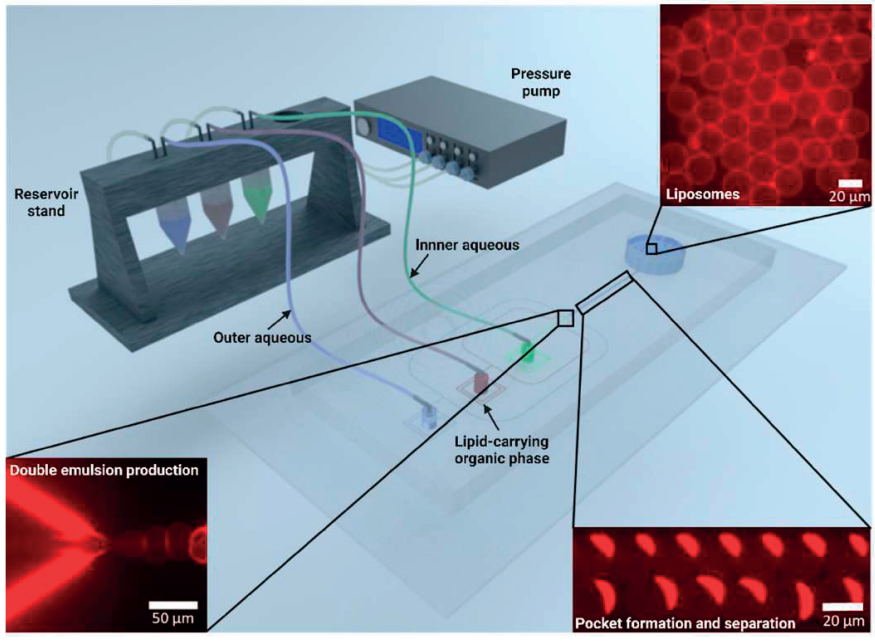

Figure 3.1: Schematic showing the assembly and working of OLA.

The pressure controller is connected to the reservoirs containing outer aqueous, lipid-in-octanol, and inner aqueous solutions. The tubes inserted into the reservoirs are connected to the respective inlets of the OLA device. Appropriate flows in the three channels lead to the formation of water-in-(lipidin- octanol)-in-water double emulsions. The formed double emulsions migrate to the exit well, during which the octanol pockets detach to form liposomes. The formed liposomes are collected at the bottom of the well for visualization and further experimentation.

process of liquid-liquid phase separation (LLPS) inside liposomes is demonstrated. For that, the required components are encapsulated inside liposomes at an acidic pH that prevents LLPS. By externally triggering a pH change and, thus, a transmembrane proton flux, phase-separated condensate droplets are formed inside the liposomes. This highlights the effective encapsulation and manipulation capabilities of the OLA system.

3.2 DETAILED PROTOCOL FOR LIPOSOME PRODUCTION

3.2.1 Fabricating the master wafer.

1. Take a 4 in (10 cm) diameter clean silicon wafer (see **Table 3.1**). Clean it further using pressurized air to remove any dust particles.
2. Mount the wafer on a spin coater, and gently dispense ~5 mL of a negative photoresist (see **Table 3.1**) in the center of the wafer. Try to avoid air bubbles, as they might interfere with the downstream printing process of the wafer.
3. To obtain a 10 µm thick photoresist layer, spin-coat the wafer at 500 rpm for 30 s with an acceleration of 100 rpm/s for initial spreading, followed by a 60 s spin at 3,000 rpm with an acceleration of 500 rpm/s. In case a different thickness is desired, change the spinning parameters according to the manufacturer's instructions.
4. Bake the wafer on a heating plate for 2 min at 65 °C and then for 5 min at 95 °C.
5. Once the wafer cools down, mount the wafer in the printing chamber of the direct-write optical lithography machine (see **Table 3.1**), and feed the OLA design (**Figure 3.2A**, **Supplementary Coding File 1** found at doi:10.3791/65032) into the software.

NOTE: The OLA design essentially consists of two OA channels, two LO channels, and one IA channel, which merge to form a six-way junction that continues as a post-production channel and ends up in the experimental well (EW).

6. Print the OLA design(s) on the coated wafer using a UV laser (see **Table 3.1**) with a dose of 300 mJ/ cm2 .
7. Once the design is printed, bake the wafer at 65 °C for 1 min, followed by 95 °C for 3 min.
8. At this point, ensure that the outline of the printed device appears on the wafer and is visible to the naked eye. To wash off the uncured photoresist, dip the wafer in a glass beaker containing the developer solution (see **Table 3.1**) until the uncured photoresist is fully removed.

NOTE: Excess developer treatment can affect the design resolution.

9. Wash the wafer with acetone, isopropanol, and deionized (DI) water in sequence, and finally, with pressurized air/N2 using a blow gun.
10. Hard-bake the wafer at 150 °C for 30 min to ensure that the printed design is firmly attached to the wafer surface and does not come off in the downstream fabrication process. The master wafer is then ready for further use (**Figure 3.2B**).

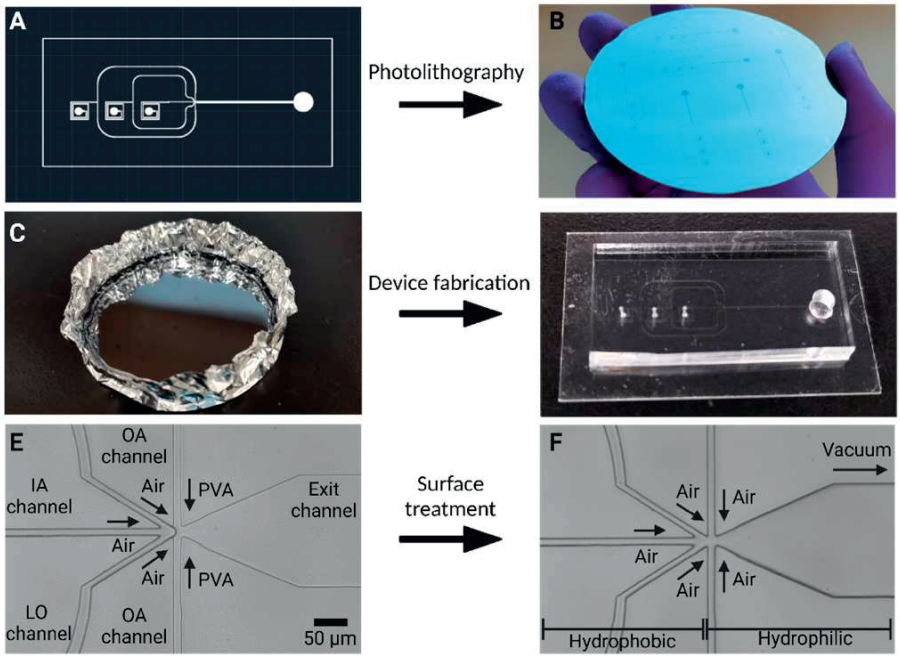

Figure 3.2 : Preparation of the OLA chip (photolithography, microfabrication, surface treatment).

(A) Digital design showing the key features of the OLA design, including three inlets, an outlet, and a six-way production junction. (B) A schematic of the master wafer showing multiple OLA designs produced using UV lithography. (C) A PDMS elastomer cast on the master wafer, placed in a well created out of aluminum foil, and cured by baking at 70 °C for 2 h. (D) A microfluidic device bonded using oxygen plasma treatment, where the PDMS block containing the OLA design is attached to a PDMS-coated glass slide. (E) Surface functionalization of the fabricated chip to make the device partially hydrophilic. This is done by flowing 5% w/v PVA for 5 min from the outer aqueous channel toward the exit channel. Positive air pressure in the other channels prevents the PVA solution from entering these channels. (F) PVA is removed by applying a vacuum in the exit channel. The device is baked at 120 °C for 15 min and is then ready to use.

3.2.2 Preparing the microfluidic device

1. Place the master wafer on a square piece of aluminum, and wrap the aluminum foil around the wafer, forming a well-like structure (**Figure 3.2C**).
2. Measure 40 g of polydimethylsiloxane (PDMS) and 4 g of curing agent (10:1, weight ratio, see **Table 3.1**) in a 50 mL centrifuge tube, and mix vigorously using a spatula or a pipette tip for 2-3 min.
3. The vigorous mixing of the PDMS and curing agent traps air bubbles inside the mixture. Spin the tube at 100 x *g* for 2-3 min to remove majority of large air bubbles.
4. Pour approximately 15-20 g of the mixture prepared in step 2.3 over the master wafer, and de-gas using a desiccator. Save the excess mixture to make PDMS-coated glass slides (step 3).
5. Incubate the assembly in an oven at 70 °C for at least 2 h. 6. Take the master wafer out of the oven and let it cool down. To remove the solidified PDMS block, remove the aluminum foil, and carefully peel off the PDMS block from the edge of the wafer.
6. Take the master wafer out of the oven and let it cool down. To remove the solidified PDMS block, remove the aluminum foil, and carefully peel of the PDMS block from the edge of the wafer.

NOTE: The wafer is fragile and might break, so it is important to do this process carefully.

7. Once the PDMS block is removed, keep the patterned structure facing upward, and using a sharp blade or a scalpel, cut individual PDMS blocks, each containing a single microfluidic device.
8. Place the PDMS block on a dark surface, and adjust the light direction (a table lamp comes in handy for this) so that the engraved channels are shiny and, as a result, visible. Make holes in the inlets and the exit channel using biopsy punches of 0.5 mm and 3 mm diameter (see **Table 3.1**), respectively.

NOTE: Use a sharp biopsy punch to avoid cracks in the PDMS, which can cause leakage later. Gently push the biopsy punch through the PDMS block, and ensure it passes completely through it. To remove the biopsy punch, gently retract it while rotating it in alternate directions. The PDMS block with the engraved OLA design is now ready to bind to a PDMS-coated glass slide.

3.2.3 Making the PDMS-coated glass slide

1. Take a transparent glass coverslip, pour approximately 0.5 mL of PDMS (prepared in excess in step 2.4) onto the center of the glass slide, and spread it across the

coverslip by gently tilting the glass slide, ensuring total coverage of the glass slide with PDMS.
2. Mount the glass slide on the spin coater, ensure its centrally placed (so that the middle of the slide overlaps with the center of the pressure shaft), and spin the glass slide at 500 rpm for 15 s (at an increment of 100 rpm/s) and then at 1,000 rpm for 30 s (at an increment of 500 rpm/s).
3. Place the PDMS-coated glass slide (coated side facing upward) on a raised platform like a block of PDMS (1 cm x 1 cm) in a covered Petri dish, and bake it at 70 °C for 2 h.

3.2.4 Bonding of the microfluidic device

1. Clean the PDMS block (prepared in step 2) by sticking and removing commercially available scotch tape (see **Table 3.1**) twice. Ensure to keep the cleaned side facing up until use.
2. Clean the PDMS-coated glass slide with pressurized air/ N2 using a blow gun, and keep the clean side facing up.
3. Place the PDMS block (engraved channels facing up) and the PDMS-coated glass slide (coated side facing up) in the vacuum chamber of the plasma cleaner (see **Table 3.1**).
4. Switch on the vacuum, and expose the contents to air plasma at a radio frequency of 12 MHz (RF mode high) for 15 s to activate the surfaces. Oxygen plasma can be seen in the form of a pinkish hue.
5. Immediately after the plasma treatment, place the PDMS-coated glass slide on a clean surface with the PDMS side facing upward. Gently place the PDMS block with the microfluidic pattern now facing toward the PDMS-coated glass slide, allowing them to bond (**Figure 3.2D**).

NOTE: Removing the air trapped in the device is crucial to ensure thorough bonding.

6. Bake the bonded devices at 70 °C for 2 h.

3.2.5 Surface functionalization of the microfluidic device

NOTE: Prior to surface functionalization, it is important to calibrate the pressure pump as per the manufacturer's protocol (see **Table 3.1**) and assemble the tubing to connect it to the microfluidic device.

3.2.5.1 Connecting the microfluidic device to the pressure pumps

1. Connect the pressure-driven flow controller to an external pressure source (up to 6 bars). At least four independent air pressure channels are required: three individual modules of 0-2 bar, and one module of –0.9-4 bar.

2. Calibrate the pressure pump according to the manufacturer's protocol (see **Table 3.1**).
3. Cut the tubing (1/16 in OD x 0.02 in ID) into four equal-sized pieces approximately 20 cm in length.
4. Insert 23 G stainless steel 90° bent connectors (see **Table 3.1**) at one end of each piece. This end is later inserted into the three inlets (OA, LO, and IA) of the microfluidic device and the fourth one is used to remove excess solution (step 5.2.5).
5. Insert the other end of the tubing into the microfluidic reservoir stand, and seal it using microfluidic fittings, ensuring the tubing is long enough to touch the bottom of the reservoir (1.5 mL tubes, see **Table 3.1**). This prevents unwanted air bubbles from entering the microfluidic device during the PVA treatment/liposome production.

3.2.5.2 PVA treatment of the exit channel

NOTE: Prior to liposome generation, it is crucial to render the device partially hydrophilic downstream of the production junction. This is done by treating these channels with 5% (w/v) polyvinyl alcohol (PVA) solution. The PVA solution is prepared by dissolving the PVA powder (see **Table 3.1**) in water at 80 °C for 3 h with constant stirring using a magnetic stirrer. Filter the solution prior to using it for surface treatment. Immediately after the bonding of the device, the microfluidic channels are hydrophilic due to the plasma-induced surface activation, and they will gradually become hydrophobic again. It is recommended to wait for 2 h after the baking (step 4.6) before starting the PVA treatment.

1. Dispense 200 µL of 5% w/v PVA solution into a 1.5 mL tube, and connect it to the microfluidic reservoir stand. Insert the tubing (the one mentioned in step 5.1.3) such that one end is submerged in the PVA solution and the other end is connected to the inlet of the OA channel of the microfluidic device. *NOTE*: A lower PVA concentration can lead to substandard surface functionalization.
2. Repeat the above step without PVA (empty 1.5 mL tube), and connect it to the LO and IA channels.
3. Increase the pressure of the OA phase to 100 mbar to flow the PVA solution in the OA channels. Increase the pressures of the IA and LO phases to 120 mbar in order to prevent the backflow of PVA solution inside these channels (**Figure 3.2E**).

NOTE: If needed, adjust the pressures of the individual channels in order to keep the meniscus steady at the production junction.

4. Flow the PVA solution in this manner for approximately 5 min, ensuring complete functionalization of the exit channel.

5. To remove the PVA solution, detach the tubing from the OA inlet, and immediately increase the pressure in the LO and IA channels to 2 bar. Simultaneously, use a tubing connected to a negative pressure channel (–900 mbar) remove excess PVA first from the exit channel and then from the OA inlet (**Figure 3.2F**).
6. Bake the device at 120 °C for 15 min, and let it cool down before use. The device can be stored under ambient conditions for at least 1 month.

NOTE: It is recommended to wait for 1 day (at room temperature) before proceeding with OLA to ensure the untreated PDMS regains its hydrophobicity after the plasma treatment.

3.2.6 Octanol-assisted Liposome assembly (OLA)

3.2.6.1 Preparing the lipid stock

NOTE: Here, a mixture of 1,2-dioleoyl-sn-glycero-3-phosphocholine (DOPC) and 1,2-dioleoyl-sn-glycero-3-phosphoethanolamine-N-(lissamine rhodamine B sulfonyl) (Liss Rhod PE) lipids (see **Table 3.1**) are used as an example; users should prepare the lipid composition they need in a similar manner.

1. Dispense 76 µL of DOPC (25 mg/mL) and 16.6 µL of Liss Rhod PE (1 mg/mL) into a round-bottom flask using separate glass syringes.
2. Keep the round-bottom flask upright, and use a compressed N2 blow gun to give a gentle stream of nitrogen to evaporate the chloroform and form a dried lipid film at the bottom of the flask.
3. Place the flask in the desiccator for at least 2 h under a continuous vacuum to remove any remaining chloroform.
4. Add 100 µL of ethanol into the round-bottom flask, followed by gentle pipetting or shaking to ensure the lipids are dissolved to form a 10% (w/v) lipid stock.

NOTE: In case a particular lipid composition is not completely soluble in ethanol, use an ethanol/chloroform mixture, keeping the volume of chloroform as small as possible.

5. Pipette the solution into a dark glass vial. Gently flush the vial with nitrogen using a blow gun to replace the air with an inert atmosphere. Seal the lid with paraffin film, and store at –20 °C.

NOTE: The stock solution can be used for up to a few months. Each time the vial is opened, gently replace the air with nitrogen, and reseal with lid with paraffin film.

3.2.6.2 Preparing solutions for OLA

1. Make stock solutions of the indispensable components: 20 mM dextran (Mw 6,000); 60% (v/v) glycerol; a buffer of choice. In this case, 5x phosphate-buffered saline (0.68 M NaCl, 13.5 mM KCl, 50 mM Na2HPO4 , 9 mM KH2PO4; pH 7.4) was prepared (see **Table 3.1**).

NOTE: As pure glycerol is highly viscous, it is recommended to cut out a small piece at the end of the pipette tip in a slanted manner for effective pipetting.

2. Prepare 100 µL of IA, OA, and exit solution (ES, the desired solution to fill the EW) samples. For ease of visualization, yellow fluorescent protein (YFP) was added to the IA solution in this particular case. Check the osmotic balance between the IA and OA by calculating the osmolarity of the encapsulated components and adding an appropriate amount of sugar or salt into the OA if needed. This is done in order to prevent the bursting or shrinking of the liposomes during production.

NOTE: The final compositions of the three phases are as follows:
IA: 15% glycerol, 5 mM dextran (Mw 6,000), 5.4 µM
YFP, 1x PBS
OA: 15% glycerol, 5% F68 surfactant, 1x PBS
ES: 15% glycerol, 1x PBS A lower concentration of F68 surfactant negatively affects the generation of double emulsions.

3. Prepare 80 µL of the LO phase by pipetting 4 µL of stock lipid into 76 µL of 1-octanol (see **Table 3.1**). The final concentration of DOPC is 5 mg/mL.
4. Centrifuge the samples at 700 x *g* for 60 s to remove any large aggregates before proceeding with the microfluidic experiments. This prevents any obvious clogging factors from entering the microfluidic chip.

3.2.6.3 Liposome production

1. Dispense the solutions (IA, LO, OA) into three 1.5 mL tubes, assemble them (as mentioned in step 5.1), and connect them to the PVA-treated microfluidic chip (step 5.2.6).
2. Apply a positive pressure on the three channels: ~100 mbar on the IA and LO channels and ~200 mbar on the OA channel.

NOTE: Since the OA pressure is higher than the others, the OA solution will be the first to arrive at EW; this is highly recommended.

3. Once the OA solution reaches EW, decrease the OA pressure to 100 mbar and increase the LO to 200 mbar. The LO solution arriving at the production junction will likely result in air bubbles because of air being displaced from the LO channels. Once the air bubbles are dispensed into the EW, adjust the LO pressure to 100 mbar. Lastly, increase the IA pressure to 200 mbar, and wait until all the air in the IA channel is removed. The ideal sequence of arrival at the junction of the three phases is, thus, OA, LO, and IA.
4. After removing the air from the three channels, adjust all the channel pressures to 50 mbar and pipette 10 μL of ES into the exit chamber. After pipetting the ES, put a cover slide on the exit hole to avoid evaporation. In case the LO is pushed back, gradually increase the LO pressure in 1 mbar increments until it starts to flow to the junction.
5. Once all three phases start co-flowing at the junction, ensure double emulsion production begins, and adjust according to its quality (**Figure 3.3A-C**). Change the pressures gradually (steps of 0.1-1 mbar) rather than abruptly unless the pressure is being changed to eliminate an unwanted clog in the channel.

NOTE: The channels to adjust depends on what is happening at the junction. For example, the IA needs to be decreased if the emulsions are too big; the OA needs to be increased if double emulsions form but burst instead of getting pinched off; and the LO needs to be decreased if the octanol pocket is too big.

6. Check that the double-emulsion droplets flow downstream to EW. As they flow, octanol pockets become more and more prominent and finally get pinched off, forming liposomes (**Figure 3.3DF**). Ensure that the post-production channel is long enough and that the migration of the double emulsions is slow enough for dewetting.

NOTE: Within minutes after decent production, liposomes and octanol droplets will exit the postproduction channel and go into the EW. As a result, being less dense than water, the octanol droplets float to the surface of the ES. Due to the addition of dextran in the IA, the liposomes are heavier than their surroundings and go to the bottom of the chamber ready for observation and further manipulation.

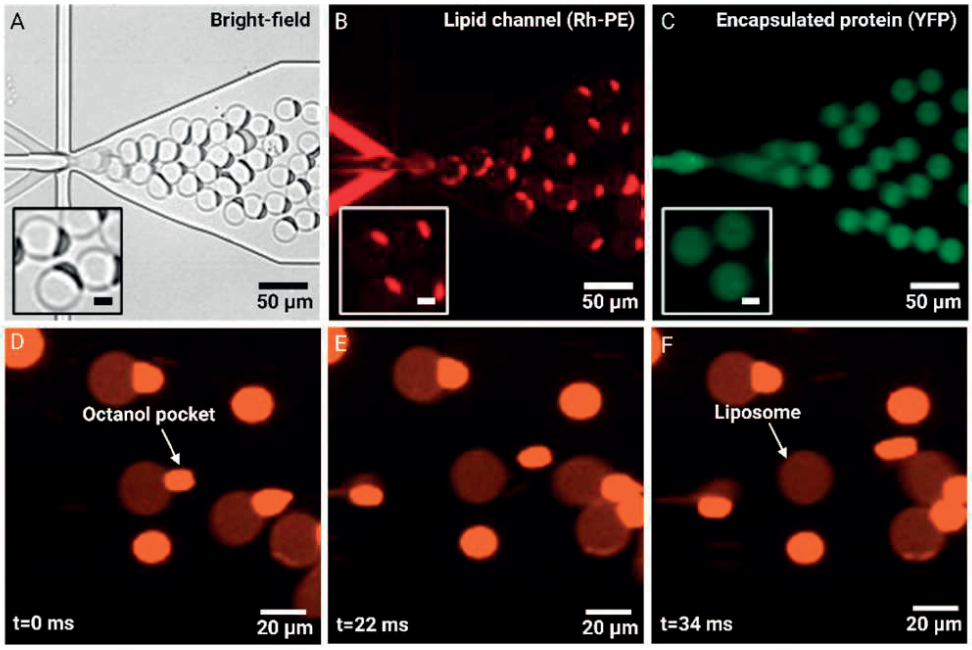

Figure 3.3: Demonstration of OLA efficiently producing monodispersed double emulsions and eventually liposomes with excellent encapsulation. (A) A bright-field image showing rapid generation of double-emulsion droplets. (B) The fluorescent lipid channel shows the formation of an octanol pocket due to partial dewetting. The lipid-in-octanol phase contained a mixture of DOPC (5 mg/mL) and Lis Rhod PE at a 1000:1 ratio. (C) The inner aqueous channel showing encapsulation of yellow fluorescent protein (YFP). The insets in (A-C) show representative zoomed-in views of the respective panels (scale bars = 10 µm). (D-F) Dewetting of the octanol pocket in the exit channel, which forms a liposome.

3.3 PH INDUCED LLPS IN LIPOSOMES

This study demonstrates the formation of membraneless condensates *via* the process of liquid-liquid phase separation (LLPS) inside liposomes as a representative experiment.

3.3.1 Sample preparation

The inner aqueous (IA), outer aqueous (OA), exit solution (ES), and feed solution (FS) are prepared as follows:

IA: 12% glycerol, 5 mM dextran, 150 mM KCl, 5 mg/mL poly- L-lysine (PLL), 0.05 mg/mL poly-L-lysine-FITC labeled (PLLFITC), 8 mM adenosine triphosphate (ATP), 15 mM citrate-HCl (pH 4)

OA: 12% v/v glycerol, 5% w/v F68, 150 mM KCl, 15 mM citrate-HCl (pH 4)

ES: 12% glycerol, 150 mM KCl, 15 mM citrate-HCl (pH 4)

FS: 12% glycerol, 150 mM KCl, 75 mM Tris-HCl (pH 9)

3.3.2 Condensate formation inside liposomes

A simple assay of pH-sensitive complex coacervation of positively charged poly-L-lysine (PLL) and negatively charged multivalent adenosine triphosphate (ATP) was selected to demonstrate the phenomena of LLPS in liposomes. To prevent phase separation of polylysine and ATP during encapsulation, the pH of the solution was maintained at 4, at which ATP is neutral. Increasing the pH of the ES by adding FS (a buffer of pH 9) eventually increased the pH inside the liposomes due to transmembrane proton flux, making ATP negatively charged and triggering its phase separation with positively charged PLL[21] (**Figure 3. *4*A**). After about 2 h of liposome generation, the IA and LO pressures were switched off. The OA channel pressure was kept at 100 mbar to flow the remaining liposomes into the observation chamber slowly. Once all the liposomes in the channel were recovered in the EW, the pressures were switched off to stop the flow and prevent the liposomes from moving. The liposomes generated at a lower pH showed a homogeneous fluorescence (from the encapsulated fluorescent PLL-FITC) in their lumen (**Figure 3. *4*B,D**). Octanol droplets floating at the surface were removed by carefully pipetting out 5 μL of solution from the top to prevent them from affecting further pipetting steps. Subsequently, 10 μL of FS buffer was added to the EW, which induced phase separation of the encapsulated PLL and ATP. The homogeneous FITC fluorescence from each liposome gradually transformed into distinct fluorescent condensate droplets. Eventually, the individual droplets merged

into one bigger condensate droplet that freely diffused within the liposomes (**Figure 3. *4*C,E-G**).

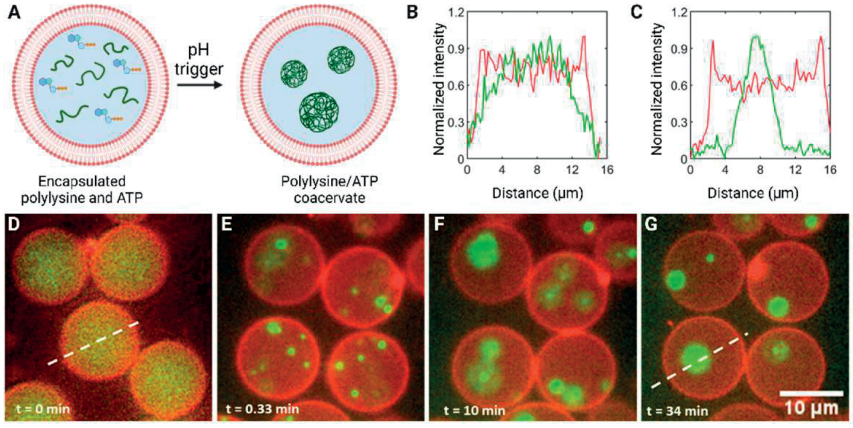

Figure 3. 4 : pH-triggered liquid-liquid phase separation of pLL/ATP within liposomes.

(a) Schematic of the pH-dependent transitioning of the homogenous solution of pLL and ATP encapsulated within the liposome (left) to phase-separated pLL/ ATP coacervates (right). The initial acidic environment in the liposome renders the molecular charge of ATP to be neutral, inhibiting coacervation. When the pH inside the liposomes equilibrates with the externally applied pH increase, ATP gains a negative charge, triggering coacervation. (B-C) Line graphs (corresponding to the dotted lines in panels (D) and (G), respectively) showing the spatial distribution of pLL (green channel) and the membrane (red channel). (D-G) Time-lapse images showing the formation of pLL/ATP coacervates within the liposomes. The external addition of a basic buffer raises the pH level inside the liposomes over the course of minutes and initiates coacervation. t = 0 min refers to the time just before the occurrence of the first coacervation event.

3.4 DISCUSSION

Cellular complexity makes it extremely difficult to understand living cells when studied as a whole. Reducing the redundancy and interconnectivity of cells by reconstituting the key components in vitro is necessary to further our understanding of biological systems and create artificial cellular mimics for biotechnological applications[22, 23, 24]. Liposomes serve as an excellent minimal system to understand cellular phenomena. A non-exhaustive list of these phenomena includes cytoskeleton dynamics and resulting membrane deformations [25, 26], spatiotemporal regulation of biomolecular condensates [27, 28] and their interaction with the membrane[29], encapsulation of a wide variety of biomolecules, including cell-free transcription translation systems[30] , cell-free lipid synthesis[31] , and evolution of proteins[32, 33, 34]. Liposomes have also been widely used as carriers for drug delivery and have been approved by the Food and Drug Administra-

tion (FDA) and European Medicines Agency (EMA) for clinical usage[11] . Liposomes and lipid-based nanoparticles are used as carriers for drug delivery, including mRNA vaccines like the recent COVID-19 vaccine[35].

This chapter describes a detailed protocol on photolithography, microfluidic assembly, and surface functionalization to perform the OLA technique in order to generate on-chip liposomes (**Figure 3.1** and **Figure 3.3**). The liposomes produced using OLA are monodispersed (coefficient of variation: 4%-11% of the mean) and in the biological cell-sized range (typically between 5-50 μm in diameter), and they can be tuned using appropriate flow velocities of the inner and outer aqueous channels[36]. For example, the liposome population seen in **Figure 3.1** has a size distribution of 23.3 μm ± 1.8 μm (n = 50). With typical production rates of 10-30 Hz, the formed liposomes are unilamellar, as was previously confirmed by inserting a single bilayer-specific transmembrane protein, alpha-hemolysin[36], into the membrane, as well as by using the dithionate-bleaching assay[37]. OLA is also compatible with a wide variety of lipid compositions, offering the user flexibility in the choice of lipids. Importantly, the initially used lipid composition is reflected in the final liposome composition[38]. Being a relatively new technology, there is further scope for improving OLA. For instance, surface functionalization using PVA is crucial but tedious to perform. An easier and simpler way to surface-functionalize the device would significantly reduce the chip fabrication time as well as chip-to-chip variability. Pluronic F68 surfactant is an important component in the outer aqueous phase to initially stabilize the double emulsions; nonetheless, its usage can be restrictive in certain cases. Replacing Pluronic F68 with a more biocompatible surfactant or complete surfactant removal may improve the versatility of the system. During the migration of generated double emulsions in the exit channel, they can burst due to shear. Upgrading the OLA design to improve the double emulsion stability and octanol pocket separation could, thus, increase the throughput. Nonetheless, OLA has several advantages, which mainly include the efficient encapsulation, monodispersed and unilamellar liposomes, and controlled on-chip experimentation. OLA has been employed and adapted in a diverse range of studies, including growth and division of liposomes[39], studying the process of liquid-liquid phase separation[27] and its interaction with the membrane[21], and understanding bacterial growth bioproduct formation in liposomes[40] . OLA-based high-throughput assays are also being used to understand ion transport across the membrane[41] and drug permeability across the lipid bilayer[37], as a drug delivery system for therapeutic purposes[42], to study the effect of antimicrobials on membrane[43] , and as a tool to encapsulate liquid crystals[44]44 . In addition to the wide range of applications of OLA technology, modified versions of OLA suited for particular purposes are being developed[45, 46, 47, 48, 49, 50]. Overall, considering the pros and cons, we strongly believe that OLA is a versatile platform for synthetic biology.

Name	Company	Catalog Number	Comments
1-Octanol	Sigma-Aldrich	No. 297887	
1.5 mL tubes	Fisher scientific	10451043	Eppendorf 3810X Polypropylene microcentrifuge tubes
ATP	Sigma-Aldrich	No. A2383	
Biopsy punch	Darwin microfluidics	PT-T983-05	0.5 mm and 3 mm diameter
Citrate-base	Sigma-Aldrich	No. 71405	
Dextran	Sigma-Aldrich	No. 31388	Mr~6,000
Direct-write optical lithography machine	Durham Magneto Optics Ltd	MicroWriter ML3 Baby	setup and software
DOPC lipid	Avanti	SKU:850375C	
F68	Sigma-Aldrich	No. 24040032	
Glass cover slip	Corning	#1, 24 x 40 mm	
Glycerol	Sigma-Aldrich	No. G2025	
Hydrochloric acid	Thermo Scientific Acros	No. 124630010	
Liss Rhod PE lipid	Avanti	SKU:810150C	
Parafilm	Sigma-Aldrich	No. P7793	
Photoresist	Micro resist technology GmbH	EpoCore 10	
Photoresist developer	micro resist technology GmbH	mr-Dev 600	
Plasma cleaner	Harrick plasma	PDC-32G	
Polydimethylsiloxane	Dow	Sylgard 184	PDMS and curing agent
Poly-L-lysine	Sigma-Aldrich	No. P7890	
Poly-L-lysine–FITC Labeled	Sigma-Aldrich	No. P3543	
Polyvinyl alcohol	Sigma-Aldrich	no. P8136	molecular weight 30,000–70,000, 87%–90% hydrolyzed
Pressure controller	Elveflow	OBK1 Mk3+	Flow controller
Scotch tape	Magic Tape Invisible Matt Tape		
Silicon wafer	Silicon Materials	0620R16002	
Spin coater	Laurell Technologies Corporation	Model WS-650MZ-23NPP	
Stainless Steel 90° Bent PDMS Couplers	Darwin microfluidics	PN-BEN-23G	
Tris-base	Sigma-Aldrich	No. 252859	
Tygon tubing	Darwin microfluidics	1/16" OD x 0.02" ID	
UV laser			365 nm wavelength

Table 3.1 :

List of chemicals, materials and machinery used in the production along with supplier details and catalogue number.

3.5 AUTHOR STATEMENT

The experiments were performed by Chang Chen and Ketan Ashok Ganar. The chapter is written and edited by Ketan Ashok Ganar, Chang Chen and Siddharth Deshpande.

3.5 ACKNOWLEDGEMENTS

We would like to acknowledge Dolf Weijers, Vera Gorelova, and Mark Roosjen for kindly providing us with YFP. S.D. acknowledges financial support from the Dutch Research Council (grant number: OCENW.KLEIN.465).

REFERENCES

1. Frezard F. Liposomes: from biophysics to the design of peptide vaccines. *Brazilian Journal of Medical and Biological Research* 1999, **32:** 181-189.
2. Monteiro N, Martins A, Reis RL, Neves NM. Liposomes in tissue engineering and regenerative medicine. *Journal of the Royal Society Interface* 2014, **11**(101)**:** 20140459.
3. Mishra H, Chauhan V, Kumar K, Teotia D. A comprehensive review on Liposomes: a novel drug delivery system. *Journal of Drug Delivery and Therapeutics* 2018, **8**(6)**:** 400-404.
4. Liu W, Hou Y, Jin Y, Wang Y, Xu X, Han J. Research progress on liposomes: Application in food, digestion behavior and absorption mechanism. *Trends in Food Science & Technology* 2020, **104:** 177-189.
5. Kamiya K, Takeuchi S. Giant liposome formation toward the synthesis of well-defined artificial cells. *Journal of Materials Chemistry B* 2017, **5**(30)**:** 5911-5923.
6. van Swaay D, DeMello A. Microfluidic methods for forming liposomes. *Lab on a Chip* 2013, **13**(5)**:** 752-767.
7. Lombardo D, Kiselev MA. Methods of liposomes preparation: Formation and control factors of versatile nanocarriers for biomedical and nanomedicine application. *Pharmaceutics* 2022, **14**(3)**:** 543.
8. Zhang H. Thin-film hydration followed by extrusion method for liposome preparation. *Liposomes: Methods and protocols* 2017**:** 17-22.
9. Filipczak N, Pan J, Yalamarty SSK, Torchilin VP. Recent advancements in liposome technology. *Advanced drug delivery reviews* 2020, **156:** 4-22.
10. Has C, Sunthar P. A comprehensive review on recent preparation techniques of liposomes. *Journal of liposome research* 2020, **30**(4)**:** 336-365.
11. Large DE, Abdelmessih RG, Fink EA, Auguste DT. Liposome composition in drug delivery design, synthesis, characterization, and clinical application. *Advanced drug delivery reviews* 2021, **176:** 113851.
12. Abkarian M, Loiseau E, Massiera G. Continuous droplet interface crossing encapsulation (cDICE) for high throughput monodisperse vesicle design. *Soft Matter* 2011, **7**(10)**:** 4610-4614.
13. Morita M, Onoe H, Yanagisawa M, Ito H, Ichikawa M, Fujiwara K*, et al.* Droplet-Shooting and Size-Filtration (DSSF) Method for Synthesis of Cell-Sized Liposomes with Controlled Lipid Compositions. *ChemBioChem* 2015, **16**(14)**:** 2029-2035.
14. Convery N, Gadegaard N. years of microfluidics. Micro and Nano Engineering. 2019; 2: 76–91.
15. Stachowiak JC, Richmond DL, Li TH, Liu AP, Parekh SH, Fletcher DA. Unilamellar vesicle formation and encapsulation by microfluidic jetting. *Proceedings of the national academy of sciences* 2008, **105**(12)**:** 4697-4702.
16. Chu LY, Utada AS, Shah RK, Kim JW, Weitz DA. Controllable monodisperse multiple emulsions. *Angewandte Chemie* 2007, **119**(47)**:** 9128-9132.
17. Pautot S, Frisken BJ, Weitz D. Engineering asymmetric vesicles. *Proceedings of the National Academy of Sciences* 2003, **100**(19)**:** 10718-10721.
18. Ota S, Yoshizawa S, Takeuchi S. Microfluidic formation of monodisperse, cell-sized, and unilamellar vesicles. *Angewandte Chemie* 2009, **121**(35)**:** 6655-6659.
19. Carugo D, Bottaro E, Owen J, Stride E, Nastruzzi C. Liposome production by microfluidics: potential and limiting factors. *Scientific reports* 2016, **6**(1)**:** 25876.
20. Deshpande S, Dekker C. On-chip microfluidic production of cell-sized liposomes. *Nature protocols* 2018, **13**(5)**:** 856-874.

21. Last MG, Deshpande S, Dekker C. pH-controlled coacervate–membrane interactions within liposomes. *ACS nano* 2020, **14**(4)**:** 4487-4498.
22. Jia H, Schwille P. Bottom-up synthetic biology: reconstitution in space and time. *Current opinion in biotechnology* 2019, **60:** 179-187.
23. Ganar KA, Leijten L, Deshpande S. Actinosomes: condensate-templated containers for engineering synthetic cells. *ACS synthetic biology* 2022, **11**(8)**:** 2869-2879.
24. Gaut NJ, Adamala KP. Reconstituting natural cell elements in synthetic cells. *Advanced Biology* 2021, **5**(3)**:** 2000188.
25. Ganar KA, Honaker LW, Deshpande S. Shaping synthetic cells through cytoskeleton-condensate-membrane interactions. *Current Opinion in Colloid & Interface Science* 2021, **54:** 101459.
26. Bashirzadeh Y, Liu AP. Encapsulation of the cytoskeleton: towards mimicking the mechanics of a cell. *Soft Matter* 2019, **15**(42)**:** 8425-8436.
27. Deshpande S, Brandenburg F, Lau A, Last MG, Spoelstra WK, Reese L*, et al.* Spatiotemporal control of coacervate formation within liposomes. *Nature communications* 2019, **10**(1)**:** 1800.
28. Love C, Steinkühler J, Gonzales DT, Yandrapalli N, Robinson T, Dimova R*, et al.* Reversible pH-responsive coacervate formation in lipid vesicles activates dormant enzymatic reactions. *Angewandte Chemie* 2020, **132**(15)**:** 6006-6013.
29. Lu T, Liese S, Schoenmakers L, Weber CA, Suzuki H, Huck WT*, et al.* Endocytosis of coacervates into liposomes. *Journal of the American Chemical Society* 2022, **144**(30)**:** 13451-13455.
30. Van de Cauter L, Fanalista F, Van Buren L, De Franceschi N, Godino E, Bouw S*, et al.* Optimized cDICE for efficient reconstitution of biological systems in giant unilamellar vesicles. *ACS Synthetic Biology* 2021, **10**(7)**:** 1690-1702.
31. Blanken D, Foschepoth D, Serrão AC, Danelon C. Genetically controlled membrane synthesis in liposomes. *Nature communications* 2020, **11**(1)**:** 4317.
32. Bouzetos E, Ganar KA, Mastrobattista E, Deshpande S, van der Oost J. (R) evolution-on-a-chip. *Trends in Biotechnology* 2022, **40**(1)**:** 60-76.
33. Kamalinia G, Grindel BJ, Takahashi TT, Millward SW, Roberts RW. Directing evolution of novel ligands by mRNA display. *Chemical Society Reviews* 2021, **50**(16)**:** 9055-9103.
34. Godino E, López JN, Foschepoth D, Cleij C, Doerr A, Castellà CF*, et al.* De novo synthesized Min proteins drive oscillatory liposome deformation and regulate FtsA-FtsZ cytoskeletal patterns. *Nature Communications* 2019, **10**(1)**:** 4969.
35. Tenchov R, Bird R, Curtze AE, Zhou Q. Lipid nanoparticles─ from liposomes to mRNA vaccine delivery, a landscape of research diversity and advancement. *ACS nano* 2021, **15**(11)**:** 16982-17015.
36. Deshpande S, Caspi Y, Meijering AE, Dekker C. Octanol-assisted liposome assembly on chip. *Nature communications* 2016, **7**(1)**:** 10447.
37. Schaich M, Cama J, Al Nahas K, Sobota D, Sleath H, Jahnke K*, et al.* An integrated microfluidic platform for quantifying drug permeation across biomimetic vesicle membranes. *Molecular pharmaceutics* 2019, **16**(6)**:** 2494-2501.
38. Schaich M, Sobota D, Sleath H, Cama J, Keyser UF. Characterization of lipid composition and diffusivity in OLA generated vesicles. *Biochimica et Biophysica Acta (BBA)-Biomembranes* 2020, **1862**(9)**:** 183359.
39. Deshpande S, Spoelstra WK, Van Doorn M, Kerssemakers J, Dekker C. Mechanical division of cell-sized liposomes. *ACS nano* 2018, **12**(3)**:** 2560-2568.
40. Jusková P, Schmid YR, Stucki A, Schmitt S, Held M, Dittrich PS. "basicles": Microbial growth and production monitoring in giant lipid vesicles. *ACS applied materials & interfaces* 2019, **11**(38)**:** 34698-34706.

41. Fletcher M, Zhu J, Rubio-Sánchez R, Sandler SE, Nahas KA, Michele LD*, et al.* DNA-based optical quantification of ion transport across giant vesicles. *ACS nano* 2022, **16**(10)**:** 17128-17138.
42. Vaezi Z, Sedghi M, Ghorbani M, Shojaeilangari S, Allahverdi A, Naderi-Manesh H. Investigation of the programmed cell death by encapsulated cytoskeleton drug liposomes using a microfluidic platform. *Microfluidics and Nanofluidics* 2020, **24:** 1-15.
43. Al Nahas K, Cama J, Schaich M, Hammond K, Deshpande S, Dekker C*, et al.* A microfluidic platform for the characterisation of membrane active antimicrobials. *Lab on a Chip* 2019, **19**(5)**:** 837-844.
44. Bao P, Paterson DA, Peyman SA, Jones JC, Sandoe JA, Gleeson HF*, et al.* Production of giant unilamellar vesicles and encapsulation of lyotropic nematic liquid crystals. *Soft Matter* 2021, **17**(8)**:** 2234-2241.
45. Yandrapalli N, Petit J, Bäumchen O, Robinson T. Surfactant-free production of biomimetic giant unilamellar vesicles using PDMS-based microfluidics. *Communications Chemistry* 2021, **4**(1)**:** 100.
46. Cama J, Al Nahas K, Fletcher M, Hammond K, Ryadnov MG, Keyser UF*, et al.* An ultrasensitive microfluidic approach reveals correlations between the physico-chemical and biological activity of experimental peptide antibiotics. *Scientific Reports* 2022, **12**(1)**:** 4005.
47. Guerzoni LP, de Goes AV, Kalacheva M, Haduła J, Mork M, De Laporte L*, et al.* High macromolecular crowding in liposomes from microfluidics. *Advanced Science* 2022, **9**(27)**:** 2201169.
48. Gonzales DT, Yandrapalli N, Robinson T, Zechner C, Tang TD. Cell-free gene expression dynamics in synthetic cell populations. *ACS synthetic biology* 2022, **11**(1)**:** 205-215.
49. Ushiyama R, Koiwai K, Suzuki H. Plug-and-play microfluidic production of monodisperse giant unilamellar vesicles using droplet transfer across Water–Oil interface. *Sensors and Actuators B: Chemical* 2022, **355:** 131281.
50. Banlaki I, Lehr F-X, Niederholtmeyer H. Microfluidic production of porous polymer cell-mimics capable of gene expression. *Cell-Free Gene Expression: Methods and Protocols* 2022**:** 237-255.

Chapter 4

Phase Separation and Ageing of Glycine-Rich Protein from Tick Adhesive

This chapter is based on

Ketan A. Ganar[1*], Manali Nandy[1*], Polina Turbina[1*], Chang Chen[1], Dennis Suylen[2], Elisa Nihoul[2], Emily Louise Pascoe[3], Stan van der Beelen[4], Leendert van den Bos[4], Constantianus J.M.Koenraadt[3], Ingrid Dijkgraaf[2§], and Siddharth Deshpande[2§]. "Phase Separation and ageing of Glycine-Rich Protein from Tick Adhesive."*bioRxiv (2023): 2023-03.*

ABSTRACT

Hard ticks feed on their host for multiple days. To ensure firm attachment, they secrete protein-rich saliva that eventually forms a solid cement cone. The underlying mechanism of this liquid-to-solid transition is not yet understood. This study focuses on the phase transitions of a disordered glycine-rich protein (GRP) that is prominent in tick saliva. We show that GRP undergoes liquid-liquid phase separation via simple coacervation to form biomolecular condensates in salty environments. Cation–π and π–π interactions mediated by periodically placed phenylalanine, tyrosine, and arginine residues are the primary driving forces that promote phase separation. Interestingly, GRP condensates exhibit ageing by undergoing liquid-to-gel transition over time and exhibit adhesive properties. Lastly, we provide evidence for protein-rich condensates in natural tick saliva. Our findings provide a starting point to gain insights into the bioadhesion of ticks, develop novel tick control strategies, and towards biomedical applications such as tissue sealants.

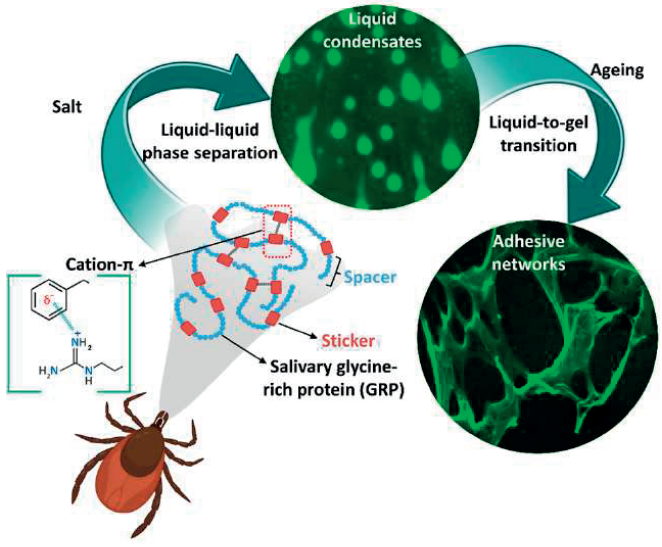

4.1 INTRODUCTION

Biological adhesives are sticky materials used by a wide variety of organisms for different purposes such as attachment, prey capture, locomotion, building, and defense[3]. The range of species that can produce bioadhesives is diverse, from bacterial biofilms and slimy garden slugs to stickleback nests and sticky spiderwebs[5]. Many animals use protein-based adhesives: sandcastle worms build reef-like mounds[7], mussels attach via proteinaceous threads[8, 9, 10] and velvet worms eject adhesive slime to entangle their prey[12]. While some bioadhesives have been studied in considerable details, knowledge on adhesive mechanisms of many others is significantly lacking. One of the unexplored and unique bioadhesives is produced by ticks, a widespread parasite of public health and economic importance[13, 14].

Ticks are arthropods that feed on their host by sucking blood over a prolonged period, usually multiple days in the case of hard ticks[15]. Importantly, the prolonged contact and transfer of saliva from the tick to the host can lead to pathogen transmission, which can result in infectious diseases in both humans and animals worldwide, notable examples being Lyme borreliosis in humans, and babesiosis, anaplasmosis, and heartwater in bovine species [16], [17]. To feed successfully, ticks first need to securely attach to the host skin, which they do so in two stages: an initial mechanical attachment, followed by bioadhesive production known as the cement cone[18] (**Figure 1a**). The mechanical attachment is achieved using the mouthparts which consist of two palps that perform sensory functions, a pair of extendable chelicerae to cut into the host tissue, and a hypostome that acts as a channel for blood as well as to penetrate the outermost layer of the epidermis[18], [19] (**Figure S4.1**). Once the hypostome has passed through the first skin layer, saliva is secreted from the salivary glands. This milky-white proteinaceous fluid has adhesive properties and undergoes a liquid-to-solid transition once exposed to air, therefore bearing the name cement[18], [20], [21]. A cement cone, resembling a wedge-shaped anchor, is formed around the incision site of the tick which strengthens attachment to the host and facilitates long feeding periods[18], [20], [21]. Adhesive production is commonly associated with hard ticks, belonging to the family Ixodidae, allowing them to remain attached to their host for up to 10 days. Thereafter, feeding begins with the formation of small blood pools, followed by intermittent ejection of saliva[18], [22]. For hydration purposes, tick saliva is also highly hygroscopic and salt-rich which helps to absorb moisture from air[22]. However, the mechanism as well as the identity of the key salivary components that are responsible for the formation of such a strong bioadhesive remains unknown.

The cement cone is protein-rich, containing tick peptides and proteins, host proteins, as well as non-peptidic molecules, exosomes, etc.[18, 22, 23]. Biochemical and bioinfor-

matic analyses have revealed that glycine-rich proteins (GRPs) are abundant in tick saliva[24, 25, 26, 27]. For example, a recent study found that 19% of the identified protein sequences from the cement cone belonged to GRPs, and the expression of GRPs significantly increased during blood feeding[28]. GRPs have been associated with various physiological functions including providing strength, insolubility and stabilization to the cement cone[18], but the mechanism by which GRPs facilitate these functions remains unknown. Glycine-rich regions are known to be commonly present in intrinsically disordered proteins (IDPs) since they can prevent protein folding due to their small size and high degree of freedom[29].

The cement cone is protein-rich, containing tick peptides and proteins, host proteins, as well as non-peptidic molecules, exosomes, etc.[18, 22, 23]. Biochemical and bioinformatic analyses have revealed that glycine-rich proteins (GRPs) are abundant in tick saliva[24, 25, 26, 27]. For example, a recent study found that 19% of the identified protein sequences from the cement cone belonged to GRPs, and the expression of GRPs significantly increased during blood feeding[28]. GRPs have been associated with various physiological functions including providing strength, insolubility and stabilization to the cement cone[18], but the mechanism by which GRPs facilitate these functions remains unknown. Glycine-rich regions are known to be commonly present in intrinsically disordered proteins (IDPs) since they can prevent protein folding due to their small size and high degree of freedom[29]. Since IDPs do not have a native state, they usually lack secondary structures and can therefore undergo large-scale conformational changes[30]. IDPs have been associated with liquid-liquid phase separation (LLPS) and the formation of biomolecular condensates because of their capacity to establish multiple interactions with neighbouring molecules due to their multivalency[31]. LLPS manifested via coacervation is driven by the interactions between multivalent biomolecules such as proteins and nucleic acids, resulting in polymer-rich droplets that are in equilibrium with a polymer-depleted phase[32]. Coacervates can be simple (single component) or complex (multicomponent) and have been found to play crucial roles in diverse cellular functions[33, 34, 35, 36]. While usually liquid-like, coacervates have been shown to undergo liquid-to-solid transition[12, 37, 38, 39, 40]. This strong link between IDPs, LLPS, and liquid-to-solid transition prompted our attention to study the possible role of tick GRPs in cement cone formation. Recently, LLPS has indeed been shown to play a role in bioadhesion via liquid-to-solid transition[5]. Various aquatic and terrestrial organisms like mussels, sandcastle worm, spiders, and velvet worms have been shown to utilize LLPS to produce strong adhesives under specific environmental triggers such as cross-linking, pH changes, and evaporation[7, 9, 10, 12, 39, 41, 42, 43]. Once deposited into the host skin, tick saliva is also subjected to various biological triggers: increased local concentrations of salt and salivary proteins, likely aided by evaporation-induced water loss during the secretion, together with a

significant temperature rise and a pH drop[22, 27, 44]. Interestingly, all these triggers are known to induce LLPS of proteins[32, 34, 38].

In this study, we provide the first experimental evidence that a tick GRP present in the saliva of *Ixodes scapularis* (Uniprot: Q4PME3) undergoes LLPS in the form of simple coacervation and forms GRP-rich condensates. Instead of protein extraction from the cement cone, which is very difficult due to the insolubility of cement cones and the harsh conditions required to isolate the proteins[5, 45], we use solid-phase peptide synthesis (SPPS) and native chemical ligation (NCL) to synthesize GRP, allowing us to investigate its biochemical properties under controlled *in vitro* conditions. Through structure prediction analysis, we show that GRP is predominantly a disordered protein and has a high propensity of undergoing LLPS. Using a combination of fluorescence microscopy and microfluidics, we demonstrate that GRP undergoes evaporation- and salt-induced LLPS, resulting in simple coacervates, mediated primarily by cation–π and π– π interactions, with a characteristic fluid-like behaviour. We further show that these condensates age over time to form solid-like aggregates and exhibit adhesive properties. Finally, we show evidence for the presence of protein-rich condensates in natural saliva from the closely related *Ixodes ricinus* tick. In conclusion, our work illustrates the ability of tick GRP to undergo liquid-to-solid transition through LLPS. These findings can shed further light on the poorly studied cement cone formation and may partly explain the role of GRPs in the saliva in the form of providing necessary adhesive properties for a successful attachment to the host. The obtained knowledge may become relevant for exploring chemicals that hinder tick attachment, consequently aiding the prevention and management of tick-associated diseases. Considering the close interactions of the cement cone with biological tissues, the findings may also prove useful for biotechnological applications, such as medical sealants.

4.2 RESULTS AND DISCUSSION

We selected one of the well-identified as well as amenable to chemical synthesis GRPs present in tick saliva (**Figure 4.1a**), simply known as GRP (Uniprot: Q4PME3) and refer to it as such here onwards. GRP is a relatively short protein containing 96 amino acid residues. The first 19 N-terminal amino acids (sequence: ^{1}MNRMFVLAATLALVGMVFA^{19}) constitute the signal peptide necessary for its translocation. The remaining 77 amino acids constitute the mature GRP sequence (20–96) and we refer to it as tick-GRP77 here onwards (to simplify things, amino acid locations within tick-GRP77 are renumbered, i.e., 1st position refers to the 20th amino acid from GRP and 77th is the 96th one). As the name suggests, tick-GRP77 is rich in glycine residues (≈26%) with most of them located in the middle of the sequence

(13–63). Further sequence composition analysis by PSIPRED[46] revealed a large fraction of other non-polar (≈44%; mainly alanine and proline) and polar (≈36%; mainly glutamic acid, arginine, and glutamine) amino acids. In comparison, the fraction of hydrophobic (≈7%; valine and isoleucine) and aromatic (≈9%; tyrosine and phenylalanine) residues was relatively small (**Figure 4.1b**). We also checked the GRP structure via Alphafold[47], an algorithm capable of computationally predicting protein structures. Indeed, the GRP sequence showed two distinct regions (**Figure 4.1c**): The N-terminus of GRP, corresponding to the signal peptide, shows an α-helical conformation. However, the remaining sequence (corresponding to tick-GRP77) gave a very low prediction score, hinting at a lack of any kind of secondary structure. IUPred3 algorithm [48], which predicts IDRs, also determined the entire tick-GRP77 to be completely disordered using long disorder mode (score above 0.5 throughout the sequence) while the short disorder mode predicted prominent disorder at both the termini (**Figure 4.1d**). Multiple other algorithms also predicted the tick-GRP77 amino acid sequence to be primarily disordered (**Figure S4.2**). We further evaluated the sequence using CIDER[49], which plots the fraction of negatively charged versus positively charged residues. Based on this, proteins can be grouped into five different regions according to the diagram of states (**Figure S4.3**). The tick-GRP77 sequence falls in the region of weak polyampholytes and polyelectrolytes, similar to many well-characterized phase-separating IDR-containing proteins like FUS[50] and viral nucleocapsid[51]. Cumulatively, our bioinformatic analysis indicated a strong inclination for tick-GRP77 to undergo LLPS.

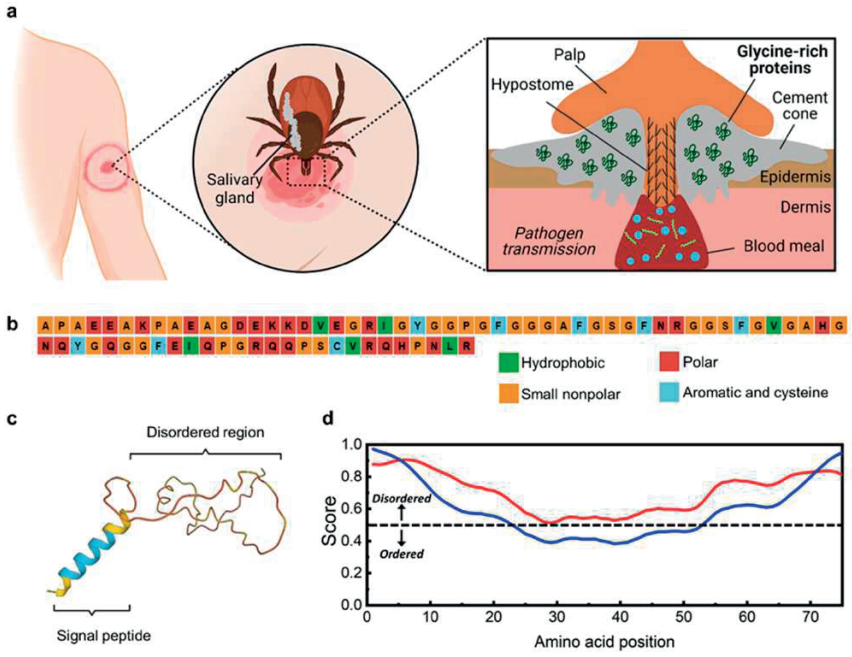

Figure 4.1: Glycine-rich protein (GRP) present in the tick saliva is intrinsically disordered and shows a high propensity for LLPS. (a) Schematic representation showing the consequence of a tick bite. The tick inserts its hypostome into the host epidermis and secretes a protein-rich saliva, abundant in glycine-rich proteins (GRPs). The saliva undergoes liquid-to-solid transition forming a hard cement cone, allowing the tick to feed on the host over several days and facilitating pathogen transmission (the shown "bull's eye" rash is typical in case of Borrelia infection). (b) Amino acid composition of tick-GRP77 shows a high proportion of non-polar amino acids (44%, out of which 26% are glycine). (c) AlphaFold correctly predicts the N-terminal signal peptide of GRP as an α-helix, while the rest of the sequence (tick-GRP77) remains unstructured, indicating a disordered region. (d) IUPred3 long disorder mode (red line) scores the entire tick-GRP77 sequence above 0.5, while short disorder score (blue line) shows prominent disorder near the termini, overall indicating tick-GRP77 as a highly disordered protein.

4.2.1 Tick-GRP77 undergoes liquid-liquid phase separation via simple coacervation

Upon confirming the disordered nature of tick-GRP77 via structure prediction analysis, we proceeded with gathering experimental evidence for its LLPS behavior. We synthesized tick-GRP77 via SPPS and NCL (see Materials and Methods for details). Since the secretion of tick saliva locally enriches its components in the host tissue, aided by water loss through evaporation, we mimicked this via a straightforward droplet evaporation assay (**Figure 4.2a**). We deposited a small sessile droplet (2 µL) of buffered tick-GRP77 solution (16-500 µM) on a glass slide and let it evaporate at ambient temperature. The non-uniform evaporation of the droplet led to what is commonly known as the coffee-ring effect[52], concentrating tick-GRP77 at the droplet

boundary. Briefly, higher evaporation rate at the air-water-glass triple contact point (the droplet boundary) results in fluid flow towards the boundary to replenish the depleting liquid, bringing along the tick-GRP77 molecules, increasing their concentration at the boundary. For better visualization, we added 5 mol% fluorescently labelled tick-GRP, OG488-GRP77 (fluorescent label: Oregon Green 488; see Materials and Methods for details), to the sample. **Figure 4.2b** shows a time-lapse, near the droplet boundary, of a 32 μM tick-GRP77 solution in phosphate buffer saline (PBS; 137 mM NaCl, 2.7 mM KCl, 8 mM Na2HPO4, and 2 mM KH2PO4 , pH 7.4) evaporating over time, while **Figure 4.2c** shows the same time-lapse in fluorescence. The droplet initially spread over the hydrophilic glass slide and after approximately 30 seconds, an outer boundary was pinned due to the rough glass surface.

A rapid non-homogenous distribution of tick-GRP77 due to the coffee-ring effect was evident in fluorescence imaging, along with intense fluorescence intensity in the region between the contact line and the droplet boundary, indicating a high local concentration of the protein (**Figure 4.2c**). We defined ti as the time interval between droplet deposition and contact line pinning. Interestingly, within a minute after the contact line was established ($t_i \approx$ 15 min), we observed the sudden appearance of numerous micron-sized droplets near the contact line (**Figure 4.2b-right**), hinting at LLPS of tick-GRP77 by surpassing the critical concentration. The GRP-rich nature of these droplets was evident from the corresponding fluorescence images (**Figure 4.2c-right**). Repeating the evaporation assay on a surface-passivated glass slide with 5% w/v polyvinyl alcohol (PVA; see Materials and Methods for details) gave a clearer picture of micron-sized, spherical tick-GRP77 condensates (**Figure 4.2d**).

The region between the contact line and droplet boundary is an inverted phase, where the continuous phase is the protein-rich condensed phase, interspersed with dilute phase droplets. This likely happens because this very thin region rapidly accumulates a high-volume fraction of the protein, and has been observed for other evaporating condensate samples[53]. Further confirmation of this dense continuous phase comes from the fact that we observed fusion of tick-GRP77 condensates with the inverted phase, and a closer look also revealed GRP-depleted dilute phase droplets (**Figure S4.4**), similar to earlier reports[53].

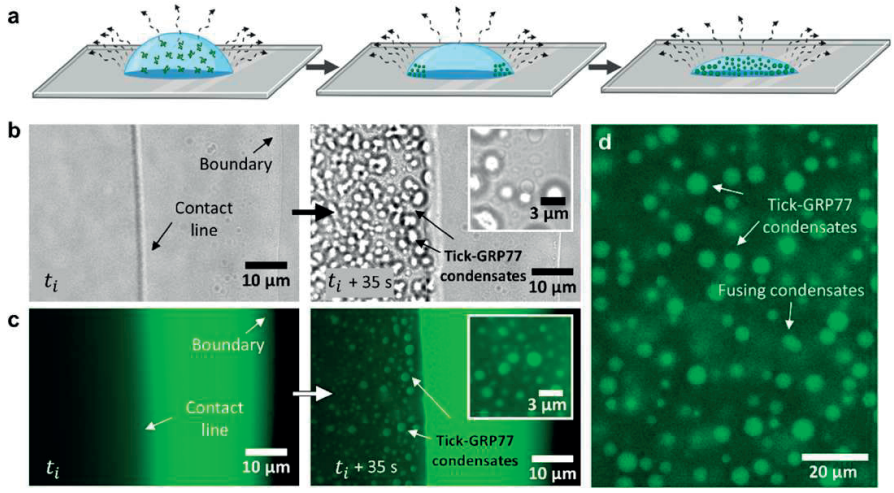

Figure 4.2: Tick-GRP77 undergoes liquid-liquid phase separation via simple coacervation to form liquid-like condensates. (a) Schematic of the droplet evaporation assay, where a droplet of a buffered tick-GRP77 solution is allowed to evaporate at room temperature, continuously increasing the protein concentration at the droplet boundary. (b-c) Evaporation of a 2 µL tick-GRP77 droplet leads to the formation of spherical condensates near the contact line ($ti \approx 15$ min) and the condensate formation rapidly spreads inward. Bright-field images are shown in (b), with corresponding fluorescence images in (c). The latter also revealed a saturated GRP region between the droplet boundary and the contact line. (d) Evaporation of tick-GRP77 on a surface-passivated glass slide showing numerous spherical tick-GRP77 condensates. Starting concentration of tick-GRP77 was 32 µM in PBS (pH 7.4) for all the experiments. In case of fluorescence imaging, the samples were doped with 5 mol% OG488-GRP77.

As coacervation is a concentration-dependent process, one would expect the time until the onset of coacervation to be dependent on the initial protein concentration. Indeed, increasing the initial protein concentration from 16 to 128 µM gradually decreased the time required for the onset of coacervation from 12.7 ± 0.7 (mean ± standard deviation) min to 7.5 ± 0.9 min, at constant initial salt concentration (PBS, pH 7.4; **Figure S4.5**). To further validate the tick-GRP77-specific nature of the formed condensates, we performed several negative controls (**Figure S4.6**): Evaporation of tick-GRP77 solubilized in 140 mM NaCl led to similar condensate formation, suggesting lack of salt-bridging between cationic amino acids and phosphates as the key driving force for phase separation. However, tick-GRP77 solubilized in pure water did not lead to the formation of condensates, suggesting a clear role of salts in promoting phase separation of tick-GRP77, probably through charge screening and allowing favorable intermolecular interactions to take place. Using bovine serum albumin (a globular protein without any disordered regions) in PBS buffer did not form any condensates but only salt crystals. Similarly, evaporation of only buffer solution (PBS at pH 7.4) did not result in any kind of LLPS behavior.

One of the hallmark properties of condensates is their ability to form spherical droplets which eventually coalesce and relax into a bigger droplet. This is due to the surface energy minimization and the rapid reorganization of molecular interactions within the liquid droplet[33, 54]. We readily observed numerous fusion events between tick-GRP77 condensates upon physical contact with each other, followed by their relaxation into a bigger spherical condensate (**Figure 4.3a**). Tracking the aspect ratio (major to minor axis ratio) of the fusing droplets showed an exponential relaxation to a sphere[55, 56]. **Figure 4.3b** shows a typical example of the evolution of aspect ratio with a fitted exponential decay $A = 1 + 1.15e^{-0.36t}$; $R^2 = 0.99$, giving a relaxation coefficient $\tau \approx 3$s ($n = 16$). Following the relation $\tau \approx l(\eta/\gamma)$, where l is the average radius of the fusing droplets, η is the viscosity of the droplet, and γ is the surface tension, a plot of τ against l gave us an inverse capillary velocity (η/γ) of 0.92 s/μm (**Figure 4.3c ;** $n = 16$; $R^2 = 0.47$; see Materials and Methods for details), implying micrometer-sized tick-GRP77 condensates behaved like liquid on a timescale longer than a second[56].

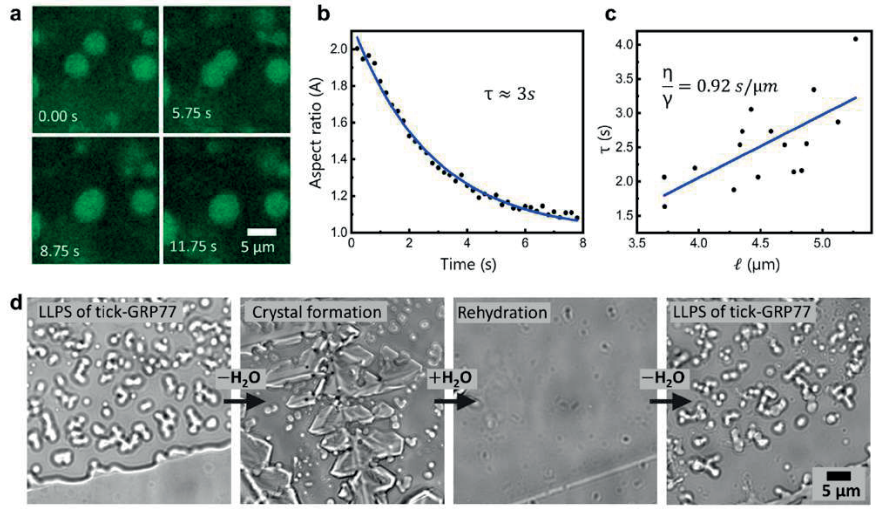

Figure 4.3:

(a) Two similar-sized condensates coalescing and relaxing into a bigger condensate over a time span of a few seconds. (b) A typical example showing the change in the aspect ratio as a function of time during a fusion event. The blue line shows an exponential decay fit (R2 = 0.99), giving the fusion timescale, $\tau \approx 3$ s. (c) A linear fit for the decay time (τ) against the characteristic length scale (l) for several fusion events (n = 16) gives the inverse capillary velocity η/γ of 0.92 s/μm (R2 = 0.47). (d) phase-separated solution eventually dries out forming salt crystals. However, rehydration of the dried sample with pure water completely resolubilizes the salt crystals as well as the condensates. Evaporation of the resolubilized sample again leads to LLPS demonstrating the reversibility of the phase separation process. Starting concentration of tick-GRP77 was 32 μM in PBS (pH 7.4) for all the experiments. In case of fluorescence imaging, the samples were doped with 5 mol% OG488-GRP77.

Another key property of LLPS is its reversible nature, at least over short time scales. We checked this by repeating the above-mentioned droplet evaporation assay (32 μM GRP in PBS, pH 7.4) but then immediately rehydrating the sample to see its effect on the condensates. As expected, we observed the formation of GRP condensates and after complete evaporation, the sample crystalized due to the presence of salts (**Figure 4.3d**). However, upon rehydrating the crystalized sample with 2 μL of pure water, we immediately observed complete re-solubilization not only of the crystals but also of the GRP condensates. This clearly demonstrated the reversible nature of the LLPS process. Upon the second evaporation cycle, GRP condensates reformed in a similar manner. In conclusion, tick-GRP77 was observed to undergo simple coacervation and form viscous liquid droplets.

4.2.2 Phase separation of tick-GRP77 is driven primarily by cation-pi and pi-pi interactions.

To identify the protein regions responsible for phase separation and the underlying intermolecular interactions, we experimented with two distinct fractions of tick-GRP77: a 32-amino acid-long N-terminus (20–51) and the remaining 45-amino acid-long C-terminus (52–96), as depicted in **Figure 4.4a**. Both fractions are predicted to be disordered (**Figure 4.1d)** and have comparable glycine contents, 9 residues (28%) and 11 residues (24%) respectively. One clear difference is that the N-terminus is rich in acidic amino acids, giving it a net negative charge of -3.4 at pH 7.4. On the contrary, the C-terminus is relatively rich in basic amino acid residues giving it a net positive charge of 2.5 at pH 7.4 (**Figure 4.4b**). Conducting droplet evaporation assays for both fractions under identical conditions (50 μM solutions in PBS, pH 7.4) revealed a significant difference between the onset time of coacervation for the two termini. The N-terminus showed a similar timescale as tick-GRP77 with respect to the onset of coacervation, with a $t_i \approx$ 13 minutes (condensates at t = 14 min are shown in **Figure 4.4c**). On the other hand, the C-terminus underwent phase separation immediately without formation of a contact line (condensates at t = 4 min are shown in **Figure 4.4d**). C-terminus condensates showed a tendency to wet the untreated glass surface (**Figure 4.4d**) but passivating the surface with 5% w/v PVA clarified the formation of spherical condensates, with OG488-GRP77 (5 mol%) readily partitioning within them (**Figure 4.4e**). Despite having equal number of cationic amino acids, the tendency of these two fractions to coacervate is drastically different under same salt concentrations. This indicates salt-bridging between phosphate ions and cationic amino acids to not be a dominant mechanism for coacervation.

Apart from electrostatic interactions, π-π, cation-π, hydrophobic, and hydrogen bonding also play important roles in the formation of condensates[31]. **Figure 4.4a** shows that the N-terminus contains four cationic (three lysine (K) and one arginine

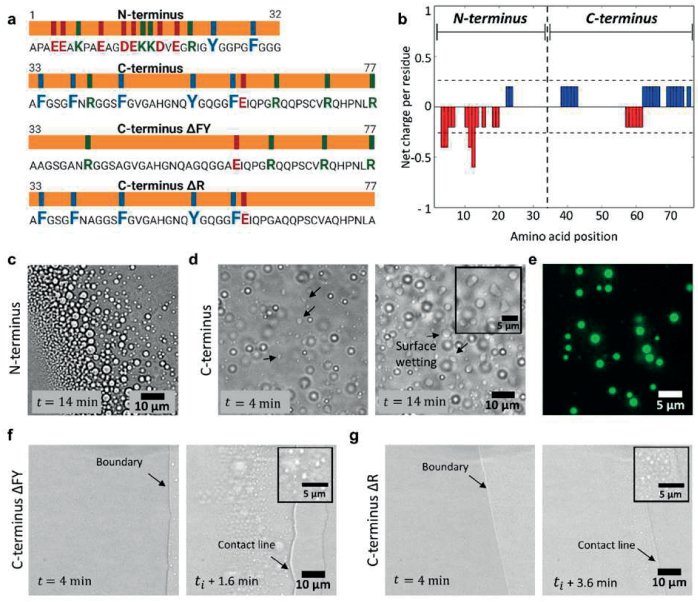

Figure 4.4: Cation-π and π-π interactions are the key drivers of phase separation of tick-GRP77. (a) Four distinct fractions of GRP77: N-terminus (1–32), C-terminus (33–77), C-terminus mutant without aromatic amino acids (*Δ* FY mutant), and C-terminus mutant without arginine residues (*Δ* R mutant). They all have a similar glycine content but varying basic (green), acidic (red) and aromatic (blue) amino acid residues. (b) Net charge per residue as a function of amino acid position for the two termini. The N-terminus is strongly negatively charged while the C-terminus is moderately positively charged. (c) Droplet evaporation assay of the N-terminus leads to phase separation and formation of micron-sized condensates on a similar time scale as that of GRP77 ($ti \approx 13$ min). (d) Droplet evaporation assay of the C-terminus leads to much quicker phase separation ($ti \approx 3$ min). The formed condensates readily wet the glass surface (e) Performing an evaporation assay on PVA-passivated glass slide prevented surface wetting leading to the formation of spherical C-terminus condensates. OG488-GRP77 (5 mol%) readily partitioned in the condensates. (f) Droplet evaporation assay of the *Δ* FY mutant did not lead to phase separation at early time point (t = 4 min) but weak phase separation was observed later (ti+1.6 min) ($ti \approx 7$ min for ΔFY mutant). (g) Droplet evaporation assay of the *Δ* R mutant did not lead to phase separation at early timepoint (t = 4 min) and only very weak phase separation was observed at ti +3.6 minutes (ti ≈ 7 min for ΔR mutant). Starting peptide concentrations were 50 µM for all the panels. All the experiments were performed in PBS, pH 7.4.

(R)) and two aromatic (one tyrosine (Y) and one phenylalanine (F)) residues. On the other hand, the C-terminus contains four cationic (all R) and five aromatic (four F and one Y) residues. Thus, the C-terminus can form extensive cation-π interactions compared to the N-terminus. Furthermore, the aromatic amino acids in the C-terminus are interspersed and separated by small groups of non-aromatic units which can be compared to the spacer-and-sticker model and capable of forming π-π interactions[57]. The five aromatic residues are fairly well-spaced and such equally spaced aromatic residues have been proposed to form liquid condensates[58]. Previous

reports also suggest that simple coacervation is more favorable if the protein contains relatively hydrophobic stickers and polar spacers[59], which indeed seems to be the case for the C-terminus with multiple serine, asparagine, and glutamine residues. Finally, arginine-glycine domains have been reported to form cation-π interactions with phenylalanine and thus promote LLPS[60, 61]. To test if aromatic amino acids (F and Y) play an active role in driving phase separation, we synthesized a mutant variant of the C-terminus by replacing F and Y (ΔFY mutant) with a non-polar amino acid alanine (A), keeping the length of the terminus same as that of wild type. Evaporation of 2 µL sessile droplet of ΔFY mutant (50 µM in PBS) showed no phase separation after 4 minutes as observed for the wild type (**Figure 4.4f**) and only weak phase separation was observed thereafter ($t_i \approx$ 7 minutes, condensates at t_i + 1.6 minutes are shown in **Figure 4.4f**). Increasing the initial concentration to 100 µM marginally reduced t_i to 6.5 minutes and led to normal phase separation (**Figure S4.7a**)**.** This suggests that the aromatic amino acids capable of forming π–π interactions are crucial to induce phase separation of C-terminus but nonetheless not strictly necessary at high protein concentrations.

On the other hand, arginine (prominent in the C-terminus) has been proven to be relatively more hydrophobic than lysine (prominent in the N-terminus) due to the presence of π-electron-rich guanidium group which allows them to form π-π bonds along with cation-π bonds[62]. To test the importance of arginine in promoting phase separation, we replaced R residues in the C-terminus with A (ΔR mutant). Similar to the ΔFY mutant, evaporation of 2 µL sessile droplet of 50 µM of ΔR mutant showed no sign of phase separation after 4 minutes (**Figure 4.4g**) and very weak phase separation was observed subsequently ($t_i \approx$ 7 minutes, condensates at t_i+ 3.6 minutes are shown in **Figure 4.4g**). Even after increasing the initial concentration to 100 µM, ti was reduced to 4.8 minutes, but formation of condensates was negligible (**Figure S4.7b**). This indicates that R plays an even more important role driving GRP phase separation through cation–π interactions with F and Y. Together, ΔFY and ΔR mutants clearly indicate that lack of these amino acids significantly weakens the phase separation process. Comparing the two mutants, it is evident that presence of both aromatic amino acids (F and Y) and arginine (R) are needed for optimum phase separation, and cation-π interactions, assisted by π–π interactions are the dominant forces in driving phase separation of tick-GRP77.

We further carried out chemical disruption experiments to probe the role of hydrogen bonding and hydrophobic interactions in the coacervation process. We first tested the role of hydrogen bonding using urea, which efficiently forms hydrogen bonds with the amide moieties[63]. We used the droplet evaporation assay for both termini (50 µM in PBS at pH 7.4) and added 2 M urea solution (0.3 µL to ≈ 1 µL droplet, so final

urea concentration ≈ 0.5 M) as soon as the condensates were formed. Microscopic visualization showed both N- and C-terminus condensates immediately dissolved upon urea addition (**Figure S4.8a**), indicating an active participation of hydrogen bonding between the peptide backbone of GRP as well as amino acid residues such as histidine and tyrosine[64]. To check the role of hydrophobic forces in driving LLPS, we exposed N- and C-terminus condensates (50 μM solutions in PBS at pH 7.4) to 1,6-hexanediol (1,6-HD) which is widely used to dissolve liquid condensates, likely by disrupting the hydrophobic protein-protein interactions[65]. We again utilized the droplet evaporation assay and 1,6-HD was added as soon as the condensates formed. We observed that N-terminus condensates dissolved already after addition of 0.5% w/v 1,6-HD (0.3 μL 1,6-HD added to ≈ 1 μL droplet, so final 1,6-HD concentration ≈ 15 mM), while C-terminus condensates remained unaffected until 1.5% w/v 1,6-HD (final 1,6-HD concentration ≈ 40 mM) and dissolved completely only at 5% w/v (final 1,6-HD concentration ≈140 mM) (**Figure S4.8b**). These results suggest that along with cation-π, additional hydrophobic interactions like π-π also actively participate in the LLPS of C-terminus and thus requires more 1,6-HD to disrupt sufficient interactions.

Based on these independent investigations of N- and C-termini, mutant studies, chemical disruption experiments, and previous studies[57, 58, 59, 62, 64, 65], we conclude that both cation-π interactions and π-π stacking involving aromatic amino acids and arginine residues are important for the phase transitioning of tick-GRP77. The observed delay in the initiation of coacervation for the N-terminus, compared to wild type C-terminus, can be attributed to the lack of these interactions as well as the electrostatic repulsion between negatively charged amino acid residues. One can thus look at the C-terminus side of tick-GRP77 as the key promoter of LLPS while the N-terminus side acting as a regulator due to its high solubility and charge repulsion delaying the LLPS process.

4.2.3 Tick-GRP77 forms liquid condensates in presence of phosphate salts.

Tick saliva is salty and hygroscopic which helps ticks to absorb moisture to stay hydrated[66]. Additionally, tick saliva also contains enzymes like apyrase[67] and acid phosphatase, which can increase local phosphate concentration through adenosine triphosphate (ATP) degradation. Studies have reported that kosmotropic ions (HPO42-, SO42-, etc.) facilitate LLPS by having strong bonding interactions with water molecules, thereby decreasing protein solubility, and promoting phase separation[68, 69]. Given our previous observation that pure GRP solution did not undergo LLPS and to test the effect of kosmotropic salts on tick-GRP77 phase transition, we chose disodium hydrogen phosphate (Na2HPO4) salt, mimicking the potential inorganic phosphate

build-up at the site of the cement cone. Indeed, addition of 1 M Na2HPO4 to 63 µM and 125 µM tick-GRP77 solutions led to instant coacervation. We tested several different GRP concentrations and incubation times up to several hours to obtain a phase diagram (**Figure 4.5a, Figure S4.9b**). As can be seen, a short incubation time of 1.5 hours at room temperature (22 °C) was enough to form condensates also at much lower concentrations of 16 µM and 31 µM. Concentrations below 16 µM did not result in condensation even after 5.5 hours, and at lower Na2HPO4 concentrations (0.5 M), we did not observe immediate condensation, but only after several hours of incubation and at high GRP concentrations (>63 µM) (**Figure S4.9a**)**.** While these phosphate concentrations needed to induce LLPS might seem too high to be biologically relevant, it should be noted that our *in vitro* experiments are conducted in highly dilute environments and at relatively low GRP concentrations (~100 µM). The tick saliva is expected to contain high amount of GRPs and is a crowded environment due to the presence of other biomolecules. We mimicked such a crowded environment, which is known to promote phase separation, by the addition of polyethylene glycol (PEG) molecules. We observed instant phase separation at much lower concentrations of phosphates in crowded conditions (**Figure 4.5b**). For example, 5% w/v PEG (8 kDa) led to instant LLPS of 125 µM GRP77 in presence of 0.5 M phosphate, while further increasing the PEG concentration to 7.5% w/v reduced the critical phosphate concentration for phase separation to 0.25 M, a realistic salt concentration range.

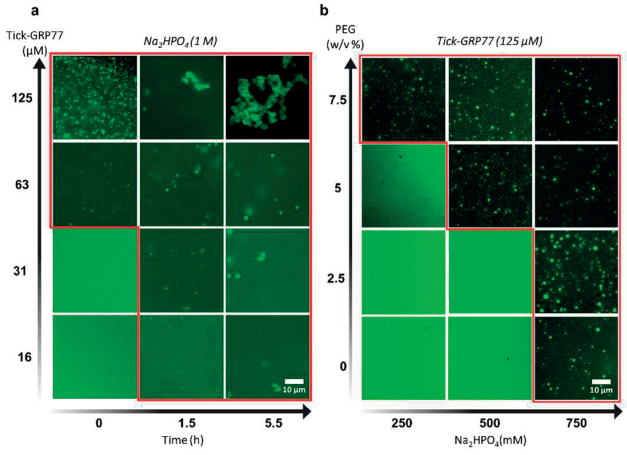

Figure 4.5: Tick-GRP77 forms condensates in presence of phosphate salts.

(a) A phase diagram showing LLPS behavior of tick-GRP77 in presence of 1 M Na2HPO4 as a function of protein concentration and incubation time. The red region indicates the condensation regime: ≥63 µM tick-GRP77 resulted in instant coacervation, whereas for lower concentrations, phase separation was observed after 1.5 h incubation at room temperature. (b) A phase diagram demonstrating that addition of crowding agents (PEG, 8 kDa) drastically lowers the critical salt concentration required for the onset of LLPS of 125 µMtick-GRP77.

To further clarify the instant nature of the coacervation, we performed flow-focusing experiments using microfluidic devices. A key feature of microfluidic systems is their laminar flow[70] owing to the low Reynolds number[71], allowing strictly diffusion-based mixing between the co-flowing fluid streams. We used a lab-on-a-chip flow-focusing device, allowing the GRP and salt streams to meet and co-flow together without mixing (see Materials and Methods for details; **Figure S4.10**). GRP solution (63 μM in pure water; 5 mol% OG488-GRP77) was injected in the inner aqueous channel and 2 M Na2HPO4 solution was injected in outer aqueous channels, forming two sharp tick-GRP77-Na2HPO4 interfaces at the junction (**Figure 4.6a; top left**). We observed immediate formation of tick-GRP77 condensate droplets at the interface, which adhered to the channel walls and continuously increased in their size as more and more condensate phase got accumulated (**Figure 4.6a; fluorescence panels**). A line profile perpendicular to the interface shows two clear fluorescence intensity peaks at the interfaces, clarifying the salt-induced condensation (**Figure 4.6b**). The liquid nature of these condensates became more evident further down the channel (approximately 500 μm downstream of the junction) where the condensate droplets wetting the channel walls were deformed by the fluid flow into tear-shaped droplets (**Figure 4.6c**). This made it clear that the formed structures are not protein aggregates or precipitates, but phase separated liquid droplets.

4.2.4 Tick-GRP77 condensates undergo liquid-to-gel transition.

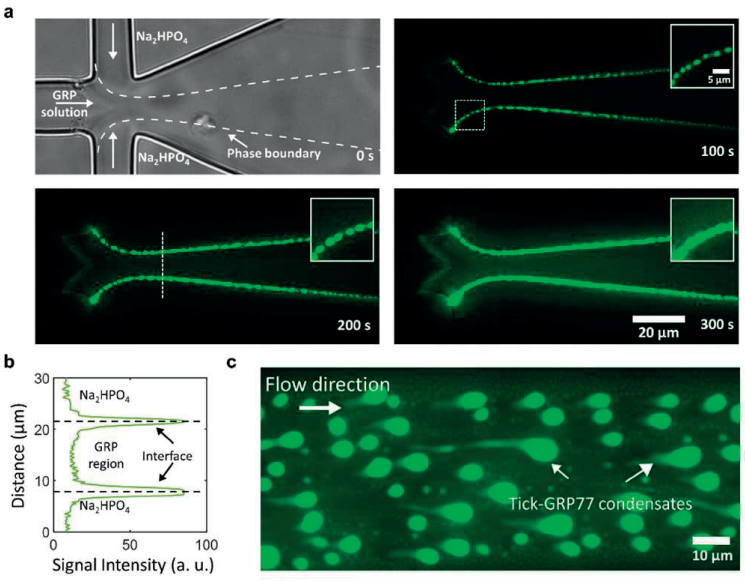

Figure 4.6: Microfluidic evaluation of tick-GRP77

(a) Left top: Bright-field image showing a flow-focusing junction of the microfluidic device. The inner stream containing 63 µM tick-GRP77 in pure water is focused by two streams of 2 M Na2HPO4. As the three streams flow side-by-side, GRP condensates are observed to form exclusively at the GRP-salt interface. The condensates wet the channel wall and become bigger over time.(b) A fluorescence intensity plot (corresponding to the dotted line in c) show the intensity profile across the interface of GRP-salt streams. (c) GRP condensates stuck to the channel walls downstream of the junction are deformed into tear-shaped droplets because of the fluid flow, indica ing their liquid-like nature.

Natural tick saliva eventually undergoes a liquid-to-solid phase transition to form a hard cement cone. We observed several instances in our experiments which indicate that LLPS may be an intermediate stage in this transition. Conducting the droplet evaporation assay using high initial tick-GRP77 concentration (initial concentration 500 µM in PBS, pH 7.4) on a hydrophobic glass slide not only led to condensate formation, but the formed condensates fused together to form network-like structures (**Figure 4.7a**). A time-lapse showing an example of a fiber formation leading to an interconnected network of tick-GRP77 condensates can be seen in **Figure 4.7b**. On similar lines, a network composed of stretched sheets and fibers adhering to a PVA-coated glass surface was obtained during an evaporation experiment, as shown in **Figure 4.7c**. These examples point to the transition of liquid condensates into viscoelastic gel-like networks on solid surfaces.

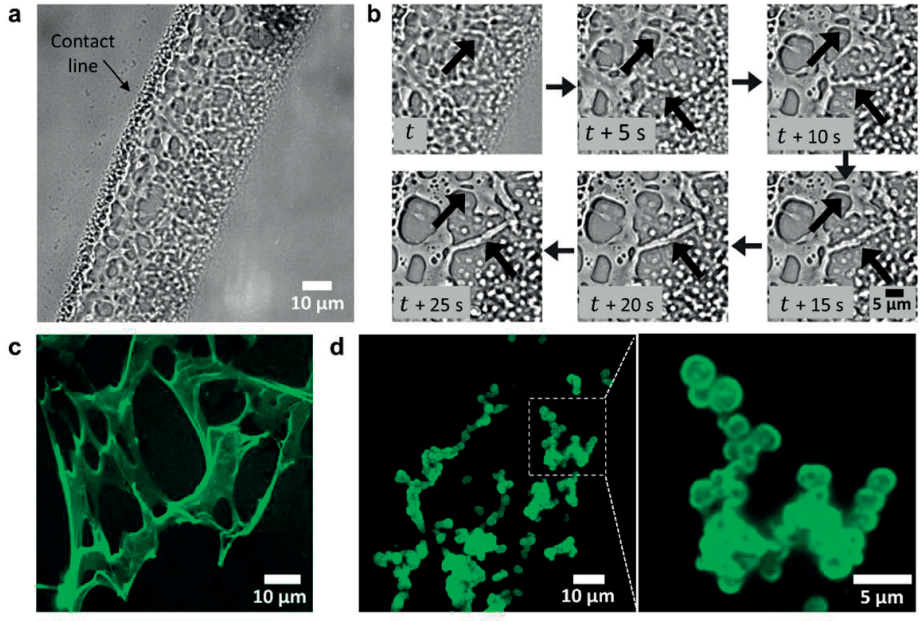

Figure 4.7: GRP condensates form viscoelastic networks and solid-like aggregates

(a)Droplet evaporation assay of a concentrated tick-GRP77 solution (500 µM in PBS, pH 7.4) resulted in the formation of condensate fibers, leading to interconnected gel-like networks. (b) Time-lapse showing the assembly of the condensates into fiber-like structures. Two such events are indicated by black arrows. (c) Fluorescence image of an interconnected stretched network formed during evaporation assay of tick-GRP77 (32 µM in 5-times concentrated PBS, pH 7.4) on a PVA-passivated glass slide. (d) Incubating tick-GRP77 solution (125 µM) in 1 M Na2HPO4 for 5.5 hours at room temperature formed stable condensate clusters, with complete arrest of coalescence. The zoom-in shows individual condensates physically connected to each other without undergoing fusion.

More solid-like structures were observed during salt-induced coacervation when using a high concentration of GRP77 (125 µM) over longer incubation times (5.5 hours). Here, the coalescence of the condensates was clearly arrested, resulting in stable grape-like clusters (**Figure 4.7d**). To verify the solidification or the ageing of GRP condensates over time, we performed fluorescence recovery after photobleaching (FRAP) experiments (125 µM tick-GRP77 in 1 M Na2HPO4). A comparative FRAP study was conducted on freshly prepared condensates (0.5 hours after preparation; **Figure 4.8a top**) and older samples (18 hours of incubation; **Figure 4.8a bottom).** We photobleached a small region within the condensates (see Material and Methods for details) and recorded the recovery of the fluorescent intensities. We quantified the fluorescence recovery over time for both freshly prepared (n = 6) and aged (n = 4) samples which revealed two important findings (**Figure 4.8b**). First, the post-

bleaching fluorescence intensity did not show full recovery in both the cases which shows the arrested motion of GRP molecules within condensates already in early stages and their apparent viscoelastic behavior.
Secondly, fresh samples showed much more recovery (≈ 49%) compared the fluorescence recovery of aged samples shows further reduction in the fraction of mobile phase over time and the transformation from liquid to a solid-like state. We fitted the normalized intensity $I(t)$ with an exponential function, $I(t) = A(1 - e^{-t/\tau})$, where A and τ indicate the amplitude of recovery and the relaxation time,respectively[56, 72]. For the fresh sample, we obtained a relaxation time, τ_{fresh} = 160 s, with the diffusion coefficient of OG488-GRP (D_{app}) in the order of ~2.2 × 10^{-3}μm^2/s (see Material and Methods for details). Using Stokes-Einstein relation $D_{app} = \frac{k_bT}{6\pi\eta R'}$, where k_bT is the thermal energy scale, η is the droplet viscosity, and R is the hydrodynamic radius of OG488-GRP77 (~2.5 nm for an unfolded 7.8 kDa protein[73]), we estimated the condensate viscosity to be ~42 Pa.s. Plugging the value into the inverse capillary velocity η/γ led to the estimation of the interfacial tension, γ ~46 μN/m, similar to the very low values reported for macromolecular liquids[74] as well as protein condensates[55]. Thus, microscopic and FRAP analysis together demonstrated tick-GRP77 condensates to be highly viscous liquids with ultralow interfacial tension, capable of forming viscoelastic networks and exhibiting ageing over the course of a few hours. This liquid-to-gel transition is highly relevant to the tick cement cone formation that also takes place over several hours[18].

We further explored whether GRP77 condensates exhibited adhesive properties. For this, we carried out force measurements on air-dried GRP77 condensates (induced in presence of 1 M Na2HPO4) using a JPK ForceRobot 300 AFM designed for force spectroscopy (see Materials and Methods for details). The AFM tip was first approached towards the surface followed by retraction (as sketched in **Figure 4.8c**), and the subsequent force-distance (FD) curves were measured (**Figure 4.8d**). In case of an adhesive substrate, tip retraction will lead to an adhesive force, allowing the work of adhesion (W_{adh}) to be measured from the area under the curve of the retracted FD curves (n = 3). The inset in **Figure 4.8d** shows the FD curves on a bare silicon substrate (n = 3). The non-adhesive silicon substrate gave us a base value of W_{adh} = 7.34 × 10^{-18}J. On the other hand, W_{adh} for the tick-GRP77-coated surface was measured to be 4.39 × 10^{-14}J, nearly four orders of magnitude higher. These measurements clearly indicate the highly adhesive nature of GRP77 condensates, which could be playing a crucial role in tick adhesion.

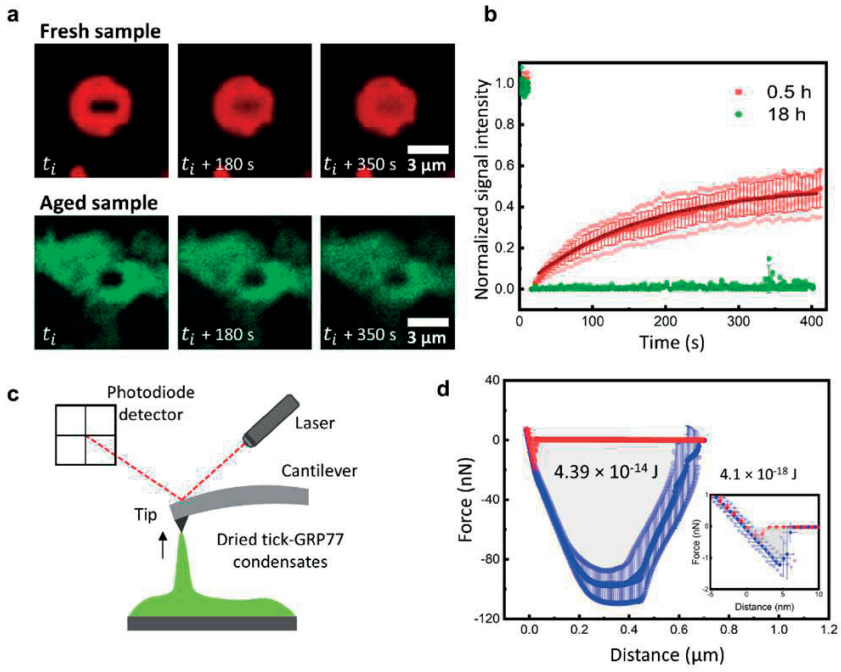

Figure 4.8: Viscous GPR77 condensates exhibit adhesive nature

(a) Time-lapse showing the fluorescence recovery of GRP condensates (125 µM) for fresh (0.5 h; n = 6) and older (18h; n = 4) samples. The condensates were formed in presence of 1 M Na2HPO4 salt. (b) Fluorescence recovery curve showing that the freshly formed condensates have a higher fraction of the mobile phase compared to matured GRP condensates. The solid line shows exponential fit to the dataset (R2 = 0.99). Samples in c, d, and e were doped with 5 mol% OG488-GRP. (c) Schematic of adhesion measurements showing the force spectroscopy set up. (d) The approach (red) and retract (blue) force-distance curves for the surface coated with GRP condensates formed in the presence of 1 M Na2HPO4 (n = 3). The work of adhesion is calculated from the area under the curve which gives nearly four magnitudes higher work of adhesion than a bare silicon substrate (n = 3). The inset shows approach and retract force-distance curves for non-adhesive silicon substrate acting as negative control. The dotted curves show individual datasets, while the error bars indicate standard deviations.

4.2.5 Natural tick saliva shows evidence of protein-rich biomolecular condensates

All the above-mentioned *in vitro* experiments indicated a strong phase separation tendency of tick-GRP77, which encouraged us to further investigate if natural tick saliva exhibits similar phase separating behavior. We collected ticks (*Ixodes ricinus*) from their natural habitat, dissected adult females, isolated the salivary glands, and extracted their contents (**Figure 4.9a** ; see Materials and Methods and **Figure S4.11** for details). A denaturing SDS-PAGE analysis of the extract showed multiple protein bands, as expected, in the 10–100 KDa range (**Figure S4.12**). An important factor

to note here is that the ticks we collected were not blood-fed and thus likely have a lower expression of GRPs compared to blood-fed ticks[28]. Additionally, it has been reported that ticks species with long hypostome like *Ixodes ricinus* have lower level of cement production[75], and thus likely lower expression of GRPs[25]. Nonetheless, microscopic visualization of multiple salivary gland extracts (3 out of 5 extractions) revealed numerous micron-sized spherical droplets (**Figure 4.9b**). We also recorded a droplet fusion event indicating their liquid nature (**Figure 4.9c**). We ruled out the possibility of these droplets being lipid or fat droplets by confirming that GRP has no affinity to partition inside oil-in-water emulsions and prefers to stay in the aqueous phase (**Figure S4.13**). Moreover, subjecting the tick salivary extract to high salt concentration (0.75 M Na2HPO4, pH 7.4) led to fiber-like structures (**Figure 4.9e**). When we doped the samples with fluorescently labelled OG488-GRP (6 μM), we observed strong partitioning of OG488-GRP (2 out of 3 samples) in these droplets/fibers, hinting at their protein-rich nature (**Figure 4.9d, e**).

We would like to note that these experiments indicate the general likelihood of GRP-rich condensates in the saliva and not particularly tick-GRP77. To emphasize this point, we compared tick-GRP77 with 20 different GRPs identified in the tick saliva across 9 different species (*I. scapularis*, *I. ricinus*, *A. variegatum*, *R. zambeziensis*, *H. longicornis*, *R. pulchellus*, *H. rufipes*, *D. pulchellus*, and *A. americanum*), with the molecular weights ranging between 7–88 kDa (**Table 4.1**). Interestingly, in addition to the high glycine content, the amino acid composition and patterning of these GRPs show striking resemblance as that of GRP77. The aromatic amino acid residues remain prominent (minimum 9% and as high as 20%) and these aromatic residues are also interspersed periodically (typically every 3 to 10 amino acids) by non-aromatic units such as glycine and proline. Thus, the GRP77 condensate mechanism that we have shown here could be a more generic path to achieve homogenous-to-coacervate-to-solid transition.

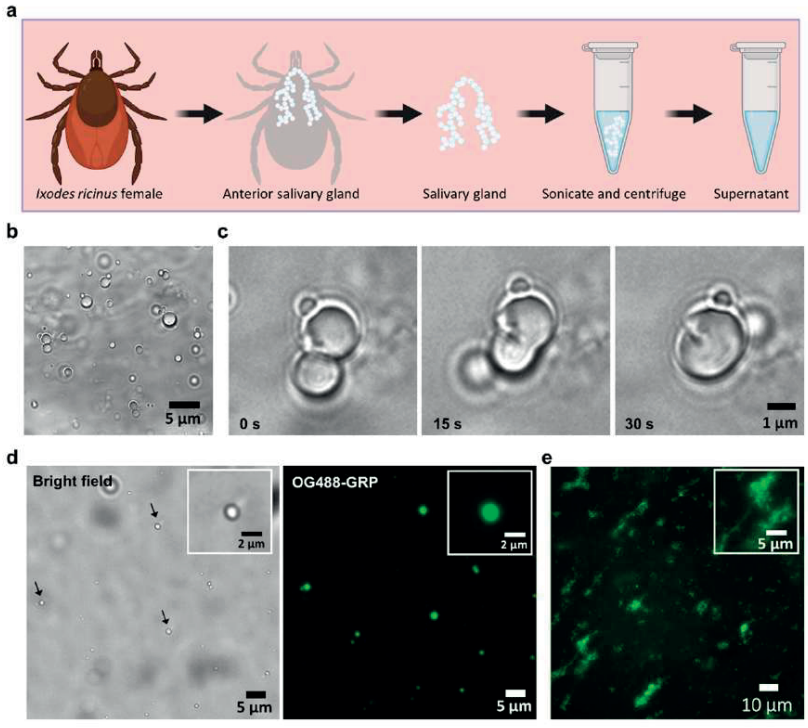

Figure 4.9: Salivary gland extracts from ticks hint at the presence of protein-rich phase- separated droplets. (a) Schematic showing the extraction of the salivary gland from a non- blood-fed tick (Ixodes ricinus). The collected supernatant was used in the following experiments. (b) Bright-field visualization of the supernatant showing numerous micron-sized spherical droplets. (c) Fusion of two droplets, indicating their liquid nature. (d) Spiking the supernatant with fluorescently labelled GRP77 (OG488-GRP77) readily led to its partitioning inside the phase-separated droplets indicating their protein-rich nature. (e) Fluorescence image showing fiber-like structures observed in the supernatant in presence of 0.75 M Na2HPO4 with OG488-GRP77 showing strong partitioning in these structures.

4.3 CONCLUSION

We have demonstrated that the glycine-rich protein (GRP; Uniprot: Q4PME3) present in tick saliva undergoes liquid-liquid phase separation and exhibits ageing behavior to form gel-like adhesive structures. We showed that GRP condensates form via simple coacervation, and they become solid-like over a time frame of a few hours. Considering that tick cement deposition and solidification is a slow process[20], our results suggest a plausible role of GRPs in the cement cone formation, namely to induce liquid-liquid and subsequent liquid-to-solid phase transition, a vital process in the attachment of ticks to their host. We further show that the phase separation of tick GRP is induced via multiple weak intermolecular interactions. Particularly, regu-

larly spaced aromatic (phenylalanine and tyrosine) and arginine residues separated by glycine-rich regions promote cation-π and π–π interactions, leading to coacervation. Additionally, hydrogen bonding and hydrophobic interactions, especially given the glycine-rich backbone, also play a significant role[76].

GRPs are also found in adhesive proteins from various other organisms such as mussels, sandcastle worms, and velvet worm, and the change in the material property of their bioadhesives, like liquid-to-solid transition, is crucial for their survival[7, 10, 41, 42, 76]. For instance, the slime proteins of velvet worm undergo LLPS to form sticky fibers[77], while the mussel foot proteins form condensates that undergo liquid-to-solid transition driven by hydrogen bonding[78]. Thus, understanding the phase transitions of GRPs may reveal possible common unifying principles in bioadhesive proteins functioning in distinct environments across diverse animal species[76]. Additionally, it will be interesting to explore the role of pH and temperature on the phase transition behavior of tick GRPs. Given that secretory proteins are prone to extensive post-translational modifications (for example, reported α-gal modifications reported in tick salivary proteins[79] and phosphorylation during tick blood feeding[80, 81]) their impact in also worth investigating. Also worth studying is the possibility of cross-linking in tick GRPs, as the tick saliva harbors essential enzymes (phenol oxidases) that convert hydroxylated tyrosine (DOPA) into DOPA-quinone, which interacts (including covalent cross-linking) with other amino acids, and could assist in the hardening process, as shown in the case of other bioadhesives [7, 18, 82]. Finally, given the fact that ticks detach from the host post blood-feeding[26, 83], a dissolution mechanism of the hardened cement cone will also be worth investigating.

Given their adhesive nature, tick GRPs could potentially be used for the development of medical sealants like tissue glues because of their biodegradable and biocompatible properties[13]. The role of GRPs in host adhesion may provide insights to manage ticks and tick-borne pathogens, a major problem worldwide, and particularly in developing regions in tropical regions, especially due to the lack of sustainable control methods[84]. Developing chemicals that can interfere with the phase transition of tick GRPs and thus inhibit cement cone formation may provide an effective solution. Anti-tick vaccines are a promising tick control strategy with the potential to provide long-term protection[84, 85, 86, 87]. Characterization of GRPs have shown they are immunogenic, play a role in host's immune system evasion, and are required for successful tick attachment, making them promising anti-tick candidates[88, 89]. Also, condensates have a high potential to be effective drug delivery systems owing to their rapid and aqueous self-assembly, possibility of targeting, and enhanced bioactivity of the cargo[90]. Thus, testing the potential of GRP-based condensates as anti-tick vaccine agents could be another outcome of this research.

4.4 MATERIALS AND METHODS

4.4.1 Materials

Chemicals – sodium chloride, potassium chloride, disodium hydrogen phosphate and dihydrogen sodium phosphate, Tris-base, PVA (polyvinyl alcohol, 87-90% hydrolyzed, average MW 30-70 kDa), bovine serum albumin, β-mercaptoethanol was purchased from Sigma-Aldrich. Eucalyptus oil (W246680) was purchased from Sigma-Aldrich while food-grade sunflower oil was from Reddy®. Precision Plus Protein dual xtra prestained protein marker, Mini-Protean Tricine Precast Gels 16.5% and 10x Tris/Glycine/SDS buffer were purchased from Bio-Rad. Coverslips #1 24 mm x 60 mm were purchased from Corning®. Sylgard™ 184 silicone elastomer and curing agent were purchased from Dow. Silicon wafer was bought from Silicon Materials. Photoresist (EpoCore 10) and photoresist developer (mr-Dev 600) were purchased from micro resist technology GmbH. Microfluidic accessories like tygon tubing 1/16" ODx 0.02" ID and stainless steel 90° bent PDMS coupler were purchased from Darwin Microfluidics.

4.4.2 GRP Synthesis and fluorescent labelling

Two different solid-phase peptide synthesis (SPPS) methods were used in this study. Boc-based SPPS was used for experiments in Fig. 2, 3c-f, 4a, 4c-e, 5a-f, Supplementary Figures 4, 6, 7a, 8, 9, 12, 14, 16, 17, 18, 20a, 21 and 22a. Fmoc-based SPPS was used for experiments in Fig. 3g, 4b, 5h and Supplementary Figures 5, 7b, 13, 15, 19, 20b and 22b.

4.4.3 Boc-based SPPS

The N- (H2N-APAEEAKPAE AGDEKKDVEG RIGYGGPGFG GG-MPAL) and C- (H2N-AFGSGFNRGG SFGVGAHGNQ YGQGGFEIQP GRQQPSCVRQ HPNLR-OH) terminal peptide fragments of the protein were synthesized on 0.10 mmol scale. 0.18 g of resin was used for both syntheses, with 4-(Hydroxymethyl) phenylacetamidomethyl (PAM) polystyrene resin with preloaded leucine (Leu) and arginine (Arg) or the N- and C-terminal peptide fragments, respectively. The first alanine residue (Ala) of the C-terminal peptide fragment sequence was replaced by a cysteine residue (Cys) (A33C mutation) for NCL. Each amino acid was activated with 0.5 M 2-(6-Chloro-1-H-benzotriazole-1-yl)-1,1,3,3-tetramethylaminium hexafluorophosphate (HCTU) in *N*,*N*-dimethylformamide (DMF) and *N*,*N*-Diisopropylethylamine (DIPEA) before coupling. The coupling time for all amino acids was 10 minutes, except for serine (Ser), threonine (Thr), Arg, and asparagine (Asn) for which the coupling time was 20 minutes. For glycine (Gly), the coupling time was also set to 20 minutes for the N-terminal peptide fragment, whereas 10 minutes double

couplings done for the C-terminal peptide fragment. After each coupling, the resin was washed with DMF, then treated with Trifluoroacetic acid (TFA) two times for 1 minute, and washed again with DMF. After glutamine (Gln) coupling (C-terminal peptide fragment synthesis), the resin was washed with DCM as well before and after TFA treatment to prevent intramolecular pyrrolidone formation. For thioester synthesis at the N-terminal peptide fragment, 3-mercaptopropionic acid (MPA) was coupled via a Leu residue and subsequent trityl group-deprotection was performed with a 95%/2.5%/2.5% TFA/Triisopropylsilane (TIS)/H2O mixture. The N- and C-terminal peptide fragments (495 mg and 440 mg, respectively) were deprotected and cleaved from the solid-phase by anhydrous hydrogen fluoride (HF) treatment for 1h at 0°C using 4% v/v *p*-cresol as scavenger. The peptides were precipitated in ice-cold diethyl ether, dissolved in a MeCN/H2O mixture containing 0.1% TFA, and lyophilized.

Native chemical ligation (NCL)

NCL of the unprotected synthetic peptide segments was performed as follows: 0.1 M TRIS buffer, pH 8, containing 6 M Gnd-HCl was added to dry peptides yielding approximately 10 mg/mL of peptide fragments. Subsequently, 1% v/v benzylmercaptan and thiophenol were added. The ligation reaction was performed in a heating block at 37 °C and the mixture was vortexed periodically to equilibrate the thiol additives. Reaction progress was analyzed with UPLC-MS. After the reaction was complete, thiophenol was removed by diethylether extraction of the reaction mixture (3 x).

Desulfurization

Desulfurization was directly performed after the native chemical ligation reaction in order to convert the first Cys residue of the *C*-terminal peptide fragment into an Ala residue and thus to obtain the original GRP sequence. Desulfurization buffer was prepared by dissolving tris(2-carboxyethyl)phosphine (TCEP; 250 mM) in 5 mL 0.1 M TRIS buffer, pH 8, containing 6 M Gnd-HCl. The pH of the desulfurization buffer was adjusted by adding solid NaOH until it reached pH 7. Then, reduced L-glutathione (GSH; 40 mM) was added to 1 mL of this desulfurization buffer. 250 µL of this solution were added to the reaction mixture and VA-044 (6.25 mM) was added. The reaction was performed at 37°C and reaction progress was monitored using UPLC-MS until the product was observed. Analytical HPLC was performed to purify GRP by using a C18 column (150 mm x 4.6 mm) connected to a Prostar HPLC (Varian).

Acm deprotection

To remove the acetamidomethyl (Acm) protecting group of the cysteine residue in the *C*-terminal peptide fragment, the peptide was dissolved at a 2 mM concentration in

0.1 M TRIS, pH 7.25, containing 6 M Gnd-HCl. Then, 10 eq. Pd-Cl2 were added and the deprotection progress at 37 °C was monitored using UPLC-MS. After reaction completion, the formed Pd-complex was reduced with 20 mM DTT for 1 hour at 37 °C. Subsequently, the reaction mixture was purified on a C4 column (Vydac, 150 mm x 4.6 mm) with an appropriate gradient on the analytical HPLC system as described above.

4.4.4 Fmoc-based SPPS

Peptides (amine fragment: GFNR GGSFGVGAHG NQYGQGGFEIQPGRQQP-SCV RQHPNLR and ester fragment: APAEEAKPAE AGDEKKDVEG RIGYGGP-GFG GGAFGS-Ocam-L) were synthesized via Fmoc-SPPS on a microwave assisted peptide synthesizer (CEM liberty lite) using a Rink-amide resin with DIC/Oxyma chemisty. The carboxyamidomethyl (Cam) ester was introduced by incubating the resin with 2 eq[91]. Fmoc glycolic acid, 2 eq. (2-(1H-benzotriazol-1-yl)-1,1,3,3-tetramethyluronium hexafluorophosphate (HBTU), 2 eq. OxymaPure and 4 eq. DIPEA for 45 min at room temperature. After fluorenylmethoxycarbonyl (Fmoc) deprotection of the glycolic acid, the ester bond was formed by incubation of 4 eq. Ser, 0.4 mM 4-Dimethylaminopyridine (DMAP) and 6 eq. *N*,*N*′-Diisopropylcarbodiimide (DIC) to the resin for 45 min at room temperature. After completion, the peptides were cleaved from the resin (95% TFA; 2.5% TIS; 2.5% H2O) and purified using RP-HPLC on a C18 column (XBridge C18 5 µm OBD 30x100 mm). Finally, the product was lyophilized (Christ alpha 2-4 LSCbasic) and checked for purity via HPLC/MS (Agilent 1100, LC-MSD SL)

Ligation

Peptides were dissolved in Tricine buffer (200 mM, pH 8.3, 4 mM TCEP) to a concentration of 1 mM ester fragment, 2 mM amine fragment and 20 µM omniligase-1[92]. The reaction was performed at room temperature for 4 hours and followed via RP-HPLC/MS (Agilent 1100, LC-MSD SL) using an MeCN/H2O gradient on a C-18 column (Phenomenex 5µm EVO C18 100 Å 150 x 4.6 mm). After completion of the ligation, the product was purified by preparative HPLC (Waters 2545, 2998, Aquity QDA) using a H2O/MeCN gradient on a C18 column (XBridge C18 5 µm OBD 30x100 mm). Finally, the product was lyophilized (Christ alpha 2-4 LSCbasic) and checked for purity via HPLC/MS (Agilent 1100, LC-MSD SL). Protein mass was verified using mass spectrometry (**Figure S4.14-19**) and the purity was checked using HPLC (**Figure S4.20-22**).

4.4.5 In vitro experimentation and microscopic visualization

Stock solution of tick-GRP77 was made in MilliQ water. Unless specified, all the evaporation experiments were performed in phosphate buffer saline (10 mM Phos-

phate buffer, 2.7 mM KCl, and 137 mM NaCl at pH 7.4). A 2 µl droplet of protein solution was transferred on a coverslip (24 mm x 40 mm, Corning™ #1.5) and mounted on Nikon-Ti2-Eclipse inverted fluorescence microscope equipped with pE-300ultra illumination system. For all the experiments, droplets were visualized using either Nikon Plan Apo 100x (numerical aperture, NA 1.45) oil objective or Nikon Plan Fluor 40x (NA 1.30) oil objective. For fluorescent visualization, the sample was doped with 5 mol% of OG488-GRP and excited via 482/35 nm excitation filter, 505 nm dichroic mirror and the emitted light was collected through 536/40 nm emission filter (Semrock). The samples were typically excited using 2-5% laser intensity and time-lapse images were acquired at exposure of 5-20 ms using a Prime BSI Express sCMOS camera. Confocal microscopy for visualizing the inverted phase and oil-in-water emulsions was recorded using Nikon C2 laser scanning confocal microscope, equipped with a 60x (NA 1.40) oil immersion objective. The sample was doped with 5 mol% OG488-GRP and was imaged using 488 nm excitation laser with excitation filter 525/50, equipped with 560 nm LP dichroic mirror and 585/65 nm emission filter. We minimized the illumination intensity (1–2% of 15 mW) to prevent bleaching of the sample.

4.4.6 Surface functionalization of coverslips

Wherever required, coverslips were coated with 5% w/v solution of polyvinyl alcohol (molecular weight 30 -70 kDa, 87 – 90 % hydrolyzed) as described previously[93]. Briefly, the coverslip was plasma treated for 30 seconds at 12 MHz (RF mode high) using a plasma cleaner (Harrick plasma PDC-32G). A 10 µL drop of PVA solution was pipetted out in the center of the glass slide and allowed to rest for 5 min followed by gently removing of PVA by tilting the glass slide. To remove free PVA, the coverslip was gently washed with milli Q water. The glass slide was baked at 70 °C for 2 hours and stored at room temperature in a clean environment. To make the glass slide hydrophobic, ~20 µL of (tridecafluoro-1,1,2,2-tetrahydrooctyl)trichlorosilane was taken in a glass vial and placed in the desiccator along with glass slides. The set up was left under partial vacuum for ~12 h to render the glass slides hydrophobic.

4.4.7 Droplet fusion experiments

A 2 µL sessile drop of tick-GRP solution (32 µM with 5% mol fraction of OG488-GRP; dissolved in PBS pH 7.4) was allowed to evaporate on a PVA-passivated glass slide. Droplet fusion events were recorded using 40x oil objective at time interval of 250 ms (exposure time of 10 ms) on Nikon Ti2 Eclipse fluorescence microscope. The aspect ratio of the fusing droplets was determined using Fiji (Image J) by appropriately thresholding and binarizing the images, and then fitting the droplet boundaries with an ellipse to calculate the aspect ratio $A = \frac{major\ axis}{minor\ axis}$, where major and minor axes are the long and short axes of the ellipse respectively. For analysis of fusing condensates, the

change in aspect ratio with respect to time was plotted and the data was fit to the function of the form $A = 1 + (A_o - 1)e^{\frac{-t}{\tau}}$; where t is the time, τ is the characteristic relaxation time, and A_0 is the initial aspect ratio. Using the relation $\tau = l(\eta/\gamma)$ where l is the average diameter of the droplets, η is the viscosity and γ is the surface tension, the inverse capillary velocity η/γ was calculated[56].

4.4.8 Microfabrication

The master wafer was prepared according to the previously described UV lithography method[94] and the protocol was adjusted to attain the channel height of 20 μm. To prepare the microfluidic device, polydimethylsiloxane (PDMS) and curing agent (SYLGARD™184 elastomer) were mixed in 10:1 weight ratio. The mixture was poured on the master, degassed using vacuum desiccator followed by baking at 70 ˚C for 4 hours. The hardened PDMS block was carefully removed, and inlets and outlet holes were punched using a biopsy punch of diameter 0.5 mm (Darwin microfluidics). The PDMS block was then bonded on a glass coverslip (Corning® #1) using a plasma cleaner (Harrick Plasma PDC-32G). The bonded device was baked at 80 ˚C for two hours and stored at room temperature. Elveflow pressure controller OB1-MK3 was used to flow GRP and salt solutions 2 M Na2HPO4 (10 mM Tris-Cl, pH 7). Microfluidic reservoir XXS (Darwin microfluidics LVF-KPT-XXS) was used to load low volume (10 μL) GRP sample. The fluid flow was maintained at constant pressure of 100 mbar and 20 mbar for the inner aqueous (GRP solution) and outer aqueous (Na2HPO4 solution) channels respectively.

4.4.9 Fluorescence recovery after Photobleaching

FRAP experiments were performed on Leica SP8-SMD microscope and 63x (NA 1.2) water objective. For bleaching, the region of interest (ROI) of approximately 1.5 μm length and 0.5 μm breadth was selected inside the condensates of approximately 5 μm in diameter. The ROI was bleached using 100% laser intensity for 2 seconds and recovery of the bleached area was recorded for every 5 seconds for approximately 6 minutes. Intensity of the bleached area was normalized using the equation, $f(t) = \frac{I_{correct}(t) - \min(I_{correct})}{I_{correct}(0) - \min(I_{correct})'}$, where $I_{correct} = c(t) * I(t)$, and $C(t) = \frac{R(0)}{R(t)}$. Here, $R(t)$ and $I(t)$ indicate the fluorescence intensity of the reference droplet at time t and the original fluorescence intensity of the bleached region at time t, respectively; $\min(I_{correct})$ indicates the minimum value of $I_{correct}$, which is obtained right after the sample is bleached67. The normalized intensity was fitted using the function $f(t) = A(1 - e^{\frac{-t}{\tau}})$ where A and τ indicate the amplitude of recovery and the relaxation time, respectively. The apparent diffusion coefficient (D_{app}) was calculated using the formula $D_{app} \sim \frac{\omega^2}{t_{(\frac{1}{2})}}$ where $t_{(\frac{1}{2})}$ is the half-life fluorescence recovery and ω^2 is the area of the bleached cross section. The half-life $t_{(\frac{1}{2})}$ was calculated using the formula $t_{(\frac{1}{2})} = \ln(2)\tau$.

4.4.10 Adhesion measurements using force spectroscopy

Force-distance measurements were performed on JPK ForceRobot 300, an AFM specifically designed for force spectroscopy. Silicon wafer was used as a substrate and the aqueous sample containing GRP condensates was drop-casted on the wafer and was allowed to dry for 1 hour. Force spectroscopy was carried out using SCANASYST-AIR silicon-nitride tips with spring constant 0.4 N/m and average tip radius of 2 nm. The obtained data were further analyzed using processing software – JPK SPM Data Processing.

4.4.11 Salivary gland extraction

For tick collection, we selected the Veluwe region in the Netherlands in the months of June and July, when ticks "quest" by climbing up grass and low-lying vegetation and waiting for a potential host to pass by, which they will grab and climb on to. We collected ticks belonging to the species *Ixodes ricinus* at different life stages – nymphs, adult males, and adult females, from the grass and small shrubs by using a tick-dragging method as previously described[95]. The adult female salivary glands of the *Ixodidae* groups consists of type I, II and III acini cells[26, 66] among which the type II acini cells are associated with cement formation[27, 96]. Female ticks were dissected to isolate their salivary glands according to a previously described protocol[97], with the exception that the ticks were not blood-fed before. Salivary glands were resuspended in 100 µL milliQ water and their contents were extracted by mechanically disrupting the glands via sonication at 45 kHz for 5 minutes, followed by debris segregation via centrifugation at 13,000 g for 10 minutes. The supernatant was collected in a fresh tube and used for experimentation.

4.5 ACKNOWLEDGEMENTS

We thank Prof. Jasper van der Gucht for his feedback on the chapter. We thank Hans Smid (www.bugsinspace.nl) for providing the images of ticks and Marcel Giesbers from Wageningen Electron Microscopy Centre for providing the scanning electron microscopy image of tick mouth parts. We acknowledge Niels Appelman for assisting with fabrication of microfluidic devices. Peptiligases, such as omniligase-1, are a patented technology by EnzyPep B.V. and omniligase-1 was obtained through EnzyTag B.V. (www.enzytag.com). S.D. acknowledges financial support from Dutch Research Council (grant number: OCENW.KLEIN.465). The schematics were made using Biorender.com.

4.6 AUTHOR CONTRIBUTIONS

K.G., P.T., and S.D. conceived the idea and designed the experiments. K.G., P.T., M.N., and C.C. performed *in vitro* experiments. K.G. and E.P. carried out tick collection and salivary gland extraction. K.G., P.T., M.N. and S.D. performed data analysis. D.S, E.N., S.v.d.B., L.v.d.B., and I.D. synthesized the proteins. K.G., P.T., M.N., I.D. and S.D. wrote the initial draft. K.G, M.N., I.D., and S.D. reviewed and edited the original manuscript. S.D. acquired funding and performed project administration and supervision.

4.7 COMPETING INTERESTS

L.v.d.B. is a minority shareholder (own stock) in EnzyTag B.V. S.v.d.B. is employee at EnzyTag B.V. Other authors declare no competing interests.

4.8 SUPPLEMENTARY FIGURES

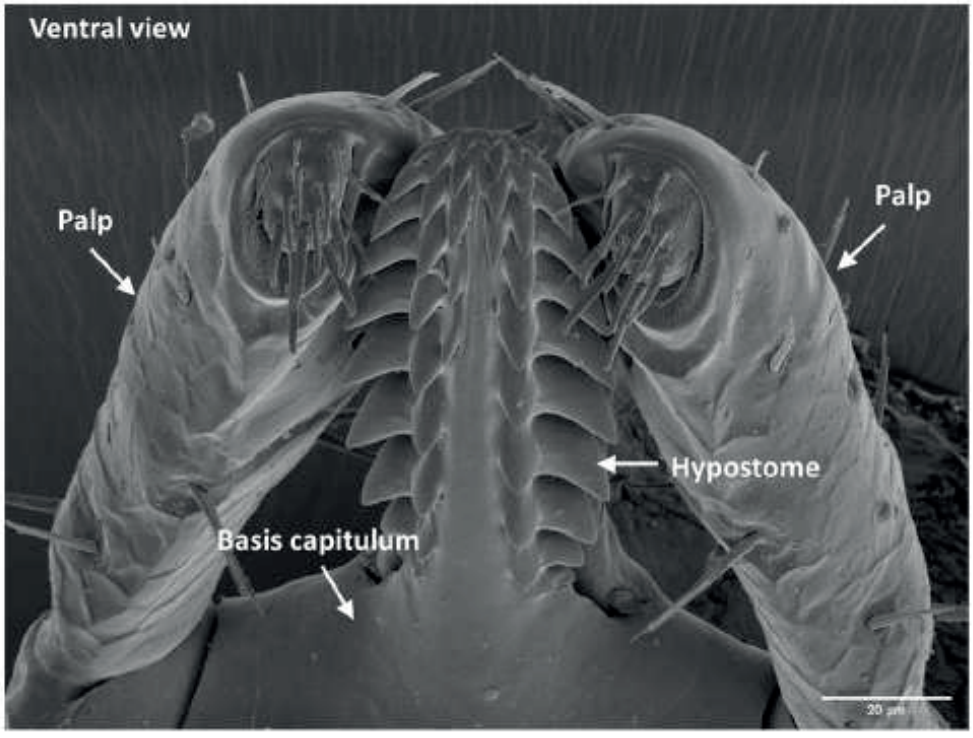

Figure S4.1: Anatomy of tick mouth parts.

Electron microscopy of tick mouth parts visualized from theventral side.

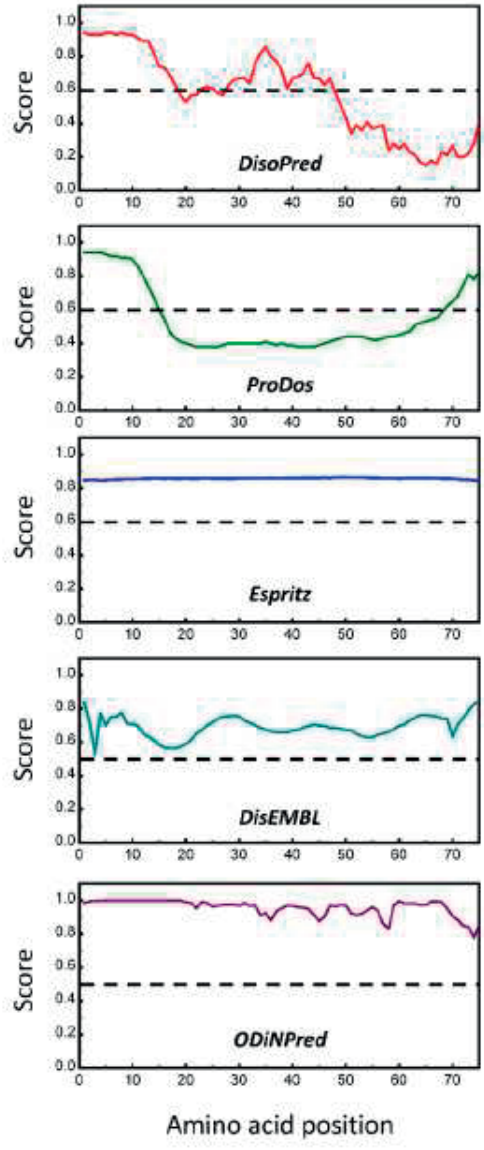

Figure S4.2: Disorder prediction in tick-GRP77.

Multiple software predict tick-GRP77 to be highly disordered or at least have prominent disordered regions. DisoPred[1] predicts that the N-terminus has a high disorder and ProDos[2] suggests both N-terminus and C-terminus as disordered regions. Espritz[4] , DisEMBL[6] and ODiNPred[11] predict entire tick-GRP77 to be completely disordered.

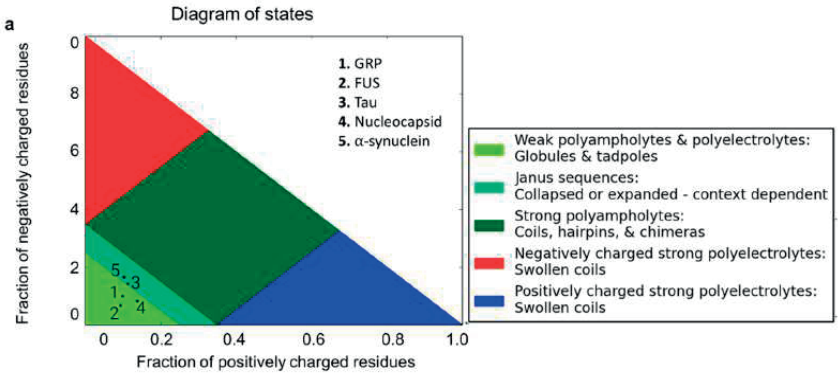

Figure S4.3:Tick-GRP77 falls in the same region within the diagram of states as many well-characterized condensate-forming proteins. Diagram of states indicating tick-GRP77 as weak polyampholytes and polyelectrolytes and falls in close vicinity of FUS, tau, nucleocapsid protein, and α-synuclein, all of which are known to phase separate.

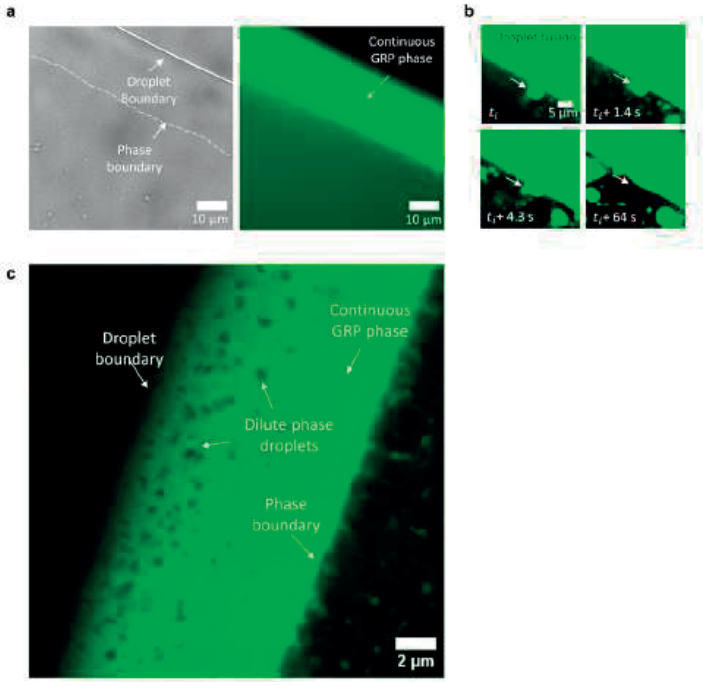

Figure S4.4: The region between the droplet boundary and the contact line is a tick-GRP77-rich condensate phase.

(a) Bright-field (left) and corresponding fluorescence image (right) showing the tick-GRP77-rich nature of this region (32 µM starting concentration). (b) An example of tick-GRP77 condensate fusing with the continuous tick-GRP77-rich phase. (c) Confocal microscopy showing tick- GRP77-depleted aqueous droplets within the inverted phase formed by evaporation assay (125 µM starting concentration). In all cases, tick-GRP77 was present in PBS (pH 7.4) and 5 mol% OG488-GRP77 was added for fluorescence visualization.

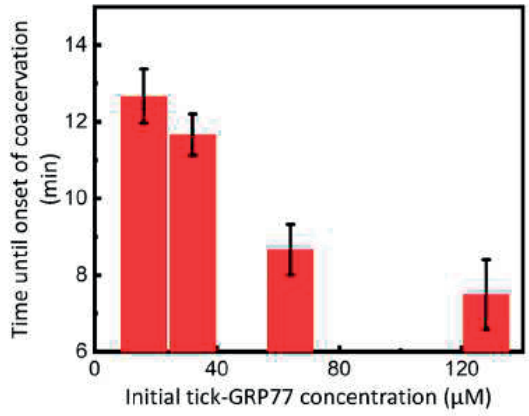

Figure S4.5: Onset of coacervation is influenced by the starting tick-GRP77 concentration.

The time required for the onset of coacervation is steadily reduced as the initial tick-GRP77 concentration is increased. The values were recorded during droplet evaporation assay in PBS (pH 7.4).

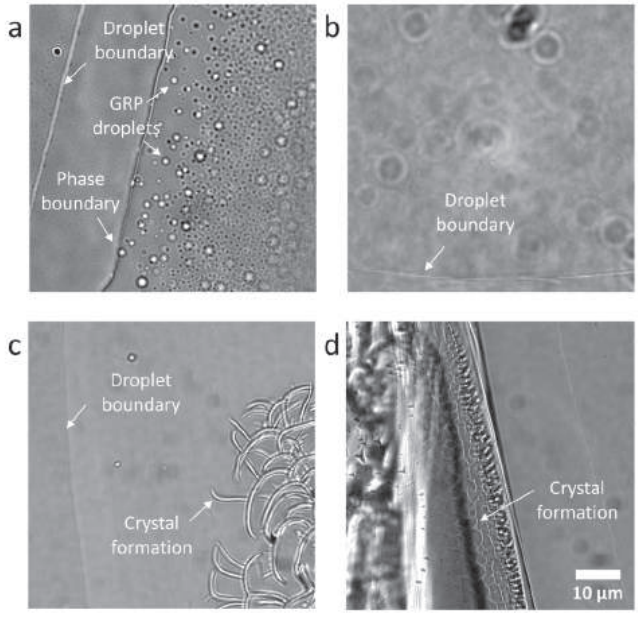

Figure S4.6: The formed condensates are specific to tick-GRP77 and need salts for their formation. (a) Evaporation of tick-GRP77 (32 μM) in presence of 140 mM NaCl resulted in the formation of condensates. (b) On the contrary, evaporation of tick-GRP77 (32 μM) dissolved in pure water did not lead to phase separation. (c) Evaporation of globular protein solution, bovine serum albumin (127 μM in PBS, pH 7.4) eventually led to the formation of salt crystals without any phase separation. (d) Similarly, just a PBS solution (pH 7.4) did not form condensates but salt crystals.

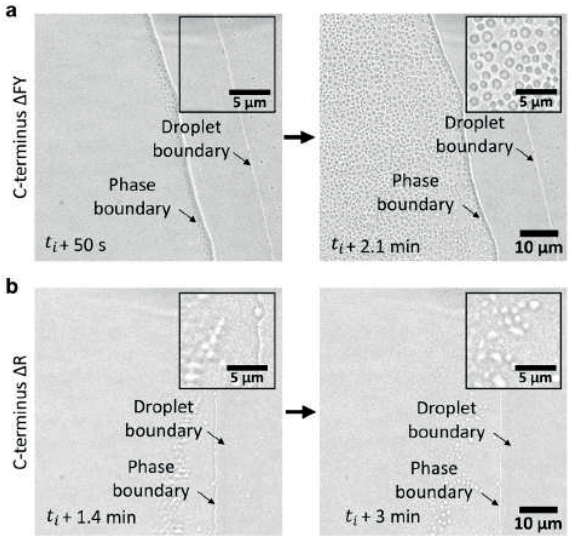

Figure S4.7: Evaporation of 100 ❁M C-terminus mutants results in delayed coacervation.

(a) Higher initial concentration of *Δ*FY mutant showed slightly faster initiation of coacervation ($ti \approx 6.5$ min) and proceeded with appreciable coacervation. (b) Higher initial concentration of *Δ*R mutant accelerated the initiation of coacervation ($ti \approx 4.8$ min) but only negligible amount of coacervates appeared near the contact line over time. The starting concentration of all the samples was 100 µM in PBS.

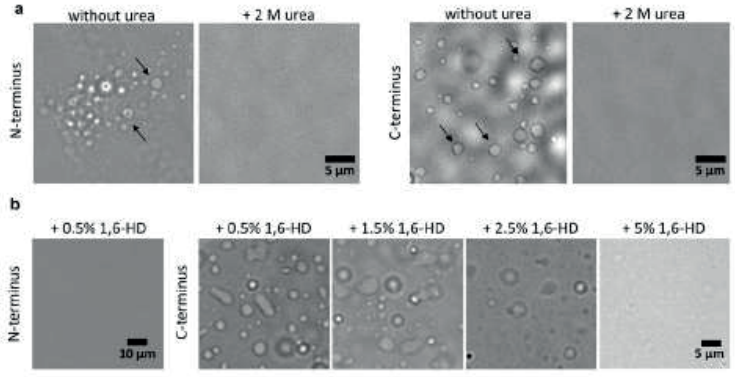

Figure S4.8: Hydrogen bonding and hydrophobic interactions are involved in phase separation of tick-GRP77. a) Both N- and C-terminus condensates formed via droplet evaporation assay dissolved upon addition of urea (≈0.5 M final concentration) indicating active role of hydrogen bonding in LLPS formation. (b) N-terminus condensates formed via evaporation dissolved upon addition of 0.5% w/v 1,6-HD (≈15 mM final concentration). On the contrary, C-terminus condensates remained unaffected in presence of 1.5% w/v 1,6-HD (≈40 mM final concentration), and completely dissolved only at 5% w/v 1,6-HD (≈140 mM final concentration), indicating a prominent role of hydrophobic interactions compared to N-terminus condensates. Starting concentrations for both termini were 50 µM in PBS (pH 7.4) for all the experiments

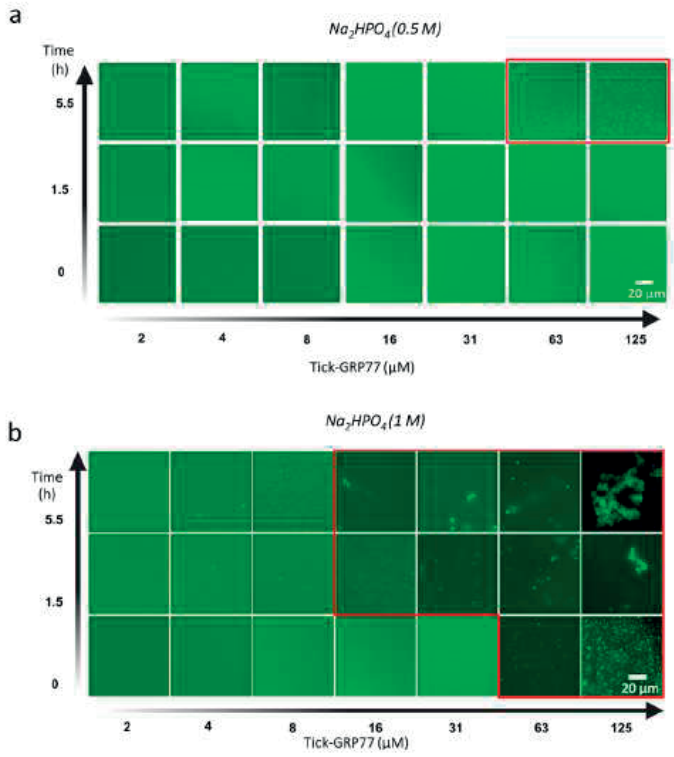

Figure S4.9: Tick-GRP77 coacervation phase diagram as a function of protein concentration and incubation time in Na2HPO4 solution. (a) Incubation of tick-GRP77 (2–125 µM) at 0.5 M Na2HPO4 did not lead to instant condensate formation. At 63 µM and above, condensates formed after 5.5 hour of incubation. (b) On the contrary, presence of 1 M Na2HPO4 led to instant coacervation of tick-GRP77 at 63 µM and above. Incubation for 1.5 hours also led coacervation down till 16 µM tick-GRP77.

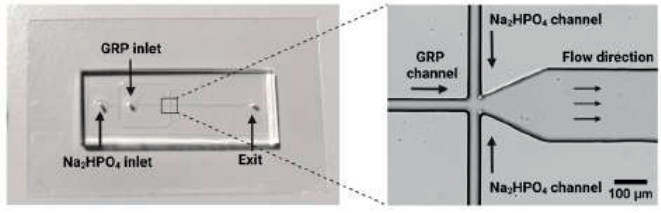

Figure S4.10: Microfluidic device used in flow-focusing experiments.

Bright-field images showing PDMS-based lab-on-a-chip device with a zoom-in showing the flow-focusing junction.

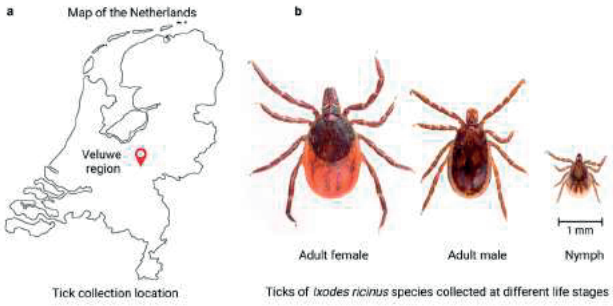

Figure S4 II:

(a) Location of tick collection in the Netherlands. (b) Ticks of species Ixodes ricinus at different life stages were collected.

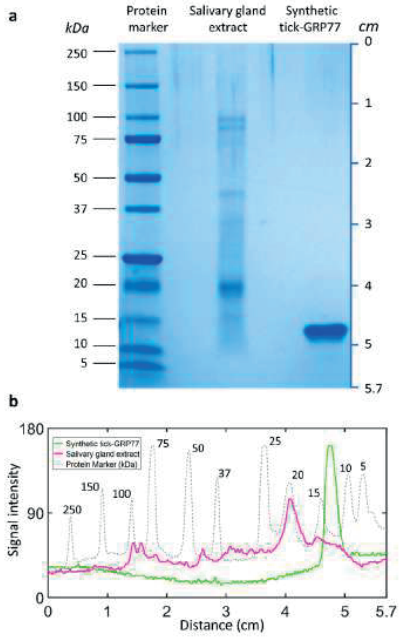

Figure S4.12: Protein gel electrophoresis of tick salivary gland extract and tick-GRP77.

(a) Denaturing SDS-PAGE of the tick salivary gland extract (middle lane) isolated from a single adult female Ixodes Ricinus show proteins of varying molecular weights ranging from 10 kDa to 100 kDa. Some prominent bands were observed, such as one corresponding to 20 kDa protein marker (first lane). Synthetic tick-GRP77 (last lane) showed intense single band between 10 kDa and 15 kDa. (b) Protein signal intensity plot versus protein migration distance showing single band intensity of synthetic tick-GRP77 (green) whereas tick salivary gland extract (magenta) shows maximum signal intensity at 20 kDa in addition to low signal dispersed between 100 kDa and 10 kDa. Protein marker (dotted line) intensities were used as reference.

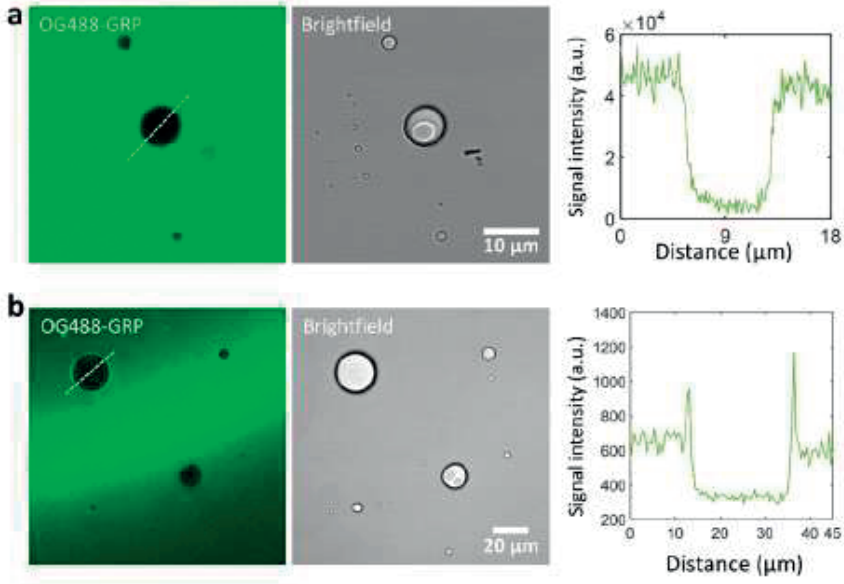

Figure S4.13: Tick-GRP77 does not partition in hydrophobic oil-in-water emulsions.

(a) OG488-GRP did not partition in sunflower oil droplets. (b) OG488-GRP also did not partition in eucalyptus oil droplets but showed some preference to remain at the oil-water interface. In both the panels, the line graphs correspond to the dotted lines and show the exclusion of OG488-GRP from the oil droplets. In all cases, the final concentration of 2 µM of OG488-GRP77 was added visualization.

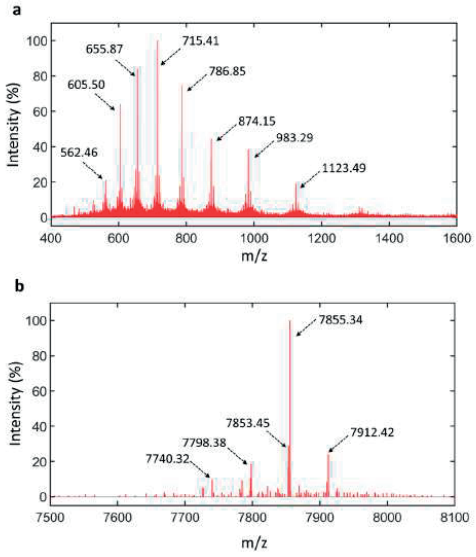

Figure S4.14: Mass analysis of tick-GRP77 synthesized by using Boc-based SPPS.

(a) ESI-MS spectrum of tick-GRP77. (b) The observed deconvoluted mass (7855.34 Da, [M+H]+) corresponds with the calculated monoisotopic mass (7853.74 Da). The deconvoluted mass corresponding to 7798.38 Da indicates a glycine residue deletion (- 57 Da) and the deconvoluted mass at 7740.32 Da is an aspartic acid residue deletion (- 115 Da). The 7912.42 Da mass could indicate a metal ion (+ 57 Da) chelated to the polypeptide

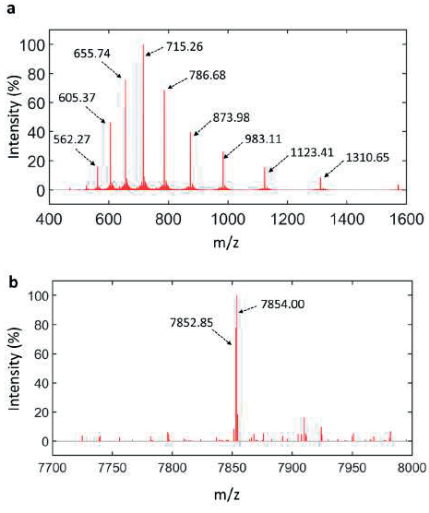

Figure S4.15: Mass analysis of tick-GRP77 synthesized by using Fmoc-based SPPS.

(a) ESI-MS spectrum of tick-GRP77. (b) The deconvoluted mass (7854.00 Da, [M+H]+) corresponds with the calculated monoisotopic mass (7853.74 Da) for tick-GRP77.

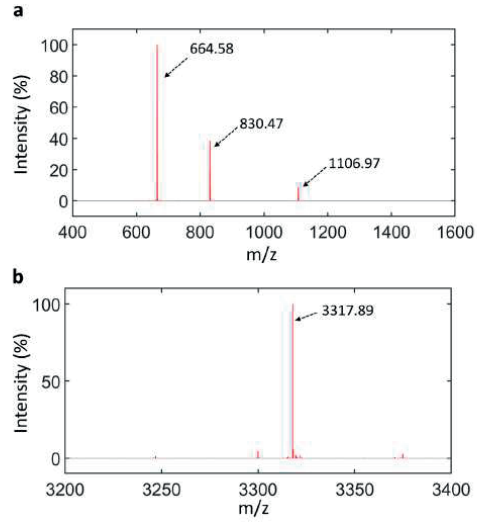

Figure S4.16: Mass analysis of the N-terminus of tick-GRP77.

(a) ESI-MS spectrum of N-terminus of tick-GRP77. (b) The deconvoluted mass (3317.89 Da, [M+H]+) corresponds with the calculated monoisotopic mass (3316.87) for the N-terminus.

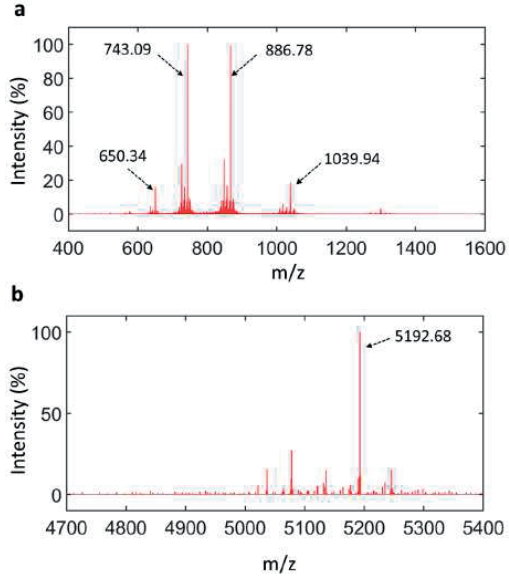

Figure S4.17: Mass analysis of the C-terminus of tick-GRP77.

(a) ESI-MS spectrum of C-terminus of tick-GRP77. (b) The deconvoluted mass (5192.68 Da, [M+H]+) correspondsa with the calculated monoisotopic mass (5191.23) for the C-terminus.

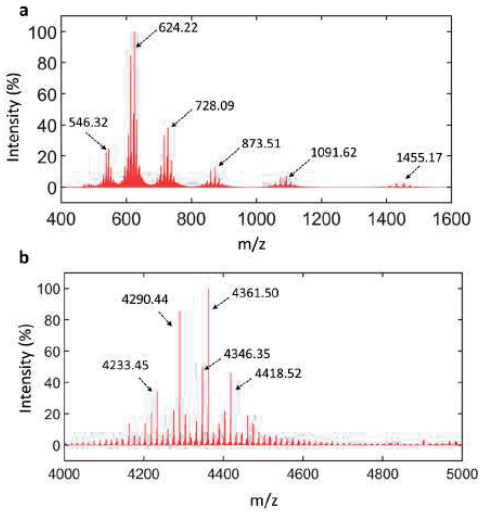

Figure S4.18: Mass analysis of the ΔFY mutated C-terminus.

(a) ESI-MS spectrum of the ΔFY mutant (b) Deconvoluted and calculated monoisotopic mass of [M+H]+ for the ΔFY mutant were 4361.50 Da and 4361.11 Da respectively. 4290.44 Da corresponds to an alanine residue deletion in the ΔFY mutant. 4233.45 Da corresponds to a glutamine residue deletion in the ΔFY mutant.

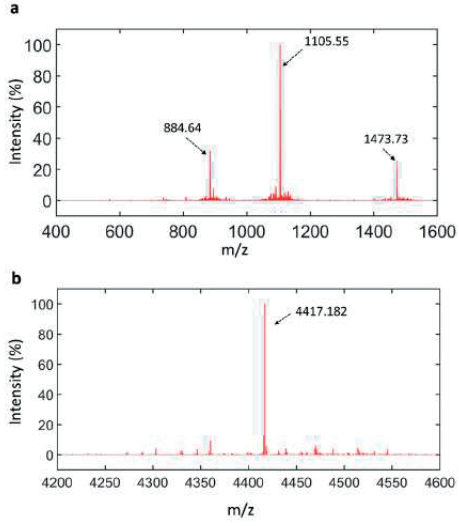

Figure S4.19: Mass analysis of the ΔR mutated C-terminus.

(a) ESI-MS spectrum of the ΔR mutant (b) Deconvoluted and calculated monoisotopic mass of [M+H]+ for the ΔR mutant were 4417.18 Da and 4417.01 Da respectively

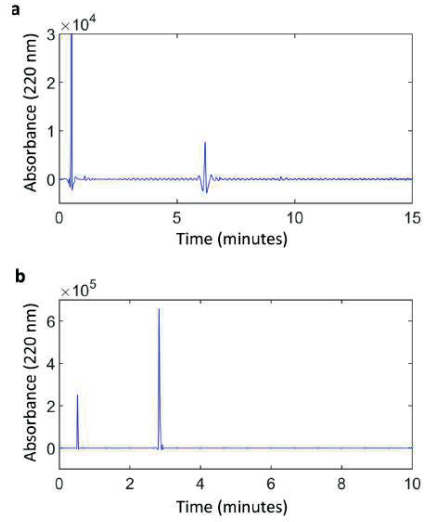

Figure S4.20: HPLC chromatograms of tick-GRP77.

(a) High-performance liquid chromatography trace of the purified tick-GRP77 synthesized using Boc-based SPPS (220 nm). The retention time of the protein is approximately 6 minutes. (b) High-performance liquid chromatography of the purified tick- GRP77 synthesized using Fmoc-based SPPS (220 nm). The retention time of the protein is approximately 3 minutes. The difference in retention time is due to the fact that different gradients have been used. The peak at 0.5 min is the injection peak.

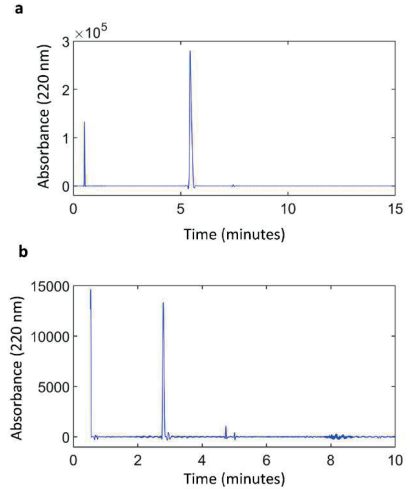

Figure S4.21: HPLC chromatograms of the N- and C-terminus of tick-GRP77.

(a) HPLC analysis of the purified N-terminus synthesized using Boc-based SPPS (220 nm). (b) HPLC analysis of the C-terminus synthesized using Boc-based SPPS (220 nm). The peak at 0.5 min is the injection peak.

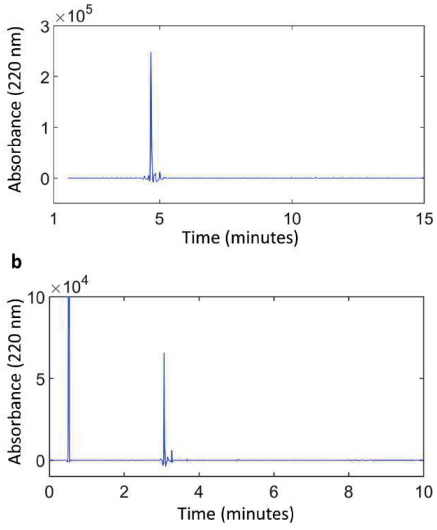

Figure S4.22: HPLC chromatograms of two C-terminus mutants.

(a) HPLC analysis of the purified C- terminus ΔFY mutant synthesized using Boc-based SPPS (220 nm). (b) HPLC analysis of C-terminus ΔR mutant synthesized using Fmoc-based SPPS (220 nm). The peak at 0.5 min is the injection peak.

Accession number / Uniprot ID	Species	% Glycine	Total aromatic amino acid (%)	Total glycine and aromatic amino acid (%)
tick-GRP77	*Ixodes scapularis*	25,97	9,09	35,06
EEC15720.1	*Ixodes scapularis*	38,89	20,84	59,73
EEC15718.1	*Ixodes scapularis*	38,57	20,00	58,57
EEC15723.1	*Ixodes scapularis*	38,09	22,53	60,62
BK007705.1	Amblyomma variegatum	36,26	12,87	49,13
A0A224YEQ4	Rhipicephalus zambeziensis	34,97	17,49	52,46
BK007224.1	Amblyomma variegatum	33,30	4,55	37,85
EEC14470.1	*Ixodes scapularis*	32,11	9,17	41,28
BK007640.1	Amblyomma variegatum	30,89	17,22	48,11
BAF36727.1	Haemaphysalis longicornis	30,16	5,29	35,45
L7M5V3	Rhipicephalus pulchellus	28,57	10,71	39,28
EEC14464.1	*Ixodes scapularis*	26,09	14,79	40,88
A0A224YEQ4	Rhipicephalus zambeziensis	26,07	15,64	41,71
L7LRH1	Rhipicephalus pulchellus	25,07	12,68	37,75
HP429186.1	Hyalomma rufipes	20,24	12,55	21,45
L7MMF9	Dermacentor pulchellus	23,15	10,34	33,49
A0A034WU73	Rhipicephalus microplus	21,88	9,38	31,26
JAG92718.1	Amblyomma americanum	20,56	10,65	31,21
JAA73102.1	*Ixodes Ricinus*	32,27	5,98	37,45
JAA73588.1	*Ixodes Ricinus*	15,86	12,42	26,2
JAA73244.1	*Ixodes Ricinus*	34,06	17,38	36,23

Table 4.1:

Comparison of glycine and aromatic amino acid composition in glycine richproteins form different species of ticks.

REFERENCE

1. Jones DT, Cozzetto D. DISOPRED3: precise disordered region predictions with annotated protein-binding activity. *Bioinformatics* 2015, **31**(6)**:** 857-863.
2. Ishida T, Kinoshita K. PrDOS: prediction of disordered protein regions from amino acid sequence. *Nucleic acids research* 2007, **35**(suppl_2)**:** W460-W464.
3. Smith AM, Callow JA. *Biological adhesives*, vol. 23. Springer, 2006.
4. Walsh I, Martin AJ, Di Domenico T, Tosatto SC. ESpritz: accurate and fast prediction of protein disorder. *Bioinformatics* 2012, **28**(4)**:** 503-509.
5. Hennebert E, Maldonado B, Ladurner P, Flammang P, Santos R. Experimental strategies for the identification and characterization of adhesive proteins in animals: a review. *Interface focus* 2015, **5**(1)**:** 20140064.
6. Linding R, Jensen LJ, Diella F, Bork P, Gibson TJ, Russell RB. Protein disorder prediction: implications for structural proteomics. *Structure* 2003, **11**(11)**:** 1453-1459.
7. Stewart RJ, Wang CS, Song IT, Jones JP. The role of coacervation and phase transitions in the sandcastle worm adhesive system. *Advances in colloid and interface science* 2017, **239:** 88-96.
8. Waite JH. Mussel adhesion–essential footwork. *Journal of Experimental Biology* 2017, **220**(4)**:** 517-530.
9. Stewart RJ, Wang CS, Shao H. Complex coacervates as a foundation for synthetic underwater adhesives. *Advances in colloid and interface science* 2011, **167**(1-2)**:** 85-93.
10. Lee BP, Messersmith PB, Israelachvili JN, Waite JH. Mussel-inspired adhesives and coatings. *Annual review of materials research* 2011, **41:** 99-132.
11. Dass R, Mulder FA, Nielsen JT. ODiNPred: comprehensive prediction of protein order and disorder. *Scientific Reports* 2020, **10**(1)**:** 14780.
12. Baer A, Schmidt S, Mayer G, Harrington MJ. Fibers on the fly: multiscale mechanisms of fiber formation in the capture slime of velvet worms. *Integrative and Comparative Biology* 2019, **59**(6)**:** 1690-1699.
13. Jongejan F, Uilenberg G. The global importance of ticks. *Parasitology* 2004, **129**(S1)**:** S3-S14.
14. Bullard R, Sharma SR, Das PK, Morgan SE, Karim S. Repurposing of glycine-rich proteins in abiotic and biotic stresses in the Lone-Star tick (Amblyomma americanum). *Frontiers in Physiology* 2019, **10:** 744.
15. Wikel SK. Host immunity to ticks. *Annual review of entomology* 1996, **41**(1)**:** 1-22.
16. Eisen L. Pathogen transmission in relation to duration of attachment by Ixodes scapularis ticks. *Ticks and tick-borne diseases* 2018, **9**(3)**:** 535-542.
17. Kugeler KJ, Schwartz AM, Delorey MJ, Mead PS, Hinckley AF. Estimating the frequency of Lyme disease diagnoses, United States, 2010–2018. *Emerging Infectious Diseases* 2021, **27**(2)**:** 616.
18. Suppan J, Engel B, Marchetti-Deschmann M, Nürnberger S. Tick attachment cement–reviewing the mysteries of a biological skin plug system. *Biological Reviews* 2018, **93**(2)**:** 1056-1076.
19. Gregson JD. Observations on the movement of fluids in the vicinity of the mouthparts of naturally feeding Dermacentor andersoni Stiles. *Parasitology* 1967, **57**(1)**:** 1-8.
20. Kemp D, Stone B, Binnington K. Tick attachment and feeding: role of the mouthparts, feeding apparatus, salivary gland secretions and the host response. *Physiology of ticks*. Elsevier, 1982, pp 119-168.
21. Trimnell AR, Davies GM, Lissina O, Hails RS, Nuttall PA. A cross-reactive tick cement antigen is a candidate broad-spectrum tick vaccine. *Vaccine* 2005, **23**(34)**:** 4329-4341.

22. Francischetti IM, Sa-Nunes A, Mans BJ, Santos IM, Ribeiro JM. The role of saliva in tick feeding. *Frontiers in bioscience: a journal and virtual library* 2009, **14:** 2051.
23. Nuttall PA. Wonders of tick saliva. *Ticks and tick-borne diseases* 2019, **10**(2)**:** 470-481.
24. Ribeiro JM, Alarcon-Chaidez F, Francischetti IM, Mans BJ, Mather TN, Valenzuela JG*, et al.* An annotated catalog of salivary gland transcripts from Ixodes scapularis ticks. *Insect biochemistry and molecular biology* 2006, **36**(2)**:** 111-129.
25. Maruyama SR, Anatriello E, Anderson JM, Ribeiro JM, Brandão LG, Valenzuela JG*, et al.* The expression of genes coding for distinct types of glycine-rich proteins varies according to the biology of three metastriate ticks, Rhipicephalus (Boophilus) microplus, Rhipicephalus sanguineus and Amblyomma cajennense. *BMC genomics* 2010, **11**(1)**:** 1-17.
26. Bullard R, Allen P, Chao C-C, Douglas J, Das P, Morgan SE*, et al.* Structural characterization of tick cement cones collected from in vivo and artificial membrane blood-fed Lone Star ticks (Amblyomma americanum). *Ticks and tick-borne diseases* 2016, **7**(5)**:** 880-892.
27. Šimo L, Kazimirova M, Richardson J, Bonnet SI. The essential role of tick salivary glands and saliva in tick feeding and pathogen transmission. *Frontiers in cellular and infection microbiology* 2017, **7:** 281.
28. Hollmann T, Kim TK, Tirloni L, Radulović ŽM, Pinto AF, Diedrich JK*, et al.* Identification and characterization of proteins in the Amblyomma americanum tick cement cone. *International journal for parasitology* 2018, **48**(3-4)**:** 211-224.
29. Nott TJ, Petsalaki E, Farber P, Jervis D, Fussner E, Plochowietz A*, et al.* Phase transition of a disordered nuage protein generates environmentally responsive membraneless organelles. *Molecular cell* 2015, **57**(5)**:** 936-947.
30. Choi UB, Sanabria H, Smirnova T, Bowen ME, Weninger KR. Spontaneous switching among conformational ensembles in intrinsically disordered proteins. *Biomolecules* 2019, **9**(3)**:** 114.
31. Dignon GL, Best RB, Mittal J. Biomolecular phase separation: from molecular driving forces to macroscopic properties. *Annual review of physical chemistry* 2020, **71:** 53-75.
32. Hyman AA, Weber CA, Jülicher F. Liquid-liquid phase separation in biology. *Annual review of cell and developmental biology* 2014, **30:** 39-58.
33. Brangwynne CP, Tompa P, Pappu RV. Polymer physics of intracellular phase transitions. *Nature Physics* 2015, **11**(11)**:** 899-904.
34. Alberti S, Gladfelter A, Mittag T. Considerations and challenges in studying liquid-liquid phase separation and biomolecular condensates. *Cell* 2019, **176**(3)**:** 419-434.
35. Abbas M, Lipiński WP, Wang J, Spruijt E. Peptide-based coacervates as biomimetic protocells. *Chemical Society Reviews* 2021, **50**(6)**:** 3690-3705.
36. Deshpande S, Dekker C. Studying phase separation in confinement. *Current Opinion in Colloid & Interface Science* 2021, **52:** 101419.
37. Shin Y, Brangwynne CP. Liquid phase condensation in cell physiology and disease. *Science* 2017, **357**(6357)**:** eaaf4382.
38. Shen Y, Ruggeri FS, Vigolo D, Kamada A, Qamar S, Levin A*, et al.* Biomolecular condensates undergo a generic shear-mediated liquid-to-solid transition. *Nature nanotechnology* 2020, **15**(10)**:** 841-847.
39. Mohammadi P, Jonkergouw C, Beaune G, Engelhardt P, Kamada A, Timonen JV*, et al.* Controllable coacervation of recombinantly produced spider silk protein using kosmotropic salts. *Journal of colloid and interface science* 2020, **560:** 149-160.
40. Kar M, Posey AE, Dar F, Hyman AA, Pappu RV. Glycine-Rich Peptides from FUS Have an Intrinsic Ability to Self-Assemble into Fibers and Networked Fibrils: Published as part of the Biochemistry virtual special issue "Protein Condensates". *Biochemistry* 2021, **60**(43)**:** 3213-3222.

41. Winkler S, Kaplan DL. Molecular biology of spider silk. *Reviews in Molecular Biotechnology* 2000, **74**(2)**:** 85-93.
42. Haritos VS, Niranjane A, Weisman S, Trueman HE, Sriskantha A, Sutherland TD. Harnessing disorder: onychophorans use highly unstructured proteins, not silks, for prey capture. *Proceedings of the Royal Society B: Biological Sciences* 2010, **277**(1698)**:** 3255-3263.
43. Kim S, Huang J, Lee Y, Dutta S, Yoo HY, Jung YM*, et al.* Complexation and coacervation of like-charged polyelectrolytes inspired by mussels. *Proceedings of the National Academy of Sciences* 2016, **113**(7)**:** E847-E853.
44. Yang X, Goldberg MS, Popova TG, Schoeler GB, Wikel SK, Hagman KE*, et al.* Interdependence of environmental factors influencing reciprocal patterns of gene expression in virulent Borrelia burgdorferi. *Molecular microbiology* 2000, **37**(6)**:** 1470-1479.
45. Bishop R, Lambson B, Wells C, Pandit P, Osaso J, Nkonge C*, et al.* A cement protein of the tick Rhipicephalusappendiculatus, located in the secretory e cell granules of the type III salivary gland acini, induces strong antibody responses in cattle. *International journal for parasitology* 2002, **32**(7)**:** 833-842.
46. Buchan DW, Jones DT. The PSIPRED protein analysis workbench: 20 years on. *Nucleic acids research* 2019, **47**(W1)**:** W402-W407.
47. Jumper J, Evans R, Pritzel A, Green T, Figurnov M, Ronneberger O*, et al.* Highly accurate protein structure prediction with AlphaFold. *Nature* 2021, **596**(7873)**:** 583-589.
48. Erdős G, Pajkos M, Dosztányi Z. IUPred3: prediction of protein disorder enhanced with unambiguous experimental annotation and visualization of evolutionary conservation. *Nucleic acids research* 2021, **49**(W1)**:** W297-W303.
49. Holehouse AS, Das RK, Ahad JN, Richardson MO, Pappu RV. CIDER: resources to analyze sequence-ensemble relationships of intrinsically disordered proteins. *Biophysical journal* 2017, **112**(1)**:** 16-21.
50. Ji Y, Li F, Qiao Y. Modulating liquid–liquid phase separation of FUS: mechanisms and strategies. *Journal of Materials Chemistry B* 2022, **10**(42)**:** 8616-8628.
51. Cascarina SM, Ross ED. Phase separation by the SARS-CoV-2 nucleocapsid protein: consensus and open questions. *Journal of Biological Chemistry* 2022, **298**(3).
52. Deegan RD, Bakajin O, Dupont TF, Huber G, Nagel SR, Witten TA. Capillary flow as the cause of ring stains from dried liquid drops. *Nature* 1997, **389**(6653)**:** 827-829.
53. Rebane AA, Ziltener P, LaMonica LC, Bauer AH, Zheng H, López-Montero I*, et al.* Liquid–liquid phase separation of the Golgi matrix protein GM130. *FEBS letters* 2020, **594**(7)**:** 1132-1144.
54. Berthier J, Brakke KA. *The physics of microdroplets*. John Wiley & Sons, 2012.
55. Elbaum-Garfinkle S, Kim Y, Szczepaniak K, Chen CC-H, Eckmann CR, Myong S*, et al.* The disordered P granule protein LAF-1 drives phase separation into droplets with tunable viscosity and dynamics. *Proceedings of the National Academy of Sciences* 2015, **112**(23)**:** 7189-7194.
56. Alshareedah I, Kaur T, Banerjee PR. Methods for characterizing the material properties of biomolecular condensates. *Methods in enzymology*, vol. 646. Elsevier, 2021, pp 143-183.
57. Wang J, Choi J-M, Holehouse AS, Lee HO, Zhang X, Jahnel M*, et al.* A molecular grammar governing the driving forces for phase separation of prion-like RNA binding proteins. *Cell* 2018, **174**(3)**:** 688-699. e616.
58. Martin EW, Holehouse AS, Peran I, Farag M, Incicco JJ, Bremer A*, et al.* Valence and patterning of aromatic residues determine the phase behavior of prion-like domains. *Science* 2020, **367**(6478)**:** 694-699.
59. Abbas M, Lipiński WP, Nakashima KK, Huck WT, Spruijt E. A short peptide synthon for liquid–liquid phase separation. *Nature Chemistry* 2021, **13**(11)**:** 1046-1054.

60. Mecozzi S, West Jr AP, Dougherty DA. Cation-pi interactions in aromatics of biological and medicinal interest: electrostatic potential surfaces as a useful qualitative guide. *Proceedings of the National Academy of Sciences* 1996, **93**(20)**:** 10566-10571.
61. Mahadevi AS, Sastry GN. Cation– π interaction: Its role and relevance in chemistry, biology, and material science. *Chemical reviews* 2013, **113**(3)**:** 2100-2138.
62. Hong Y, Najafi S, Casey T, Shea J-E, Han S-I, Hwang DS. Hydrophobicity of arginine leads to reentrant liquid-liquid phase separation behaviors of arginine-rich proteins. *Nature Communications* 2022, **13**(1)**:** 7326.
63. Sagle LB, Zhang Y, Litosh VA, Chen X, Cho Y, Cremer PS. Investigating the hydrogen-bonding model of urea denaturation. *Journal of the American Chemical Society* 2009, **131**(26)**:** 9304-9310.
64. Lim J, Kumar A, Low K, Verma CS, Mu Y, Miserez A*, et al.* Liquid–liquid phase separation of short histidine-and tyrosine-rich peptides: sequence specificity and molecular topology. *The Journal of Physical Chemistry B* 2021, **125**(25)**:** 6776-6790.
65. Lin Y, Fichou Y, Longhini AP, Llanes LC, Yin P, Bazan GC*, et al.* Liquid-liquid phase separation of tau driven by hydrophobic interaction facilitates fibrillization of tau. *Journal of molecular biology* 2021, **433**(2)**:** 166731.
66. Bowman AS, Sauer J. Tick salivary glands: function, physiology and future. *Parasitology* 2004, **129**(S1)**:** S67-S81.
67. Ribeiro JM, Mans BJ. TickSialoFam (TSFam): A database that helps to classify tick salivary proteins, a review on tick salivary protein function and evolution, with considerations on the tick sialome switching phenomenon. *Frontiers in cellular and infection microbiology* 2020, **10:** 374.
68. Lo Nostro P, Ninham BW. Hofmeister phenomena: an update on ion specificity in biology. *Chemical reviews* 2012, **112**(4)**:** 2286-2322.
69. Zhang Y, Cremer PS. Interactions between macromolecules and ions: the Hofmeister series. *Current opinion in chemical biology* 2006, **10**(6)**:** 658-663.
70. Bouzetos E, Ganar KA, Mastrobattista E, Deshpande S, van der Oost J. (R) evolution-on-a-chip. *Trends in Biotechnology* 2022, **40**(1)**:** 60-76.
71. Convery N, Gadegaard N. 30 years of microfluidics. *Micro and Nano Engineering* 2019, **2:** 76-91.
72. Poudyal RR, Guth-Metzler RM, Veenis AJ, Frankel EA, Keating CD, Bevilacqua PC. Template-directed RNA polymerization and enhanced ribozyme catalysis inside membraneless compartments formed by coacervates. *Nature communications* 2019, **10**(1)**:** 490.
73. Fleming PJ, Fleming KG. HullRad: Fast calculations of folded and disordered protein and nucleic acid hydrodynamic properties. *Biophysical journal* 2018, **114**(4)**:** 856-869.
74. Aarts DG, Schmidt M, Lekkerkerker HN. Direct visual observation of thermal capillary waves. *Science* 2004, **304**(5672)**:** 847-850.
75. Lynn GE, Černý J, Kurokawa C, Diktaş H, Matias J, Sajid A*, et al.* Immunization of guinea pigs with cement extract induces resistance against Ixodes scapularis ticks. *Ticks and Tick-borne Diseases* 2022, **13**(6)**:** 102017.
76. Hofman AH, van Hees IA, Yang J, Kamperman M. Bioinspired underwater adhesives by using the supramolecular toolbox. *Advanced materials* 2018, **30**(19)**:** 1704640.
77. Lu Y, Sharma B, Soon WL, Shi X, Zhao T, Lim YT*, et al.* Complete sequences of the velvet worm slime proteins reveal that slime formation is enabled by disulfide bonds and intrinsically disordered regions. *Advanced Science* 2022, **9**(18)**:** 2201444.
78. Guo Q, Zou G, Qian X, Chen S, Gao H, Yu J. Hydrogen-bonds mediate liquid-liquid phase separation of mussel derived adhesive peptides. *Nature Communications* 2022, **13**(1)**:** 5771.

79. Villar M, Pacheco I, Mateos-Hernández L, Cabezas-Cruz A, Tabor AE, Rodríguez-Valle M, *et al.* Characterization of tick salivary gland and saliva alphagalactome reveals candidate alpha-gal syndrome disease biomarkers. *Expert Review of Proteomics* 2021, **18**(12)**:** 1099-1116.
80. Agwunobi DO, Wang N, Huang L, Zhang Y, Chang G, Wang K, *et al.* Phosphoproteomic analysis of Haemaphysalis longicornis saliva reveals the influential contributions of phosphoproteins to blood-feeding success. *Frontiers in Cellular and Infection Microbiology* 2022, **11:** 1440.
81. Wang H, Zhang X, Wang X, Zhang B, Wang M, Yang X, *et al.* Comprehensive analysis of the global protein changes that occur during salivary gland degeneration in female ixodid ticks Haemaphysalis longicornis. *Frontiers in Physiology* 2019, **9:** 1943.
82. Walker AR, Fletcher JD, Gill HS. Structural and histochemical changes in the salivary glands of Rhipicephalus appendiculatus during feeding. *International journal for parasitology* 1985, **15**(1)**:** 81-100.
83. Sauer J, McSwain J, Bowman A, Essenberg R. Tick salivary gland physiology. *Annual review of entomology* 1995, **40**(1)**:** 245-267.
84. Estrada-Peña A, Venzal JM, Kocan KM, Sonenshine DE. Overview: ticks as vectors of pathogens that cause disease in humans and animals. 2008.
85. de la Fuente J. Controlling ticks and tick-borne diseases… looking forward. *Ticks and tick-borne diseases* 2018, **9**(5)**:** 1354-1357.
86. Bhowmick B, Han Q. Understanding tick biology and its implications in anti-tick and transmission blocking vaccines against tick-borne pathogens. *Frontiers in Veterinary Science* 2020, **7:** 319.
87. de la Fuente J. Translational biotechnology for the control of ticks and tick-borne diseases. Elsevier; 2021. p. 101738.
88. Trimnell AR, Hails RS, Nuttall PA. Dual action ectoparasite vaccine targeting 'exposed'and 'concealed'antigens. *Vaccine* 2002, **20**(29-30)**:** 3560-3568.
89. Zhou J, Gong H, Zhou Y, Xuan X, Fujisaki K. Identification of a glycine-rich protein from the tick Rhipicephalus haemaphysaloides and evaluation of its vaccine potential against tick feeding. *Parasitology research* 2006, **100:** 77-84.
90. Liu J, Spruijt E, Miserez A, Langer R. Peptide-based liquid droplets as emerging delivery vehicles. *Nature Reviews Materials* 2023, **8**(3)**:** 139-141.
91. Nuijens T, Toplak A, van de Meulenreek MB, Schmidt M, Goldbach M, Quaedflieg PJ. Improved solid phase synthesis of peptide carboxyamidomethyl (Cam) esters for enzymatic segment condensation. *Tetrahedron Letters* 2016, **57**(32)**:** 3635-3638.
92. Toplak A, de Oliveira EFT, Schmidt M, Rozeboom HJ, Wijma HJ, Meekels LK, *et al.* From thiol-subtilisin to omniligase: Design and structure of a broadly applicable peptide ligase. *Computational and structural biotechnology journal* 2021, **19:** 1277-1287.
93. Deshpande S, Dekker C. On-chip microfluidic production of cell-sized liposomes. *Nature protocols* 2018, **13**(5)**:** 856-874.
94. Chen C, Ganar KA, Deshpande S. On-Chip Octanol-Assisted Liposome Assembly for Bioengineering. *JoVE (Journal of Visualized Experiments)* 2023(193)**:** e65032.
95. Salomon J, Hamer SA, Swei A. A beginner's guide to collecting questing hard ticks (Acari: Ixodidae): a standardized tick dragging protocol. *Journal of Insect Science* 2020, **20**(6)**:** 11.
96. Roe RM, DONOHUE K, KHALIL S, BISSINGER B, Zhu J, SONENSHINE D. Biology of Ticks. 2014.
97. Patton TG, Dietrich G, Brandt K, Dolan MC, Piesman J, Gilmore Jr RD. Saliva, salivary gland, and hemolymph collection from Ixodes scapularis ticks. *JoVE (Journal of Visualized Experiments)* 2012(60)**:** e3894.

Chapter 5

Cell-free screening of CRISPR-Cas activity by microfluidics-assisted *in vitro* compartmentalization

ABSTRACT

CRISPR-Cas systems are an immune mechanism of prokaryotic cells that have been adapted to a powerful genome-editing tool. On the other hand, the applicability of native CRISPR-Cas nucleases can be restricted by several constraints. Protein engineering through rational design and directed evolution have presented a variety of synthetic variants with altered properties circumventing many existing constraints. Commonly, directed evolution of CRISPR-Cas systems is combined with *in vivo* selection schemes which however can suffer from transformation bottlenecks, cell toxicity and selection pressure escapees. *In vitro* compartmentalization abolishes the need of living cells in favour of cell-free gene expression inside artificial compartments and has been successfully applied for endonuclease evolution. This chapter demonstrates the activity of CRISPR-Cas systems using cell-free transcription and translation extract and prototyping fluorescence-based gene circuits to allow screening of CRISRP-Cas activity. Using high-throughput on-chip microfluidics technology, we produced water-in-oil-in-water double emulsions and used it as synthetic *in vitro* compartments to link CRISPR-Cas system to fluorescent GFP expression. Using these micro-confinements, we demonstrated fluorescence-based screening for target sgRNA genotypes in a model compartment population using fluorescence-activated cell sorter and retraced phenotype-to-genotype linkage.

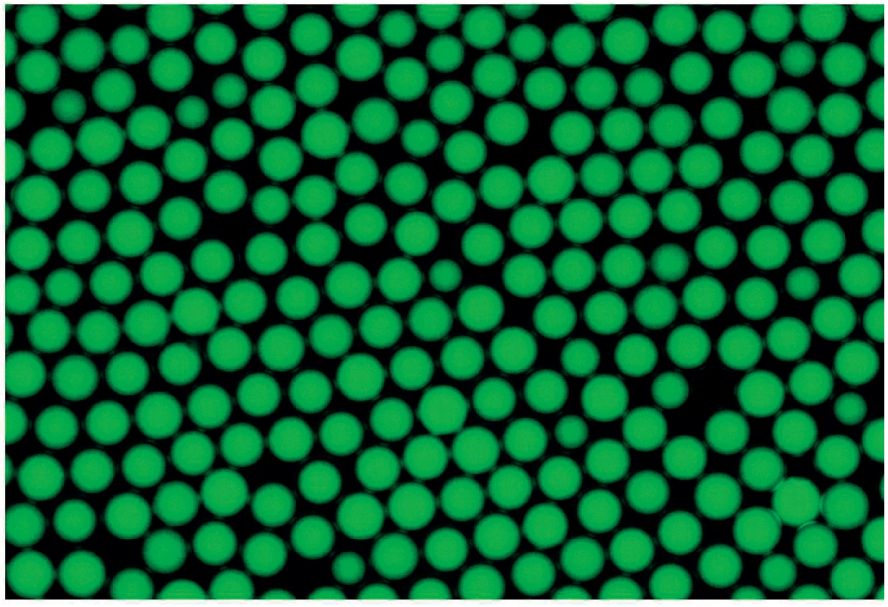

5.1 INTRODUCTION

CRISPR-Cas system is an adaptive immune response in prokaryotic cells, defending against viral infections and other mobile genetic elements[1, 2]. CRISPR-Cas consists of two main components, namely the Cas-effector protein and a guide RNA (gRNA) that form a ribonucleoprotein (RNP) complex[3]. This RNP complex proceeds to interrogate large double stranded DNA sequences to find a 20-30nt long target sequences (also called protospacers) for base complementarity with the variable part of the gRNA[4, 5]. Prerequisite for initiating the formation of the heteroduplex between gRNA and target DNA strand is the presence of a 3-8nt long sequence, named protospacer adjacent motif (PAM), at the 5' or 3'-end of the protospacer, depending on the CRISPR-Cas system[6, 7]. After formation of an R-loop structure (formation by the gRNA/target DNA heteroduplex and displacement of the non-target strand), specific cleavage of both DNA strands is catalysed by the nuclease domains of the Cas-effector[4, 5]. The ease of programming target sequence cleavage in a variety of host organisms has set CRISPR-Cas systems as a versatile platform in the field of genome engineering, gene therapy, strain engineering, and diagnostics[8, 9, 10].

The ease of programmable target sequence cleavage by CRISPR-Cas systems has had huge impact in the field of genetic engineering[11, 12]. Yet, naturally occurring Cas-effector variants often fail in certain applications, leaving room for innovation and improvement of Cas applicability. Some well-known constraints of native CRISPR-Cas systems are low specificity (high off-target interference), requirement of specific PAM motifs, and low nuclease activity under certain physiological conditions[13]. Protein engineering of Cas-effectors has produced a variety of synthetic variants with new properties such as altered PAM compatibility, increased specificity and/or activity[14, 15, 16].

Synthetic variants of Cas-effector can be rational when the tertiary structure is available or alternatively can be engineered through random mutagenesis[17, 18]. Random mutagenesis is commonly performed in combination with an *in vivo* selection system in microorganisms such as *Escherichia coli*, yeast or mammalian cells[14, 15, 16, 19, 20]. However, *in vivo* selection systems can suffer from low gene expression, transformation bottlenecks and host genome mutations[21, 22].

In vitro compartmentalization (IVC) eliminates the use of living cells in favour of cell-free, gene expression inside synthetic compartments[23, 24]. IVC has been successfully applied for selection of endonucleases and other nucleic acid-interacting protein variants[25, 26, 27, 28]. Genotype-to-phenotype linkage is ensured by including the target sequence in the nucleic acid fragment that also encodes the protein of interest. In

the case of endonucleases, the link was based on the ligation of an adaptor sequence to the cohesive ends found in the cleaved dsDNA products. These adaptor sequence subsequently served as a primer binding site for subsequent PCR reaction, amplifying only the genotypes that encoded active enzymes[29, 30]. CRISPR-Cas systems can have multiple cleavage patterns and therefore different cohesive ends can be produced from one Cas-effector, thus complicating the design of adaptor sequences[31, 32]. Also deactivated Cas-effector can still interfere with target sequences and they have adapted to valuable tools for gene expression regulation[33, 34, 35]. We envisioned to adapt the classic IVC approach to a high throughput screening scheme based on fluorescence level alterations, omitting the need of an adaptor sequence.

Our adaptation is based in the generation of monodisperse water-in-oil-in water emulsions with on-chip microfluidics devices and their subsequent screening with a fluorescent activated cell sorter (FACs)[36]. On-chip microfluidics technology allows manipulation of fluids at the micrometre scale allowing the generation of highly monodisperse compartments at high speeds[37]. Uniform compartment size ensures homogenous encapsulation of biomolecules, making it easy to compare gene activity to fluorescence intensity[38]. The double emulsion nature of the compartments sets them compatible with common cell sorting equipment and abolishes the need for complex microfluidics devices[39, 40]. However, double emulsions are prone to deformation under shear[41] and can also rupture in an osmotic imbalance environment[42]. Thus, downstream calibration is still necessary for the screening procedure by the cell sorter. Brower KK et. al. developed sdDE-FACS (single droplet Double Emulsion-FACS) and extensively optimized instrument settings (laser, flow rate, and drop delays) for commercially available cell sorters, enabling droplet recovery up to 70%[43].

In this study, we set out to develop an IVC platform that allows cell-free and high-throughput screening of CRISPR-Cas activity based in alterations in fluorescence levels. We tested and prototyped genetic circuits that connect CRISPR-Cas activity to fluorescence intensity. We proceeded to engulf the genetic components of the gene circuits along with a cell-free transcription translation (TXTL) extract into water-in-oil-in-water confinements to observe the expected fluorescence relation between the tested conditions. Next, we demonstrate fluorescence-activated screening of the artificial compartments and enrichment of the target genotype from a model droplet population using a cell sorting device. Having demonstrated phenotype-to-genotype linkage and target sequence enrichment, the described *in vitro* screening strategy may provide the basis for future screening of complex CRISPR-Cas gene libraries.

5.2 RESULTS AND DISCUSSION

5.2.1 On-chip encapsulation of cell-free TXTL extract in double emulsions

To generate micron-sized water-in-oil-in-water double emulsions (DEs), we fabricated PDMS-based microfluidic devices with two consecutive flow-focusing junctions connected by a resistance loop (**Figure 5.1a**). A horizontal channel designated to carry the inner contents of the DEs, and hereafter referred to as inner aqueous channel, feeds into the first flow-focusing junction formed by two perpendicular oil channels carrying the continuous oil phase (**Figure 5.1a; Figure S5.1**). The exit of the first junction is strategically designed as a single loop which effectively increases the length of the channel providing enough resistance to optimize the pressures in inner aqueous and oil channels during production. The resulting single emulsions (SEs) are then directed to the second junction, where perpendicular channels facilitate the pinching off of the SEs by a surfactant-containing outer aqueous phase, forming DEs (**Figure 5.1a**). A snapshot of the formation of double emulsions is shown in **Figure S5.3**. The generated DEs flow through the exit channel and are collected via the exit hole and stored in a glass vial. Prior to the production of DEs, the microfluidic devices undergo surface passivation to make the exit channel hydrophilic (details in Material and Methods; **Figure S5.2**). This prevents the oil phase wetting the microfluidic channels.

To assess the encapsulation and retention of small molecules, 10 μM of fluorescein isothiocyanate (FITC) fluorescent dye dissolved in PBS was used as the inner aqueous phase. The produced DEs efficiently encapsulated and retained the FITC dye for >24 hours (**Figure 5.1b**) indicating retention of small molecules. For a typical experiment, the DEs were produced with an average diameter of 37.6 ± 1.8 μm (N = 1875; coefficient of variation = 4.6%) (**Figure 5.1c**) and with a throughput of around 500 Hz, producing >10^6 droplets in an hour. After characterizing the stability, encapsulation, retention, and monodisperse nature of the DEs, we further tested its biocompatibility. We produced DEs with inner aqueous phase consisting of cell-free transcription and translation (TXTL) machinery along with 1 nM of green fluorescent protein (GFP) encoding plasmid (**Figure 5.1d**). While TXTL is a complex cell extract with the precise osmolarity not known, 1% Tween-20 surfactant in PBS pH 7.4 in the outer aqueous phase resulted in stable DEs. Upon incubation at 30°C for 16 hours, the DEs showed bright fluorescence intensity (1044 ± 217; mean ± standard deviation; N = 412) indicating successful transcription and translation of the GFP protein (**Figure 5.1e-f; Figure S5.4**). Under identical imaging conditions, a negative control (no GFP plasmid but only TXTL) showed negligible fluorescence intensity.

Two-tailed significance test also confirmed significant different between two samples with p value < 0.001.

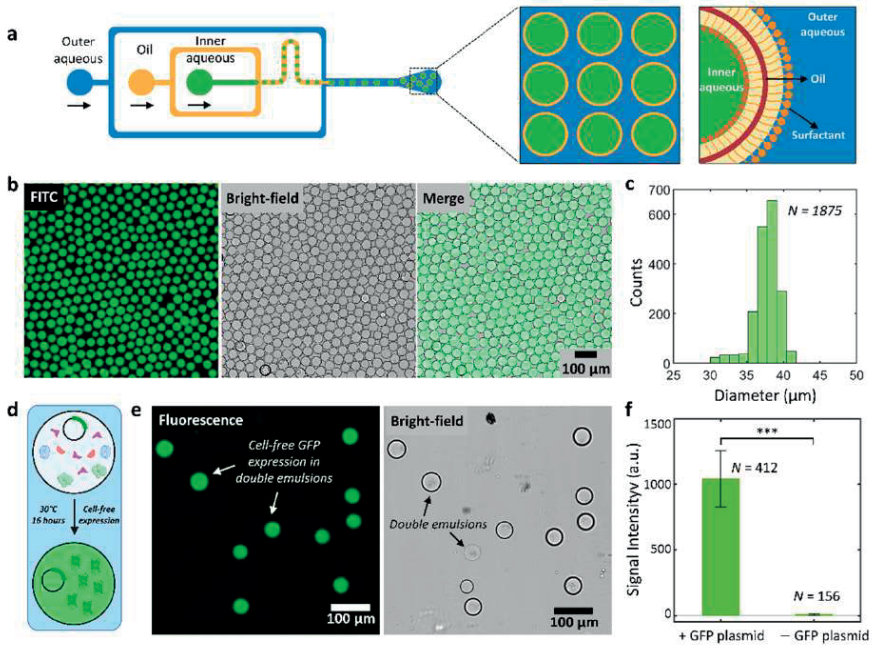

Figure 5.1: On-chip controlled generation of TXTL-compatible double emulsions.

(a) A schematic depicting the two-junction flow-focussing device for high-throughput production of double emulsions. The initial flow-focussing junction generates water-in-oil single emulsions, with the inner aqueous phase depicted in green and the oil phase in yellow. Subsequently, the second junction generates water-in-oil-in-water double emulsions. The water/oil interface of both the inner aqueous core and outer aqueous continuous medium are stabilized via surfactants. (b) Demonstration of encapsulation and retention of small molecules, such as fluoresceine isothiocyanate (FITC), within the double emulsions stored for 24 hours. (c) The size characterization of the generated double emulsions reveals monodisperse confinements, with a diameter measuring 37.6 ± 1.8 µm (mean ± standard deviation; N = 1875). (d) Schematic depicting encapsulation of cell-free transcription and translation machinery along with green fluorescent protein (GFP) encoding plasmids in double emulsions, and the expression of GFP protein upon incubating at 30°C for over 16 hours. (e) Fluorescent microscopy images showing successful in vitro cell-free expression and retention of GFP protein within the double emulsions Images acquired post 16 hour incubation at 30°C. (f) Quantitative analysis of average fluorescence signal intensity in double emulsions encapsulating GFP plasmids (N = 412) showed significantly higher intensity than in the absence of GFP plasmid (while retaining cell-free transcription and translation machinery (N = 156) with a p-value < 0.001. Error bars represent standard deviations among the fluorescence measured in different compartments.

5.2.2 CRISPR-Cas activity in double emulsions

Robust activity of CRISPR-Cas systems has previously been demonstrated with the *Escherichia coli* cell-free extract commonly referred to as transcription and translation mix (TXTL)[44]. TXTL drives efficient cell-free expression with the *E. coli* endogenous RNA polymerase and sigma-70 (σ70) factors[45]. We tested four known σ70 promoters driving deGFP expression in the cell-free extract (**Figure S5.10**). As expected, we observed detectable but varying protein expression between the σ70 promoters, whereas no deGFP expression was detected when using the T7 promoter (**Figure S5.10**). Next, we tested the activity of CRISPR-Cas systems in TXTL. We tried three different CRISPR nucleases for three different spacers on the deGFP expression cassette: the Type II-A SpCas9 nuclease from *Streptococcus pyogenes*, the Type II-C ThermoCas9 nuclease from *Geobacillus thermodenitrificans* T12 and the miniature, Type V-F AsCas12f1 nuclease from *Acidobacillus sulfuroxidans* (**Figure S5.11**). All three nucleases demonstrated robust guided repression of deGFP expression for all tested target positions (**Figure S5.11**). In this section, we detail the genotype-to-phenotype linkage strategy using SpCas9 as a model protein.

In this approach, SpCas9 in presence of targeting sgRNA cleaves the deGFP-encoding gene resulting in lower amount of deGFP (**Figure 5.2a**). While in presence of non-targeting sgRNA, the SpCas9 is unable to find desired site on the deGFP plasmid hence no nuclease activity occurs (**Figure 5.2b**). We validated this gene circuit by monitoring fluorescence intensity in the plate reader. The measurements showed gradual increase in fluorescence intensity in presence of non-targeting sgRNA (NT) (**Figure 5.2c**), while targeting sgRNA actively inhibited the expression of deGFP. Additionally, we tested three different targeting sites (Sp3, Sp6 and Sp9) on the deGFP encoding plasmid and all of them showed similar deGFP expression profile (**Figure 5.2c**). After confirming robust activity of SpCas9 in TXTL in bulk measurements, we proceeded to compartmentalize the cell-free expression reaction mix for the SpCas9 nuclease in DEs.

Similar to bulk measurements, we observed notably lower fluorescence in compartments engulfing a targeting spacer sequence than in compartments engulfing a non-targeting (NT) spacer sequence (**Figure 5.2d,e; Figure S5.5**). The time required for gene expression, ribonucleoprotein complex formation and eventually target interference explains the observed fluorescence (indicating deGFP expression) during the initial stages of the cell-free expression reaction. This results in lower but yet detectable levels of fluorescence even in the case of a non-targeting spacer (**Figure 5.2d,e; Figure S5.5**). Background-corrected fluorescence intensity revealed that the DEs containing gene circuit with non-targeting sgRNA displayed a signal intensity of approximately 609 ± 111 (N = 66) (**Figure 5.2e**). In contrast, when targeting guide

RNA (sgRNA9) was present, the fluorescence intensity measured 339 ± 70 (N = 57). The two populations were found to be statistically significant (p-value < 0.001, see Materials and Methods for details). These results demonstrate differentiation between different sgRNA using this gene circuit.

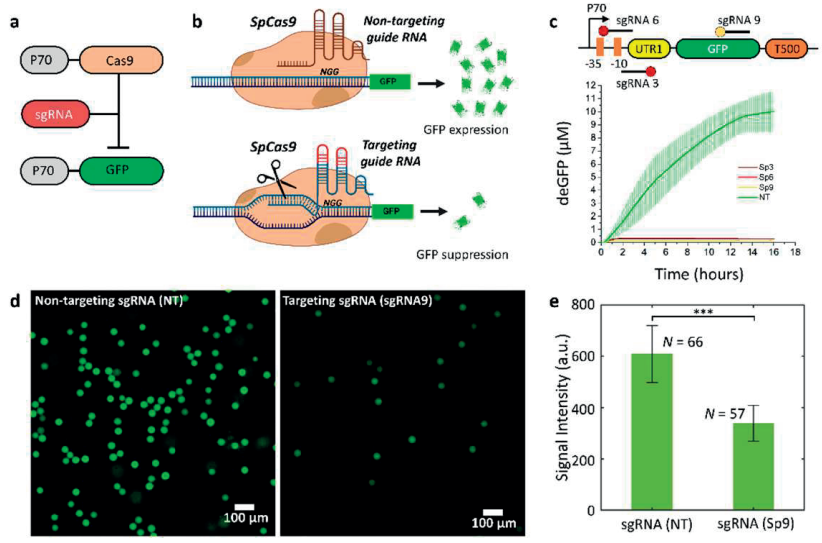

Figure 5.2: Guided regulation of protein expression by CRISPR-Cas systems inside double emulsions. (a) Guided DNA-interference by CRISPR-Cas systems on a deGFP encoding DNA template results in decreased fluorescence levels. (b) Schematic representation of the molecular mechanisms behind fluorescence level alterations due to CRISPR-Cas guided DNA interference. (c) Kinetic measurements of deGFP(μM) concentration in presence of 1nM: pP70a_deGFP, 3nM: pJ23108_Cas and 1nM: pJ23119_sgRNA. Three target sites in the deGFP expression cassette are shown. Circles represent the PAM sequence and straight lines the spacer sequence. Error bars represent the SD from three repetitions. (d) Microscopy images of double emulsions encapsulating cell-free extract supplemented with 1nM: pP70a_deGFP, 3nM: pJ23108_SpCas9 and 1nM pJ23119_sgRNA 9 or 1nM pJ23119_sgRNA NT. Images acquired post 16 hour incubation at 30°C. (e) Quantitative analysis shows that the average fluorescence intensity of GFP in presence of gene circuit with non-targeting sgRNA (NT) (N = 66) is significantly higher compared to gene circuit consisting of targeting sgRNA (Sp9) (N = 57) with a p-value <0.001.

Next, we sought to investigate the differentiation between a synthetic variant and a wild-type variant. (**Figure 5.3a**). We chose to compare the wild type SpCas9, wtSpCas9, that requires for 3'-NGG PAM, with the nearly PAM-less SPRYCas9, a synthetic variant for targeting protospacers with the non-canonical, 3'-YAC, PAM[46] (**Figure 5.3b**). Three protospacers, flanked by the 3'-YAC PAM motif, were tested in cell-free TXTL reactions supplemented with plasmid vectors encoding either for wtSpCas9 or SPRYCas9 (**Figure 5.3b**). Expectedly, wtSpCas9 failed to interfere with

the non-canonical PAM targets, which resulted in no fluorescence alteration when compared with a non-targeting spacer (**Figure 5.3c**). On the other hand, SPRYCas9 successfully interfered with the non-canonical PAM

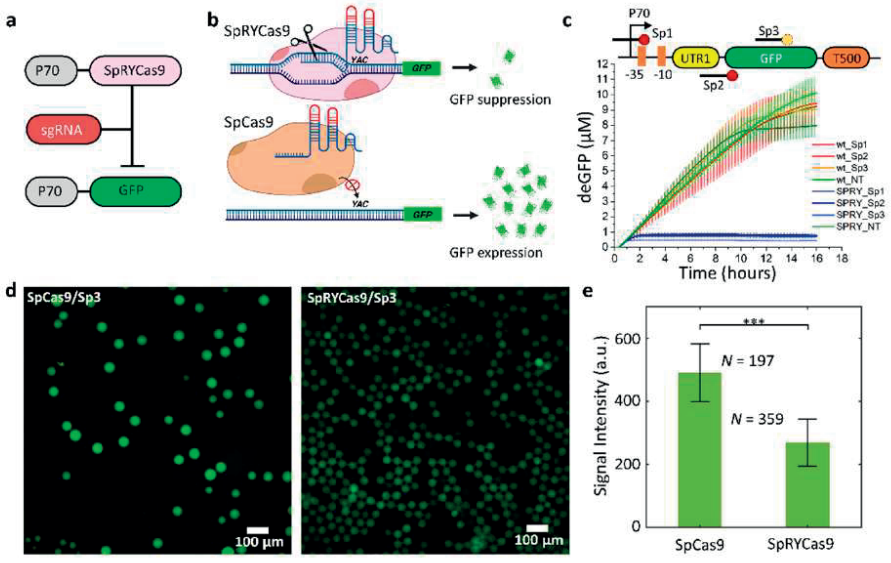

Figure 5.3: PAM recognition in TXTL.

(a) Guided DNA-interference by CRISPR-Cas systems on a deGFP encoding DNA template results in decreased fluorescence levels. (b) Schematic representation of the molecular mechanisms behind fluorescence level alterations due to PAM-identification by CRISPR-Cas. (c) Kinetics measurements of deGFP concentration is presence of 1nM: pP70a_deGFP, 3nM: pJ23108_Cas (wtSpCas9 or SPRYCas9) and 1nM: pJ23119_sgRNA. Three target sites for non-canonical PAMs in the deGFP expression cassette are shown. Circles represent the PAM sequence and straight lines the spacer sequence. Error bars represent the SD from three repetitions. (d) Microscopy photographs of double emulsions encapsulating cell free extract supplemented with 1nM: pP70a_deGFP, 3nM: pJ23108_SpCas9 or pJ23108_SPRYCas9 and 1nM: pJ23119_sgRNA Sp3 or 1nM: pJ23119_sgRNA NT. Images acquired post 16 hours incubation at 30°C. (e) Quantitative analysis shows that the average fluorescence intensity of GFP within double emulsion droplets showed significantly high fluorescence in case of gene circuit consisting of SpCas9 (N = 197) compared to the gene circuit consisting of SpRYCas9 (N = 359) with a p-value <0.001.

targets, in all three cases and resulted in reduced deGFP concentration (**Figure 5.3c**). We the proceeded by creating DEs engulfing either wtSpCas9 or SPRYCas9 along with the non-canonical PAM targeting spacer Sp3 (**Figure 5.3d; Figure S5.6**). Verifying our previous observations, compartments that encapsulated SPRYCas9 plasmid vectors demonstrated significantly lower fluorescence than those engulfing wtSpCas9 plasmid vectors (**Figure 5.3d,e; Figure S5.6**). Analysing the fluorescent intensities

in the DEs under identical imaging conditions revealed a signal intensity for SpCas9 around 490 ± 91 (*N*= 197) (**Figure 5.3e**). The signal intensity for the SpRYCas9 variant was noted to be 269 ± 75 (*N* = 359) **Figure 5.3e**). The two populations were found to be statistically significant (p-value < 0.001). This concludes the versatile nature of this gene circuit to link genotype-to-phenotype.

5.2.3 Linking CRISPR-Cas activity to increased deGFP expression in TXTL

Despite the inherent advantages of directly targeting the GFP gene, some notable concerns persist. The stochastic nature of biomolecule encapsulation DEs introduce a potential challenge, wherein the failure to encapsulate essential biomolecules in DEs may affect GFP expression. This circumstance could be misjudged as enzyme-assisted gene cleavage, leading to a false positive interpretation. Moreover, the irreversible nature of SpCas9-mediated cleavage of the GFP gene rules out the possibility of recovering the GFP plasmid.

To surmount this limitation, we investigated an alternative approach by linking the deGFP expression to SpCas9 through the integration of a repressor. In this novel gene circuit, deGFP expression is governed by the repressor cl protein which binds to P70a promotor on the deGFP plasmid and thus supresses deGFP protein expression (**Figure 5.4a**). Now instead of deGFP, the SpCas9 is directed to target the cl gene in such a way that in presence of targeting sgRNA, SpCas9 cleaves the cl gene, consequently enabling uninterrupted expression of deGFP and resulting in high fluorescence (**Figure 5.4a,b**). In contrast, in the presence of non-targeting sgRNA, SpCas9 fails to cleavage the cl gene, leading to active cl-based suppression of deGFP, resulting in the loss of fluorescence (**Figure 5.4b**). A degradation tag, ssrA was genetically fused with the cl protein so that enough time was provided for the formation of nucleoprotein complex. Guided repression of the cI-ssrA expression resulted in higher deGFP concentration for all three tested targeting sites when compared to a non-targeting sgRNA (**Figure 5.4c**). We proceeded to compartmentalize the cell-free extract supplemented with SpCas9 plasmid vectors and the non-targeting sgRNA or the cI-ssrA targeting spacer (Sp3). As expected, compartments encapsulating the targeting sgRNA exhibited higher fluorescence than compartments encapsulating the non-targeting spacer (**Figure 5.4d,e; Figure S5.7**). Microscopically measuring the fluorescence intensity of these DEs after 16 hours, under identical conditions, showed that DEs in presence of NT sgRNA showed an average fluorescent intensity of 105 ± 24 (N = 723). On the contrary, average fluorescence intensity of the droplets in presence of targeting sgRNA Sp3 was 423 ± 119 (N = 921).

Finally, we optimized the repression cascade to increase the fluorescence gain ratio. We substituted the P70a_promoter which drove cI-ssrA expression with the equal strong

but constitutively active J23119 promoter (**Figure S5.10**; **Figure S5.12**). Stronger repression from the J23119_cI-ssrA resulted in higher fluorescence gain when interference was guided with SpCas9 and a targeting sgRNA (**Figure S5.13**).

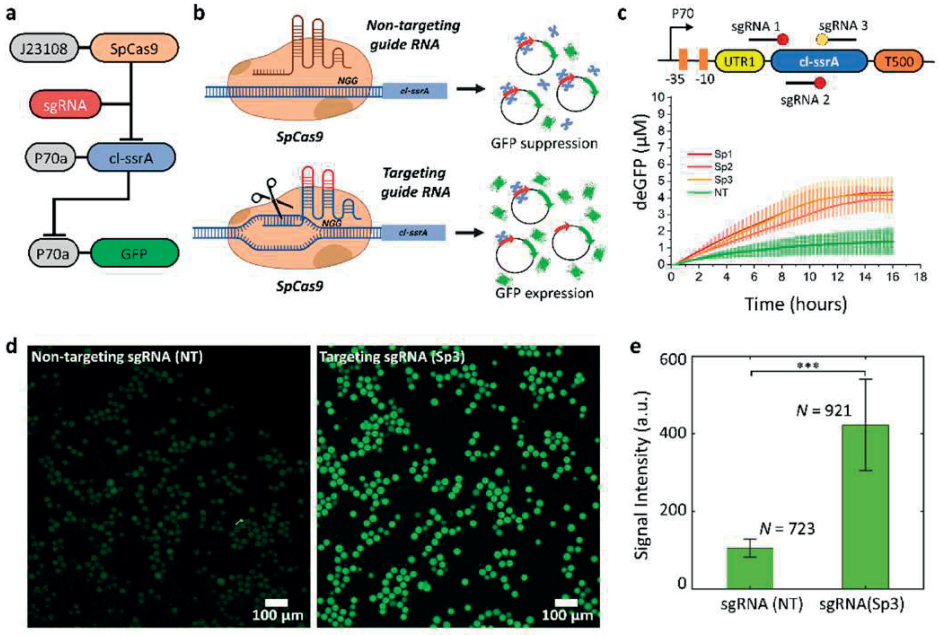

Figure 5.4: Indirect linkage of CRISPR-Cas activity with increased fluorescence.

(a) Guided DNA-cleavage by CRISPR-Cas systems of the cI_ssrA prevents transcriptional repression of P70a promoter resulting in increased fluorescence levels. (b) Schematic representation of the molecular mechanisms behind increase in the fluorescence levels due CRISPR-Cas guided DNA interference on the cI_ssrA gene. (c) Kinetics measurements of deGFP concentration is presence of 1nM:pP70a_deGFP, 1nM:pP70a_cI-ssrA, 3nM:pJ23108_Cas and 1nM: pJ23119_sgRNA. Three target sites in the cI_ssrA expression cassette are shown. Circles represent the PAM sequence and straight lines the spacer sequence. Error bars represent the SD from three repetitions. (d) Microscopy photographs of double emulsions encapsulating cell free extract supplemented with 1nM: pP70a_deGFP, 1nM: pP70a_cI-ssrA 3nM: pJ23108_SpCas9 and 1nM: pJ23119_sgRNA Sp3 or 1nM: pJ23119_sgRNA NT. Images acquired post 16 hour incubation at 30°C. (e) Quantitative measurement of the average fluorescence intensity within the double emulsions showed significantly lower expression of GFP in gene circuit consisting of non- targeting sgRNA (NT) (N = 723) compared to gene circuit with targeting sgRNA (Sp3) (N = 921) with a p-value <0.001.

5.2.4 Genotype enrichment from a model droplet population using a commercial cell sorter

In the previous sections, we showed that in each CRISPR/Cas gene circuit the genotype had a significant effect on the phenotype confirmed using both qualitative and quantitative analysis. But could we retrace the genotype from phenotype? For this we used the commercially available fluorescence activated cell sorter (FACS). (Since DEs are larger and more deformable than cells[47] significant optimization of FACS settings was required (details in Material and Methods). To show proof-of-principle retracing of genotype from phenotype, we generated two DE populations encapsulating cell-free extract supplemented with wtSpCas9 and either (i) a non-targeting spacer vector or (ii) the targeting spacer (Sp9) vector as shown in **Figure 5.2c**. Separate microfluidic chips were used for DE generation to prevent cross contamination of sgRNAs. Both the emulsions were incubated overnight for the cell-free expression to take place and were mixed in a 1:1 volume ratio prior analysing using FACS (**Figure 5.5a**). Size-based analysis of approximately 15000 events (each event corresponds to a sample passing through the detector) using forward scattering width (FCS-W) and backward scattering area (BSC-A) (**Figure 5.5b**) showed that approximately 48% (N=7318) of the population was in the high FSC-W region (500 < FSC-W < 2000) and high BSC-A region (10^5 < BSC-A < 10^7). We observed a broad distribution of fluorescence intensity ranging from 10^3 to 10^5. However, two distinct peaks of higher (H) and lower (L) fluorescence could be gated and sorted accordingly (**Figure 5.5c**). The double emulsion samples before and after sorting were imaged using fluorescence microscopy. The pre-sort mixture microscopically showed droplets of varying fluorescence intensity visually (**Figure 5.5d**) and quantitative analysis also showed a broad distribution of the signal intensities (**Figure 5.5e**). Similarly, microscopic examination of the DE populations post-sorting showed double emulsions in Gate-H having a relatively higher fluorescence intensity compared to double emulsions in Gate-L (**Figure 5.5d; Figure S5.8**). This was further confirmed by analysing the fluorescence intensity of the recovered DEs. Double emulsions in Gate-H (79 ± 21; N = 248) were slightly more fluorescent as compared to that for Gate-L (63 ± 17; N= 233) with a significant p-value < 0.001) (**Figure 5.5f**).

The sorted H and L compartment double emulsions and unsorted mixed model population were next submitted to PCR for amplification of the sgRNA expression cassettes. After verification of correct amplicon size, amplicons were cleaned and concentrated and submitted for sanger sequencing. Subsequent alignment with the in-silico maps of the sgRNA plasmid vectors revealed spacer genotype enrichment according to fluorescent intensity (**Figure 5.5g**), validating retracing of the genotype from phenotype.

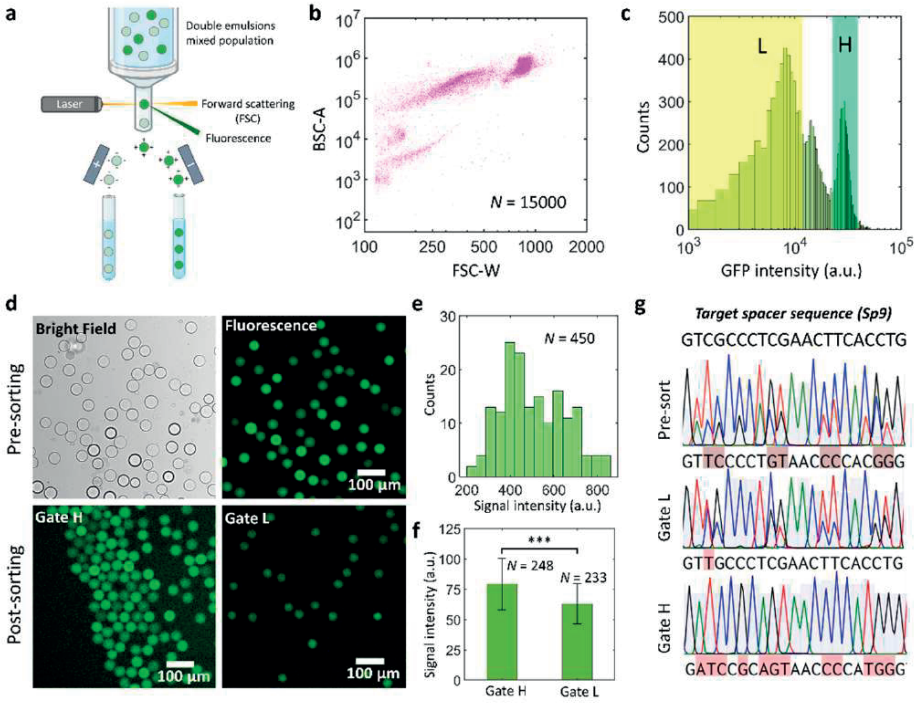

Figure 5.5: Retracing phenotype to genotype using fluorescence-assisted sorting of double emulsions. (a) Schematics illustrating the process of fluorescence-assisted sorting of double emulsions (b) Size-based analysis of the mixed double emulsion population. The input sample comprised two distinct double emulsions: the first with SpCas9, GFP, and targeting sgRNA, and the second with gene circuit SpCas9, GFP, and non-targeting sgRNA. Approximately 48% (N = 7318) of the total population (N = 15000) exhibited high forward scattering (500 < FSC- W < 2000) and backward scattering (105 < BSC-A < 107). (c) Analysis of the entire population based on GFP-associated fluorescence intensity revealed two distinct peaks between 103 and 105. Gate-L was designated for the low fluorescence intensity population, while Gate-H was assigned to the high fluorescence intensity population. (d) Microscopic imaging of the pre- sorting droplet population using bright-field and fluorescence channels. Fluorescent images showcase recovered double emulsions post-sorted in Gate-H and Gate-L. Images acquired post 16 hour incubation at 30°C followed by 4 hour storage at 25°C (e) Histogram depicting the fluorescence intensity within measured within pre-sorted double emulsion droplets ranging between 200 and 800 a.u. (f) Normalized signal intensity measured in the double emulsion droplets in Gate-H and Gate-L, indicating 79 ± 21 (mean ± standard deviation : N = 248) and 63 ± 17 (mean ± standard deviation : N= 233) respectively, with p-value < 0.001 indicating significant different between the two populations. (g) Pre-sort: Alignment of sequenced amplicon of pre-sorted sample vs target spacer 9 sequence. Gate L: Alignment of sequenced amplicon of Gate L sorted sample versus target spacer 9 sequence. Gate H: Alignment of sequenced amplicon of Gate H sorted sample versus target spacer 9 sequence. The sorted and recovered and double emulsion droplets showed sgRNA genes corresponding to targeting and non-targeting population in Gate-L and Gate-H respectively.

5.3 CONCLUSION

The demand for precision genome editing is important particularly in the field of gene therapy, requiring efficient and accurate CRISPR/Cas editing systems. While directed evolution is an important tool to engineer proteins the traditional use of cells to evolve protein often fails due to varied gene expression levels, loss of gene in the iteration process, transformation bottleneck, and gene toxicity. In this chapter, we aimed to tackle this problem by using synthetic confinements along with cell-free extract to express the CRISPR/Cas system and link the enzymatic activity to fluorescent GFP. We developed an on-chip microfluidic device to generate water-in-oil-in-water double emulsions, serving as artificial cell-like confinements. Owing to the two junction flow-focus design, the double emulsions generation is a single-step process while maintaining its encapsulation efficiency, along with high production rate (up to 500 Hz).

To establish genotype-to-phenotype link we used fluorescence-based assay, presenting two distinct strategies connecting CRISPR/Cas system to regulate GFP protein expression. In the direct approach, Cas9 targeted and cleaved GFP encoding gene, leading to reduced GFP production and thus resulting in lower fluorescence of double emulsion. This strategy is versatile, and we demonstrated screening of both sgRNA and different variant of Cas9-like SpRYCas9. On the contrary, the indirect approach involved introducing a repressor to inhibit GFP production, with Cas9 targeting the repressor. Correct sgRNA enabled Cas9 to cleave the repressor, facilitating uninterrupted GFP expression and resulting in increased fluorescence of the double emulsion droplets. We believe these strategies hold potential in evolving new variants of CRISPR/Cas system with higher specificity and activity.

The chapter further demonstrated the fluorescence-based screening of double emulsions using commercially available FACS. By creating a model population with distinct double emulsions containing either targeting or non-targeting sgRNA, we successfully sorted double emulsions based on varying fluorescence intensity, from low to high. The genotype corresponding to each phenotype was accurately retraced. In conclusion, this chapter outlines a straightforward procedure for creating artificial cell-like confinement through on-chip microfluidics, details methodologies linking CRISPR/Cas9 activity to GFP production, and illustrates fluorescence-based sorting of double emulsions.

5.4 MATERIALS AND METHODS

5.4.1 Microfluidic chip fabrication.

The master wafer was prepared using previously described UV lithography[48] and the protocol was adjusted at attain for channel height of 20 µm. as described in previous study. To prepare the microfluidic devices, polydimethylsiloxane (PDMS; SYLGARD™184 elastomer) and curing agent were mixed in 10:1 weight ratio. The mixture was poured on the master, degassed using vacuum desiccator and baked at 70°C for 4 hours. The hardened PDMS block was carefully removed and inlet and exit holes were punched using a biopsy punch of 1.2 mm diameter (PT-T983-05, Darwin Microfluidics). The PDMS block was then bonded to PDMS-coated glass slide (1mm thickness, Corning 2947-75x25) and incubated at 80°C for 2 hours. To produce water-in-oil-in-water DEs the outer aqueous and exit channels were passivated by flowing 5 % w/v polyvinylalcohol (Sigma-Aldrich P8136) solution making these channels hydrophilic. The device is then baked at 120 °C for 15 minutes and stored at room temperature in a dry place. The device was rested for at least 12 hours before using to generate double emulsion. To flow the fluid through the microfluidic channel PTFE tubing (LVF-KTU-15, Darwin microfluidic) was connected to microfluidic reservoir XS (LVF-KPT-4XS, Darwin microfluidics). The fluid flow was controlled using pressure controller OBK1 Mk3+ (Elveflow).

5.4.2 Fluid Composition.

The inner aqueous consisted of 1 nM of deGFP encoding plasmid, 1 nM of spacer guide RNA encoding plasmid, 3 nM of Cas encoding plasmid, and TXTL mixture according to manufacturer's protocol. The oil phase consisted of HFE-7500 with 2% w/w Floursurf-C (EU-FSC-V10-2%-HFE7500, Darwin microfluidics). The outer aqueous consisted of PBS pH7.4 with 1% Tween-20.

5.4.3 Microscopic visualization of droplets.

All the microscopic images were acquired using Nikon-Ti2-Eclipse inverted fluorescence microscope equipped with pE-300ultra illumination system. The droplets were visualized using Nikon CFI Plan Fluor 10x Objective. The fluorescence of green fluorescence protein was observed using 482/35 nm excitation filter, 505 nm dichroic mirror and the emitted light was collected through 536/40 nm emission filter (Semrock). The bright field images were captured at 10 ms exposure while the fluorescent images were captured by varying the exposure between 0.2-1 s using a Prime BSI Express sCMOS camera.

5.4.4 Image analysis.

All the fluorescence intensity of GFP within the droplets were analyzed using Fiji Image 1.5.2. For each experiment the images were acquired at identical conditions and stacked together prior adjusting the brightness and contrast. For analysis, the background-corrected signal intensity was used which is calculated as the difference between the fluorescence intensity within the double emulsions and the background intensity (fluorescence signal intensity outside the DEs).

5.4.5 Statistical analysis.

The background-corrected fluorescence intensities difference between two distinct double emulsion populations was determined using a two-tailed significance test indicated.

5.4.6 Fluorescence assisted cell sorting.

Prior to sorting, the double emulsions were diluted in 1:5 v/v ratio in PBS. The fluorescence-based sorting was performed using Sony sorter SH800 (Sony Biotechnologies) using a 130 µm sorting chip. The sorting conditions were optimized according to previously described study [43] along with manufacturer's manual.

5.4.7 deGFP Purification and fluorescence-intensity standard curve.

deGFP gene was fused with a C-terminal 6x His-tag in a pET28b vector. The pET28b-deGFP vector was transformed into chemical competent *E. coli* BL21 (DE3) cells[49]. A single colony of cells was inoculated into LB-media until OD_{600} approximately 0.5. Recombinant deGFP expression was induced by 0.5 mM IPTG, over 16 hours at 20°C. Cell pellet was resuspended in binding and wash buffer (50 mM NaH_2PO_4, 300 mM NaCl, 20 mM imidazole, pH = 8.0), complemented with protease inhibitors (Roche complete, EDTA-free Protease Inhibitor Cocktail). Cells were lysed by a Q500 Sonicator, at 30% power through consecutive run and pause rounds of 1 s and 2 s, respectively, over 15 minutes. Cell lysate was filtered using 0.22 µm filters and applied to a Histrap HP (GE Lifesciences) nickel column. After sample application, the column was washed with 5x column volumes of binding and wash buffer. The bound protein was eluted with elution buffer (50 mM NaH_2PO_4, 300 mM NaCl, 500 mM imidazole, pH = 8.0) and a fraction of 1ml was collected and analysed by SDS-PAGE gel electrophoresis. Fractions were pulled together and dialyzed in 500 mL buffer of 20 mM Tris-HCL, pH = 8.0, overnight at 4°C using a dialysis tube (Sigma Aldrich #D0505-100FT). The dialyzed protein solution was used for anion exchange chromatography using HiTrap Q HP column. Bound protein was eluted into 1 mL fractions by applying a gradient of elution buffer (20 mM Tris-HCL, NaCl 1M, pH = 8.0) up to 50%. Eluted fractions were analysed in SDS-PAGE gel and pulled together accordingly (**Figure S5.9a**). deGFP protein was quantified at 280 nm (Ext. coef-

ficient = 20525 $M^{-1}cm^{-1}$, MW:26.454 kDa) with three technical replicates. deGFP protein was diluted accordingly in PBS 1X and fluorescence intensity was measured in a biotek synergy Neo2 plate reader at excitation and emission of 485 nm and 528 nm respectively, and a standard curve was prepared as shown in **Figure S5.9b**.

5.4.8 Fluorescence kinetic measurements in TXTL

Cell-free TXTL extract was provided under the commercial name myTXTL Sigma 70 Master Mix Kit by Arbor Biosciences. myTXTL reactions were assembled according to manufacturer's instructions and as described previously[50]. Plasmid vectors were purified using the Zymoclean midiprep kit (#D4200) and further cleaned and concentrated using Zymoclean Clean and Concentrator (#D4013) according to manufacturer's instructions. In short, pCas was used at 3 nM, pTarget at 1 nM and pQUIDE at 1 nM. When expression was driven by linear templates, GamS protein (ArborBiosciences #501024) was added at 10 μM.

Each 12 μL reaction was split in two wells of a PP, V-bottom plate 96 well plate (greiner BIO-ONE, 651201) for two technical replicates (5.5 μL per replicate). Fluorescence (Ex = 485 nm, Em = 528 nm) was monitored on a biotek synergy Neo2 plate reader for 16 hours at 30°C with point measurements being taken every 3 minutes.

5.5 AUTHOR CONTRIBUTION

Ketan Ashok Ganar (K.A.G), Evgenios Bouzetos (E.B), Siddharth Deshpande (S.D) and John van der Oost (J.V.D.O) conceived of the presented idea. E.B designed gene circuits and performed bulk experiments. K.A.G fabricated microfluidic devices, performed emulsion studies, image analysis and droplet sorting. The initial draft was written by K.A.G and E.B and edited by S.D and J.V.D.O. All authors discussed the results and contributed to the final version of this chapter.

5.6 ACKNOWLEDGEMENT

We acknowledge financial support by the Innovation Program Microbiology of Wageningen University (IPM-3 grant 6145010520) to S.D. and by the European Research Council (ERC AdG 2018-834279) to J.V.D.O.

5.7 SUPPLEMENTARY FIGURES

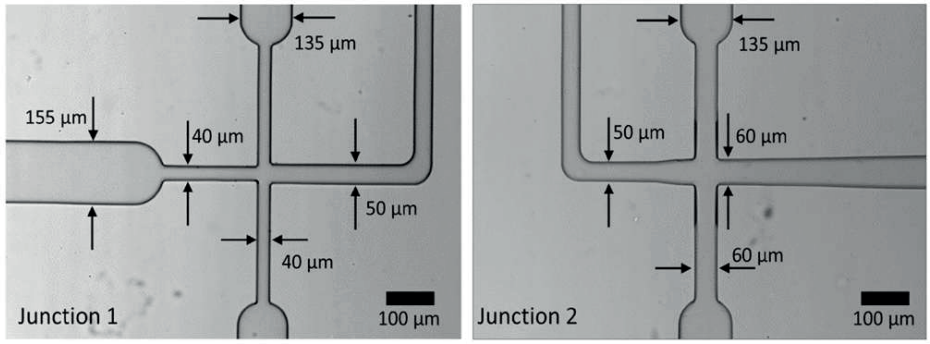

Figure S5.1: Dimensions of the two-junction microfluidic device used for production of double emulsions.

Junction 1 consists of horizontal inner aqueous channel (40 µm width) intercepted by perpendicular oil channels (40 µm width each) resulting in a loop of slightly larger opening of 50 µm width designed to hold single emulsions. Junction 2 consists of single emulsion containing horizontal loop (50 µm) intercepted by perpendicular outer aqueous channels (60 µm) leading to cone shaped exit channel. All the channels are approximately 20 µm in height.

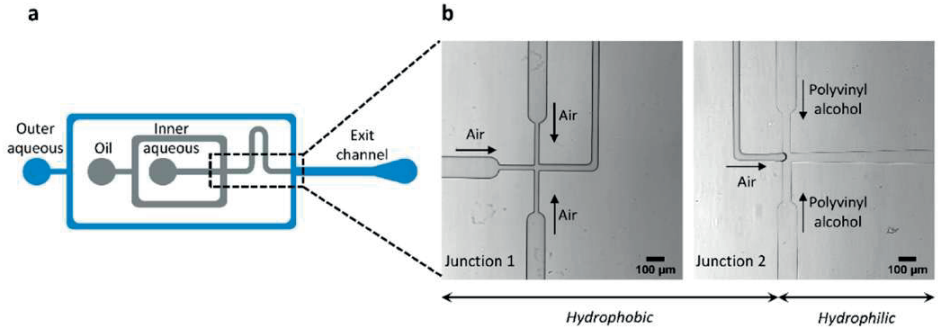

Figure S5.2: Surface functionalization of the microfluidic device.

(a) Schematic depicting the hydrophobic channels (grey) and hydrophilic channel (blue) post surface functionalization. (b) To make the device post junction 2 hydrophilic, 5% w/v polyvinyl alcohol (PVA) solution is flown through the outer aqueous channel and exiting via the exit channel. Positive air pressure is maintained in the inner aqueous and oil channels to prevent the back flow of PVA in the loop.

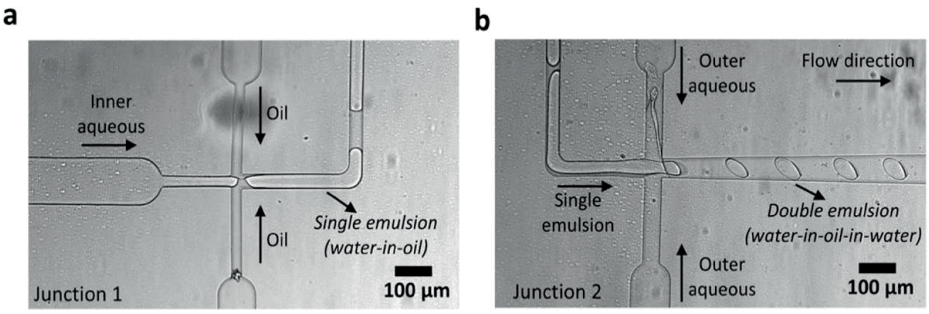

Figure S5.3: Microfluidic production of double emulsion.

(a) Production of water-in-oil- in-water single emulsion at Junction 1 formed by flowing FITC-containing PBS through the surfactant-containing oil phase. The formed single emulsion travels to the second junction via the loop. (b) Production of water-in-oil-in-water double emulsion by pinching- off the single emulsion by perpendicular current of surfactant-containing aqueous phase.

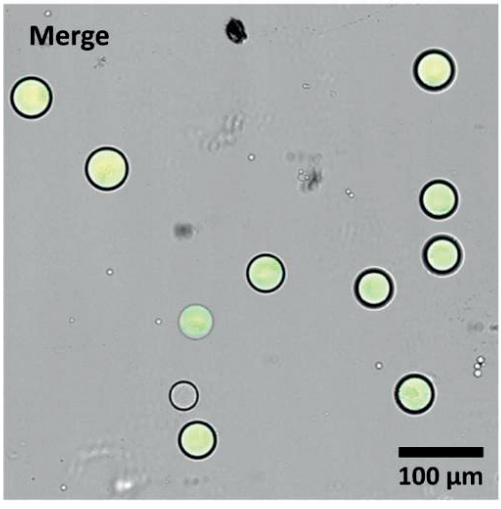

Figure S5.4: Cell-free expression of deGFP in double emulsions.

Double emulsions encapsulating deGFP encoding plasmid along with TXTL mixture. Merged image of bright-field and fluorescence channels showing expression of deGFP within the double

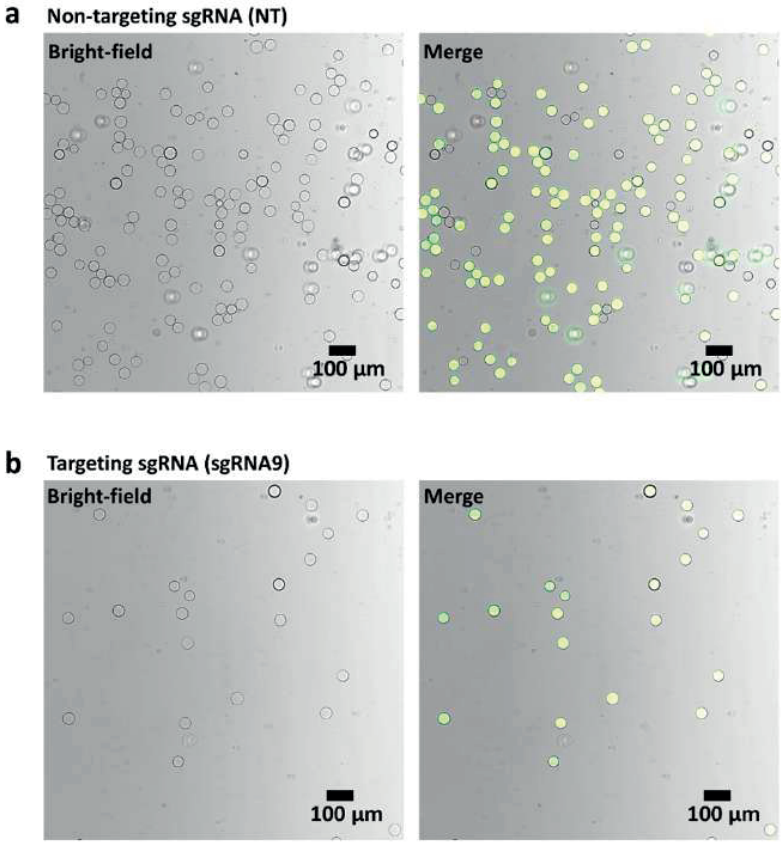

Figure S5.5: Double emulsions consisting of CRISPR-Cas9 gene circuit which directly targets deGFP encoding plasmid.

(a) Microscopic images of double emulsions in bright-field, and bright-field and fluorescence merged channels showing SpCas9- linked deGFP expression in presence of (a) Non-targeting sgRNA (NT) and (b) deGFP repression in presence of targeting sgRNA9.

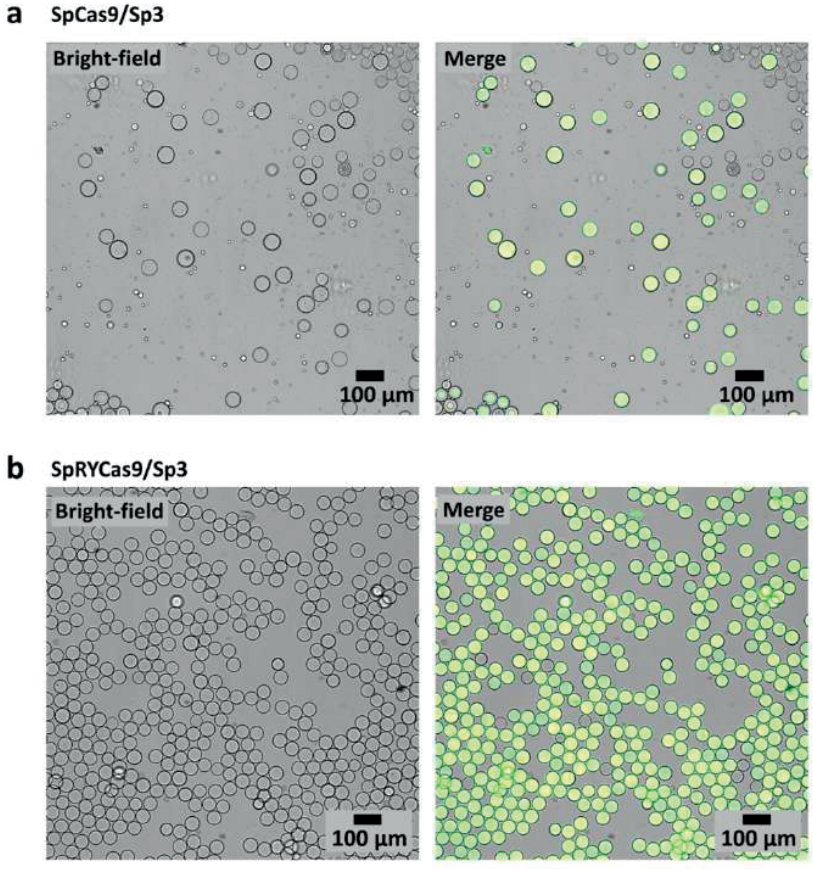

Figure S5.6: Double emulsions consisting of CRISPR-Cas9 encoding gene circuit in presence of targeting sgRNA.

(a) Microscopic images of double emulsions in bright- field and bright-field and fluorescence merged channels showing SpCas9-linked deGFP repression in presence of targeting sgRNA (Sp3). (b) Bright-field and bright-field and fluorescent merged images of gene circuit encoding SpRYCas9 along with targeting sgRNA (Sp3) repressing deGFP.

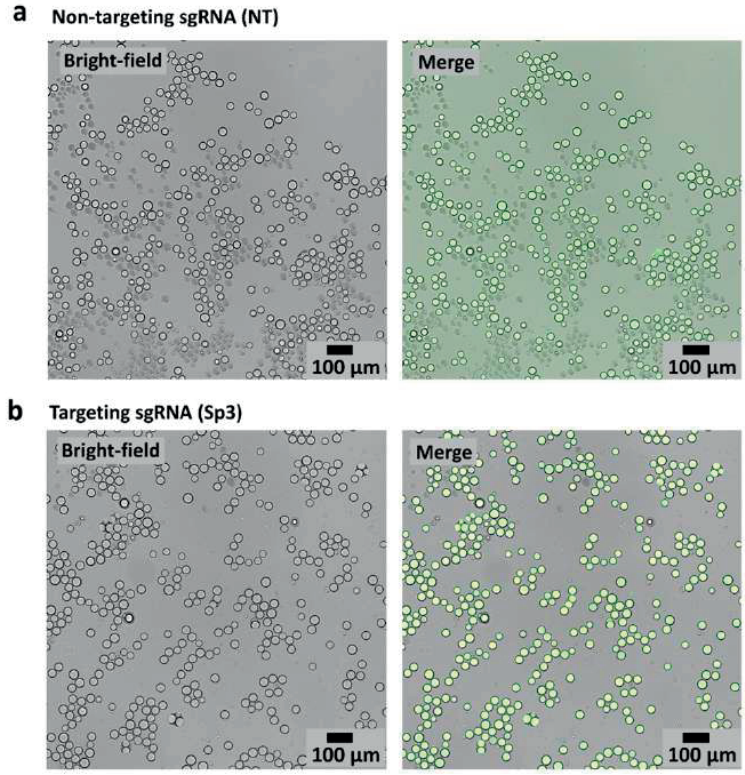

Figure S5.7: Double emulsions consisting of CRISPR-Cas9 gene circuits along with deGFP, cI-ssrA gene, and sgRNA construct.

(a) In presence of non-targeting sgRNA (NT), the microscopic images of double emulsions in bright-field and bright-field and fluorescence merged channel showed repression of deGFP modulated via SpCas9-linked expression of cI-ssrA. (b) In presence of targeting sgRNA (Sp3), the SpCas9 complex inhibited cI-ssrA repressor allowing uninterrupted expression of deGFP.

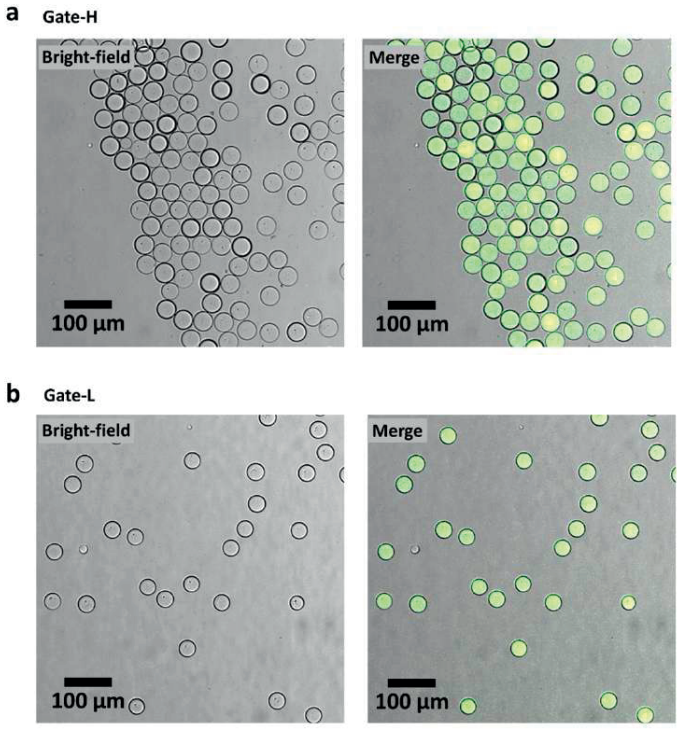

Figure S5.8: FACS-based sorting of mixed double emulsion population consisting of CRISPR-Cas9 gene circuit along with deGFP-encoding plasmid and either targeting or non-targeting sgRNA. Microscopic images of double emulsions in bright-field and merged channels post-sorting in (a) Gate-H and (b) Gate-L.

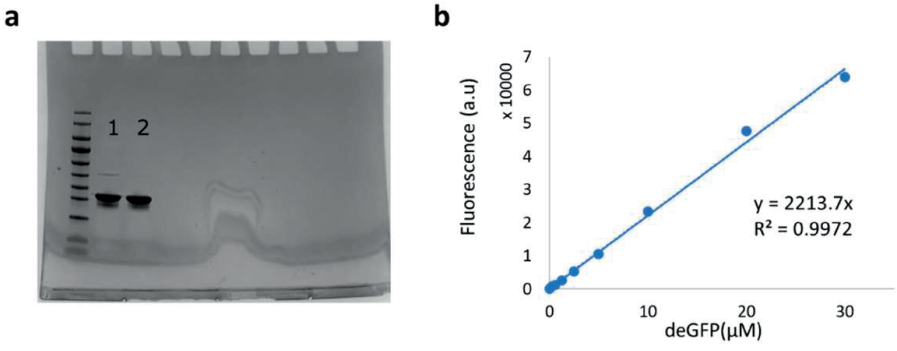

Figure S5.9: deGFP purification and calibration curves.

a) SDS-PAGE gel loaded with 9.5 µg protein enriched for deGFP-his. Lane 2 was chosen for regression analysis. b) Fluorescence-based standard curve of deGFP.

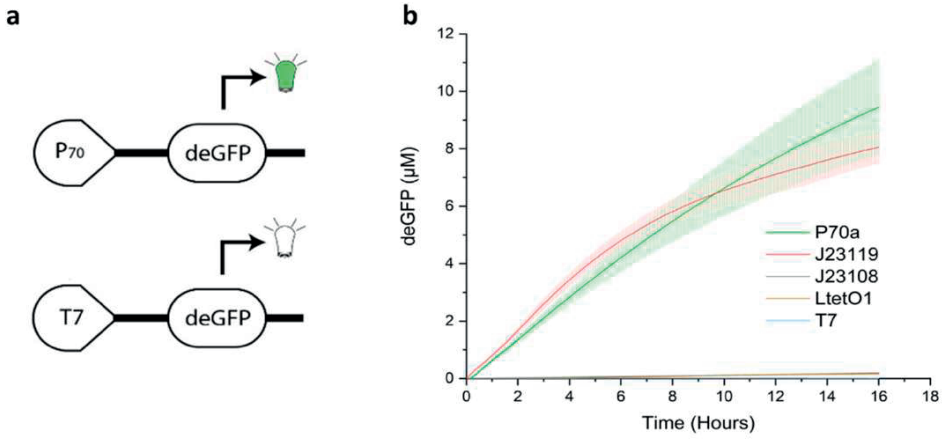

Figure S5.10: Varying promoter strength in TXTL.

(a) Gene transcription in TXTL is driven only by the E. coli endogenous σ70 factor. (b) Kinetics measurements of deGFP concentration in presence of 1nM: pP70_deGFP or 1nM: pT7_deGFP as negative control. Error bars represent the SD from three repetitions.

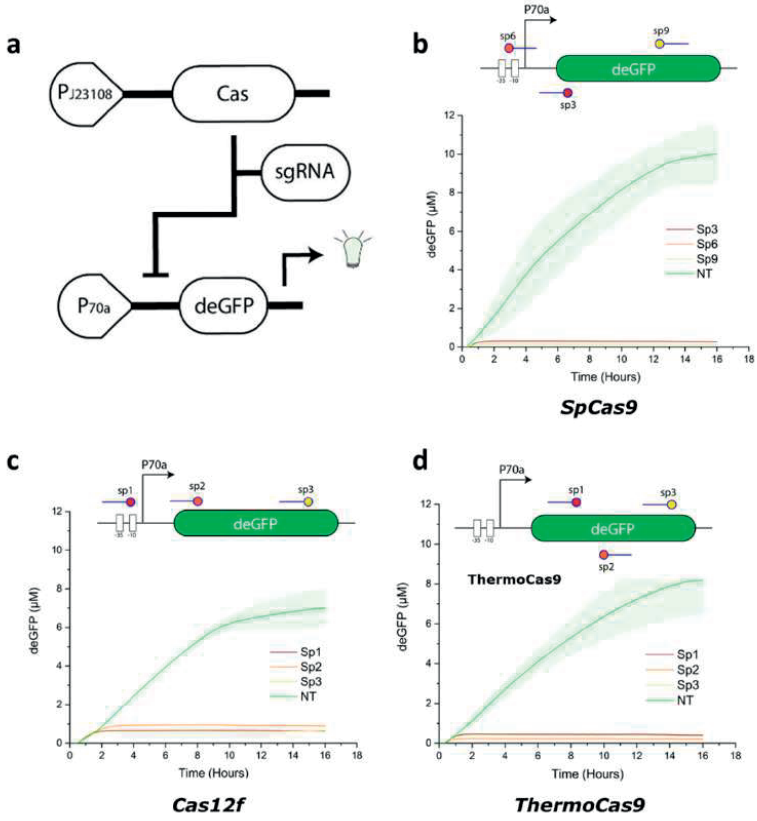

Figure S5.11: Guided regulation of protein expression by CRISPR-Cas systems in TXTL.

(a) Guided DNA-cleavage by CRISPR-Cas systems prevents protein expression due to DNA- degradation. (b) Kinetics measurements of deGFP(μM) concentration is presence of 1nM: pP70a_deGFP, 3nM: pJ23108_Cas and 1nM: pJ23119_sgRNA. Target sites for three different CRISPR-Cas systems in the deGFP expression cassette were designed. Circles represent the PAM sequence and straight lines the spacer sequence. (c) Kinetics measurements of deGFP(μM) concentration is presence of 1nM: pP70a_deGFP, 3nM: pJ23108_Cas12f and 1nM: pJ23119_sgRNA. (d) Kinetics measurements of deGFP(μM) concentration is presence of 1nM: pP70a_deGFP, 3nM: pJ23108_ThermoCas9 and 1nM: pJ23119_sgRNA. Error bars represent the SD from three repetitions.

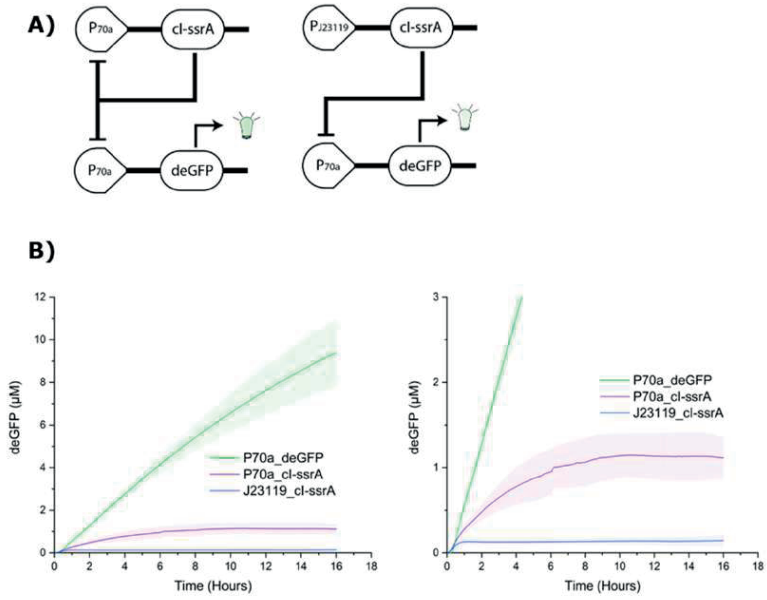

Figure 5S.12: Promoter negative regulation in TXTL.

cI protein dimers bind to the operator sites of the P70a promoter and obstruct interaction with σ70 factors thus preventing transcription. B) Kinetics measurements of deGFP(μM) concentration in presence of 1nM: pP70a_deGFP and 1nM: pP70a_cI-ssrA or 1nM: pJ23119_cI-ssrA. Error bars represent the SD from three repetitions.

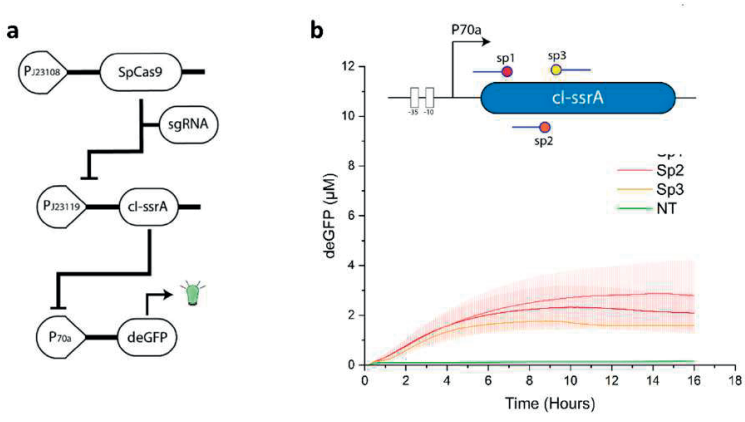

Figure S5.13: Repression cascade of protein expression only based on CRISPR-Cas systems results in higher fluorescence-gain ratio. A) Guided DNA-cleavage by CRISPR-Cas systems of the cI_ssrA preventing transcriptional repression of P70a promoter and target sites of SpCas9 in the cI_ssrA genes. B) Kinetics measurements of deGFP concentration is presence of 1nM:pP70a_deGFP, 3nM: pJ23108_SpCas9 and 1nM:pJ23119_sgRNA. Error bars represent the SD from three repetitions.

REFERENCES

1. Mohanraju P, Makarova KS, Zetsche B, Zhang F, Koonin EV, Van der Oost J. Diverse evolutionary roots and mechanistic variations of the CRISPR-Cas systems. *Science* 2016, **353**(6299)**:** aad5147.
2. Swartjes T, Staals RH, van der Oost J. Editor's cut: DNA cleavage by CRISPR RNA-guided nucleases Cas9 and Cas12a. *Biochemical Society Transactions* 2020, **48**(1)**:** 207-219.
3. Deltcheva E, Chylinski K, Sharma CM, Gonzales K, Chao Y, Pirzada ZA*, et al.* CRISPR RNA maturation by trans-encoded small RNA and host factor RNase III. *Nature* 2011, **471**(7340)**:** 602-607.
4. Jinek M, Chylinski K, Fonfara I, Hauer M, Doudna JA, Charpentier E. A programmable dual-RNA–guided DNA endonuclease in adaptive bacterial immunity. *science* 2012, **337**(6096)**:** 816-821.
5. Gasiunas G, Barrangou R, Horvath P, Siksnys V. Cas9–crRNA ribonucleoprotein complex mediates specific DNA cleavage for adaptive immunity in bacteria. *Proceedings of the National Academy of Sciences* 2012, **109**(39)**:** E2579-E2586.
6. Deveau H, Barrangou R, Garneau JE, Labonté J, Fremaux C, Boyaval P*, et al.* Phage response to CRISPR-encoded resistance in Streptococcus thermophilus. *Journal of bacteriology* 2008, **190**(4)**:** 1390-1400.
7. Mojica FJ, Díez-Villaseñor C, García-Martínez J, Almendros C. Short motif sequences determine the targets of the prokaryotic CRISPR defence system. *Microbiology* 2009, **155**(3)**:** 733-740.
8. Jinek M, East A, Cheng A, Lin S, Ma E, Doudna J. RNA-programmed genome editing in human cells. *elife* 2013, **2:** e00471.
9. Cho SW, Kim S, Kim JM, Kim J-S. Targeted genome engineering in human cells with the Cas9 RNA-guided endonuclease. *Nature biotechnology* 2013, **31**(3)**:** 230-232.
10. Jiang W, Bikard D, Cox D, Zhang F, Marraffini LA. RNA-guided editing of bacterial genomes using CRISPR-Cas systems. *Nature biotechnology* 2013, **31**(3)**:** 233-239.
11. Knott GJ, Doudna JA. CRISPR-Cas guides the future of genetic engineering. *Science* 2018, **361**(6405)**:** 866-869.
12. Van der Oost J, Patinios C. The genome editing revolution. *Trends in Biotechnology* 2023, **41**(3)**:** 396-409.
13. Peng R, Lin G, Li J. Potential pitfalls of CRISPR/Cas9-mediated genome editing. *The FEBS journal* 2016, **283**(7)**:** 1218-1231.
14. Kleinstiver BP, Prew MS, Tsai SQ, Topkar VV, Nguyen NT, Zheng Z*, et al.* Engineered CRISPR-Cas9 nucleases with altered PAM specificities. *Nature* 2015, **523**(7561)**:** 481-485.
15. Lee JK, Jeong E, Lee J, Jung M, Shin E, Kim Y-h*, et al.* Directed evolution of CRISPR-Cas9 to increase its specificity. *Nature communications* 2018, **9**(1)**:** 3048.
16. Zhang L, Zuris JA, Viswanathan R, Edelstein JN, Turk R, Thommandru B*, et al.* AsCas12a ultra nuclease facilitates the rapid generation of therapeutic cell medicines. *Nature communications* 2021, **12**(1)**:** 3908.
17. Kleinstiver BP, Pattanayak V, Prew MS, Tsai SQ, Nguyen NT, Zheng Z*, et al.* High-fidelity CRISPR–Cas9 nucleases with no detectable genome-wide off-target effects. *Nature* 2016, **529**(7587)**:** 490-495.
18. Hino T, Omura SN, Nakagawa R, Togashi T, Takeda SN, Hiramoto T*, et al.* An AsCas12f-based compact genome-editing tool derived by deep mutational scanning and structural analysis. *Cell* 2023, **186**(22)**:** 4920-4935. e4923.

19. Casini A, Olivieri M, Petris G, Montagna C, Reginato G, Maule G, *et al.* A highly specific SpCas9 variant is identified by in vivo screening in yeast. *Nature biotechnology* 2018, **36**(3)**:** 265-271.
20. Xu X, Chemparathy A, Zeng L, Kempton HR, Shang S, Nakamura M, *et al.* Engineered miniature CRISPR-Cas system for mammalian genome regulation and editing. *Molecular cell* 2021, **81**(20)**:** 4333-4345. e4334.
21. Chen Z, Zhao H. A highly sensitive selection method for directed evolution of homing endonucleases. *Nucleic acids research* 2005, **33**(18)**:** e154-e154.
22. Packer MS, Liu DR. Methods for the directed evolution of proteins. *Nature Reviews Genetics* 2015, **16**(7)**:** 379-394.
23. Tawfik DS, Griffiths AD. Man-made cell-like compartments for molecular evolution. *Nature biotechnology* 1998, **16**(7)**:** 652-656.
24. Bouzetos E, Ganar KA, Mastrobattista E, Deshpande S, van der Oost J. (R) evolution-on-a-chip. *Trends in Biotechnology* 2022, **40**(1)**:** 60-76.
25. Lee YF, Tawfik DS, Griffiths AD. Investigating the target recognition of DNA cytosine-5 methyltransferase Hha I by library selection using in vitro compartmentalisation. *Nucleic acids research* 2002, **30**(22)**:** 4937-4944.
26. Doi N, Kumadaki S, Oishi Y, Matsumura N, Yanagawa H. In vitro selection of restriction endonucleases by in vitro compartmentalization. *Nucleic acids research* 2004, **32**(12)**:** e95-e95.
27. Tay Y, Ho C, Drőge P, Ghadessy FJ. Selection of bacteriophage λ integrases with altered recombination specificity by in vitro compartmentalization. *Nucleic acids research* 2010, **38**(4)**:** e25-e25.
28. Ghadessy FJ, Ong JL, Holliger P. Directed evolution of polymerase function by compartmentalized self-replication. *Proceedings of the National Academy of Sciences* 2001, **98**(8)**:** 4552-4557.
29. Zheng Y, Roberts RJ. Selection of restriction endonucleases using artificial cells. *Nucleic acids research* 2007, **35**(11)**:** e83.
30. Takeuchi R, Choi M, Stoddard BL. Redesign of extensive protein–DNA interfaces of meganucleases using iterative cycles of in vitro compartmentalization. *Proceedings of the National Academy of Sciences* 2014, **111**(11)**:** 4061-4066.
31. Wu Z, Zhang Y, Yu H, Pan D, Wang Y, Wang Y, *et al.* Programmed genome editing by a miniature CRISPR-Cas12f nuclease. *Nature chemical biology* 2021, **17**(11)**:** 1132-1138.
32. Jiang F, Doudna JA. CRISPR–Cas9 structures and mechanisms. *Annual review of biophysics* 2017, **46:** 505-529.
33. Perez-Pinera P, Kocak DD, Vockley CM, Adler AF, Kabadi AM, Polstein LR, *et al.* RNA-guided gene activation by CRISPR-Cas9–based transcription factors. *Nature methods* 2013, **10**(10)**:** 973-976.
34. Wu WY, Mohanraju P, Liao C, Adiego-Pérez B, Creutzburg SC, Makarova KS, *et al.* The miniature CRISPR-Cas12m effector binds DNA to block transcription. *Molecular Cell* 2022, **82**(23)**:** 4487-4502. e4487.
35. Larson MH, Gilbert LA, Wang X, Lim WA, Weissman JS, Qi LS. CRISPR interference (CRISPRi) for sequence-specific control of gene expression. *Nature protocols* 2013, **8**(11)**:** 2180-2196.
36. Stucki A, Vallapurackal J, Ward TR, Dittrich PS. Droplet microfluidics and directed evolution of enzymes: an intertwined journey. *Angewandte Chemie International Edition* 2021, **60**(46)**:** 24368-24387.
37. Romanowsky MB, Abate AR, Rotem A, Holtze C, Weitz DA. High throughput production of single core double emulsions in a parallelized microfluidic device. *Lab on a Chip* 2012, **12**(4)**:** 802-807.

38. Vallapurackal J, Stucki A, Liang AD, Klehr J, Dittrich PS, Ward TR. Ultrahigh-Throughput Screening of an Artificial Metalloenzyme using Double Emulsions. *Angewandte Chemie International Edition* 2022, **61**(48)**:** e202207328.
39. Larsen AC, Dunn MR, Hatch A, Sau SP, Youngbull C, Chaput JC. A general strategy for expanding polymerase function by droplet microfluidics. *Nature Communications* 2016, **7**(1)**:** 11235.
40. Miller OJ, Bernath K, Agresti JJ, Amitai G, Kelly BT, Mastrobattista E*, et al.* Directed evolution by in vitro compartmentalization. *Nature methods* 2006, **3**(7)**:** 561-570.
41. Chen Y, Liu X, Zhang C, Zhao Y. Enhancing and suppressing effects of an inner droplet on deformation of a double emulsion droplet under shear. *Lab on a Chip* 2015, **15**(5)**:** 1255-1261.
42. Neumann S, Scherbej I, Van Der Schaaf U, Karbstein H. Investigations on the influence of osmotic active substances on the structure of water in oil emulsions for the application as inner phase in double emulsions. *Colloids and Surfaces A: Physicochemical and Engineering Aspects* 2018, **538:** 56-62.
43. Brower KK, Carswell-Crumpton C, Klemm S, Cruz B, Kim G, Calhoun SG*, et al.* Double emulsion flow cytometry with high-throughput single droplet isolation and nucleic acid recovery. *Lab on a Chip* 2020, **20**(12)**:** 2062-2074.
44. Marshall R, Maxwell CS, Collins SP, Jacobsen T, Luo ML, Begemann MB*, et al.* Rapid and scalable characterization of CRISPR technologies using an E. coli cell-free transcription-translation system. *Molecular cell* 2018, **69**(1)**:** 146-157. e143.
45. Shin J, Noireaux V. Efficient cell-free expression with the endogenous E. Coli RNA polymerase and sigma factor 70. *Journal of biological engineering* 2010, **4**(1)**:** 1-9.
46. Walton RT, Christie KA, Whittaker MN, Kleinstiver BP. Unconstrained genome targeting with near-PAMless engineered CRISPR-Cas9 variants. *Science* 2020, **368**(6488)**:** 290-296.
47. Ma S, Huck WT, Balabani S. Deformation of double emulsions under conditions of flow cytometry hydrodynamic focusing. *Lab on a Chip* 2015, **15**(22)**:** 4291-4301.
48. Chen C, Ganar KA, Deshpande S. On-Chip Octanol-Assisted Liposome Assembly for Bioengineering. *JoVE (Journal of Visualized Experiments)* 2023(193)**:** e65032.
49. Green R, Rogers EJ. Transformation of chemically competent E. coli. *Methods Enzymol* 2013, **529:** 329-336.
50. Marshall R, Beisel CL, Noireaux V. Rapid testing of CRISPR nucleases and guide RNAs in an E. coli cell-free transcription-translation system. *STAR protocols* 2020, **1**(1)**:** 100003.

Chapter 6

General Discussion

In this thesis, we initially discussed our approach to designing a synthetic cell by leveraging the potential of biomolecular condensates. Furthermore, we explored on-chip microfluidic technology to create cell-sized confinements with high encapsulation capacity. On-chip technology has a wide range of applications, and in this thesis, we presented two distinct examples that highlight its role in both understanding fundamentals of complex biological phenomena and its application in biotechnology. Firstly, we demonstrated an on-chip production of monodispersed liposomes and encapsulated synthetic bioinspired polymers along with natural biomolecules. We then demonstrated pH-induced activation of membraneless confinements within these liposomes, taking one more step closer towards building a synthetic cell. We further developed and fabricated microfluidic devices to generate water-in-oil-in-water double emulsions in a high-throughput fashion. By encapsulating complex gene circuits along with cell-free transcription and translation machinery, we showcased Cas9 (a nuclease enzyme)-regulated expression and suppression of green fluorescent protein, establishing a connection between the functionality of enzyme to fluorescence emission. In addition to this, we also improved our understanding of how protein-rich condensates can potentially assist the process of tick clinging on the host. Using a model glycine-rich protein from tick saliva, we systematically discussed the physiological conditions as well as the role of specific amino acids leading to phase separation. In this final chapter, we summarise the recent advancement in synthetic cells, with a particular focus from the point-of-view of biomolecular condensates. We discuss advantages of on-chip techniques for confinement creation together with technological limitations and further ideas for improvements. In the final section, we highlight some of our important findings on the role of biomolecular condensate in tick-host interaction and discuss strategies to enhance our understanding of the underlying mechanism. Finally, we conclude by providing an aerial view on applications of biomolecular condensates.

6.1 CONTRIBUTION OF THIS THESIS TOWARDS DEVELOPING SYNTHETIC CELLS AND UNDERSTANDING BIOMOLECULAR CONDENSATES.

We are still at the initial stages of the monumental and exciting prospect of building autonomous, functional synthetic cells. Out of the numerous functional modules that synthetic biologists are seeking to build in a bottom-up manner, this thesis has focused, in general, on the shaping and structuring of synthetic cells and with specific emphasis on creating membrane-bound and membraneless confinements. Looking back at the thesis, we contributed in multiple ways towards designing of synthetic cell.

1) Building a synthetic cell requires confining biomolecules to conduct biochemical reactions. In **Chapter 2**, we successfully demonstrated development of biomolecular condensates to form a proteinaceous confinement which we named as actinosomes. Some salient features of actinosomes include micron-sized confinement, ease of production, efficient encapsulation and retention of biomolecules, pore size of 5 nm and capability to perform complex biochemical reactions like protein expression.
2) In **Chapter 3**, we discussed a detailed protocol explaining microfluidics-based Octanol-assisted Liposome Assembly (OLA) to generate liposomes. The lipid bilayer of liposomes makes them resemble the cellular membrane in its minimal form and its semipermeable nature enables diffusion of smaller molecules across the membrane. By encapsulating condensate-forming synthetic material (like poly-L-lysine and adenosine triphosphate), we demonstrated that external addition of buffer initiates the process of liquid-liquid phase separation (LLPS) inside the liposome.
3) Liposomes serve as an excellent cell-mimicking confinement, especially to understand the role of membrane-interacting biomolecules. Nonetheless, they are fragile and difficult to handle, thus limiting their application. On the contrary, double emulsions are robust and can serve as an equally capable confinement to perform complex biochemical assays. In **Chapter 5**, we developed an on-chip high-throughput platform to generate double emulsions (production rate of 500 Hz). We used them as *in vitro* confinements to express complex gene circuits using cell-free transcription and translation machinery. We subsequently linked the enzymatic activity of Cas9 protein (a DNA cleaving enzyme) to the expression of green fluorescent protein (GFP), serving as a crucial link to bring about protein evolution. Using cell sorter, we also separated double emulsions based on the amount of GFP produced.
4) Exploring our curiosity to understand disordered proteins, in Chapter 4, we characterized glycine-rich proteins from ticks and determined the physiological conditions together with amino acids compositions that promote liquid-liquid phase separation behavior in these proteins. Our experiments showed the liquid-like nature of phase separated droplets and the transition into a gel-like state upon aging. These findings are the first report that highlight a possible mechanism on how ticks adhere to their host.

6.1.1 Our approach towards shaping synthetic cells.

It is difficult to precisely define a synthetic cell in a single sentence, however, one can agree that a synthetic cell is a broad idea to create a man-made mimicry of a biological cell. The bottom-up on-chip approach can immensely help in addressing complex biological phenomena, acknowledging the fact that the concept of a synthetic cell in

itself is inherently subjective. For instance, a molecular biologist, who employs cells to produce proteins would view synthetic cells as protein-producing factories. A medical practitioner would interpret a synthetic cell as an entity to deliver therapeutic molecules and possibly replace defective cells in the human body with better functional ones. A biophysicist, interested in understanding life, may envision a synthetic cell to be a minimal entity that has the capability to self-replicate its components and eventually divide, thus completing the circle of life.

In this thesis, we have illustrated different methods to confine biomolecules in a micron-sized space and subsequently demonstrated a cascade of complex biochemical reactions within these confinements. This being shown, we can take inspiration from living cells to build an autonomous, self-dividing entity. Broadly, cellular division has two main segments, duplication of the genetic material followed by division to create daughter cells. During this process, the membrane also undergoes essential morphological changes reorganizing cellular content[2]. Prior to cell division, the membrane deforms giving rise to a dumbbell-shaped structure segregating cellular contents in these lobes. Furthermore, various cell types perform different functions, and these functions directly result from the characteristics of their membrane. While neuron cells are long and designed to transmit signals, intestinal cell membranes have microvilli to absorb nutrients. These examples suggest that structuring membranes is an important consideration for building a synthetic cell. *In vitro* studies have manipulated liposomes and demonstrated replication of genetic material[3], lipid synthesis[4], growth of membrane[5] as well as mechanical division of liposomes[6]. The bottleneck is to combine all these modules in a single unit to achieve an autonomous self-dividing entity. This gap could possibly be reduced by further reorganizing the membrane, particularly by inducing membrane deformations. One way to achieve this could be the use of multiple biomolecular assemblies. Using biomolecular condensates can spatiotemporally organize the cellular environment by regulating cellular kinetics and localizing proteins by sequestering them. Secondly, cytoskeleton proteins like actin and myosin motors could actively deform the membrane by exerting mechanical force. Directing biomolecular condensates to the membrane along with the collective effort of cytoskeleton could potentially bring morphological changes in liposomes (**Figure 6.1**).

The recent discovery of biomolecular condensates has opened up new directions toward achieving and guiding cellular organization. Previous reports, as discussed in **Chapter 1,** suggest that biomolecular condensates have a direct effect on the cytoskeletal self-assembly within the cellular interior and at the membrane. In corroboration, our findings in in **Chapter 2** also provide further evidence that biomolecular condensates can spatiotemporally localize the actin cytoskeleton at the interface. Recent

study demonstrated phosphorylated membrane proteins LAT (linker for activation of T cell) along with binding partners undergo phase separation and actively recruit Arp2/3 actin protein and induce polymerization[7]. Since it is difficult to always use naturally occurring protein-based biomolecular condensates, various synthetic models inspired from biopolymers have been developed. Complex coacervates are frequently used models for synthetic biomolecular condensates made using negatively charged nucleoside triphosphate/RNA along with positively charged polylysine/polyarginine[8]. Unlike multiple components required for complex coacervation, elastin-like-polypeptide (ELP) can undergo simple phase separation triggered via pH, temperature and salt[9]. Additionally, recent reports have provided extensive temperature responsive[10] and pH-responsive[11] ELP libraries.

The surface-active nature of biomolecular condensates allows them to actively interact with the lipid membrane of liposomes [12, 13, 14]. Thus, condensates can be used as a sticky material to localize proteins at the membrane. It is important to note that lipid-lipid phase separation of membrane lipids is a different phenomenon which can spatially segregate molecules at the membrane along with creating an asymmetry in the membrane itself[15, 16]. Condensates can localize at membrane while maintaining lipid homogeneity.

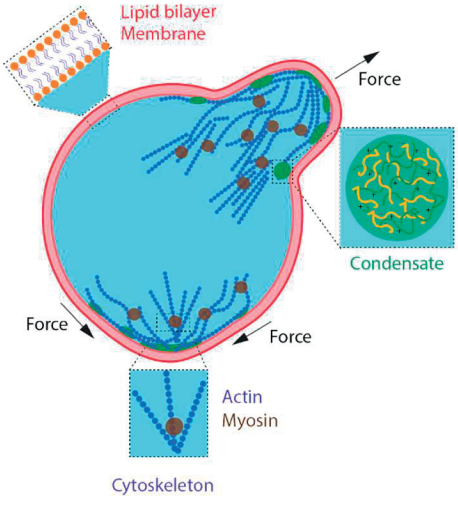

Figure 6.1:

Schematic depicting in vitro reconstituted minimal system to understand cellular morphogenesis via the interplay between cytoskeleton (actomyosin cortex), condensates (synthetic coacervates) and membrane (composed of lipid bilayer).

Additionally, the dominant surface forces in condensates can also contribute to membrane morphogenesis[17]. The material and mechanical properties of condensates are hidden in their viscoelastic behavior and interfacial interactions, which can lead to a net mechanical output on the surrounding components. A recent study demonstrated that external addition of biomolecular condensates composed of synthetic charged polymers led to active interaction with the outer leaflet of the lipid bilayer, resulting in membrane deformations in liposomes[18]. These charged biomolecular condensates could also penetrate the lipid bilayer of the liposome[19]. Additionally, naturally occurring biomolecular condensates like glycinin condensates also bring morphological deformations in vesicles[20]. These reports suggest that biomolecular condensates could thus themselves perform mechanical work on soft interfaces. Livings cells are extremely crowded in nature, and even in such crowded environment, cells are capable of segregating biochemical reactions in different regions. Thus, taking into account the effect of a crowded environment is crucial in building a synthetic cell. While the use of molecular crowders can mimic the viscous environment of the cell, creating sub-compartments within such environment remains unexplored. Synthetic biomolecular condensates serve as an excellent model system to create sub-compartments within liposomes. One slight drawback of using biomolecular condensates is their natural tendency to coalesce which eventually leads them to sink at the bottom of the liposome. Regulating their coalescence behavior would help to further assist the spatial organization within liposomes. But how do we achieve this? One strategy could be to use segregative phase separation to spatially organize biomolecular condensates. A simple example of segregative phase separation is that of polyethylene glycol (PEG) and dextran, which under certain concentrations segregate to form two distinct phases, a PEG-rich phase and a dextran-rich phase (**Figure 6.2a**). A preliminary study showed that a phase separated dextran phase localized at the membrane of liposomes led to budding-like membrane deformations (**Figure 6.2b**)[1]. Employing this strategy could assist in both spatiotemporal regulation of condensates together with controlled membrane deformation.

In the rapidly changing interdisciplinary field of synthetic biology, newer methodologies, like microfluidics[21, 22] and DNA nanotechnology[23], are playing increasingly important roles. The encapsulation efficiency and overall control over vesicle production can be significantly improved using newly developed microfluidic techniques[24, 25]. At the same time, tuning of key physical parameters proves highly beneficial to moderate shape changes in vesicles. One of the most important parameters seems to be the membrane tension which can be easily controlled externally by the addition of buffer. For instance, addition of hypertonic buffer (higher concentration of solute) drives efflux of water from the vesicle reducing the membrane tension, resulting in a floppy

membrane. This greatly facilitates membrane deformation by cytoskeletal forces, and we expect to see extensive use of this strategy in the future.

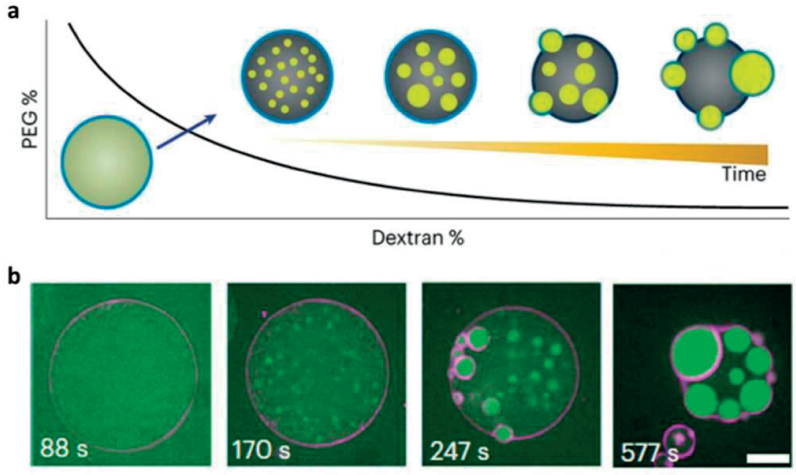

Figure 6.2: Segregative phase separation-induced morphological change.

(a) Schematic depicting membrane (blue) deformations induced via segregative phase separation of polyethylene glycol (grey) and dextran (yellow)within a liposome. (b) Time-lapse showing membrane (magenta) deformations induced via phase separated dextran-rich droplet (green). Scale bar, 10 µm. Figure adapted from WU Su et. al[1].

Research in shaping synthetic cells could be a stepping-stone towards the development of emerging materials for biotechnological applications. One such application could be for the development of synthetic tissue, where the cytoskeleton along with biomolecular condensates could organize multicellular systems. Additionally, tuning the physicochemical parameters could further impact material properties and thus help in designing specific synthetic tissues. The versatile nature of the minimalist bottom-up approach could further extend its application in therapeutics, diagnostics and developing novel vaccine platforms.

6.1.2 Advantage of using on-chip technology in synthetic cell research.

Bulk techniques to create confinements are particularly popular among scientists, owing to their technical simplicity. This comes at the expense of compromised encapsulation, varying confinement size, lack of experimental control which eventually affects experimental reproducibility. These drawbacks can be resolved by using an on-chip

microfluidic platform. In **Chapter 3** and **Chapter 5**, we showed a glimpse of how a microfluidic-based approach can have higher control over confinement creation. Other salient features like high-throughput production, monodispersity, and efficient encapsulation results in increased reproducibility of the assay. These are vital assets for both fundamental understanding of biological phenomena and in biotechnological applications.

6.1.3 Limitations and improvements in on-chip microfluidic technology.

Through our research in this thesis, we have realized that the bottleneck of PDMS-based microfluidics setup, especially in the context of generating vesicles, is the surface functionalization of microfluidic channels. Prior to the generation of double emulsions or liposomes, the microfluidic channels need to undergo surface passivation, so that the microfluidic channels for generation of water-in-oil emulsions are hydrophobic whereas channels for water-in-oil-in-water double emulsions are hydrophilic. Failure to achieve such a hybrid device immensely impacts the process of vesicle production. In this thesis, we used polyvinyl alcohol to hydrophilize the channels. While this process is technically challenging, further simplification of this process would immensely increase the assay reproducibility along with saving user's time.

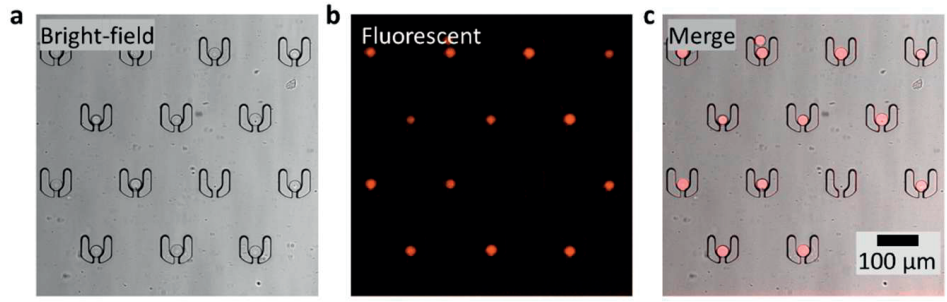

Figure 6.3: Microscopic image of microfluidic traps for double emulsions.

(a) Bright field image of U-shaped traps holding double-emulsions. (b) Fluorescent image showing encapsulation of fluorescently labelled elastin-like-polypeptides within double emulsions. (c) Merged image of bright-field and fluorescence images.

Water-in-oil-in-water double emulsions are robust in nature allowing both recovery and long-term storage. However, long-term continuous observation of double emulsions under a microscope using mere a glass slide is difficult particularly due to flow induced by sample evaporation. A simple practical solution would be to fabricate a

microfluidic chamber consisting of a U-shaped barrier that could trap and hold these double emulsions as shown in (**Figure 6.3a**) Additionally, these traps are treated with polyvinyl alcohol to prevent bursting of double emulsions. Retention of biomolecules (fluorescent protein in this case) within double emulsions as shown in (**Figure 6.3bc**) confirms this. This setup could be further used to manipulate double emulsions by flowing buffers of different kinds.

Unlike double emulsions, the fragile nature of liposomes already makes them difficult to recover and store. Despite the advantages of using OLA to generate liposomes, external manipulation is performed at the exit hole. This setup has one major disadvantage that addition of even a small volume of liquid creates enough flow for liposomes to move out of focus, hindering the image acquisition process. Furthermore, recovering liposomes out of the chip is also a tedious process. These drawbacks urge an upgrade of the existing OLA design with a sophisticated collection chamber which could further ease the imaging of liposomes.

6.2 ADVANTAGE OF ON-CHIP PROTEIN EVOLUTION.

Traditionally speaking, bacterial cells are a popular choice for protein engineering. But, factors like the risk of antibiotic resistance, rejection of genes, and cellular toxicity often limit its usage. Despite cells being easy to handle, the phenotypic cell-to-cell variability also hampers the reproducibility of the assay. The use of synthetic emulsion-based confinements along with cell-free expression systems outweigh these drawbacks. Bulk techniques to generate emulsions are undesired due to confinement size variation and low encapsulation efficiency. On-chip microfluidic technology overcomes these limitations owing to its features like high-throughput, uniform size distribution and ease of manipulation, thus benefiting protein evolution assays.

6.2.1 Overcoming on-chip limitations for protein evolution.

While microfluidics in its true sense is an engineering field, its increasing application in facilitating life-science research is capturing the attention among the community[26, 27]. One obvious and major disadvantage of the current state of microfluidic technology is its restriction to specialized laboratories and the need of specialized personnel. Decentralization of on-chip technology to make it easily accessible to users will boost the process of protein evolution. One such example is that of paper-based microfluidic (a sub-division of microfluidics to understand fluid flow in porous materials) which have led to the development of lateral flow assays. This technology is now widely used in developing rapid, low-cost sensing of molecules[28] including development of diagnostic tests like hormone-based pregnancy[29] and antibody-based COVID-19

tests[30]. Similarly, standardization and commercialization of microfluidic setups by building a user-friendly economic microfluidic emulsion generation would provide higher accessibility to non-specialized users and positively impact assay consistency.

Fluorescence-based retracing of a desired phenotype to its genetic origin (phenotype-to-genotype) is a commonly used strategy in double emulsions. Due to commercially available fluorescence-activated cell sorters (FACS), fluorescence-based assays have become the norm for sorting double emulsions. Nevertheless, the system is primarily designed for cell sorting. Using FACS to sort double emulsions requires additional optimization and yet it often results in a lower yield of recovered double emulsions. Simplifying the sophisticated FACS and its upgrading to optimize the sorting of double emulsions will streamline the downstream processing. Since it is not possible to always use a fluorescence-based screening method, the need to further explore and develop fluorescence-free screening techniques such as on-chip absorbance-assisted droplet sorting is of prime importance[31].

6.2.2 Unresolved queries in *in vitro* protein evolution

Currently, the genotype-to-phenotype linkage confers a strict rule of a single gene per confinement. Assuming a Poisson distribution, this implies that the majority of the containers are left empty, leading to a wastage of precious resources. One option could be to aim for multiple genes per droplet (in the order of 10 to 100) which reduces wastage, while being aware that this might come at the cost of performing multiple iterations. Additionally, a single copy of gene is often insufficient to bring about the desired genotype-to-phenotype linkage. Clonal amplification of genes within an emulsion by using droplet polymerase chain reaction will positively benefit the assay.

Secondly, the cycle of laboratory evolution is a multistep process, with each step requiring a specialized equipment. This also requires extensive human intervention and skilled personnel limiting its usage to a few laboratories. Can this process be standardized and made more accessible? An idea would be to make next generation chips with integrated modules like emulsion generation, droplet incubation chamber, and sorting module. Further integrating high-throughput and accurate sequencing modules like nanopore sequencing[32] will truly make directed evolution a single step sample-in-result-out technique. Apart from currently preferred confinements (single emulsions, double emulsions, and liposomes), other synthetic confinements like polymersomes and actinosomes could perhaps also be useful for laboratory evolution.

6.3. IMPACT OF TICKS ON GLOBAL HEALTHCARE.

Vector-borne diseases are increasing globally, accounting for around 17% of all infectious diseases. Additionally, global warming extend favorable seasons for vector breading and thus extend the disease transmission period. Mosquitoes are the source of most vector-borne diseases, and a recent survey reported that an additional 4.7 billion people may be at the risk of malaria and dengue by 2070[33]. Similarly, tick-borne diseases like Lyme disease and tick-borne encephalitis are caused by transmitting bacteria of *Borrelia* species and tick-borne encephalitic virus, respectively[34, 35]. Similar to mosquito borne diseases, tick-borne Lyme disease is also a growing burden on public healthcare[36]. In corroboration to this, the national survey of the Netherlands showed a 4-fold increase in the cases of Lyme disease from the year 1994 to 2021 (**Figure 6.4**). While the prevalence of Lyme disease increases everywhere in the Netherlands, the northeastern provinces of Drenthe and Groningen seem to be particularly affected compared to other western and southern provinces. Although the exact reason of this rise remains unknown, these data urge the need to understand the fundamental process of tick-host interaction. This will assist in implementing appropriate measures to manage and prevent the spread of tick-borne diseases. In **Chapter 4**, we reported our findings on tick-host interactions and the following section discusses a roadmap for future investigations.

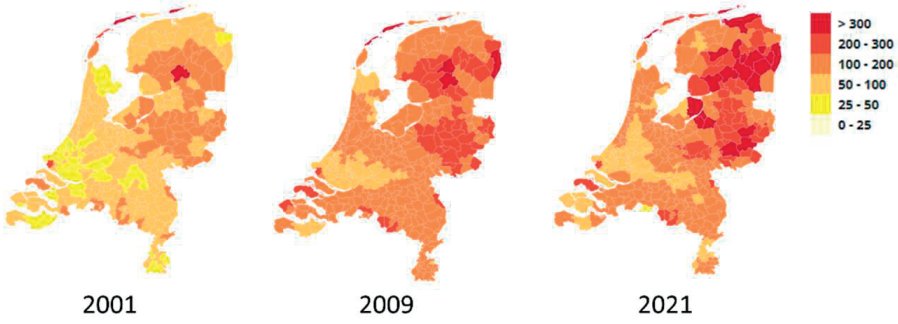

Figure 6.4:

Epidemiological survey reporting number of cases (per 100000 people) with erythema migrans, an early symptoms of Lyme disease. (Image source from tekenradar.nl RIVM)

6.3.1 Future landscape of biomolecular condensate investigations in ticks

Protein phase separation is gaining interest in biology owing to its diverse role in regulating cellular functions. On the other hand, research exploring its role apart from cellular regulation has just began. In this thesis, we characterized the LLPS behavior of

intrinsically disordered glycine-rich protein (hereby referred to as GRP77), a secretory protein in tick saliva highlighting its role in host adhesion. Since glycine-rich proteins form one of the largest family of proteins found in tick saliva, we used GRP77 as a model protein. We are aware that this does not accurately resemble the complex tick salivary composition. While using tick saliva seems to be a reasonable approach, the complication to extract tick-saliva along with sample-to-sample variability makes this an unviable approach. A good compromise would be to gradually increase the complexity like investigating different GRPs from the large family. One particular protein of interest would be 64P, especially due to its tendency to elicit an immune response in the host. Reports suggest that administration of a host with recombinant 64P is highly effective against adult ticks and the anti-64P antibodies target the tick-feeding site impairing attachment and also cross react with the tick midgut[37]. Future investigation combining GRP77 and 64P will offer new insights in tick adhesion and may lead to a potential solution in developing an efficient anti-tick vaccine strategy. We also showed that physical parameters like salt highly affect the process of GRP77 LLPS; at the same time, other physiological factors like temperature and pH could also affect this process. Interestingly, the N-terminus of GRP77 is concentrated with charged amino acids like glutamic acid, aspartic acid and lysine whereas basic amino acids like arginine are interspersed in the C-terminus. This distribution of charged amino acids also urges the need to explore the effect of pH. Since we used chemically synthesized GRP77, the effect of post-translation modification is not taken into account, however these modifications can also influence GRP77 LLPS. Multiple reports on a sticker and spacer model[38, 39, 40] suggest that stickers interspersed with nonpolar amino acids intermolecularly interact to form protein droplets. In corroboration with this model, GRP77 also exhibits similar patterns (**Figure 6.5a**). Our results also showed that cation-pi interactions are the driving force of GRP77 LLPS (**Figure 6.5b**). We further demonstrated that ageing of condensates changes their material properties, making them more gel-like. Wu Xi et al. has attributed the liquid-to-gel transition to aromatic amino acids[41], but further investigation is required to verify if similar phenomena take place in GRP77 LLPS. Spectroscopic observations have reported that proteins in biomolecular condensates can further order themselves into a β-sheet conformation[42, 43]. On the other hand, there is still a clear gap in explaining this ordering within biomolecular condensates. Additionally, it will be interesting to see if the process of liquid-to-solid transitioning of biomolecular condensates can be slowed down, reversed of perhaps even prevented? This question is particularly relevant and in corroboration with ticks, especially since the mechanisms of tick detachment post blood-feeding is still unknown. One hypothesis suggests that post-feeding, ticks secrete protease-rich saliva which partially dissolves the cement cone[44], thus facilitating tick detachment but concrete experimental evidence supporting this hypothesis is still lacking.

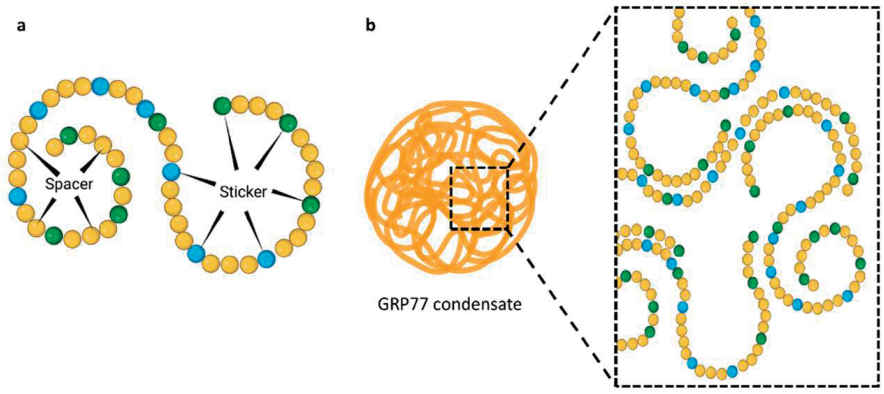

Figure 6.5: Molecular interaction in biomolecular condensates.

(a) Illustration of simplified schematic of GRP77 where yellow, green, and blue spheres are nonpolar, basic, and aromatic amino acids respectively. (b) Schematic showing GRP77 intermolecular cation-pi interaction of basic and aromatic amino acids.

6.4 EMERGING APPLICATIONS IN BIOMOLECULAR CONDENSATES.

Therapeutics

Biomolecular condensates are increasingly gaining attention in understanding cellular functions. Importantly, their dysfunction has been linked to pathological conditions including neurodegenerative disorders, viral infections and cancer[45]. Despite this being a young field, synthetic biomolecular condensates are gaining interest in therapeutics. The intrinsic property of biomolecular condensates to selectively sequester molecules can be of vital importance to sequester and deliver drugs. Several chemotherapeutic agents like Cisplatin and Mitoxantrone have been identified to partition into transcriptional condensates influencing their condensate phase behavior. This phenomenon is gaining attention especially among pharmaceutical industries[46]. In 2019, Bayer invested $100 million in Boston and Dresden-based condensate-focused therapeutics company, Dewpoint therapeutics[47]. Additionally, a proof-of-principle study also showed that synthetic biomolecular condensates can suppress aggregation of proteins associated with neurodegenerative disorder[48], suggesting biomolecular condensates would play a prominent role in therapeutics.

Adhesive material

Although ageing-associated hardening of biomolecular condensates in cells is regarded as a negative effect in cellular biochemistry, the same process proves to be a crucial phenomenon for certain organisms. For example, condensate-based glue helps sandcastle worms to build reef [49], phase separating mussel foot protein assists mussel adhesion to a substrate [50] and spider silk-inspired proteins phase separate to form thick fiber-like structures[51]. This liquid-to-solid transitioning of biomolecular condensates can be of key importance to develop biomolecular condensate-based adhesive materials.

Emerging sustainable materials

With growing concerns of rapid consumption of limited natural resources, the need to improve and innovate novel sustainable materials is at the peak. Inspired from biological soft matter including biomolecular condensates, *van Lange, et al.* have prototyped coacervate-based recyclable and sustainable materials exhibiting similar material properties to covalently cross-linked plastics[52]. Similarly, harvesting the material properties of biomolecular condensates can have various applications in designing emerging materials. For instance, droplets formed via phase-separation of chitosan (naturally occurring polysaccharide) along with hyaluronic acid (fluid in eyes and joints) have been shown to be possible candidates as a bio-based ink for 3D printing[53]. Focused on recycling the biowaste, a study has reported the use of pH-induced phase separation of keratin, isolated from waste wool, to make synthetic fibers[54, 55]. Another example of complex coacervate composed of naturally occurring polymers (chitosan and cellulose) is for developing filtration membranes to separate oil droplets from oil-in-water emulsions[56].

6.5 SOCIETAL RELEVANCE OF THE FINDINGS FROM THE THESIS.

With advancement in technology, modern science is able to reveal the basic operating principles of life. While scientists have extensively explored the fundamental understanding of cells, the basis of complex life, we still lack the primary understanding of how the molecular soup involved in cellular interactions operate in a collective manner. This thesis approached the use of bottom-up technology to understand life in a minimalist way. Employing microfluidics in **Chapter 3** and **Chapter 5** we showed that we can synthetically create membrane bound cell-like micron-sized confinements. These studies demonstrated the use of microfluidics to encapsulate and retain biomolecules in a membrane-bound confined space. Secondly, in **Chapter 2** we made the use of the intrinsic property of synthetic membraneless organelles to sequester biomolecules, eliminating the need of sophisticated setups. We subsequently trans-

formed these synthetic membranelles organelles into a hollow, shell-like confinement, which we termed actinosomes and employed them for cell-free protein production. Although these findings just scratch the surface of designing a synthetic cell, this path will assist the development of unprecedented new applications in many areas such as medicine, food, biomaterials, and sustainable energy as discussed in the previous section. Finally, in **Chapter 4**, we explored and investigated the role of tick salivary glycine-rich protein in host adhesion via cement cone formation. Our findings are the first report suggesting a possible mechanism of tick cement cone formation via the process of liquid-liquid phase separation, assembling nanometer-sized individual proteins, into micron-scale sticky structures. Through our systematic assessment, we determined the important physiological conditions and molecular patterns that drive this process. These findings serve as a starting point for researchers to further investigate in chemical or natural compounds that could prevent tick adhesion together with creating a general protocol to prevent tick bites with possible implication in developing anti-tick vaccination strategies.

REFERENCES

1. Su W-C, Ho JC, Gettel DL, Rowland AT, Keating CD, Parikh AN. Kinetic control of shape deformations and membrane phase separation inside giant vesicles. *Nature Chemistry* 2023**:** 1-9.
2. Heald R, Cohen-Fix O. Morphology and function of membrane-bound organelles. *Current opinion in cell biology* 2014, **26:** 79-86.
3. Van Nies P, Westerlaken I, Blanken D, Salas M, Mencía M, Danelon C. Self-replication of DNA by its encoded proteins in liposome-based synthetic cells. *Nature communications* 2018, **9**(1)**:** 1583.
4. Blanken D, Foschepoth D, Serrão AC, Danelon C. Genetically controlled membrane synthesis in liposomes. *Nature communications* 2020, **11**(1)**:** 4317.
5. Deshpande S, Wunnava S, Hueting D, Dekker C. Membrane tension–mediated growth of liposomes. *Small* 2019, **15**(38)**:** 1902898.
6. Deshpande S, Spoelstra WK, Van Doorn M, Kerssemakers J, Dekker C. Mechanical division of cell-sized liposomes. *ACS nano* 2018, **12**(3)**:** 2560-2568.
7. Su X, Ditlev JA, Hui E, Xing W, Banjade S, Okrut J*, et al.* Phase separation of signaling molecules promotes T cell receptor signal transduction. *Science* 2016, **352**(6285)**:** 595-599.
8. Yewdall NA, André AA, Lu T, Spruijt E. Coacervates as models of membraneless organelles. *Current Opinion in Colloid & Interface Science* 2021, **52:** 101416.
9. MacEwan SR, Chilkoti A. Elastin-like polypeptides: Biomedical applications of tunable biopolymers. *Peptide Science: Original Research on Biomolecules* 2010, **94**(1)**:** 60-77.
10. Simon JR, Carroll NJ, Rubinstein M, Chilkoti A, López GP. Programming molecular self-assembly of intrinsically disordered proteins containing sequences of low complexity. *Nature chemistry* 2017, **9**(6)**:** 509-515.
11. de Haas RJ, Ganar KA, Deshpande S, de Vries R. pH-Responsive Elastin-Like Polypeptide Designer Condensates. *ACS applied materials & interfaces* 2023, **15**(38)**:** 45336-45344.
12. Last MG, Deshpande S, Dekker C. pH-controlled coacervate–membrane interactions within liposomes. *ACS nano* 2020, **14**(4)**:** 4487-4498.
13. Love C, Steinkühler J, Gonzales DT, Yandrapalli N, Robinson T, Dimova R*, et al.* Reversible pH-responsive coacervate formation in lipid vesicles activates dormant enzymatic reactions. *Angewandte Chemie* 2020, **132**(15)**:** 6006-6013.
14. Deng NN, Huck WT. Microfluidic formation of monodisperse coacervate organelles in liposomes. *Angewandte Chemie* 2017, **129**(33)**:** 9868-9872.
15. Kobayashi M, Noguchi H, Sato G, Watanabe C, Fujiwara K, Yanagisawa M. Phase-Separated Giant Liposomes for Stable Elevation of α-Hemolysin Concentration in Lipid Membranes. *Langmuir* 2023, **39**(32)**:** 11481-11489.
16. Dreher Y, Jahnke K, Bobkova E, Spatz JP, Göpfrich K. Division and regrowth of phase-separated giant unilamellar vesicles. *Angewandte Chemie International Edition* 2021, **60**(19)**:** 10661-10669.
17. Bergeron-Sandoval L-P, Michnick SW. Mechanics, structure and function of biopolymer condensates. *Journal of molecular biology* 2018, **430**(23)**:** 4754-4761.
18. Lu T, Liese S, Schoenmakers L, Weber CA, Suzuki H, Huck WT*, et al.* Endocytosis of coacervates into liposomes. *Journal of the American Chemical Society* 2022, **144**(30)**:** 13451-13455.
19. Lu T, Hu X, van Haren MH, Spruijt E, Huck WT. Structure-Property Relationships Governing Membrane-Penetrating Behaviour of Complex Coacervates. *Small* 2023**:** 2303138.
20. Mangiarotti A, Chen N, Zhao Z, Lipowsky R, Dimova R. Wetting and complex remodeling of membranes by biomolecular condensates. *Nature Communications* 2023, **14**(1)**:** 2809.

21. Ferry MS, Razinkov IA, Hasty J. Microfluidics for synthetic biology: from design to execution. *Methods in enzymology*, vol. 497. Elsevier, 2011, pp 295-372.
22. Gach PC, Iwai K, Kim PW, Hillson NJ, Singh AK. Droplet microfluidics for synthetic biology. *Lab on a Chip* 2017, **17**(20)**:** 3388-3400.
23. Göpfrich K, Platzman I, Spatz JP. Mastering complexity: towards bottom-up construction of multifunctional eukaryotic synthetic cells. *Trends in biotechnology* 2018, **36**(9)**:** 938-951.
24. Shang L, Cheng Y, Zhao Y. Emerging droplet microfluidics. *Chemical reviews* 2017, **117**(12)**:** 7964-8040.
25. Deshpande S, Brandenburg F, Lau A, Last MG, Spoelstra WK, Reese L*, et al.* Spatiotemporal control of coacervate formation within liposomes. *Nature communications* 2019, **10**(1)**:** 1800.
26. Convery N, Gadegaard N. 30 years of microfluidics. *Micro and Nano Engineering* 2019, **2:** 76-91.
27. Sackmann EK, Fulton AL, Beebe DJ. The present and future role of microfluidics in biomedical research. *Nature* 2014, **507**(7491)**:** 181-189.
28. Toley BJ, Das D, Ganar KA, Kaur N, Meena M, Rath D*, et al.* Multidimensional paper networks: a new generation of low-cost pump-free microfluidic devices. *Journal of the Indian Institute of Science* 2018, **98**(2)**:** 103-136.
29. Khelifa L, Hu Y, Jiang N, Yetisen AK. Lateral flow assays for hormone detection. *Lab on a Chip* 2022, **22**(13)**:** 2451-2475.
30. Budd J, Miller BS, Weckman NE, Cherkaoui D, Huang D, Decruz AT*, et al.* Lateral flow test engineering and lessons learned from COVID-19. *Nature Reviews Bioengineering* 2023, **1**(1)**:** 13-31.
31. Duncombe TA, Ponti A, Seebeck FP, Dittrich PS. UV–Vis spectra-activated droplet sorting for label-free chemical identification and collection of droplets. *Analytical Chemistry* 2021, **93**(38)**:** 13008-13013.
32. Branton D, Deamer DW, Marziali A, Bayley H, Benner SA, Butler T*, et al.* The potential and challenges of nanopore sequencing. *Nature biotechnology* 2008, **26**(10)**:** 1146-1153.
33. Colón-González FJ, Sewe MO, Tompkins AM, Sjödin H, Casallas A, Rocklöv J*, et al.* Projecting the risk of mosquito-borne diseases in a warmer and more populated world: a multi-model, multi-scenario intercomparison modelling study. *The Lancet Planetary Health* 2021, **5**(7)**:** e404-e414.
34. Rochlin I, Toledo A. Emerging tick-borne pathogens of public health importance: a mini-review. *Journal of medical microbiology* 2020, **69**(6)**:** 781.
35. Madison-Antenucci S, Kramer LD, Gebhardt LL, Kauffman E. Emerging tick-borne diseases. *Clinical microbiology reviews* 2020, **33**(2)**:** 10.1128/cmr. 00083-00018.
36. Lippi CA, Ryan SJ, White AL, Gaff HD, Carlson CJ. Trends and opportunities in tick-borne disease geography. *Journal of medical entomology* 2021, **58**(6)**:** 2021-2029.
37. Trimnell AR, Hails RS, Nuttall PA. Dual action ectoparasite vaccine targeting 'exposed'and 'concealed'antigens. *Vaccine* 2002, **20**(29-30)**:** 3560-3568.
38. Wang J, Choi J-M, Holehouse AS, Lee HO, Zhang X, Jahnel M*, et al.* A molecular grammar governing the driving forces for phase separation of prion-like RNA binding proteins. *Cell* 2018, **174**(3)**:** 688-699. e616.
39. Martin EW, Holehouse AS, Peran I, Farag M, Incicco JJ, Bremer A*, et al.* Valence and patterning of aromatic residues determine the phase behavior of prion-like domains. *Science* 2020, **367**(6478)**:** 694-699.
40. Abbas M, Lipiński WP, Nakashima KK, Huck WT, Spruijt E. A short peptide synthon for liquid–liquid phase separation. *Nature Chemistry* 2021, **13**(11)**:** 1046-1054.

41. Wu X, Sun Y, Yu J, Miserez A. Tuning the viscoelastic properties of peptide coacervates by single amino acid mutations and salt kosmotropicity. *Communications Chemistry* 2024, **7**(1)**:** 5.
42. Peran I, Mittag T. Molecular structure in biomolecular condensates. *Current opinion in structural biology* 2020, **60:** 17-26.
43. Shen Y, Chen A, Wang W, Shen Y, Ruggeri FS, Aime S*, et al.* The liquid-to-solid transition of FUS is promoted by the condensate surface. *Proceedings of the National Academy of Sciences* 2023, **120**(33)**:** e2301366120.
44. Suppan J, Engel B, Marchetti-Deschmann M, Nürnberger S. Tick attachment cement–reviewing the mysteries of a biological skin plug system. *Biological Reviews* 2018, **93**(2)**:** 1056-1076.
45. Mitrea DM, Mittasch M, Gomes BF, Klein IA, Murcko MA. Modulating biomolecular condensates: a novel approach to drug discovery. *Nature Reviews Drug Discovery* 2022, **21**(11)**:** 841-862.
46. Klein IA, Boija A, Afeyan LK, Hawken SW, Fan M, Dall'Agnese A*, et al.* Partitioning of cancer therapeutics in nuclear condensates. *Science* 2020, **368**(6497)**:** 1386-1392.
47. Marx V. Cell biology befriends soft matter physics. *Nature Methods* 2020, **17**(6)**:** 567-570.
48. Lipiński WP, Visser BS, Robu I, Fakhree MA, Lindhoud S, Claessens MM*, et al.* Biomolecular condensates can both accelerate and suppress aggregation of α-synuclein. *Science advances* 2022, **8**(48)**:** eabq6495.
49. Stewart RJ, Wang CS, Song IT, Jones JP. The role of coacervation and phase transitions in the sandcastle worm adhesive system. *Advances in colloid and interface science* 2017, **239:** 88-96.
50. Guo Q, Zou G, Qian X, Chen S, Gao H, Yu J. Hydrogen-bonds mediate liquid-liquid phase separation of mussel derived adhesive peptides. *Nature Communications* 2022, **13**(1)**:** 5771.
51. Mohammadi P, Beaune Gg, Stokke BT, Timonen JV, Linder MB. Self-coacervation of a silk-like protein and its use as an adhesive for cellulosic materials. *ACS macro letters* 2018, **7**(9)**:** 1120-1125.
52. van Lange SG, Te Brake DW, Portale G, Palanisamy A, Sprakel J, van der Gucht J. Moderated ionic bonding for water-free recyclable polyelectrolyte complex materials. *Science Advances* 2024, **10**(2)**:** eadi3606.
53. Khoonkari M, Es Sayed J, Oggioni M, Amirsadeghi A, Dijkstra P, Parisi D*, et al.* Bioinspired Processing: Complex Coacervates as Versatile Inks for 3D Bioprinting. *Advanced Materials* 2023**:** 2210769.
54. Sun J, Monreal Santiago G, Yan F, Zhou W, Rudolf P, Portale G*, et al.* Bioinspired Processing of Keratin into Upcycled Fibers through pH-Induced Coacervation. *ACS Sustainable Chemistry & Engineering* 2023, **11**(5)**:** 1985-1994.
55. Sun J, Monreal Santiago G, Zhou W, Portale G, Kamperman M. Water-processable, stretchable, and ion-conducting coacervate fibers from keratin associations with polyelectrolytes. *ACS Sustainable Chemistry & Engineering* 2022, **10**(48)**:** 15968-15977.
56. Li L, Baig MI, de Vos WM, Lindhoud S. Preparation of Sodium Carboxymethyl Cellulose–Chitosan Complex Membranes through Sustainable Aqueous Phase Separation. *ACS Applied Polymer Materials* 2023, **5**(3)**:** 1810-1818.

Summary

Even the simplest forms of life exhibit remarkable complexity. Cells, the basic units of life, function by organizing their chaotic interior into discrete confinements. These compartments can be broadly categorized into two distinct classes. The first class consists of membrane-bound organelles like mitochondria and nucleus composed of a physical boundary in the form of a lipid membrane. The second class includes membraneless confinements, like the nucleolus and P-granules, formed via the process of liquid-liquid phase separation (LLPS). In this thesis, we have developed various cellular mimics inspired by membrane-bound and membraneless organelles and explored tactics for structuring synthetic cells.

In **Chapter 2**, we developed an easy technique to produce protein-based, cell-sized, porous confinements. Using a complex coacervate composed of positively charged polylysine and negatively charged nucleoside triphosphate as a synthetic model for membraneless organelles, we localized actin monomers on the surface of the coacervate. Polymerizing the actin monomers along with osmotic gradients, the coacervate transformed into a hollow micron-sized container, with the surface composed of a mesh of actin filaments and polylysine; we named such a container actinosome. The formed actinosomes are micron-sized confinements with a porous surface allowing diffusion of small molecules (< 5 nm diameter) across the surface while retaining larger molecules within their interior. Additionally, the intrinsic property of coacervates to sequester biomolecules allowed us to easily encapsulate complex biomolecules like RNA along with cell-free translation machinery. Finally, we demonstrated that actinosomes are biocompatible, and as an example, we expressed green-fluorescence protein (GFP) within them. This easy and affordable technique to make biocompatible confinements can have wide applications in the field of bioengineering.

In **Chapter 3**, we detailed the protocol on using microfluidic-based Octanol-assisted Liposome Assembly (OLA) for generation of liposomes in a controlled and high-throughput manner. In a simplistic view, cells can be seen as aqueous confinements bound by a membrane. OLA-produced liposomes represent this simplistic model of cells architected with a membrane composed of a lipid bilayer. Liposomes produced using OLA are monodispersed, micron-sized, with efficient encapsulation capacity, and require very small sample volumes (~50 µL), beneficial when working with crucial biologicals. We further demonstrated the formation of a complex coacervate composed of polylysine and adenosine triphosphate within liposomes, thus creating a model membraneless organelle within membrane-bound confinements. This serves as a starting point in building and architecting a synthetic cell.

In **Chapter 5**, we designed an on-chip microfluidic platform for high-throughput and robust production of micron-sized double emulsion-based confinements, which

are much more stable than liposomes and thus suitable for specific applications. The fabricated microfluidic chip consisted of two flow-focusing junctions that generate monodispersed water-in-oil-in-water double emulsions in a high-throughput fashion (production rate up to 10^6 double emulsions per hour). The surfactant-stabilized oil layer keeps the double emulsions stable for long durations (up to weeks) while preventing leakage of biomolecules. To test their biocompatibility, we encapsulated cell-free transcription and translation machinery along with GFP-encoding gene and demonstrated cell-free expression of GFP within double emulsions. We used these double emulsions as *in vitro* confinements to carry out directed protein evolution experiments. We first linked the gene-editing CRISPR-Cas9 system with GFP expression. Using this fluorescence-based assay, we demonstrated novel *in vitro* strategies to link the genotype to the phenotype, a prerequisite for laboratory protein evolution. Using commercially available fluorescence-assisted cell sorter, we sorted the double emulsions based on varying fluorescence and successfully retraced the genotype from the phenotype. This study provides a framework to conduct fluorescence-based *in vitro* protein evolution studies.

With growing interest in understanding the role of intrinsically disordered proteins in cell biology, in **Chapter 4**, we investigated one such secretory protein from ticks, known as the glycine-rich protein (GRP77), in order to identify its role in tick adhesion to the host. During the process of blood feeding, ticks adhere to their host for long duration (up to weeks), for which a firm attachment to the host is needed. This attachment is supported by the formation of cement cone which is a complex mixture including proteins from the glycine-rich protein family. We demonstrated two mechanisms—evaporation and kosmotropic salt-induced—that drives LLPS of GRP77. Further dissecting the intermolecular forces involved in this process, we noted heterogenous distribution of amino acids in the GRP77 sequence, where the N-terminus region is rich in basic and acidic amino acids while the C-terminus is rich in aromatic and cationic amino acids. Systematic investigation of these termini showed that cation–π interactions between arginine and aromatic amino acids (tyrosine and phenylalanine) is the primary driving force for GRP77 phase separation. We further used microfluidics to deform GRP77 droplets by flow-induced shear, confirming their liquid-like nature. Importantly, we showed that GRP77 droplets age over time, drastically altering their material properties and undergo a liquid-to-gel transition. Force adhesion measurements also revealed that GRP77 droplets are adhesive in nature. Lastly, we extracted salivary glands from ticks of species *I. ricinus* and provided evidence for protein-rich condensates in natural tick saliva. This study is the first report describing a possible mechanism for the formation of tick cement cone and thus acts as a starting point to gain insights into the development of novel tick-control strategies along with vaccine development.

LIST OF PUBLICATION

This thesis

- Shaping synthetic cells through cytoskeleton-condensate-membrane interactions. **KA Ganar**, LW Honaker, S Deshpande*. **2021** Current Opinion in Colloid & Interface Science 54, 101459 (**Chapter 1**).

- (R) evolution-on-a-chip. E Bouzetos, **KA Ganar**, E Mastrobattista, S Deshpande, J van der Oost*. **2022** Trends in Biotechnology 40 (1), 60-76 (**Chapter 1**).

- Actinosomes: condensate-templated containers for engineering synthetic cells. **KA Ganar**, L Leijten, S Deshpande*. **2022** ACS synthetic biology 11 (8), 2869-2879 (**Chapter 2**).

- On-Chip Octanol-Assisted Liposome Assembly for Bioengineering. C Chen † , **KA Ganar** † , S Deshpande* **2023** Journal of Visualized Experiments, e65032 (**Chapter 3**).

- Phase separation and ageing of glycine-rich protein from tick adhesive. **KA Ganar** † , M Nandy † , P Turbina † , C Chen, D Suylen, S van der Beelen, EL Pascoe, CJM Koenraadt, I Dijkgraaf*, S Deshpande* bioRxiv, **2023**.03. 27.534361 (accepted Nature Chemistry) (**Chapter 4**).

- Cell-free screening of CRISPR-Cas activity by microfluidics-assisted in vitro compartmentalization. E Bouzetos † , **KA Ganar** † , S Deshpande * , J van der Oost * (Submitted) (**Chapter 5**).

Other Work

- Elastin-Like Polypeptide condensates as reversible triggerable compartments for synthetic cells. C Chen, **KA Ganar**, RJ de Haas, N Jarnot, E Hogeveen, R de Vries, S Deshpande*. (Submitted)

- pH-Responsive Elastin-Like Polypeptide Designer Condensates. RJ de Haas, **KA Ganar**, S Deshpande, R de Vries* (**2023**) ACS applied materials & interfaces 15 (38), 45336-45344.

- Continuous counter-current electrophoretic separation of oleosomes and proteins from oilseeds. K Ayan, **KA Ganar**, S Deshpande, RM Boom, CV Nikiforidis* (**2023**) Food Hydrocolloids 144, 109053.

- Multidimensional paper networks: a new generation of low-cost pump-free microfluidic devices BJ Toley*, D Das, K Ganar, N Kaur, M Meena, D Rath, N Sathishkumar, S Soni (**2018**) Journal of the Indian Institute of Science 98 (2), 103-136.

- Emergence of a deviating genotype VI pigeon paramyxovirus type-1 isolated from India **K Ganar**, M Das, AA Raut, A Mishra, S Kumar* (**2017**) Archives of virology 162, 2169-2174.

- Avian paramyxovirus: a brief review P Gogoi, **K Ganar**, S Kumar* (**2017**) Tran boundary and emerging diseases 64 (1), 53-67.

- Molecular characterization of chicken anemia virus outbreaks in Nagpur province, India from 2012 to 2015. **K Ganar**, M Shah, BP Kamdi, NV Kurkure, S Kumar* (**2017**) Microbial pathogenesis 102, 113-119.

- Newcastle disease virus: current status and our understanding. **K Ganar**, M Das, S Sinha, S Kumar* (**2014**) Virus research 184, 71-81.

† authors contributed equally
* corresponding authors

ACKNOWLEDGEMENTS

The train of thoughts to thank people can only begin by thanking you **Siddharth**. Firstly, I cannot thank you enough for choosing Wageningen over Dresden. The past four years, right from setting-up the lab to submitting the thesis, have been a great learning experience for me. The journey definitely had a rough start but thanks to your guidance, patience and endless support that kept me going while being sane. While not all the projects succeed, with your vision we definitely managed to hit some good home runs. You always ensured that we kept having fun while doing experiments. I definitely enjoyed having our one-on-one meetings in marathi and enjoyed slipping in some Vidarbhan vocabulary in it. The summer and winter EmBioSys group activities kept building a good chemistry among the members and in evidently helped keeping a stress-free and friendly atmosphere in the group. I thank you for all the opportunity and always having my back during this journey. I absolutely enjoyed every bit of it!

Jasper thanks for your valuable inputs during the update meetings. You are one of the most relaxed group chairs I have experienced and your humble and kind approach puts people at ease. Your efforts to maintain a healthy working environment is the primary reason for PCC being such a lucrative work place with unique flavors of interdisciplinary scientists. Thanks for giving me the opportunity and freedom to work on multiple projects of my choice. You are truly a great promotor.

Mara, Leonie and **Claudia** let me first apologies for often writing the wrong project number on order request form. I cannot emphasize this enough that you are the core of PCC in maintaining a stable, happy, healthy and safe environment. Thanks a lot for unburdening me from administrative and financial work.

Geeta, thanks for hosting the dinners and particularly cooking comforting India food. I am guilty for unintentionally teaching Siddharth some Vidarbhan Marathi and I promise from now on there will be no more work talks at the dinner. Thanks again for the support. Vivan and **Paritosh** you guys are pure gold of entertainment and I had a lot of fun talking to you guys. It is a pleasure to see you guys grow and I wish you all the best for your adventure in coming middlebare school.

Larry, your knowledge of random stuff is incredible and thanks for enlightening with all that random interesting fun facts from you. Thanks for proof reading the manuscripts and having all the short conversations which always ended up in long ones. It was pleasure to work with you. **Chang**, my man! thanks for being my lab buddy and paranymph. You are an extremely hardworking person with huge contribution in this thesis. Moreover you constantly kept giving me the moral support needed to keep

going. but more importantly introducing the special menu of the eastern express, it changed my lunch habit and now I can't get enough of it. Thanks for being such a great support Chang. **Manali**, you joined the tick project and what a ride it has been since then. You brought some of the most interesting technical expertise and your understanding of physical chemistry has immensely helped the story. Getting this far without your help seems just impossible. Thanks for all the help and wish you all the best for future! **Xuefeng**, you are the best of officemate I could have asked for, thank you for teaching me how to be relaxed and be focused. I wish you good luck with the completion and looking forward to join you on your biking adventures. **Vinayaka**, thanks for introducing me to the world of Raman spectroscopy and more importantly performing the experiments while I was hardly of any use. I have huge respect for you to go through the torture of tender process and administration stuff. I wish you all the best with your new Raman and optical tweezer setup.

To all the students **Liza, Selena, Polina, Annemarie, Willem** and **Elisa** working with you guys I had so much fun. All of you guys took a risk and fearlessly dived into new projects without thinking of the consequences. Your research is directly or indirectly embedded in this thesis and I thank you all for your gigantic contribution in making this book. I wish you all the best with your future endeavors. **Pim, Teresa** and **Simon**, I supervised you very shortly during ASM and you were one hell of a smart, motivated, hardworking and independent group. Pim, you joined the Embiosys lab later and it was a great vibe to have you in the microscopy room with "down with the sickness" playing in the background. You definitely have "PhD is a paid vacation" vibe \m/. **Noor**, it was great to have you in the ASM practical group, and your creative thinking out of the box attitude definitely helped getting some cool results out of the project. I wish you all the best for you future.

John van der Oost, it was an absolute pleasure to work with you on the directed evolution story. Even when things went south, your positivity and directing the project in right direction, resulted in a beautiful chapter and soon a good publication. I thank you for providing all the valuable inputs in the last four years. **Eugene**, what a journey it was, I learnt a lot about CRISPR from you. You always aimed at making things perfect and this is what was essential for the directed evolution project. Although we didn't evolve the protein, I am satisfied the way this project evolved in past 4 years. Thanks a lot again for everything and I wish you all the best with completion. **Kubra**, you are a driven person and also a fast learner. Thanks for taking the lead on the biomolecule separation project. I can vouch that this project wouldn't have been possible without you. **Costas** I really like the relaxed chill vibe you have and enjoyed working with you. Thanks for introducing the food aspect of physical chemistry to me. I always enjoyed having small chats in your office. **Emily**, lets go tick hunting!

You have such a cool job of going in the forest on sunny days to catch ticks. Thanks for taking me along with you and training me to acquire the art of tick hunting. I had a lot of fun working with you and again thanks for teaching me tick dissection. **Sander**, thanks for giving feedback on the manuscript, and allowing me to sneak in some of the entomology group events. **Ingrid**, thanks for sending kilos of GRP and other peptides. The tick project wouldn't have been possible without you. This project was challenging and heavily dependent on the supply of proteins. It was your readiness to provide proteins and its variant timely that made it possible. Thanks a lot for all you help.

Renko, thanks for all the collaborative efforts over multiple projects. It was fun work on the ELP project and I hope that the collaboration keeps going forward with other lab members. **Tom**, thanks for providing simple solutions for complicated problems and thanks for the nice discussions and good advices after group meeting presentations. **Hanne**, I like your style of working more in the late evenings. I enjoyed having scientific and non-scientific discussion with you. Thanks for your inputs. **Frans**, thanks for the short and long discussions on the physics of coacervates.

Remco, thanks for all the help in setting-up the microscope along with the microfluidic setup. **Diana**, thanks for the help in 6070 lab, I promise that the PDMS station will be cleaner from now on. **Raoul**, thanks for building the amazing setup to take nice images. A big shoutout to all the three of you for the assistance in keeping the labs functioning.

Dr. Martijn van Galen, crossing your office 6071 was always a risky business. To enter/exit 6070 lab meant a tax of 15 minutes of conversation had to be paid to you. Nonetheless, I am happy to pay that tax. You were a great support in the last stretch of the PhD, especially the writing part. Thanks for being a cheerful energy around. **Mr. Rob de Haas**, oops sorry your highness, Dr. Haas thanks for keeping 6083 functioning and I absolutely enjoyed using the resources form 6083 especially the best pipettes. It was fun to collaborate on the ELP in double emulsion project and winning the prestigious collaboration of the year award. Jokes apart thanks for being a great support in this journey. **Nicolo**, el patron, thanks for the parties you hosted and all the fun times. **Riccardo**, signore, thanks for the chess games during lunch break, coffee break, and other unaccounted breaks. **Vahid**, it was always good to have conversations with you and I wish you all the best for future. **Akankshya**, thanks for asking me to join the dutch class, I can finally reply in Jaa… and Nee... I wish you all the best with wrapping up and good luck for the future. **Sophie**, thanks for suggesting me some good articles, especially the one from van Lange et. al helped me in finishing the discussion. **Ellard** thanks for having good discussion during coffee

breaks. I hope your child is allowing you to sleep better now. **Ayushi**, it is always fun to talk to someone in Hindi, thanks for the short talks and I wish you all the best for your journey. A big shoutout to the **PhD** and **Post doc** community of PCC for their assistance.

To my office mates **Ram, Huy, Sven, Niek** and **Prathap** thanks for helping me out with settling in the group. Ram I enjoyed your sambhar rice a lot. **Berend, Zohaib** and **Nirzar** although we shared the office for very short time, I enjoyed the time with you guys. **Xuefeng**, thanks for being a great officemate, your support during the writing phase was definitely needed to finish the writing.

Becky, Rebecca Stephan I have known you since the first day I arrived in this flat land, and I cannot thank you enough for your support in this journey. But let me begin with this, thanks for saving my life by educating me how to switch on the heating! Whether it be a coffee in Wageningen or dinner in Waterfirehouse/Bennekom/Ede our unfiltered conversations on what's happening in life helped a lot to go through this process of PhD. Thank you for being my paranymph. Meiden van H8 boven **Becky, Bea, Jody** and **Raquel** you were one of the first people I knew in the Wageningen and thanks for giving me the AID tour in cold December. I enjoyed our house dinners, secret santa and the parties we went together. PS I will keep making the "holy" rice whenever you visit. **Ludooo**… having you as a housemate in waterhouse during covid was amazing. Learning the Italian culture, exploring the abandoned firehouse, and occasionally breaking the covid rules, and hosting large barbeques were one of the most memorable days. Thank you for all the fun times. **Laney** (Eline) I had such fun times having you as a housemate. The spontaneous plans to go for a coffee which changed liked the dutch weather and ended up drinking a couple of Wageningse blond. I admit now that kringloops are better thank buying firsthand and haarweg dropbox is even better. Thanks for always being there. **Chandan**, the master chef, thanks a lot for making all the delicious food and more importantly feeding this hungry belly. I like you positive attitude and keep rocking at the Salsa parties. Mr. **Martijn**, thanks for coming to that one dinner in waterhouse, life would have been so different for you if you haven't joined :D. Jokes apart, it is absolute fun to have you around for dinners, outings and all the long bike rides. I hope to have much more bike rides with you in future. **Klaudia** you passion for climbing is remarkable and I wish you all the best for both climbing sport and career. Thanks for sharing your thesis template with me, I wouldn't have met the thesis submission deadline without your help. Mighty **Mites** what an amazing personality you are! Thanks for being such high- spirited person and organising the Sking trip. Despite being a bambi on the snow, secretly I enjoyed sking and would like to do it again. Thaks for joining the biking events. **Domi** it was

fun to join the sking holidays with you and I wish you all the best for future endeavours. Mr. Hendricks **Filip**, the first time we met you helped me move to waterhouse and spontaneously took me to IC. Since then it has been pleasure to have you around. I am happy for your new adventure at SCB as docent and I hope to keep seeing you more often there. Corrie/**Kori**/Corie your vast knowledge over random stuff always intrigued me but importantly thanks for sharing the "braai" knowledge. Wish you all the best with the coming the T20 championship, I hope its not the kangaroos again. **Amber** it has been great to have you around for the c-squad events and I wish you and Kori all the best for little extension of your family. **Christoph** you stayed with us for a short span, but it felt like you were part of the bennekom house forever. I had interesting fun conversations with you and thanks for providing the Gottingen tour from you. **Mark** you have been a great addition to the bennekom house. Pulling off the wood event in the forest was definitely worth the hastle to keep the bennekom house warm. **Alesandro** Roman, thanks for introducing Nintendo in my life and approving the masala pasta. I am looking forward to move to Italy and opening the Bella Masala Pasta restaurant. **Antonio** signore! thanks for teaching me the only important Italian vocabulary, which I cannot write here. It is always fun to have you around with your laid-back personality. **Berte** Armano, you perfectionist suta madre it was great to have you as neighbor in waterhouse and thanks for all the good dinners, international knowledge transfer and fun times.

Ellen, thanks for making sure I keep my health in good condition and not become a couch potato. It was always fun to do steps and indoor biking class with you. I enjoyed joining your farewell lessons and I wish you a very happy retirement. PS: I am already looking forward for my retirement. **Ingi**, although I am graduating, I will still keep coming to bongards and join your classes for some more time. Thanks of the intense indoor biking sessions . Oscar, onze relatie begon als leraar en student, maar voelt nu meer als een vriendschap, bedankt voor alles wat je mij hebt geleerd. Hopelijk ik zie je vaker in Ede.

Reflecting on the past decade when it all began, the PhD journey in itself seem relatively short. The process to build the foundation started in 2013 when I opted for molecular virology course and it was you teaching **Sachin** sir that made the most complicated viral pathways easy and fun to learn. Having you as a bachelor and master's thesis supervisor made me realise that research is not a job but more of a lifestyle. I want to thank you for being a fantastic teacher, mento, supervisor, and guiding me through this process. **Sudhir, Manisha, Polakshee, Barnali, Moushumee, Aditi, Vishnu** and **Rakeshji** you guys were my first lab mates and I salute you for bearing with the 21 year old me in the lab. On the positive not, I finally started wearing long pants in labs, use gloves and no more taking naps in the lab.

Aur bhai log "finally project mil gaya". Vivek Amar**Nani** aab tuzhe shukriya kaise bolu ? 14 saal ki dosti hai, muzhe behtar tu muzhe janta hai. Bohot baar saab chodke naukri karna kaa maan kiya lekin tune bhatkne nahi diya. Yaha tak pohochane ke liye shukriya is kaamyabi ka eak bada hissa tere naam. **Sumi**nakshi tumhara yogdaan mera mansik santulan banake rakhne main atulya hai. Ghar se door rehneke baad bhi pure Bollywood, Roadies and Splitsvilla ki khabre muzhtak pohochti rahi tu, Dhanyawaad! Entra **Pinnam**neni Jaivardhan rao, Civaraga nenu biotechlo scopni kanugonnanu, asalu scopeu technichelo alcherlo undi. Neha **Tadi**chetty, biotechki EP kante merugani scope undi :D. Pun aside thanks a lot you guys for your love and support. **Aditya** Sarma and Surendra **Swami** thanks for sharing the knowledge of all the random games, Netflix account and the fun times travelling through the mountains and dessert. Tushar **Thulkar** aur Sanket **Somku**war hostel main thode jyada hi maje ho gaye the. Tumhe dhanyawad bolne se behtar main mafi hi mangta leta hu ki tumhe muhze zhelna pada. Par kuch bhi bolo AOE se zabardast dustra game nahi aur "Player" se behetar koi movie nahi. Shukriya bhai log is safar main saath dene ke liye. **Anvay** Meshram, thanks alto for support during the Narayana days, teaching adobe illustrator in IITG and now designing my thesis cover. Saurabh **Soni** thanks for helping me with networking. I would not be in the Netherlands if you wouldn't have connected me to the right people. Rit **Prateek** Mishra and **Manju** Nath thanks for all teaching the balance between study and sporty time.

Dr. **Bhushan** Toley thanks for giving me the opportunity to work on one of the most exciting projects of point of care diagnostics. Your vision and determination to make hi-tech laboratory setups accessible to common people inspired me to think one step beyond. I absolutely enjoyed the whole informal and friendly atmosphere at the Toley Lab. Thank you for the opportunity to work with you. Shruti **Soni** sorry Dr. Shruti Soni, my lab neighbor, your childish curiosity to know everything and fearlessly asking the most silly non-scientific questions was such an charm. Thanks a lot for asking me all the molecular biology question and helping me strengthen my understanding of mol-bio. Dr. **Navjoth** Kaur your dedication, hardwork and staying focused helped me a lot in this journey to not deviate from the goal. Thanks for the help and assistance in the lab. **Sathish, Saylee, Andrea, Dharitri, Mithilesh** and **Suraj** thanks for all the good times and fun conversations during the tea breaks.

Vaseefoo…. the time has finally come, the book is ready and it's time to end this chapter only to open a new one. Thanks for providing all the mol-bio resources in laboratory and helping me with troubleshooting. But more than that thanks for helping me out with preparing applications, SOP and all the great music sessions at R-Block. Your support in IISc was indeed a big contribution for me being here. Sushant **Sarkar** aapke saath baithne main to kuch alag hi mahol ban jata tha. Gold

nanoparticle ke baadshah ho aap, aur larger than life mansikta ke saath aapne IISc ka mahol kuch rangeen hi kar diya. Shukirya aap dono ko is safar main mera saath dene ke liye. Abinav **Mishra**, thanks for introducing me to the group workout sessions at Cult fit. So far this has been my favourite type of workout and I still continue to do it whenever I can.

During the stay in Bengaluru, **Kartik** Suvarna you were like home away from home at Prestige Wellington Park. Watching cricket, working out, day trips and the list goes on, what fun times huh! **Praveen** uncle thanks for hosting all the friday evening mandatory 5072 dinks session and **Geeta** aunty for the board game nights. **Shanta** maushi, thanks for providing all the sunday morning poha, I still continue the tradition. **Anu** if I can go back in time, I will relive the fun music sessions in the balcony of 8093 with Kartik singing in his melodious voice while **Vicky** plays guitar and you constantly saying "Don't pakao yaar". What good times we had. Also, **Vicky** hope you finally got the dream guitar and enjoy jam session with your daughter. The two most lovable fur babies **Scotch** (may his soul rest in peace) and **Crunchy** were the best stress buster after a long day at work. Captain **Vishnu** thanks for share all the thrilling flying stores. I can listen to them for hours. Dr. **Soumya** thanks for the Goa and Trivandrum trip, it was indeed very fun trip and a lot of amazing food.

Varun, Kaustubh, Neville and **Aadar** thanks for making the TISS channel and importantly doing all the bhankas on the podcast. I found the channel at the food delivery app ratings episode and main saab chatish. HandoP you guys have made this PhD journey feel much smoother and fun. Wish you all the best and hope to see you live soon.

Aaji, Kausalyabai Ganar, thanks for taking care of me in my young age. I will always remember you making "kala" after school, and "chaha poli" in evening. Thank you for every single thing you did for me. **Baba**, Ashok Ganar, I never got the chance to express my gratitude for your unconditional support during the whole education phase. I can finally say that I am now done with school and you can stop asking " शाळेत गेलो होता? ". I promise everytime I visit you I will make sure to bring your special gift along with me. **Aai**, Sunita Ganar, only one person can offer unconditional love and that is you. The amount of promotions you rejected to be able to provide to me and Sonu is unimaginable. Thanks for spoiling me a little, I refuse to grow and will always be your childish dada. **Sonu**, aee Bonga, this is just the beginning we have a long way to go from here on. Thanks for being the supportive sister I needed. Your are the real glue of Ganar family who keeps everyone together. I wish you all the best with raising **Oshin**. **Sonu** and **Pankaj**, this is the first trip for you to visit me and I hope this is just the beginning and more adventure times are awaiting

for us. Thank you guys for taking care of the family especially during Covid and all the love and support you gave me.

Sevanand kaka and **Kalpana** kaku, everytime I visit Yavatmal, the party is incomplete without your presence. Kaka, whenever I come I will make sure there is always a new bottle of whiskey waiting for you. Kaku, your cooking style is amazing especially "khur mundi", thankyou for all the " पाहुणचार ". **Mayank**, we had a lot of fun roaming around the streets of Yavatmal in 2017, especially early morning car ride. I hope to see you more often and wish you all the best for your upcoming adventure. **Sumu** and **Chotu**, thanks for all the fun party times, but you guys have to join more often from now on. **Geeta** atya and **Atul** mama thanks for always visiting me whenever I come to Yavatmal. However, I hope to see you more often here in NL from now on. **Bakul**, having you around in Wageningen is like having family around, thanks for the support and wish you all the best with your PhD. Mothi aai, thanks for all your support since 1993, I will always remember the magical "डाळ भाजी" in Agrawal layout. **Swati** tai, **Nitin** Bhauji, **Vibha** tai and **Pritam** bhauji it is always a pleasure to visit you. I will never give up the chance of being the younger brother and keep getting pampered from you guys. **Rucha**, I wish you were here to support me in this ceremony, you will always be in my heart, may your soul rest in peace. **Mothe** Baba, thankyou for supporting me in this journey, may your soul rest in peace.

Sanidhya, Aanya, Sanvi, Aavya and **Oshin** you gen-z and Gen-alpha kids, it is absolute pleasure to see you guys grow. Just like your mothers have pampered and spoilt me, I will definitely take the liberty to pamper you guys and maybe spoil you a little bit :D. I am sure you guys have a very bright future waiting for you. Keep working hard and wish you all the success.

Ik denk dat ik kan nu dit zegen, mijn nieuwe vlaamse familie **de Linthouts**. Bedankt **Marc** voor alle goede diners, barbecue een allen goede wijnen. Ik vind het leuk om met uw te praten en hoop je vaker te zien. Mevrouw **Dorien** voor nu mijn vlaamse is gewoon " Ja maar Ja alle…" maar hoop ik dat in de toekomst me je in vlaamse kan praten. Jonathan, meneertje thanks for making it to the ceremony, I appreciate all you efforts to come here all the way form Zwitserland. It means a lot to me. Oma bedankt voor al de biertjes dat je me hebt aangeboden. Hopelijk In binnenkort wij zijn allemaal "toopen". **Meme** bedankt voor de lekker eten een beertjes. Ik zal nog niet meer kraantwater drinken.

And Finally… to my dearest **Charlotte**…Shlot…Shilooo…. you have been by far the most important person who kept me sane throughout this PhD. When I was struggling with tick project you introduced me to experts from your group. During

stressful intense writing phase you lifted my spirit up. From Haarweg to now you have been the constant of my life. Thanks for being my travel buddy, cooking partner, my chauffer, and importantly the person that keeps reminding me that I cannot just sit on couch the whole and do nothing :D Thanks for baring with my laziness and mostly annoying habits, I am so grateful to have you by my side and I cannot wait to step in the next stage of the life with you Shilo….

Ketan – Ede 2024

Ketan Ashok Ganar was born on February 11, 1993, in Yavatmal, Maharashtra, India. He spent his early education years until the age of 15 in Yavatmal where he was enrolled at Free Methodist English High School. In the year 2008, during the final two years of his high school education, he relocated to Hyderabad, a city in southern India, to prepare for national competitive examinations.

In the pursuit of his engineering aspirations, Ketan moved to Guwahati, a city in the northeast of India, in 2010. There he enrolled in Bachelor of Technology program in Biotechnology at the Indian Institute of Technology, Guwahati (IIT Guwahati). As a part of his undergraduate thesis, he worked on cloning and purifying nucleocapsid protein of Newcastle disease virus gaining hands on training in molecular biology. Furthermore, Ketan opted for a Master's in in the Biosciences and Bioengineering at IIT Guwahati. During his master's thesis under the supervision of Prof. Sachin Kumar he worked on a project focused on identifying and characterizing viruses infecting avian species. He characterized and reported seven virulent strains of chicken anemia virus isolated from dead chickens and one virulent strain of avian paramyxovirus type-1 isolated from dead pigeon.

By the conclusion of his academic journey at IIT Guwahati, Ketan explored the diagnostic aspect of infectious diseases. Consequently, he relocated to Bengaluru, a city in southern India, in 2017. There, he assumed the role of a research fellow under the supervision of Dr. Bhushan Toley at the Department of Chemical Engineering, Indian Institute of Science Bengaluru. He primarily worked on project focused on developing low cost diagnostic kit for the detection of drug-resistant Mycobacterium tuberculosis in resource limiting setups. He prototyped a paper-based lateral flow assay which could detect *M. Tuberculosius* rpoB gene.

In 2019, Ketan began his PhD journey at the Laboratory of Physical Chemistry and Soft Matter under the supervision of Dr. Siddharth Deshpande and Prof. Jasper van der Gucht of Wageningen University and Research, Netherlands. This thesis, entitled "Drops of life: Designing membrane bound and membraneless confinements" is the outcome of research projects performed during this period.

OVERVIEW OF COMPLETED TRAINING AND SUPERVISION ACTIVITIES

Discipline-specific activities

- Han-sur-Lesse Winterschool, PCC Wageningen University, Han-sur-Lesse (BE), 2020
- Dutch Biophysics conference, NWO, Veldhoven (NL), 2020 †
- Dutch Biophysics conference, NWO, Veldhoven (NL), 2021 †
- Designing functional biomolecular assemblies: Beyond biology, EMBO, Bled (SL), 2021
- Synthetic cell international conference, European synthetic cell initiative, Hague (NL), 2022 ‡
- Dutch Biophysics conference, NWO, Veldhoven (NL), 2022 †
- International Soft Matter Conference, NanoBioMedical centre of the Adam
- Wickiewicz University, Poznan (PL), 2023 ‡
- Dutch Biophysics conference, NWO, Veldhoven (NL), 2023 ‡
- Physics of Life, NWO, Amsterdam (NL), 2023 ‡

General courses

- Project and time management, WGS, Wageningen (NL), 2020
- PhD Week, VLAG, Barlo (NL), 2020
- How to present in soft matter, BW Science, Eindhoven (NL), 2021
- Scientific Integrity, WGSs, Wageningen (NL), 2021
- Data viissualization workshop, The Data Vision Lab, Wageningen (NL), 2022
- Scanning electron microscope training, WUR, Wageningen (NL), 2022

Assisting in teaching and supervision activities

- Advanced Soft Matter Practical, PCC WUR, Wageningen (NL), 2021-2023
- General Chemistry, PCC WUR, Wageningen, 2020-2021
- Supervision of thesis students, PCC WUR, Wageningen, 2020-2023

Other activities

- Preparation of research proposal, PCC WUR, Wageningen, 2020
- Weekly group meetings, PCC WUR, Wageningen, 2019-2023 ‡
- Journal club, EmBioSys group meetings, PCC WUR, Wageningen, 2019-2023

† Poster presentation
‡ Oral presentation

Thesis Cover design by Anvay Meshram and author.

Thesis formatted and printed by ProefschriftMaken.nl.

The work was financed by PCC Sectorplan. Financial support from Wageningen University for printing this thesis is gratefully acknowledged.